Doctoral Dissertation
Doctoral Program in Electrical, Electronics & Communications Engineering (36th Cycle)

Introducing Advanced Conductors and Semiconductors in 3D polymeric composites for further electronic & photocatalytic applications

Alejandra Salas
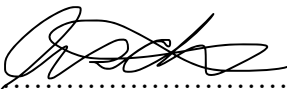* * * * * *

Supervisors
Prof. Cocuzza Matteo
Prof. Pirri Candido

Politecnico di Torino

September 28, 2024

I hereby declare that the contents and organisation of this dissertation constitute my own original work and does not compromise in any way the rights of third parties, including those relating to the security of personal data.

....

Alejandra Salas

Turin, September 28, 2024

I would like to dedicate this thesis to my loving father for supporting me and showing me how greatness can be accomplished & my mother for turning me into the woman I am now.

Not only my parents but my grandparents & extended family, for being there for me in my worst possible times.
As I believe that having solid roots, can make you grow and standby the hardest life conditions.

Acknowledgments

Table of Contents

Chapter 1

Chapter 2

Chapter 3

Chapter 4

Chapter 5

List of Abbreviations

AM Additive Manufacturing

3DP 3-Dimensional Printing

CAD Computer-Aided Design

TMPTA Trimethylpropyl triacrylate

BPA-dma Bisphenol A dimethacrylate

$Ti_3C_2T_z$ Titanium Carbide

TMSPM Trimethoxysylylpropyl methacylate

HS Hybrid System

PEGDA Propyleneglycol diacrylate

FTIR Fourier-transform infrared spectroscopy

FESEM Field Emission Scanning Electron Microscopy

XRD X-Ray Diffraction

XPS X-Ray Photoelectron Spectroscopy

RhB Rhodamine B

PhCN Phenyl Carbonitride

TiO_2 Titanium oxide

PL Photoluminescence

SC Semiconductor

CB Conduction Band

VB Valence Band

SLA Stereolithography

µ-SLA Micro-stereolithography

2PP Two-Photon Polymerization

CAL computed Axial Lithography

DLP Digital Light Processing

CLIP Continuous Liquid Interface Production

MJP Multijet Printing

FFF Fused Filament Fabrication

ADAM Atomic Diffusion AM

PAMS Pressured Assisted Micro-Syringes

MJF Multijet Fusion

SPJ Single-Pass Jetting

SLS Selective Laser Sintering

DMLS Direct Metal Laser Sintering

LENS Laser Engineered Net Shape

EBAM Electron Beam AM

LMD-e Laser Metal Deposition with wire,

WAAM wire arc AM

LOM Laminated Object Manufacturing

UAM ultrasonic AM

HF Hydrofluoric acid

HCl Hydrochloric acid

LiF Lithium fluoride

NH_4OH Ammonium hydroxide

NH_4HF_2 Ammonium bifluoride

NaF Sodium fluoride

KF Potassium fluoride

RT Room temperature
TBAOH Tetrabutylammonium hydroxid
Phr Part per Hundred
VP Vat photopolymerization
PI Photoinitiator
MOF Metal-Organic Framework.

DMSO Dimethyl sulphoxide
DI Deionized water.

List of Tables

List of Figures

14

Summary

Additive Manufacturing (AM) permits the development of complex printed architectures, rendering them from a computer-aided design (CAD) towards a physical structure. This technology allows the combination of multiple scientific approaches, starting from the chemistry in the materials, the kinetics & processing of the solidification reactions, and the AM technique applied, which variables would strictly depend on the final product's desired properties. 3D polymeric printing can enclose a whole set of science behind the spatially controlled solidification of its monomeric/oligomeric parts depending on the method chosen, such as fused filament fabrication (FFF), selective laser melting (SLM), inkjet, and vat photopolymerization methods that can include great printing fidelity (<35 μm) and fast printing times (<1h) like Stereolithography (SL) or Direct Light Processing (DLP). Nowadays, for the latter, the market offers inexpensive and more commercial options such as Liquid Crystal Display (LCD) technology.

The photopolymeric resin formulations normally include a polymeric matrix and embedded additives that can provide specific properties as will be explained in this thesis work. Usually, structural characteristics like flexibility and rigidity are attributed to the polymeric matrix, as well as reactivity or even the capacity to withstand extreme conditions depending on the chosen monomers/oligomers. Regarding the additives, there is a whole set of fillers, colorants, and radical scavengers that can be included in the formulation to adjust or incorporate functional properties to the printed structure for specific applications.

The scope of this Ph.D. thesis was to study the inclusion of advanced conductor/semiconductor materials as fillers in 3D printable polymeric matrixes to develop 3D structures for electronic or photocatalytic applications. The use of DLP and LCD was selected as printing technology, allowing fast material processing in their liquid state, and acquiring high-resolution 3D objects. Both printing methods employ photopolymerization, defined as the assembling of monomers/oligomers initiated by the reaction of a photoinitiator with incident light. The reaction starts when a projection of the light pattern from the layer to print arrives on the screen which is in contact with the vat, and slices are rapidly cured, producing a 3D structure in a layer-by-layer process. However, a load of additives and specifically fillers may limit the light absorption of the photoinitiator due to photoblocking

activity or light scattering, leading to a decrease in the reaction kinetics affecting the printing process.

In the first part of the research, the development of polymeric MXene/composites was investigated for the later production of 3D-printed objects applied in electronics. A MXene being a 2D material based on transition metal carbides, carbonitrides, or nitrides with huge research interest given their novelty, and properties such as high electrical conductivity, hydrophilicity, and thermal endurance. The MXene composition used in this study is $Ti_3C_2T_z$, to deliver its electrical properties to build 3D conductive objects by photopolymerization. These were then introduced into a monomer formulation of Bisphenol A dimethacrylate (BPA-dma) and Trimethylolpropane triacrylate (TMPTA), whose reactions kinetics was studied by photorheology, while chemical characterization and IV measurements were performed to study the material properties. The choice of these monomers was based on their compatibility with an annealing post-process, which was further exploited to enhance the electric conductivity of the 3D structures.

The innovation of this study relies on the use of MXenes in DLP as a printing method and the study of the influence of Titanium carbide ($Ti_3C_2T_z$) inside the vat photopolymerization. Also, in the exploration of how its properties are affected when including them in 3D objects and submitting them to high temperatures when using the annealing as post-process.

In the second part of the research, the use of a specific advanced semiconductor photocatalytic material was explored also as filler in DLP and LCP printing methods for the development of 3D printed composites. The semiconductor chosen being a hybrid system, composed of phenyl carbonitride as the organic part and TiO_2 in its anatase phase as the inorganic one, forming a heterojunction of Phenyl carbonitride and Titanium oxide (PhCN/TiO_2) known for its great performance in photocatalysis. The purpose of this investigation was to explore the inclusion of PhCN/TiO_2 in 3D printing vat photopolymerization and how its photocatalytic performance was affected when included in the printed structures. As a polymeric matrix, a polyethylene glycol diacrylate (PEGDA) formulation was considered adding a silane monomer 3-(trimethoxy silyl)propyl methacrylate (TMSPM) to improve mechanical resistance and the ability of the matrix to withstand the photocatalysis reaction. Furthermore, comparing the best method to include PhCN/TiO_2 in 3D printing and translating its photocatalytic activity which was evaluated by the degradation under visible light irradiation of Rhodamine B (RhB), the material was considered also under a coating strategy. For this, the silane monomer was used as a coupling agent between the organic matrix and the inorganic part of the hybrid system, via the sol-gel technique.

The innovation of this part is the inclusion of this hybrid system inside the vat photopolymerization and as a post-treatment, for the analysis of its application as photodegradation capacity at visible light. Also, its influence in the PEGDA system, and how by adding TMPSM in the matrix properties are improved to withstand the inside reactions. In the last set of experiments, a glassy polymeric composite approach was also utilized for its inertness over extreme environments with the

same polymeric matrixes, which is going to be introduced in the appendix as it did not work effectively.

Throughout the Ph.D. and this manuscript, the development of different polymeric matrixes and their optimization was done to improve the quality of the final composite when including the fillers in the formulation. 3D printing can serve for fabricating objects with added values, in combination with multi-scientific approaches. The design can applied in a wide set of application fields as seen during these years, as electronics and photocatalysis.

Chapter 1

1. Additive Manufacturing

1.1. Background & Evolution

Additive Manufacturing (AM) technology is a digital technology that has integrated machinery, computers, numerical control, and materials in the global advanced manufacturing field for the past 30 years (Y. Shi et al., 2021). It is a multi-disciplinary field that requires interaction between scientists, engineers, software developers, and 3D designers. Also known as three-dimensional printing (3DP), this technique has the advantage of generating superior components with complex shapes in any possible geometry with simple production steps, considering lower production time, high flexibility, and minimal wastage of material.

In the 1980s, when the invention of binder jet printing was settled by MIT (Massachusetts Institute of Technology), the definition of 3DP was "A process under development at MIT for the rapid and flexible production of prototype, end-use parts, and tools directly from a CAD model" (Kaczynski, 1989). Though, it was Hideo Kodama in 1980 who developed the earliest 3D printer, prototyping a machine that created parts layer-by-layer using a resin that could be polymerized by UV light (Kodama, 1980). Today this concept is much broader, involving new advancements and even portable personalized printers, disregarding this definition, as it did not effectively describe the term anymore. According to the American Society for Testing and Materials (ASTM), AM is the process of creating three-dimensional (3D) objects by successive addition of material (International, 2012). However, even if AM and 3DP fall under the same definition and are commonly considered synonyms, the two terms are usually employed to refer to different domains: where AM is mainly used at an industrial level, involving enterprise and supply chain; 3DP is associated with low-cost techniques, beyond industry areas, like research centers, business stores, and equipment.

Historically, AM technology was introduced in the 1980s, and limited to prototyping (Saleh Alghamdi, John, Roy Choudhury, & Dutta, 2021). On the other hand, only after 2009, its development started to increase rapidly, witnessed by an increasing number of scientific publications. Figure 1.1 reports the publications recorded in the SCOPUS database, from 1980 to now, with 73,557 documents, noteworthy the main increment in publications is seen after 2008 and, currently, the curve is still growing.
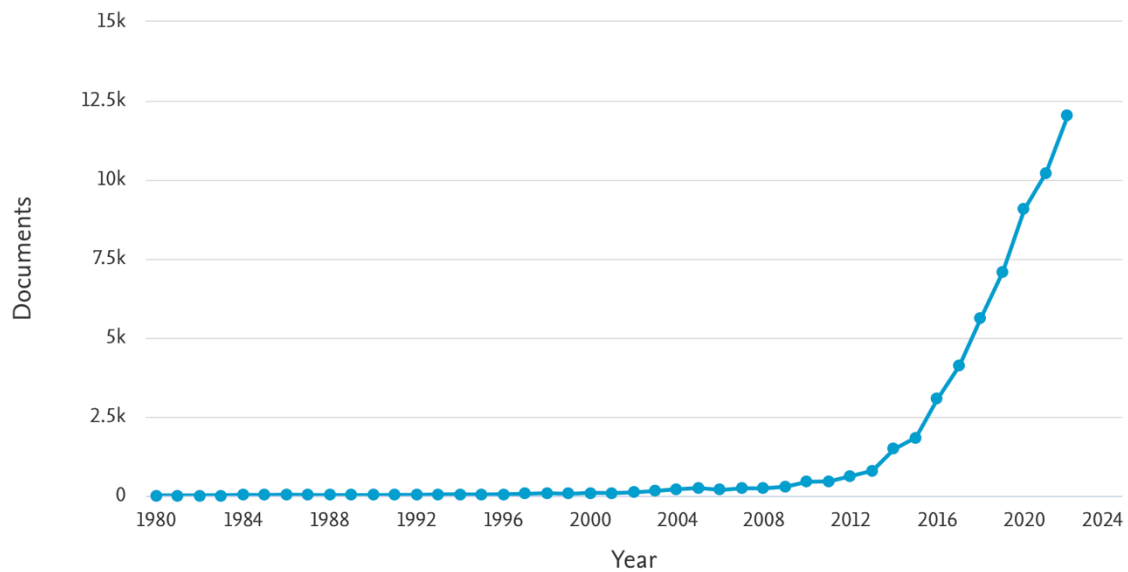
Figure 1.1. Results of documents in SCOPUS from 1980 up to now using the keywords "Additive Manufacturing"

The aim of the 3DP is the creation of objects from a computer-aided design (CAD) tool in a single machine. The products are created through a selective and successive material addition, in a layer-by-layer approach, in which each layer corresponds to a cross-section of a digital file. Currently, depending on the technology used and the client's demands, materials can be designed or combined to achieve the best performance. Describing in general the process, this consists of translating the CAD file into a digital format compatible with the printer (g-code), to generate the printing pattern, which is implemented to fabricate the desired object and finally, depending on the final application, a post-processing can be also considered (Figure 1.2). Among its various advantages, AM can be employed with diverse materials, including metals, ceramic, and polymers along with its different combinations, to form composites, hybrids, graded functional materials, and hydrogels in different physical states (solid, liquid, viscoelastic, and gels) (Saleh Alghamdi et al., 2021).

1. Creation of the CAD model and storage as a readable file (.stl)

2. Slicing if the model into cross-sectional layers

3. File transfer & Machine setup

4. Printing process

5. Post-processing

6. 3D object
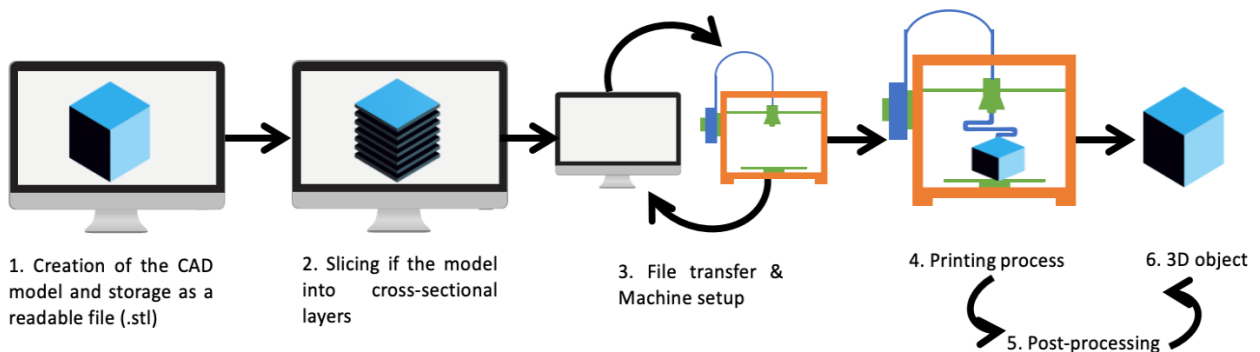
Figure 1.2. Schematic representation of the 3DP process

In this regard, the AM process is very broad and consequently, the ASTM has formulated a set of standards that classify the range of AM into 7 general categories (ISO/ASTM 52900:2015). The 7 types are: jetting, binder jetting, vat photopolymerization powder, powder bed fusion, material extrusion, energy deposition, and sheet lamination (Shahrubudin, Lee, & Ramlan, 2019). These processes are categorized using parameters depending on speed, material strength, resolution, scalability, build volume, cost, quality, and surface finish. The following Table 1.1 shows each category with common 3DP examples, the materials that can be used, and the corresponding advantages and drawbacks of each technology.

Nowadays, 3DP is widely used in industry and research departments for the development of customized products. The versatility of this technology has made it possible to use it in a wide range of applications and fields, such as aerospace, automotive, machinery, medical implants, handling and robotics, electronics, lifestyle products, etc (Al Rashid, Khan, G. Al-Ghamdi, & Koç, 2020). Though, the main problem relies upon the scalability of the processes and production to scale-up to an industrial level.

Table 1.1. Seven AM categories according to the ASTM classification

Category	Image	3DP Tech.	Advantages	Drawbacks	Material
Vat-Photopolymerization (VP)		SLA, μ-SLA, DLP, CLIP, 2PP, CAL	High accuracy, fast building speed, tailored formulations	Overcuring & scanned line shape, high cost for supplies	Polymer, Ceramic, composite
Material Jetting (MJ)		Polyjet, MJP, NPJ	High accuracy, multiple materials	Require support, low-strength material	Polymer, ceramic, composite, hybrid
Material Extrusion (ME)		FFF, PAMS, ADAM	Inexpensive, multiple materials	Less accuracy, poor resolution	Polymer, composite
Binder Jetting (BJ)		MJF, SPJ	Different colors, wide range of materials	Post-processing, high porosity	Polymer, ceramic, metal, composite

Powder Bed Fusion (PBF)		SLS, SLM, DMLS/SLS, EBM	High precision, no support, range of materials, high strength parts	High power usage, post-processing	Polymer, ceramic, composite, hybrid, metal
Direct Energy Deposition (DED)		LENS, EBAM, LMD-e, WAAM	Extremely fast, part repair	Post-processing, poor resolution	Metal, hybrid
Sheet Lamination (SL)		LOM, UAM	High speed, low cost	Post-processing	Polymer, metal, ceramic, hybrid

*The abbreviations for the different 3DP technologies can be found here: SLA stereolithography, μ-SLA micro-stereolithography, 2PP two-photon polymerization, CAL computed axial lithography, DLP digital light processing, CLIP continuous liquid interface production, MJP multijet printing, FFF fused filament fabrication, ADAM atomic diffusion AM, PAMS pressured assisted micro-syringes, MJF multijet fusion, SPJ single-pass jetting, SLS selective laser sintering, DMLS direct metal laser sintering, LENS laser engineered net shape, EBAM electron beam AM, LMD-e laser metal deposition with wire, WAAM wire arc AM, LOM laminated object manufacturing, UAM ultrasonic AM.

** This table has been adapted from the following ref (Nazir, Abate, Kumar, & Jeng, 2019; Sefene, Hailu, & Tsegaw, 2022).

In this context, this thesis is focused on 3DP technologies for the development of liquid printable resins based on photopolymerization. Therefore, the following sections will describe the science behind these topics in detail.

1.2. Polymers in AM

Table 1.1 shows that 6 out of 7 AM categories can be applied to polymeric materials, giving its advantages and drawbacks, and DED was excluded as it is used mainly in metal printing. This section will briefly describe their principles and use in polymers, focusing on Vat-Photopolymerization (VP), which will be explained in detail in section 1.2.1 given its importance in the development of this thesis.

MJ – Material Jetting

A jet printer is comprised of a print head with thousands of nozzles, which are employed to fabricate the 3D structures by depositing ink droplets onto a substrate

(base platform), in a layer-by-layer form (Ligon, Liska, Stampfl, Gurr, & Mulhaupt, 2017). The surface tension, viscosity, and volatility of the material play a vital role in the printing (Chou, Gamboa, & Morales, 2021). As per ISO/ASTM BJ and MJ use the same printing mechanism handling different materials. According to the technology, the printer heads deposit droplets of melted material or photocurable resin containing additives onto a build platform, where it solidifies or is cured.

ME – Material Extrusion

The 3D object is fabricated by selectively dispensing the printing material or ink and binder through an orifice. This system uses computer-spatially controlled methods to disperse the ink and to deposit the melted filament layer-by-layer, to finally obtain a 3D structure (Lewis & Gratson, 2004). There are 2 main types of extrusion-based systems: PAMS (Pressured Assisted Micro-Syringes) and FDM (Fused Deposition Modelling), with the difference between them mostly related to the used material (solid wires for FDM, gels or pastes for PAMS). These methods are the most widespread due to cost and rate of production.

PBF – Power Bed Fusion

In this process, powders are selectively melted to form a 3D object using thermal energy (e.g. a laser). The printing begins by feeding powder into the building chamber, where it is homogenized before exposure to a high-power laser beam. As the laser passes point-by-point, it melts the particles to form a joint 2D layer. The build platform then steps down to a height equal to the layer thickness, then a second layer is spread on the first layer and sintered on it using the laser. The procedure is then repeated until it forms the desired 3D structure (Lakkala, Munnangi, Bandari, & Repka, 2023). The critical process parameters include the bed thickness, temperature, and powder properties like particle density, shape, size, and size distribution.

BJ- Binder Jetting

In a BJ printer, the printing head sprays a liquid agent (binding agent solution) selectively as per the CAD design onto a powder bed. The subsequent chemical reaction leads to the joining of powder particles, employing the evaporation of solvent or curing. Once a section is formed, another layer of powders is deposited, and the process is repeated until the formation of the object.

SL – Sheet Lamination

This process involves the shaping and bonding of material sheets. The laminated object manufacturing is conducted by trimming the material sheets into the required dimensions and sticking them together with an adhesive to produce a

3D object. this technology can be used also for metals, using ultrasonic AM welding (Bhatt, Kabir, Peralta, Bruck, & Gupta, 2019).

1.2.1. Vat photopolymerization (VP)

Vat photopolymerization is an AM technology where the photopolymerization occurs in a resin tank, commonly known as vat, which contains a formulation of monomers, additives, photoinitiators, and fillers, that will be specified in sections afterward (Pagac et al., 2021). The setup includes a light source that is employed for the photopolymerization reaction which, in turn, performed layer-by-layer, leads to the fabrication of the 3D object. The advantages, disadvantages, and types of VP are mentioned in Table 1.1.

The process consists of spatiotemporal-controlled photoactivated polymerization enabling precise localized solidification of resin materials, resulting in high-shape fidelity of the final 3D object to the CAD file (Salas, Zanatta, Sans, & Roppolo, 2023). The light irradiates perpendicular to the XY plane, and depending on its resolution, it outlines a minimum volume unit or voxel. A scheme of how the light is guided throughout the different VP technologies is reported in Figure 1.3.a, whereas Figure 1.3.b. shows the two possible configurations of the build platform.
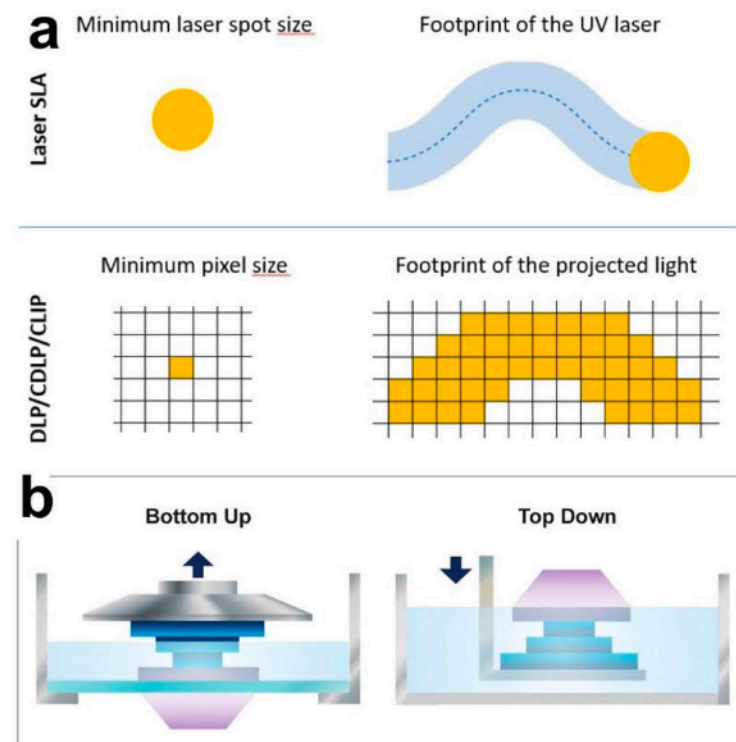
Figure 1.3. SLA-based technologies. a) Methodologies to solidify photopolymer resins in laser-based SLA and DLP. Image reproduced from ref (Pagac et al., 2021) b) Differences between bottom-up and top-down technologies. Image taken with permission from ref (M. Lee, Rizzo, Surman, & Zenobi-Wong, 2020).

1.2.2. Principles of photo polymerization applied to 3D printing.

Photopolymerization is a polymerization method that employs the energy provided by photons (i.e. light) to initiate the reaction; it occurs only by polyaddition, meaning the continuous addition of propagating species with unreacted monomers. Usually, the monomers used in 3D printing are multifunctional (i.e. bearing more than one reactive species, so as the reaction propagates the macromolecules form crosslinking points, and by consequence thermoset polymers (J.-P. Fouassier, 1995). Photopolymerization is typically divided into three main steps: initiation, propagation & termination (Yagci, Jockusch, & Turro, 2010).

1.2.2.1. Initiation

The step in which active species are generated by light exposure. The reaction starts when a photoinitiator (PI) absorbs a specific wavelength of light radiation and generates initiating species. At this point, the reaction can follow two different pathways, directly generating the reactive species (Norrish I photoinitiators) or aided by a co-initiator (Norrish II photoinitiators) (Garra, Fouassier, Lakhdar, Yagci, & Lalevée, 2020; Junyi Zhou, Allonas, Ibrahim, & Liu, 2019).

The Norrish I photoinitiator absorbs light that excites the molecule to a triplet state, which then decays into a singlet state, with a consequent cleavage of a σ-bond generating 2 radicals that subsequently react with a monomer and/or oligomer. A Norrish type II photoinitiator absorbs the light and the excited molecule extracts an H-atom from a donating co-initiator (e.g. amines), decaying to an equilibrium state, whereas the co-initiator starts the polymerization. For both cases, the initiation mechanism follows Eq.1.1 (J.-P. Fouassier, 1995).

$$PI \xrightarrow{h\nu} R \cdot R_i = \Phi_i I_Z \varepsilon [PI]$$
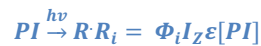
Where $R\cdot$ is the initiating reactive species, R_i is the initiation rate, Φ_i is the initiation quantum yield, ε is the molar extinction coefficient at a given wavelength, $[PI]$ the molar concentration of the PI and I_Z is the incident photonic flux. This last coefficient is related to the incident radiation I_o (i.e. surface radiation), defined in the Eq.1.2 (J.-P. Fouassier, 1995).

$$I_Z = I_o(10^{-A})$$

A being the absorbance, as defined by the Lambert-Beer law in Eq.1.3 (Mayerhöfer, Pahlow, & Popp, 2020)

$$A = \varepsilon z c$$

Where c is the concentration of the absorbing species, which in the present case is the PI and z is the length of the light path. Therefore, the initiation rate is related to both the chemical properties of the PI (via Φ_i) and the light intensity. In contrast, it can also happen that given a certain light source (i.e fixed I_o) increasing the [PI], the light penetration decreases. In VP 3D printing, where the slicing is fixed by the operator (Z steps), there is a better control of the light penetration allowing an efficient adhesion of the different layers and precise printing, avoiding uncontrolled polymerization beyond the desired voxel.

1.2.2.2. Propagation

Here photogenerated species react with stable monomers, leading to an increase in molecular weight and the formation of the polymeric chains or networks. The second step of photopolymerization starts when R· reacts with a monomer (*M*), hence generating a propagating reactive molecule that interacts with other monomers and leads to a growing polymeric chain P·. This process is described in Eq.1.4 (J.-P. Fouassier, 1995)..

$$R^{.} + M \rightarrow RM^{.} \xrightarrow{M} P^{.} R_p = k_p[P^{.}][M]$$
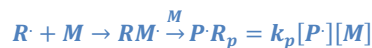
Where R_p is the polymerization rate and k_p is the chain propagation constant.

Most of the time, the photopolymerization goes by chain-growth mechanism, typical for monomers with unsaturated bonds (e.g. vinyl, acrylate, methacrylate) or rings (e.g. epoxy). Though, an alternative mechanism is the step-growth, which is typically given in reactions with thiol-ene/ -yne (Hoyle & Bowman, 2010; M. Lee et al., 2020). Figure 1.4 embodies a schematic representation of both mechanisms and the difference in their kinetic profile.

Chain-growth polymerization

A

Step-growth polymerization

B

C

M_n

Time

— Step-growth   - - Chain-growth
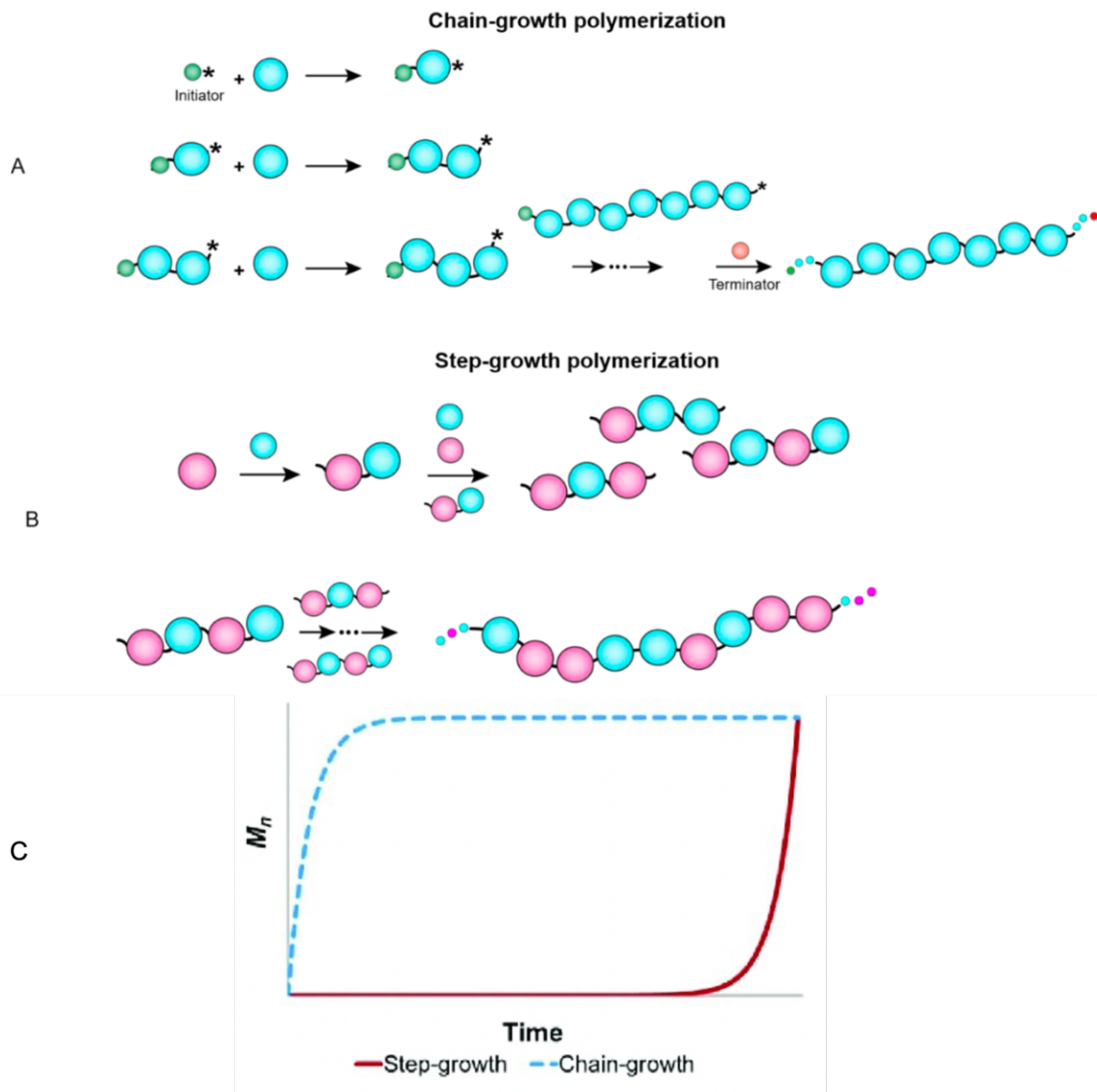
Figure 1.4. Random copolymerization of building blocks (cyan and pink circles represent different monomers or oligomers) (A) via chain-growth polymerization and (B) via step-growth polymerization. Asterisks represent radical species. Image taken from ref (Esmaili, Eldeeb, & Moosavi-Movahedi, 2021). (C) Polymer growth kinetic profiles for both mechanisms. Image taken from ref (Colebatch & Weller, 2019).

The extent of the propagation step determines the molecular weight, which later establishes the gel-point, mechanical, and physicochemical properties of the polymer (Nicholson, 2012). Taking advantage of this knowledge, the design of custom-made photocurable resins is done to achieve faster kinetics that would be translated in 3D printing as shorter irradiation times and controlled solidification. The use of multifunctional monomers is also preferred, which would generate highly cross-linked polymers with rapid gelation, and higher molecular weights (Figure 1.4 C) can reach an infinite molecular weight. Additionally, mono-functional monomers lead to linear polymers, which are generally soluble in their monomers, restricting the possibility of obtaining solid objects.

1.2.2.3.   Termination

The final step, in which polymerization ends, can be defined as the stage when the propagating radical species cease to react to form a stable polymer. This occurs when two growing polymeric chains react, following the mechanism in Eq.1.5 (J.-P. Fouassier, 1995)..

$$P^{\cdot} + P^{\cdot} \rightarrow Polymer \quad R_t = k_t[P^{\cdot}]^2$$

Where the R_t is the termination rate and the k_t is the kinetic constant of the reaction and combining these relations, in Eq. 1.6 we can define the polymerization rate (R_p) (J.-P. Fouassier, 1995)..

$$R_p = \frac{k_p}{k^{0.5}} \, [R_i]^{0.5} \, [M]$$

This last equation is demonstrated to work particularly for mono-functional monomers, but as in 3D printing multi-functional monomers are preferred, modifications in the kinetic should be considered (J.-P. Fouassier, 1995), as it has been demonstrated in literature (Andrzejewska, 2001). Remarkably, the polymerization kinetics in this case is proportional to the first power of the monomer concentration and the square root of light intensity. Resulting that, the quantum yield of the polymerization is:

$$\Phi_P = \frac{R_p}{I_z}$$

Where the quantum yield decreases with increasing light intensity. Moreover, Eq.1.5 demonstrates that the polymerization rate is proportional to the second power of the concentration of the propagating polymeric species (P$^{\cdot}$), which depends directly on the [PI]. As a consequence, by limiting the concentration of PI molecules present, one could speed up the polymerization, but exceeding could lead to termination (Krongauz & Trifunac, 2013). Therefore, an optimum concentration should be selected.

1.2.2.4. Optimizing photopolymerization steps towards better 3D printing

To obtain precise structures it is necessary to have spatial control over the polymerization (Ahn, Stevens, Zhou, & Page, 2020). Resolution is empirically obtained by adjusting the quantity, type of PI, and printing parameters, such as layer exposure time and light intensity. Likewise, other parameters are also important, like monomer reactivity, viscosity, and temperature.

Besides that, to enhance the printing precision two strategies can be applied. The first one is the use of dyes and photoabsorbers to control light penetration and the excess of photocuring on initial layers. The latter are molecules that absorb light in the same spectral range of PI, but without generating reactive species. The absorbance of a formulation is described as(J.-P. Fouassier, 1995).:

$$A_f = z \sum \varepsilon_i \ c_i$$

Equation 1.8

Where A_f at a given wavelength with a given optical path length (z) is the sum of the contributions for the concentration (c_i) of every absorbing species i multiplied for the corresponding molar extinction coefficient (ε_i). Meanwhile, dyes compete with the PI in photon absorption, increase the absorbance, and instead decrease the initiation rate (Eq.1.1) affecting the photopolymerization mechanism. Herein, the dyes in VP 3D printing allow a finer control on the XY plane, decreasing propagation out of the pixel irradiation (Gastaldi et al., 2020).

In this context, the following equation must be taken into consideration:

$$C_d = D_p ln \left(\frac{E_{MAX}}{E_c}\right)$$

Equation 1.9

Where C_d is the curing depth, D_p is the light penetration depth, E_{MAX} is the energy dose per unit of area, and E_c is the critical activation energy. D_p is empirically defined as;

$$D_p = \frac{1}{2.3\varepsilon[PI]}$$

Equation 1.10

Showing, inversely proportional to ε and to [PI]. It emerges that the presence of dyes increases the molar extinction coefficient and decreases the curing depth. Given this, dyes allow for control of the curing depth simulating the Z step of the 3D printing process (Ahn et al., 2020; Lin, Liu, Chen, & Cheng, 2019; Vitale & Cabral, 2016).

The second strategy is the use of radical scavengers. These chemical compounds stabilize free radicals to avoid further polymerization. They interact with either initiating species or propagating species, inducing termination, and avoiding post-curing. The main drawback of their presence in the formulation is that they can reduce the polymerization rate (Cook et al., 2020).

In any case, 3D printable resins and formulation content will be defined and explained more in detail in the next chapter. Nonetheless, it is important to settle that light-curable 3D materials are defined as photopolymerizable resins that are composed mainly of a photoinitiator, and a polymeric matrix that determines the mechanical properties and 3D resolution of the final printed object, besides, that it is possible to add fillers with diverse chemistry to envisage specific desired properties or even colorants for improving resolution, by regulating light-penetration and maintain a proper 3D definition.

1.2.3. Types of VP
1.2.3.1.   SLA (Stereolithography)

In SLA machines, polymer solidification is accomplished by focusing the laser on one specific point using a galvanometric head on the building platform to create the first layer (H. Li, Fan, & Zhu, 2020). The XY- resolution is determined by the laser spot size. Then, the polymer remains attached to the building platform. After the first layer is formed, the platform is raised or lowered depending on the specific configuration, as depicted in Figure 1.3.b. The wavelength and intensity of the light determine its penetration, which also depends on the resin's optical transparency and viscosity. Classic SLA technologies can achieve XY resolution down to 10 μm (Juskova, Ollitrault, Serra, Viovy, & Malaquin, 2018).

The light penetration depth is an important factor that determines each step size, as it needs to be sufficient for curing the entire layer, neither too much as it would lead to over-curing and a decrease of resolution. For this, parameters such as layer thickness, irradiation time, and light intensity need to be optimized. Thus, the Z-axis steps should be optimized to reach a compromise between high resolution and short building times. Mechanically, the vertical resolution depends on the precision of the stepper printer's motor screw and the rotational screw that controls the motion of the building platform (Enders, Siller, Urmann, Hoffmann, & Bahnemann, 2019). Usually, the first layers should ensure a robust binding to the platform with longer polymerization times, followed by the subsequent layers with the optimized parameters. As seen in Figure 1.2, usually post-processing is needed, which is

considered by washing the residual resin on the object with common solvents (e.g. water or alcohols) and the post-curing.

The post-curing enhances the long-term structural stability of the printed structure because it assures the complete conversion of the resins. This step maximizes the probability of reaching the gel point by increasing the cross-linking density, thus the degree of polymerization, by the subsequent light exposure.

The bottom-up approach is the usual configuration since lesser volumes of resin are necessary, as only the bottom of the vat should be covered to allow the process, and the vat depth does not limit the construction volume. Another advantage is that in this process, the newly formed layer has no contact with oxygen as photopolymerization always happens at the bottom, and usually, all the printing is covered/flooded in resin improving the kinetics and curing rate (Lian, Yang, Xin, & Li, 2017).

1.2.3.2 μ-SLA

In the early 1990s, micro-stereolithography was developed differing from normal SLA because the laser spot size was about 5 μm instead of 10 μm (Ikuta & Hirowatari, 1993). Lately, the use of more precise lasers has enabled the generation of submicron structures (Y. Liu et al., 2016), down to 0.??? μm, which is at the limit for a single-photon technology. Nowadays, this technology is commonly used for optic & photonics (Gao et al., 2023) applications to develop microlenses and arrays, also, (Maruyama, Hirata, Furukawa, & Maruo, 2020) developed multi-material μ-SLA printing system with multicolor photocurable resins in high resolution. They proposed a micro-stereolithography system with a linear translational stage for the material exchange, integrating a cleaning step with a solvent to avoid contamination. In the system, a 405 nm laser beam incident to a Galvano mirror passes through a variable neutral density filter and a shutter, to regulate intensity and exposure time, . Afterwards, it is focused on the boundary surface of the photocurable resin and the glass plate using an objective lens with a numerical aperture of 0.1 (magnification x10). This system reaches scanning speed of 1mm/s, a laser intensity of 1mW, with a stacking deviation in the printed structures of approximately 20 μm.

1.2.3.3 DLP

Digital Light Processing consists of the same principle as SLA, however instead of accomplishing polymer solidification in an specific point in space and time, it photopolymerizes the resin by layer-by-layer projections. Therefore, leaving a footprint of the projected light as seen in Figure 1.3.a. The printer directs the light with digital mirror device (DMD) chips, as seen in Figure 1.5. Here each micro-mirror on the DMD represents one pixel from the digital image in the layer to be solidified, achieving a resolution up to 3-5 μm in the XY plane (Yu et al., 2020) in optimized conditions. Each layer consists of an entire projected cross-

section of an object, which usually translates into faster printing times for larger areas. Currently, the best commercial DLP printers claim a resolution of about 20 μm (Gonzalez, Roppolo, Pirri, & Chiappone, 2022).
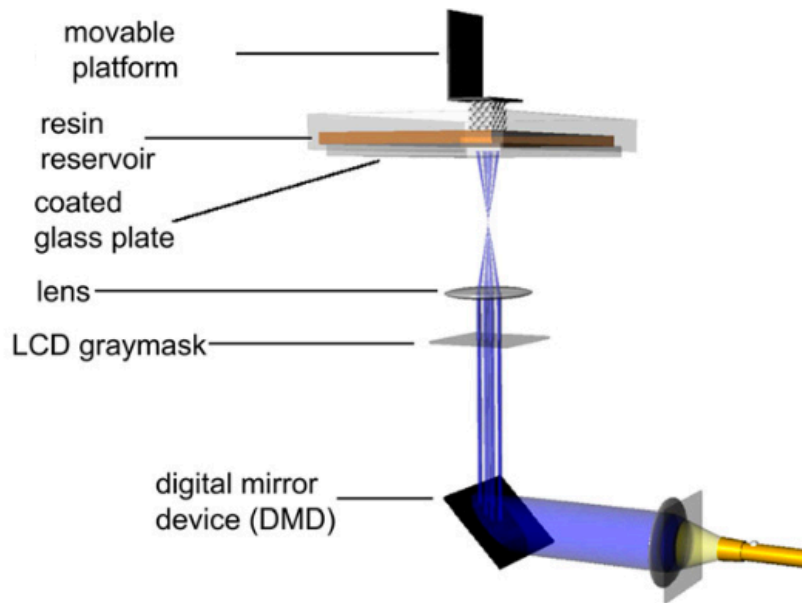
This printing method is promising for the construction of 3D and 4D structures, incorporating micro and nano-scale (Sajjad et al., 2023) features with the usage of light as cross-linking source, curing directly to the vat in a matter of seconds and consisting of a Z-directional motor achieving a moveable platform. However, cheaper printers include LCD screens with lower resolutions and power intakes which have been developed due to the high demand of the low technical level market.

1.2.3.4   CLIP

Maintaining the same working principles of DLP, CLIP printers usually uses a light-emitting diode (LED) array at 405 nm (Pagac et al., 2021) or 385 nm (de Beer et al., 2019) or a liquid-crystal display (LCD) screen, which acts as a mask that directs the layer polymerization. The main difference with DLP consists in the presence of a controlled interfacial layer of oxygen, created at the bottom of the vat through an oxygen-permeable window. Such layer acts as a polymerization inhibitor in the window interface, allowing a continuous interface for

polymerization, near the bottom window, resulting in layer-less printing and increasing the printing speed (500 mm/h). Prof. Mirkin's group recently reported a breakthrough that enhance the printing area and speed, branding it high-area rapid printing (HARP) (Tumbleston et al., 2015), where a flow of fluorinated oil in the base of the printing bed avoids the adhesion of the materials and facilitates the continuous cooling of the printing front at high speed.

1.2.3.5   2PP

In this type of printing, the process is activated by the simultaneous absorption of two photons generated by a pulsed pico- or femtolaser (A. K. Nguyen & Narayan, 2017). The absorption happens in the more energetic part of the laser spot, which starts the free-radical polymerization resulting in structures in the range of 100 nm. The main drawback of this technique is the high cost of the equipment, the limited printing volume (<1 mm in height), and the low printing velocity (0.5-1 mm/s), however it has a great resolution.

1.2.3.6   CAL

Developed at Lawrence Livermore National Laboratory as a volumetric technique, this employs computed tomography (CT) images to generate a hologram within a controlled photopolymer volume. The hologram is generated by the simultaneous projection of several 2D images while the vat tank rotates continuously. The images combine through the liquid resin from different angles, resulting in a 3D hologram with enough energy to photopolymerize a volume of resin. The key parameters are angular velocity and the resin's viscosity. The key point in the technology is the control of the rotation speed which must be enough to prevent the relative shift of the 3D-printed model and the rest of the liquid resin. Another advantage is that as it works volumetrically it has high surface definition and smoothness.

1.2.3.7   XOLO

A different type of volumetric 3D printing, xolography works as a dual color technique, which employs two-wavelength photoswitchable photoinitiators to induce local polymerization inside a confined monomer volume upon linear excitation. This is achieved by intersecting light beams with different wavelengths (Regehly et al., 2020). This technique includes higher resolutions than CAL and a higher printing volume than 2PP, with rapid printing times and minimizing unwanted polymerization with laser sheet-induced curing.

Chapter 2

2. Introducing Polymeric Composites terms for VAT 3DP

This chapter was written based on the published article (Salas, Zanatta, et al., 2023).

2.1. Introduction & General Concepts

Photocurable formulations can be suitable for different VAT 3DP technologies, as mentioned in Chapter 1, i.e. SLA, SLP, CLIP, etc. The liquid resins employed need at least two components to be converted into a polymeric network: monomers/oligomers and photoinitiator(s) (Crivello & Reichmanis, 2014; Layani, Wang, & Magdassi, 2018). Beyond those, for matters of resolution, additives such as radical scavengers or colorants can be added too, more importantly, fillers can be also added to conceive properties; the so fabricated materials are called polymeric composites.

The vat photopolymerization (VP) printing process starts once the patterned light exposure radiates over the resin, generating reactive species or radicals, that promptly convert the liquid monomers into a cured covalent network (Appuhamillage et al., 2019). The involved PI must be compatible with the light source, which is usually UV or visible, the latter being safer and compatible with even cell-laden water-based inks (M. Lee et al., 2020; Samadian, Maleki, Allahyari, & Jaymand, 2020). The PI then reacts with photocurable species, hence, monomers or oligomers that contain single or multiple active groups (mono or multifunctional) e.g. (meth)acrylate moieties, as side or chain-ends. They will enable their association onto a cross-linked network mainly on the irradiated regions, outside of that would be considered over-curing (A. Bagheri & Jin, 2019). Therefore, for an optimal 3D printable formulation, there should be a trade-off between the composition, desired properties, and resolution. The latter depends on the curing kinetics and penetration depth that, combined with parameters such as light

intensity and exposure time, allow an optimized VP regarding speed, precision, and mechanical integrity.

On the other hand, a basic requirement for all additive manufacturing (AM) light-based technologies is that the polymerized object must not be soluble in the ink while being printed, as it must have continuous contact with the liquid resin. This condition is achieved by supplying enough energy to reach the material's gel point (Ng et al., 2020). The next sections will introduce the chemistry of the main components in a 3D printable formulation.

2.2.   Formulations

A formulation for 3DP Vat photopolymerization consists of the addition of different chemical reagents, where each one has a particular role in specific ratio to achieve an homogeneous solution (Liska et al., 2007). The main roles to be fitted inside a formulation are: photoinitiator (s), monomers/oligomers & crosslinker(s), and for modulating parameters a printing definition, printing time, and/or mechanical resistance, additives as radical scavengers, colourants or fillers can be added. In the next subsections, each reagents role would be explained and exemplified.

2.2.1.   Photoinitiators (PI)

A photoinitiation system is considered efficient when it enables fast photopolymerization and high-quality 3D printing, so it should have an adequately high molar extinction coefficient at the light source wavelength and generate active initiating species (e.g. free radicals) upon photoexcitation (A. Bagheri & Jin, 2019). PIs can follow Norrish I or Norrish II type mechanisms, as explained in detail in Chapter 1, section 1.2.2.1, and, generally, they can be either radical or cationic, according to the reactive species they generate (Jing Zhang & Xiao, 2018). For an efficient initiation, the absorption wavelength of the selected PI must match the emission of the used 3D printer (Ikemura & Endo, 2010). Nowadays, many PIs are commercially available and well-known for their photochemical properties, Figure 2.1 shows most of them with their maximum absorption wavelength being in the UV and visible range, even though some can have multiple absorption peaks (Al Mousawi et al., 2017; Corrigan, Xu, & Boyer, 2016; Hong, Park, & Park, 2019;

Shanmugam, Xu, & Boyer, 2016; J. Xu, Shanmugam, Fu, Aguey-Zinsou, & Boyer, 2016; Jing Zhang et al., 2016).
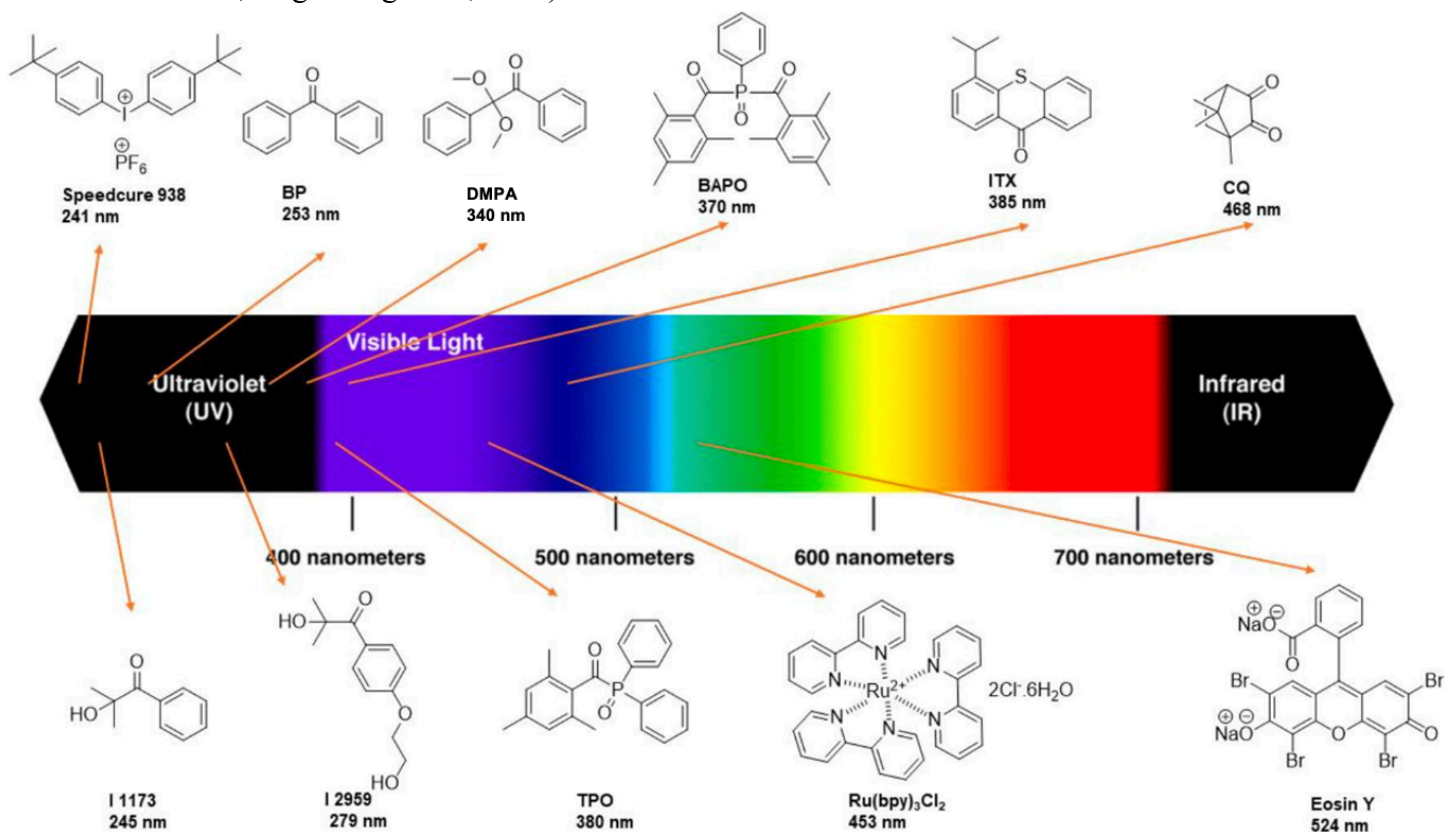
Figure 2.1. PI absorption. Chemical structures and maximum absorption wavelength of the recalled PIs used for 3D photopolymerization. Image taken from ref (Salas, Zanatta, et al., 2023).

The most used PIs are usually Norrish type I, such as 2,4,6-trimethylbenzoyldiphenyl phosphine oxide (TPO) and phenylbis (2,4,6-trimethyl-benzoyl)phosphine oxide (BAPO or Omnicure 819 previously known as Irgacure 819) (Dietlin et al., 2015; Jing Zhang & Xiao, 2018). As seen in the above figure, they usually absorb UV and visible light, which is compatible with the VP techniques, particularly DLP which often exploits light-emitting lamps at 405 nm (J. P. Fouassier, Allonas, & Burget, 2003). Whereas, cationic PIs usually need more energetic light sources that are more compatible with SLA, that uses wavelength at 355 nm (Marco Sangermano, 2012).

Dividing PIs according to their chemical nature, their solubility and high reactivity are the main considerations for their efficiency. For radical PIs, benzyl ketals are efficient PIs based on the formation of a methyl and benzoyl radical both being very reactive radicals. Examples used in SLA for their UV absorbance are 2-hydroxy-2-methyl-1-phenylpropane-1-one (I 1173), 2,2-dimethoxy-2-phenylacetophenone (DMPA or I 651) and 2-hydroxy-4'-(2-hydroxyethoxy)-2-methylpropiophenone (I 2959) (Fischer & Radom, 2001). Another very efficient group is represented by phosphine oxides, which given their lower energy levels in their excited states due to the proximity between the phosphorous atom and the carbonyl group, can absorb wavelengths at 400 nm, and are widely used in DLP

(Fantino, Chiappone, Calignano, et al., 2016; Fantino, Chiappone, Roppolo, et al., 2016). Acyl phosphine oxides such as diphenyl (2,4,6-trimethylbenzoyl) phosphine oxide (MAPO or TPO) and *bis*(2,4,6-trimethylbenzoyl) phenylphosphine oxide (I 819, BAPO) provide photosensitivity under UV and visible light radiation (Patel et al., 2017; Stassi et al., 2017).

Norrish II PIs differ from type I in a bimolecular process. They produce free radicals through direct hydrogen abstraction or electron transfer once they reach the excited triplet states under light exposure and the presence of a co-initiator. Considering chemical stability and blocking effects, these groups possess more advantages for the initiation process, however, they have low water solubility, discoloration, low reactivity, and higher volatility given to their amine nature (Jauk & Liska, 2005). The most used examples in 3D printing are, camphorquinone (CQ), benzophenone (BP), isopropyl thioxanthone (ITX), & Eosin Y, commonly being tertiary amines (Lalevée, Fouassier, Graff, Zhang, & Xiao, 2018).

Besides Norrish reactions, redox reactions are also reported in the literature for PIs. Eosin Y can also be considered under this category (Fors & Hawker, 2012). In this type of reaction, the excited PI oxidizes phenolic tyramine groups into tyrosyl radicals, cross-linking into a tyramine network (Ohtsuki, Goto, & Kaji, 2012). Another type of molecule that proceeds under redox reactions are organometallic complexes, e.g. tris(2,2'-bipyridyl)-ruthenium(II) chloride hexahydrate ([Ru(II)(bpy)3]Cl2), which has long-lived excited states and suitable redox potentials (K. S. Lim et al., 2016). Ru (II) complexes are water soluble and with a persulphate, they can accept electrons when Ru is photoexcited to a triple state (Khoon S. Lim et al., 2019). Once the Ru (III) is formed, the persulphate dissociates into sulphate radicals that follow the free-radical or thiol-ene chain polymerization. Instead, regarding the cationic process the usual PIs are diazonium salts such as Bis-(4-t-butyl phenyl)-iodonium hexafluorophosphate (Speedcure 938) (Villotte, Gigmes, Dumur, & Lalevee, 2019) and triaryl sulfonium salts, alkyl sulfonium, iron arene salts, sulfonyl ketone, and triaryl siloxane used with monomers as epoxies, vinyl esters, acetals, cyclic esters, etc. The activation of these salts involved the photoexcitation and decay of the resulting excited singlet state, with heterolytic and homolytic cleavages (M. Sangermano, Roppolo, & Chiappone, 2018). The generated cationic radicals are organic cations generated during the photolysis that further react with the formulation components, mainly monomers (Yağci & Reetz, 1998). The strength of this acid is the key to determining whether and how the polymerization proceeds. If the acid is not strong enough, due to the anion's strong nucleophilicity this combines with the carbon cationic center and polymerization does not proceed.

2.2.2. Monomers & Crosslinkers

Monomers & oligomers can be photopolymerised during the VP 3D printing process, in the presence of suitable PIs, and determine the final properties of the printed objects. Most commercial photo polymerizable formulations are

confidential, however, not all the available market options satisfy special applications. Therefore, there is a need to design and develop new formulations, using diverse monomers/oligomers for 3D printing of materials with required properties.

Monomers are the organic molecules responsible for the binding during the photopolymerization process. They have to be engineered to generate photosensitive liquid resins with low viscosity (Rasaki et al., 2021). In turn, it will result in the formation of a slurry with rheological properties, such as fluidity, photosensitivity, and viscosity, that must match the different kinds of photopolymerization-based AM techniques. Typical monomers with these properties are acrylates, methacrylate epoxides, vinyl ethers, (meth)acrylamides (some examples of the used monomers are reported in Figure 2.2), propenyl ethers, siloxanes, cyclic acetals, and furfurals (C.-J. Bae, Ramachandran, Chung, & Park, 2017; Manapat, Chen, Ye, & Advincula, 2017). A .

Oligomers, on the other hand, have similar properties but consist of two or more structural units of the latter mentioned. Thus, they exhibit larger molecular structures and higher viscosity, otherwise referred to as prepolymers or macromonomers (Ikemura & Endo, 2010).

Formulations include a blend of photoactive monomers, which are categorized according to their molecular length, weight, and present functionalities. When more than one active site (or capable of being a polymerized bond) is present, they are considered crosslinkers, like di-, tri-, and tetra-functional acrylates. They are included to make inside bonds inter different macromolecules in the polymeric network. Their chemistry and binding capacity can affect the kinetics, morphology, and mechanical performance of the polymeric matrix, where usually the amount of cross-linker used for the polymerization permits to obtain a more rigid, and stable porous material.

The higher amounts of unsaturated units per molecule in the chemical structure of crosslinker results in higher mechanical stability and binding efficiency, e.g. polymers synthesized with trimethylolpropane triacrylate in comparison with the ones synthesized with ethylene glycol dimethacrylate (Y.-J. Park, Lim, Kim, Joo, & Do, 2012). Also, the presence of multiple functionalities in reactive species leads to an auto-acceleration in the early propagation phase. This could mean faster kinetics but a higher viscosity and denser network, leading to a considerable amount of unreacted bonds (M. Lee et al., 2020). The monomer molecular weight has also an impact on the kinetics. The higher the weight the more restricted the mobility of the chains, requiring a diluent in some cases.

At last, it must be noted that most of these compounds are commercially available, nevertheless many more can be found in literature, according to their properties and final goals. While a complete list of photocurable monomers is out of the scope of this thesis, more information can be found in relevant literature(Lai, Peng, Li, Zhu, & Xiao, 2022; Peer et al., 2018).
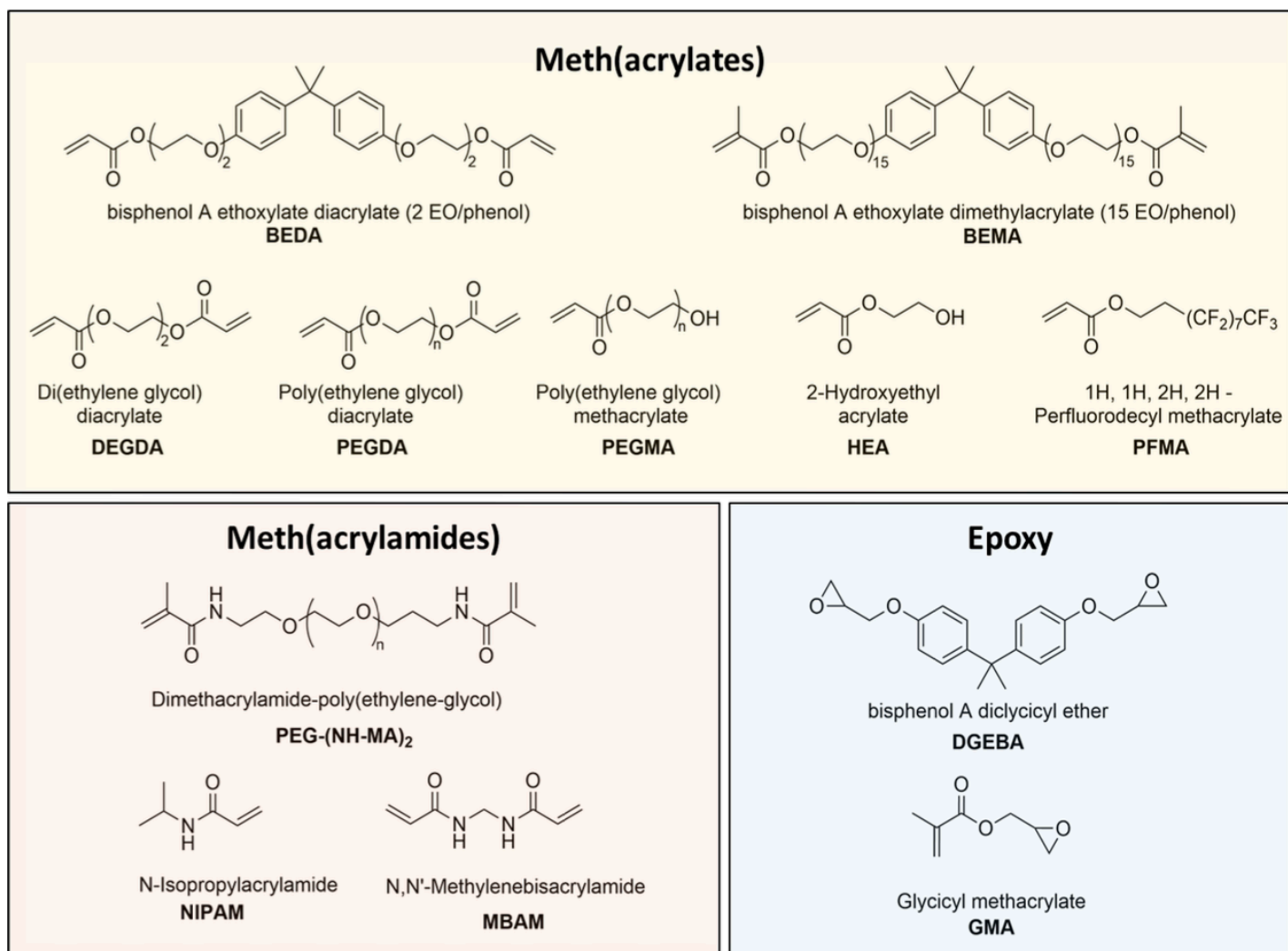
Figure 2.2.Chemical structure of commercially available oligomers & monomers for 3D printing. Image taken from ref (Salas, Zanatta, et al., 2023).

2.2.2.1. Acrylic acid derivatives as monomers/oligomers in VP 3D printing

Free-radical polymerizable resins are frequently based on highly reactive (meth)acrylate functionalities (J. Fouassier & Lalevée, 2012). These are employed as building blocks to develop bigger molecules due to their reactivity upon light irradiation, well-established mechanisms, and commercial availability (Narupai & Nelson, 2020). Figure 2.2 shows the most common monomers and oligomer derivatives from acrylates of, and similar nature used in VP (Scott et al., 2020; Zhao et al., 2018). These kinds of monomers tend to follow a chain-growth polymerization. In the previous chapter this mechanism has been explained, and in Figure 2.3 A) a schematic representation for photopolymerization can be appreciated.

The main criteria for monomer selection depend on their functionality (mono, di- or poly-), viscosity, reaction kinetics, hydro(phobicity/philicity), shrinkage, cost, shelf-life, volatility, toxicity, and the final mechanical and functional characteristics of the product (A. Bagheri & Jin, 2019). Also, the reactive groups mainly control the kinetics, while the backbone influences the physicochemical and mechanical strength of the polymer (Jing Zhang & Xiao, 2018).

The preference for acrylates is due to their fast reactivity related to their chain growth-polymerization mechanism and oxygen inhibition, which allows good adhesion between printing layers (Jing Zhang & Xiao, 2018). However, they tend to shrink when cured, leading to poor resolution, internal stress, or even damage to printed objects. Meanwhile, methacrylate monomers reduce the shrinkage problem, but have a slower curing rate. Aromatic or high-molecular-weight (meth)acrylates are characterized instead by lower shrinkage and adequate kinetics (Gonzalez, Chiappone, Dietliker, Pirri, & Roppolo, 2020).

2.2.2.2. Other monomers/oligomers in VP 3D printing

Monomers with a wide range of functionalities have been reported to be compatible with photo-induced AM technologies (A. Bagheri & Jin, 2019). The main monomer moieties are reported in Figure 2.3 , together with the mechanism they can undergo when induced by light to form the polymeric network.

(Meth)acrylamides and vinyl esters follow the same chain-growth polymerization pathway as (meth)acrylates (Figure 2.3(A1 and A2)). The reactivity of these moieties decreases together with the inductive effect, given this also, methyl-functionalized molecules have a lower tendency to homopolymerize. Hence, reactivity can be modulated by electron acceptor groups that impart stability to intermediate radical species during the reaction (Beuermann, Paquet, McMinn, & Hutchinson, 1996). Furthermore, molecules with a polymerizable double bond such as methacryloyl groups can be used on the backbone of unreactive species, by esterification of hydroxy or amino groups to provide photoreactivity enabling further functionalization of some natural (e.g. gelatine, chitosan, or cellulose) and synthetic polymers (Mondschein, Kanitkar, Williams, Verbridge, & Long, 2017).
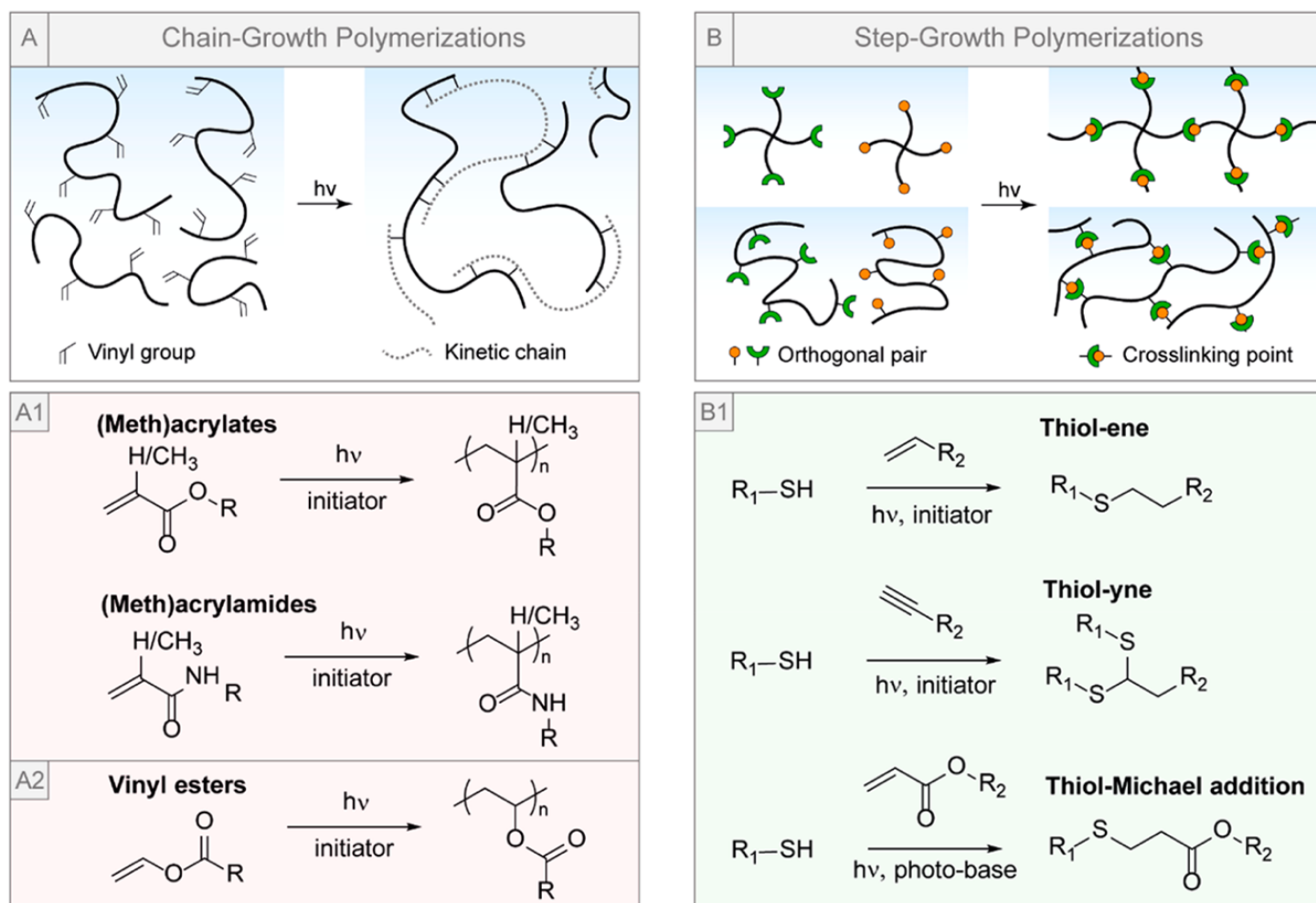
Figure 2.3. Schematic representation of (A) chain-growth and (B) step-growth formation of the polymer network. Examples of "constructive" photochemical reactions to form and functionalize hydrogels by 3D biofabrication techniques: (A1) (meth)acrylates and (meth)acrylamides; (A2) vinyl esters. (B1) thiol−ene, thiol−yne, and thiol−Michael addition. Image taken from ref (M. Lee et al., 2020)

For niche applications, thiol -ene/-yne systems and epoxy are used in VP, known for their reduced shrinkage, lower stress, and higher conversion compared with acrylate resins (Nair, Cramer, Scott, Bowman, & Shandas, 2010; Sycks, Wu, Park, & Gall, 2018). In Figure 2.3 B1 are reported the possible polymerization mechanisms in thiols' presence following a step-growth polymerization. The advantages of thiol-ene networks include their high rate of reaction and conversion under ambient conditions, with reduced shrinkage due to the delay in the gel point and mechanical stress, as well as their lower susceptibility to oxygen inhibition compared with the first mechanism and the formation of less brittle networks. These photoinduced reactions have orthogonal click chemistry because each available thiol group reacts only once with one alkene double bond, producing homogeneous networks with consistent bulk and local properties (Bertlein et al., 2017). This selectivity can be exploited by performing the reaction in an off-stoichiometric ratio to control the reaction's conversion and still have residual functionalities from the excess component and perform post-printing functionalization (Hoyle & Bowman, 2010).

44

Finally, epoxy resins can be cured by cationic-induced mechanisms. In this case, the PI generates a cationic active center after UV light irradiation, which in turn initiates the polymerization of epoxy or vinyl ether monomers. Cationic photopolymerization is slower than radical polymerization, but offers some advantages such as reduced shrinkage and residual stresses, which enhance the mechanical properties of the components (M. Sangermano et al., 2018).

2.2.2.3.   Monomers for developing hybrid polymeric networks in VP 3D printing

A hybrid network is defined by a monophasic morphology where an organic phase is interconnected with an inorganic one, without the possibility to clearly define the boundaries between the two phases (Amerio et al., 2008; Malucelli et al., 2005). These materials combine the attractive properties of ceramics, such as thermal stability and high modulus, with the low-temperature processing conditions of polymers (A. Chiappone et al., 2016). UV curing or photopolymerization can be used on the organic phase of the network allowing even the formation of 3D structures, while the sol-gel process undergoes at the same time to unify the inorganic with the organic phase (schematic representation in Figure 2.4 B). A sol-gel chemical process describes the reaction in which a sol evolves into a gel, where sol is a colloidal dispersion of small particles in a liquid, and a gel is a substance composed of a continuous network encompassing a continuous liquid phase (*Sol-Gel Processing and Applications*, 2012). This reaction is based on the subsequent network formation through hydrolysis and condensation reactions of inorganic alkoxide monomers. At this point, the use of a coupling agent is necessary to permit the interconnection in the network and prevent macroscopic phase separation.

Reported articles of this type of material usually contain precursors as acrylate monomers for the organic phase, a coupling agent, and as an inorganic precursor a metal alkoxide or metal-alkoxysilane (Amerio et al., 2008). Chiappone *et al.* utilize 3-(trimethoxysilyl) propyl methacrylate (TMSPM) as a coupling agent and tetraethyl orthosilicate (TEOS) as the inorganic/ceramic precursor (A. Chiappone et al., 2016) (Figure 1.4 (A)). Also, Amerio et al. have studied this reaction for scratch-resistant acrylic coatings (Amerio et al., 2008) and Malucelli et al. for composites utilizing PEGDA 600 and BEMA 1400 (Bisphenol A ethoxylate (15 EO/phenol) dimethacrylate) as monomers (Malucelli et al., 2005). The same explored sol-gel reaction has been used after dispersion polymerization processes for preparing hybrid copolymers by Bae-Jun et al (Jun, Hong, Park, & Suh, 2003).

A

TMSPM   TEOS

B

$$R'O - \underset{\underset{OR'}{|}}{\overset{\overset{OR'}{|}}{Si}} - OR' \quad + \quad H_2O \quad \xrightarrow{H^+} \quad R'O - \underset{\underset{OR'}{|}}{\overset{\overset{OR'}{|}}{Si}} - OH \quad + \quad R'OH \qquad \textbf{Step 1} \quad \text{Hydrolysis}$$

$$R'O - \underset{\underset{OR'}{|}}{\overset{\overset{OR'}{|}}{Si}} - OH + R'O - \underset{\underset{OR'}{|}}{\overset{\overset{OR'}{|}}{Si}} - OR' \quad \xrightarrow{H^+} \quad R'O - \underset{\underset{OR'}{|}}{\overset{\overset{OR'}{|}}{Si}} - O - \underset{\underset{OR'}{|}}{\overset{\overset{OR'}{|}}{Si}} - OR' \quad + R'OH \quad \textbf{Step 2a}$$

Condensation with
alcohol formation

$$2\,R'O - \underset{\underset{OR'}{|}}{\overset{\overset{OR'}{|}}{Si}} - OH \quad \xrightarrow{H^+} \quad R'O - \underset{\underset{OR'}{|}}{\overset{\overset{OR'}{|}}{Si}} - O - \underset{\underset{OR'}{|}}{\overset{\overset{OR'}{|}}{Si}} - OR' \quad + H_2O \qquad \textbf{Step 2b}$$

Condensation with
water formation
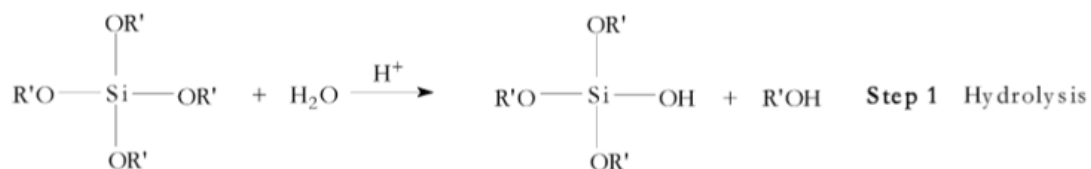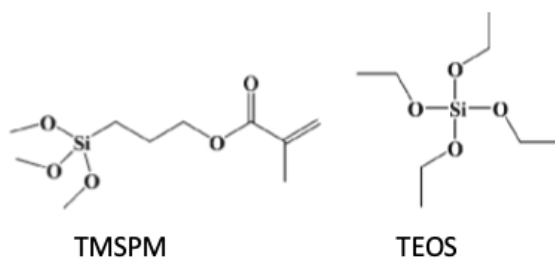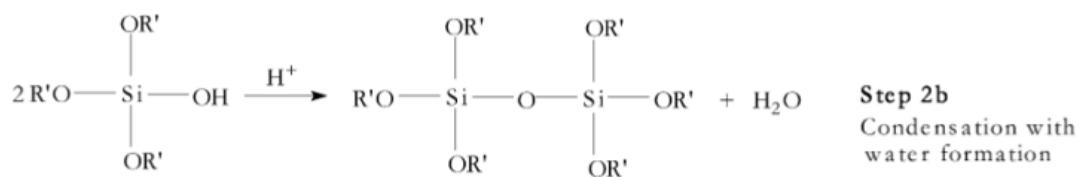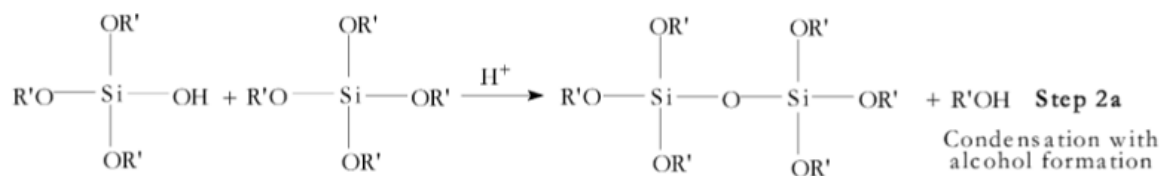
Figure 2.4. (A) Chemical structures of the coupling agent (TMSPM) and the inorganic precursor (TEOS). (B) Schematic representation of the sol-gel process, adapted from ref (Malucelli et al., 2005)

2.2.3.Additives
2.2.3.1.   Fillers

The addition of fillers is the most common strategy to overcome polymeric materials limitations, introduce controlled anisotropy, or obtain specific properties such as electrical(Gonzalez et al., 2017) or thermal conductivity (Riccucci et al., 2021), improving rheology (Mun et al., 2021), adding luminescence (Frascella et al., 2018), stiffness (L. Chen et al., 2021; Schwarz, Pagac, Petrus, & Polzer, 2022), electromagnetic shielding (Kruzelak, Kvasnicakova, Hlozekova, & Hudec, 2021), or antibacterial properties (Parajuli et al., 2022). In addition, fillers can reduce shrinkage and consequently result in better accuracy or resolution.

The use of carbon materials (T. Zhou et al., 2020) (e.g. graphene, nanotubes), ceramic and metal powders, such as 2D materials (Maleski, Ren, Zhao, Anasori, & Gogotsi, 2018) in particular, and glassy and fibrous materials (e.g. cellulose (J. Wang et al., 2018)) as fillers they reinforce the structure and improve mechanical properties. Meanwhile, to improve thermal, chemical, and UV resistance, the most common fillers are minerals (e.g. titanium (Kang et al., 2019)) and even bio-fillers (e.g. coffee grounds, wood flour) (Sztorch et al., 2022).

In some cases, the filler content can be higher than the main matrix material turning out to be the main component. In every case though, the selection of the filler should be done considering that the composite resin must have solubilization stability during the whole process. This means a in an homogeneous suspension that does not suffer from sedimentation, agglomeration, or collateral reactions (Angelopoulos, Samouhos, & Taxiarchou, 2021). Additionally, the fillers cannot present excessive absorption that compromises the reactivity of the blend or generates scattering phenomena.

Based on the composition, fillers can be divided into organic, inorganic, and hybrid types. The organic types are represented by natural polymers (e.g. cellulose), generally with an intrinsic fibrillar structure, and synthetic polymers (polyamide or polyester). Inorganic compounds include oxides and hydroxides ($Al(OH)_3$, $Mg(OH)_2$, TiO_2, Fe_3O_4), salts ($CaCO_3$, $BaSO_4$), metals and silicates (Mazzanti, Malagutti, & Mollica, 2019). In this Thesis work two types of fillers were employed: MXenes and photocatalytic semiconductor materials as a hybrid type.

So, being out of the scope of this introductive chapter to illustrate a comprehensive literature review of composites in Vat 3DP, in the next sections the literature related to these two fillers will be briefly summarized, giving more examples then in Chapter 3.

2.2.3.1.1. MXene/composites in VP 3D printing

A complete description of MXene will be given in Chapter 3 of this Thesis, along with the main reported properties. Nevertheless, here a brief overview related to their use in VP 3D printing will be given. Their use as fillers in polymeric composites throughout AM technologies has been explored in applications such as sensors, energy, biomedical, electromagnetic shielding, and electrochemistry (K. Gong, Zhou, Qian, Shi, & Yu, 2021; T. Li, Jabari, McLellan, & Naguib, 2023). Their negative surface zeta potential and hydrophilicity make them easily dispersible in many aqueous media, therefore also polymeric inks. In a colloidal solution, they can be tuned over a large viscosity due to their clay-like behavior, enabling MXenes versatility for introducing them in polymeric inks.

Achievements so far have been reported for VP 3D printing, where MXenes have been used with LCD (Y. Li, Kankala, Chen, & Wang, 2022) for tough thermally resistant nanocomposites, CLIP (B. Huang et al., 2021) in hydrogels as an adhesive sensor, and DLP (Salas, Pazniak, et al., 2023) for its particular conductivity and used in electronics. As part of the work developed has been on this topic, the other chapter will include the work presented in DLP, explaining in detail their chemistry and performance.

2.2.3.1.2. Photocatalytic semiconductor materials in VP 3D printing

A photocatalyst is a material that employs light to activate and/or to accelerate chemical reactions (Aguirre-Cortés et al., 2023). Its efficacy depends on four key elements: light absorption ability, the density of active sites, redox capacity, and photoinduced electron-hole recombination rate (Ahmad et al., 2023). In the case of semiconductor (SC) photocatalysts, they show a moderate band gap (E_g <3.5 eV), so that light exposure with sufficient energy leads to the promotion of electrons(e^-) from the valence band to the conduction band, leaving positive holes (h^+) in the valence. For the photogeneration of the e^-/h^+ pairs, the irradiated light energy (hv) must overcome the band gap. This way both can initiate a redox process on the substances present in the surrounding area (K. Rokesh, Sakar, & Do, 2021). Which subsequently, would cause catalytic degradation of possible pollutants in solution, defined as the decline or reduction of the molecular mass of a particular material caused by catalytic photoinduced reaction (Yousif & Haddad, 2013). This term is used further in the thesis referring to photodegradation to simplify the term photocatalytic degradation.

Even though, their intrinsic definitions can be overlapped, the first one is defined as an advanced oxidation process that can be used to degrade pollutants with high concentration, complexity, and low biodegradability (Alves, de Farias, Breslin, Pinto, & Cadaval, 2022), and the second as the change in a material by light, caused by subsequent oxidation or hydrolysis of it (Alves et al., 2022).

Whereas, photobleaching is defined as a photophysical phenomenon wherein fluorophores undergo permanent chemical damage caused by prolonged excitation, often due to oxidation by free radicals within the imaging solution, and as a result of this damage the fluorophore no longer produces a fluorescent signal (Demchenko, 2020). Figure 2.5 shows the mechanistic differences between photocatalytic degradation & photobleaching.
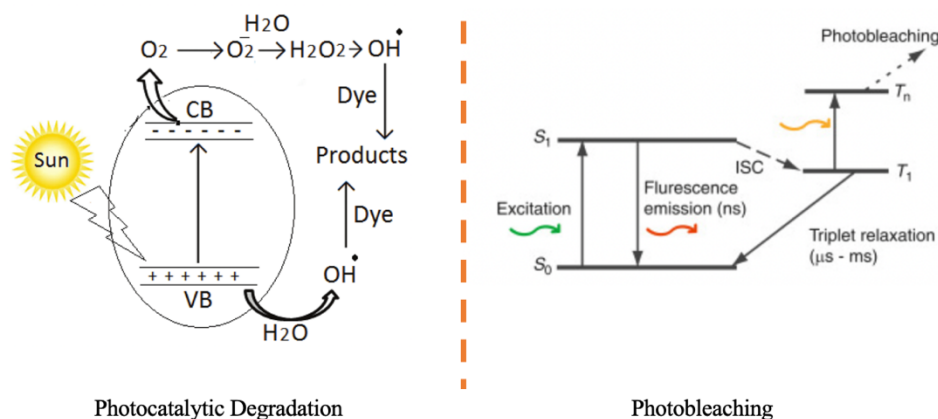
Figure 2.5 Mechanistic difference between photocatalytic degradation (Saeed, Usman, & Haq, 2018)& photobleaching (Y. Wu et al., 2016). This image has been adapted from the references mentioned besides their corresponding words.

The inclusion of these SC photocatalyst materials in VP 3D printing techniques has been explored both as fillers and in post-processing (N. Li, Tong, Yang, & Du, 2022). In the first case, Metal-Organic Frameworks (MOFs) are the principal material added to the resins' preparation. Halevi et al. embedded copper benzene-1,3,5-tricarboxylate as MOF into polymeric structures using DLP to degrade methylene blue colorant and Zhang *et al*. used a porphyrinic Zr MOF in SLA, specifically as a PI for Photoinduced electron/energy transfer reversible addition-fragmentation chain transfer (PET-RAFT polymerizations (L. Zhang et al., 2021).

Alternatively, such photoactive materials can be deposited onto printed substrates o used as coating. For example, Mei et al. loaded a 3D printed sintered carbon-ceramic support with Molybdenum disulfide for RhB degradation (Mei, Huang, Liu, Pan, & Cheng, 2019). Surface modifications can also be done in already printed materials, like Medina et al that coated SLA fabricated carbon devices with hyperporous carbon to extract RhB from contaminated water (Medina et al., 2019) . Other techniques for their inclusion in post-processing will be further explored in the post-treatment section, as for the dip-coating processing.

2.2.3.2. Colorants or dyes

D,
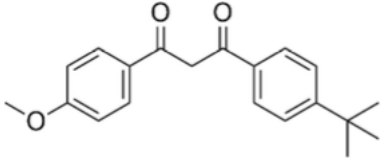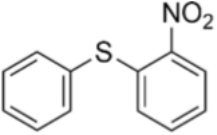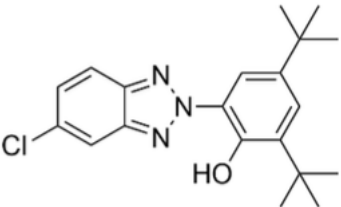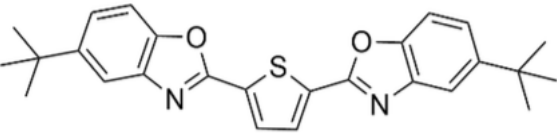
yes are typically UV and visible light absorbers (e.g. azobenzenes & benzotriazoles families). These additives can be dispersed in the liquid formulation
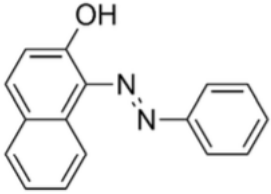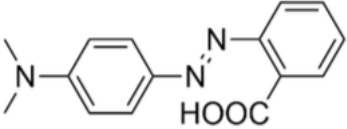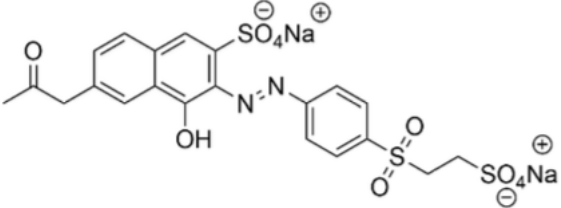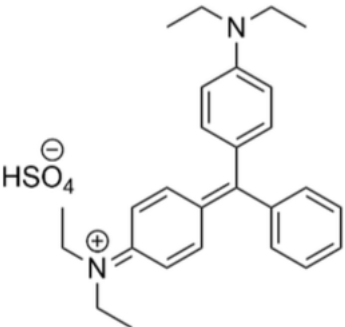
or covalently linked to the monomer/polymer chains (Ligon et al., 2017). The most common dyes are listed in Table 2.1 with their applications.

In 3DP technologies, the fundamental roles of the dye are printability and resolution. Generally, dyes are used for controlling polymerization, fundamental for high-fidelity printing, for avoiding a loss of features and precision by attenuating light absorption and its penetration, or just for the aesthetics aspects. However, their use results in an undesired final color (Gastaldi et al., 2020).

The selection of the correct dye must be done considering the absorption spectrum of the used PI and the dye, and the emission wavelength of the printing machine. Commonly, the PIs absorb in a similar working range to the 3D printing machines, e.g. around 355 nm for some SL lasers, to 385/405 for common DLP. For this reason, in general, the dyes also absorb in the UV range or at wavelengths below 500 nm (Ligon et al., 2017). Sudan I is probably the most common photo-absorber and its use has been thoroughly investigated to limit the curing depth and obtain better Z resolution (Vitale & Cabral, 2016).

Table 2.1. List of reported common dyes used in VP 3D printing.

Name and Structure	λ_{max} (nm)	Polymer used with and Application
Avobenzone; butylmethoxy-dibenzoyl-methane	357	PEGDA for biomedical applications (Warr et al., 2020) PEGDA for microfluidic channels (H. Gong, Bickham, Woolley, & Nordin, 2017)
2-nitrophenyl phenyl sulfide (NPS)	360	PEGDA for microfluidic channels (H. Gong et al., 2017; Warr et al., 2020) and microchannels (H. Gong, Woolley, & Nordin, 2018)
Tinuvin 327; 2-(2′-Hydroxy-3′,5′-di-tert-butyl-phenyl)-5- chlorobenzo-triazole	365	IBXA HDDA /BEDA mixture for 3D microstructures (Choi, Wicker, Cho, Ha, & Lee, 2009)
Benetex OB; 2,2'-(2,5-thiophenediyl) bis(5-tert-butylbenzoxazole)	375; 435	PEGDA for microfluidics channels (H. Gong et al., 2017)

50

Dye	λ	Applications
Sudan I; solvent yellow 14; solvent orange R	418; 476	PEGDA for improved printing resolution (M. P. Lee et al., 2015) Tango Plus (Commercial elastomer), miniaturized for soft robotics (Y.-F. Zhang et al., 2019) PEGDMA for antimicrobial hydrogel scaffolds (Garcia et al., 2018) Acrylate/allyl/ thiol mixture for uniformity study (Vitale & Cabral, 2016)
Methyl red; acid red 2	410; 520 (pH < 4.4)	Bio-based acrylate monomer for high printing resolution (Cosola et al., 2020) Starch for hydrogels (Noè, Tonda-Turo, Chiappone, Sangermano, & Hakkarainen, 2020) Phosphorescent bio-based resin (Maturi et al., 2020)
Reactive orange 16; remazol; Brilliant orange 3R	388; 494	PEGDA/AETAC mixture for monolithic ion absorbers (Simon & Dimartino, 2019) PEGDA for precise conductive structures (Fantino, Chiappone, Calignano, et al., 2016) BEDA for microcantilever (Stassi et al., 2017)
Brilliant green; diamond green; Emerald green; ethyl green	650; 440	PEGDA/CNC for hydrogel (J. Wang et al., 2018)

2.2.3.3. Radical Scavengers

A radical scavenger is a chemical substance added to a polymer mixture to remove or deactivate impurities and undesired secondary reaction products (Cook et al., 2020; Strohmeier, Frommwald, & Schlogl, 2020). The polymeric radical scavengers are preferred as easily separable antioxidants or as films having antioxidant activity. For instance, to improve the storage stability of a rubber formulation, a radical scavenger can be applied to reduce premature cross-linking

reactions under dark conditions (Strohmeier et al., 2020). Common examples are tocopherol and naringenin, free-radical scavengers that act as antioxidants or synthetic catalytic scavengers.

2.3. Post-Curing & Post-treatments

Consider the last step in AM to produce a 3D object, as seen during the first chapter. At this point, one or more of the following can be included: (i) clean off residue liquid polymer from the surface, (ii) remove the support structures, (iii) post-curing that includes the final exposure of the structure to light, and/or specific post-treatments which can go depending on the final desired properties for a specific application, (iv) coating, (v) thermal treatments. Henceforward, the post-processing phases used in DLP will be presented.

2.3.1. Cleaning

In both approaches, bottom-up and top-down, used for VP the printed object emerges from the unpolymerized ink in the vat with residual unreacted products on the printed structure. This residual ink needs to be removed due to further gelation by natural light over the desired object and then complete curing in further process. Generally, the object is rinsed and sonicated in solvents like isopropyl alcohol, ethyl alcohol, water, or acetone depending on the material used. However, overexposure to these solvents may lead to swelling or cracking affecting the surface of the printed structure (R. Chaudhary, 2022).

2.3.2. Removal of the support

In the manufacturing of complex 3D structures, support is often required, though changes in the printing orientation may mitigate the necessity of adding supporting buildings. This should be later removed from the printed bodies before the post-curing to avoid complete attachments or damage to the 3D structure.

2.3.3. UV Post-curing

To get at an optimal cross-linking point of the printed polymer, ultimately it must be exposed to UV radiation. The exposure time is the main variable in this stage, as a too short time can lead to under-cured objects and too long, to over-curing or even shrinkage and cracking. This action is performed in a UV oven, to achieve better mechanical properties (Pagac et al., 2021).

2.3.4. Surface Post-treatments

Post-treatments can assure higher performance products or enhancements of desired properties from the material used. The main properties that can be enhanced include mechanical, thermal, and conductivity quality (Yuewei Li, Wang, Wu, &

Kankala, 2023). This can be given, by adding or modifying the surface of the printed objects by coating treatments, posterior reactions (e.g. chemical vapor deposition), or inducing them to different temperature treatments.

2.3.4.1. Coating techniques

The initial role of surface coatings in industrial applications emerged to protect from corrosion and to provide mechanical resistance (Jiang, Cao, Xiao, Zhu, & Lu, 2017). Recently, polymer-/nanocomposite-based coatings have been developed and utilized for diverse applications such as biomedical, photocatalysis, electronics, optics, mechanical stability, etc (Amerio et al., 2008; Jiang et al., 2017; Sander van Loon, 2018; Sharma, Gupta, & Mudgal, 2022). Figure 2.5 shows the most recent coating techniques reported in the literature so far for polymeric substrates. Nevertheless, dip-coating would be the technique explained in detail as it has been used during the experimentation of the thesis.
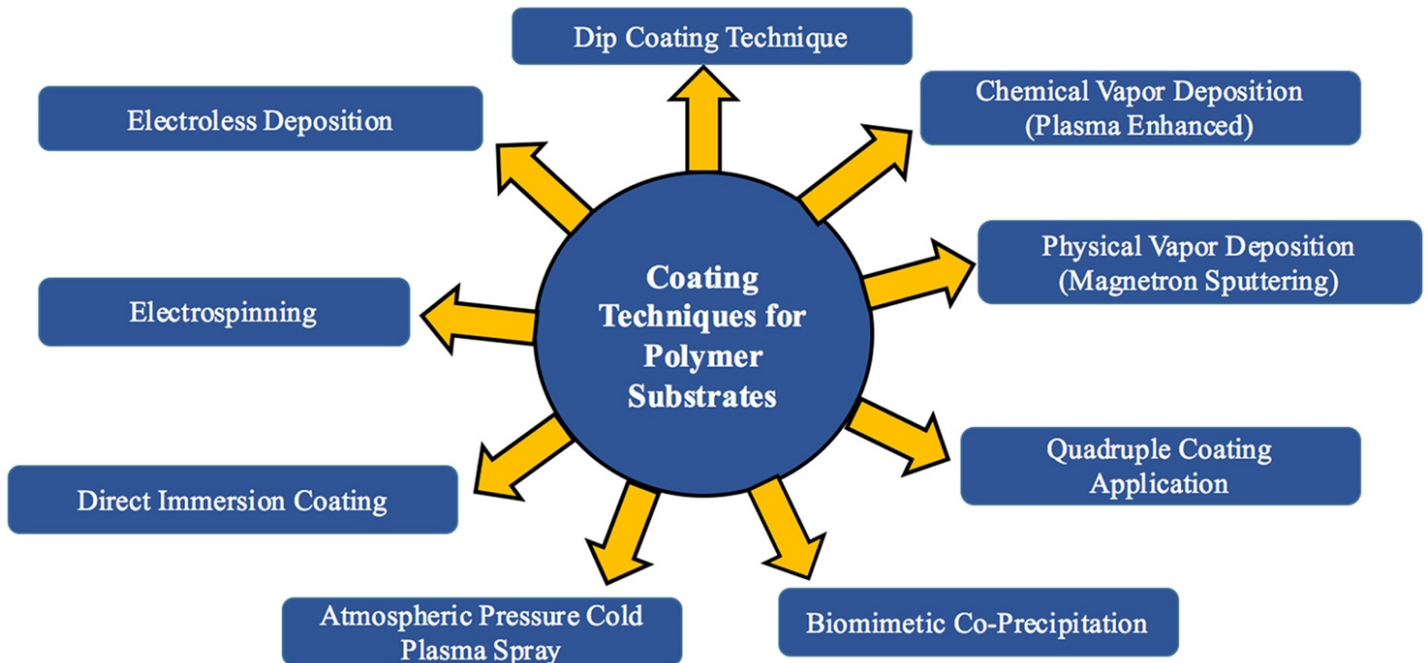
Figure 2.6. Schematic representation of the most recent coating techniques. Permission granted to reproduced this image (Sharma et al., 2022).

2.3.4.1.1. Dip-Coating

Dip coating is a well-established method that involves a precise and controlled immersion and withdrawal of a substrate from a solution. The main stages involved are: immersion, dwelling, withdrawal, drying and/or curing (in some cases). For polymers, this technique includes the immersion of the polymeric substrate in a polymer melt or solution, then withdrawal of the substrate, solvent evaporation (Erkoc & Ulucan-Karnak, 2021), followed by drying, as seen in Figure 2.6. For the

successful attachment of the active material onto the surface, it useful to have surface functionalities that can react with the coated material.

Two different types of dip-coating can be found, the first one consists in batch dip-coating, and the second in continuous dip-coating (Shakeel Ahmad, Pandey, & Abd Rahim, 2017). The final coating thickness is determined by the interaction of the polymer surface with the active coated material, the viscosity of the solution, drainage, and attachment/capillary forces. The combination of the three regimes ultimately determines the thickness vs withdrawal speed behavior for a film.

Depending on the material added to the coating, it can provide resistance against scratches, wear, corrosion, external elements, or other applications like the one here studied photocatalysis. If an active substrate is used, like metals, organic solutions, inorganic precursors, or hybrid materials, different applications can be obtained. For example, for the development of metallic coatings Sonawane et al. used Fe-doped with TiO_2 films over polyethylene glycol to improve the wear resistance and to provide photocatalytic properties (Sonawane, Kale, & Dongare, 2004)- While, for organic functionalization Xuelin Li et al. studied the deposition of poly(methyl methacrylate) over bioceramics for corrosion protection (Xuelin Li & Zhitomirsky, 2020).. Moreover, Navidpour et al. also studied the deposition of tin oxide semiconductors for photocatalytic applications like methylene blue degradation . Even inorganic precursors, like orthosilicates, were used in literature to change hydrophilicity of the materials and wear resistance by in situ silica generation (Soloukhin, Posthumus, Brokken-Zijp, Loos, & de With, 2002).

For photocatalytic activity, semiconductors such as TiO_2 in thermoplastics for the degradation of methylene blue (J.-H. Yang, Han, & Choy, 2006) have been reported in the literature. Sol-gel dip coating has also been used to better coupling the substrate for the same purpose, by adding polyethylene glycol (PEG) to the surface and using a Ti-peroxy sol-gel for posterior dip coating (Sonawane et al., 2004).
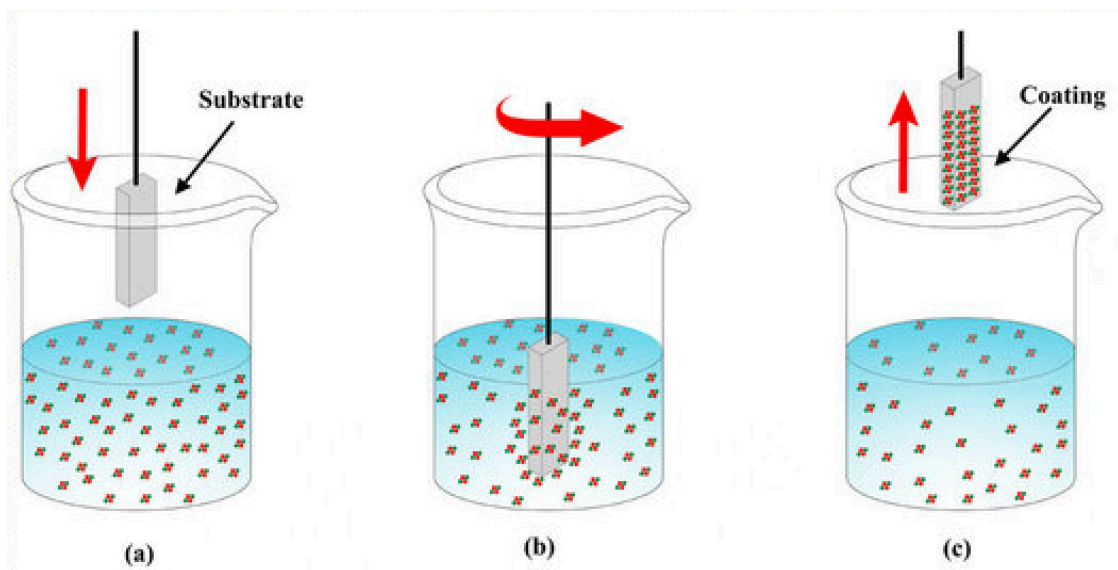
Figure 2.7. Schematic representation of the dip-coating process (a) dipping (b) formation of the coated layer (c) evaporation and sealing. Image adapted from ref (Taşdemir, Şenaslan, & Çelik, 2021)

54

2.3.4.2. Thermal treatments for 3D-printed structures

Thermal post-processing is used on the other hand to alleviate residual stresses, reduce cracking, and homogenize microstructures for particular enhancements (X. Peng, Kong, Fuh, & Wang, 2021). These are used when exposing the composite to high temperatures in particular environments, to obtain a desired property from the 3D product. However, shrinkage tends to be a critical factor affecting thermal treatment due to organic degradation inside the structure (X. Peng et al., 2021).

Annealing is a heat treatment in which the material is heated to a specified temperature and then slowly cooled (Dinita et al., 2023). It can also be subjected to specific gasses, typically inert such as argon, helium, or nitrogen, reductive environments considering a percentage of hydrogen or oxidative environments using air as an inlet gas. This is a common method used in AM, where the temperature and holding times will depend on the material used. Overheating or prolonged exposure to high temperatures may lead to material degradation in thermoset and melting in thermoplastics, leading to a decrease in tensile properties.

Also, inducing polymers to post-processing enables structural changes of amorphous parts into crystalline parts, e.g. PLA annealing at 100ºC for 90 min can improve its thermomechanical stability (Pastorek & Kovalcik, 2018). Instead in biobased thermosets, e.g aromatic resins developed with vanillin, gualacol or eugenol; the subjection to thermal annealing increased up to a 2000% the Young's modulus improving the mechanical response (Cortés-Guzmán et al., 2023)..

Finally, thermal treatments as post-processing can be used to improve performance in electrical conductivity and electromagnetic interference. Annealing procedures have been used in CNT composites (Nguyen Thi et al., 2022), graphene, carbon nanofillers (Deng, Bilotti, Zhang, Loos, & Peijs, 2010), and including MXenes (Rakhi, Ahmed, Hedhili, Anjum, & Alshareef, 2015; Salas, Pazniak, et al., 2023). First, increasing the temperature can induce re-orientation and distribution of CNTs increasing the interconnection between them, while for graphene composites and MXene composites the temperature can affect the material surface or even its concentration inside the composite (Kotsilkova et al., 2019) enhancing their performance in specific applications as electronics (Salas, Pazniak, et al., 2023).

Chapter 3

3. Fillers used throughout this research for 3D VP printing envisaging specific properties.

3.1. MXenes

3.1.1.   Historical Development

For more than 20 years, beginning with the finding of single-layer graphene, two-dimensional (2D) materials have been of interest in material science, condensed matter physics, and chemistry fields because of their wide set of applications (Jia et al., 2020; Zeranska-Chudek, Lapinska, Siemion, Jastrzębska, & Zdrojek, 2020). This interest led to a new wave of research, where the limelight has been focused on metal dichalcogenides, and boron nitride, following novel 2D materials that also include MXenes (Wee, Hersam, Chhowalla, & Gogotsi, 2016; Hua Zhang, 2015).

MXenes correspond to a big family of 2D materials, where each 2D flake is composed of *n+1* (*n=1-3*) layers of transition metals (M, elements in blue in Figure 3.1.1.a) interacting with *n* layers of carbon and /or nitrogen (X, elements in grey in Figure 3.1.1.a) with a general formula $M_{n+1}X_nT_z$, that precedes the name of this material. On the other hand, the T_z represents the surface termination groups such as O, OH, F, and/or Cl (elements in orange in Figure 3.1.1) which are bonded to the outer M layers (Babak Anasori, Lukatskaya, & Gogotsi, 2017), and their presence depends on the etching method chosen that will be later explained.

The MXene field has significantly increased in the number of research areas and publications (Babak Anasori & Gogotsi, 2019; Gogotsi & Anasori, 2019), where more than 1450 institutions from 72 countries have already developed research lines on this topic (Saravanan, Rajeswari, Kumar, Rajasimman, & Rajamohan, 2022). MXenes were discovered in 2011 at Drexel University, where

the first stable composition $Ti_3C_2T_z$ was made with no prior prediction (M. Naguib et al., 2011). This research also included Michel W. Barsoum as lead scientist, who participated in the renaming of the MAX phases. Since then, theoretical calculations have predicted 100 possible compositions and more than 40 MXenes structures have been synthesized changing their compositions, structures, and synthesis methods (Dadashi Firouzjaei, Karimiziarani, Moradkhani, Elliott, & Anasori, 2022).

To witness the interest that MXenes are raising, in 2018 the 1st International Conference on MXenes was held at Jilin University in Changchun, China. The latest one was the 4th International Conference in May 2022 in Nanjing, China.

3.1.2. The origin of the MAX phase: a brief summary of its history and composition.

The MXene synthesis starts with the topochemical selective etching of the precursor material, MAX phases. They play an essential role in the quality of the MXene, as their properties can be affected by the preparation process, composition, and structure of the MAX phase (Ghosh, Pal, Das, Chatterjee, & Das, 2022).

MAX phases were initially named and published by Barsoum in the 2000s (Barsoum, 2000) which was initially followed by the synthesis and characterization of H-phases (Jeitschko, Nowotny, & Benesovsky, 1963) and ceramics. H-phases are ternary systems based on a transition metal, a metalloid, and carbon, that drew interest at the beginning given their oxidation resistance, mechanical properties, machinability, and electrical properties. These H-phases had a hexagonal crystal structure, e.g. Ti-Al-C, V-Al-C, Nb-Al-C, Cr-Al-C, Ti-Sn-C, and V-Ga-C (Gonzalez-Julian, 2020). However, MAX phases and H-phases had the same crystal structures. MAX phases use the general formula "$M_{n+1}AX_n$" where "M" corresponds to a transition metal, "A" from an A-group element, X is usually a C and/or N, and "n" can be 1,2, or 3 (Barsoum, 2000). The possible elements employed in MAXs are displayed in Figure 3.1.1. b. Their main characteristic is their combination of properties between a ceramic material and a metal, and the most attractive compositions are Ti_3SiC_2, Ti_2AlC, Ti_3AlC_2, and Cr_2AlC.

(a)

M_2XT_x $M_3X_2T_x$ $M_4X_3T_x$
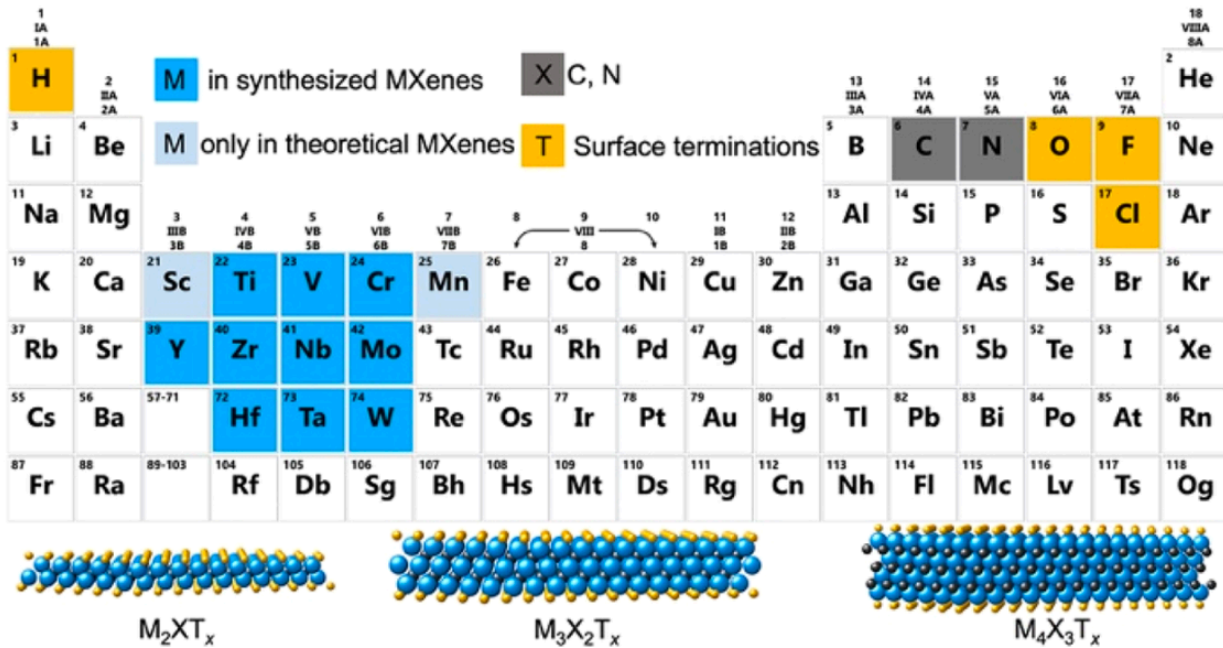
(b)
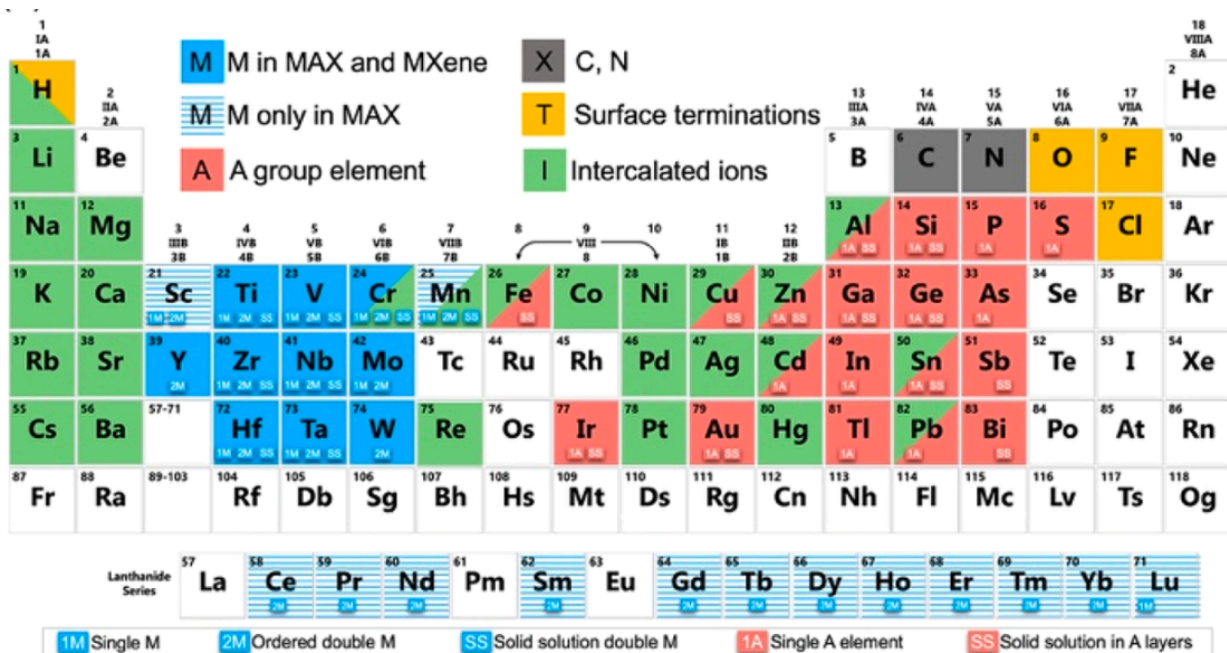
Figure 3.1.1. Periodic tables showing compositions of MXenes & MAX phases. (a) Elements used to build MXenes. The schematics of the possible structures are displayed at the bottom of the table. (b) Elements used to build MAX phases, MXenes, and their intercalated ions. The elements in red, regarding the A group, are present in MAX phases and can be selectively etched to make MXenes. The green elements have been used so far to intercalate MXenes. 1M and 1A indicate the formation possibility of a single transition metal and A element MAX phase and MXene. SS indicates the solid solutions in transition metal atomic planes or A element planes. 2M shows the formation possibility of an ordered double-transition metal MAX phase or MXene (in-plane or out-of-plane) (Babak Anasori & Gogotsi, 2019). The image is taken from ref (Gogotsi & Anasori, 2019).

3.1.3. MXene Compositions

In MXene arrangements M covers n layers of X in an $[MX]_nM$, giving 3 possible structures M_2X, M_3X_2, and M_4X_3. Figure 3.1.2 shows the theoretically predicted (marked in grey) and experimental (marked in blue) reported species, where mono-transition metal and compositions with more than one M element exist.

A unique feature of this material happens when there are two or more transition metals MXenes. They could exist in 2 forms: solid solutions (SS) and ordered phases; the possible examples are shown in Figure 3.1.2. In the first one, a random arrangement of 2 different M is observed between the layers (marked in green). In the ordered phases, transition metals can form ordered structures in a single flake, either by atomic sandwiches of M planes ($n \geq 2$) such as $Mo_2TiC_2T_z$ or in-plane ($n=1$) ordered structures such as $(Mo_{2/3}Y_{1/3})_2CT_z$. Density functional theory (DFT) calculations showed that for certain M combinations, ordered MXenes (marked in red) are energetically more stable than their SS counterparts (Babak Anasori et al., 2015).

It has also been reported an ordered divacancy structure, though only possible for M_2C structures, makes an $M_{1.33}C$ composition due to almost 33 atom % of vacancies in the M layers (Babak Anasori & Gogotsi, 2019). This composition is marked in pink on the next table.
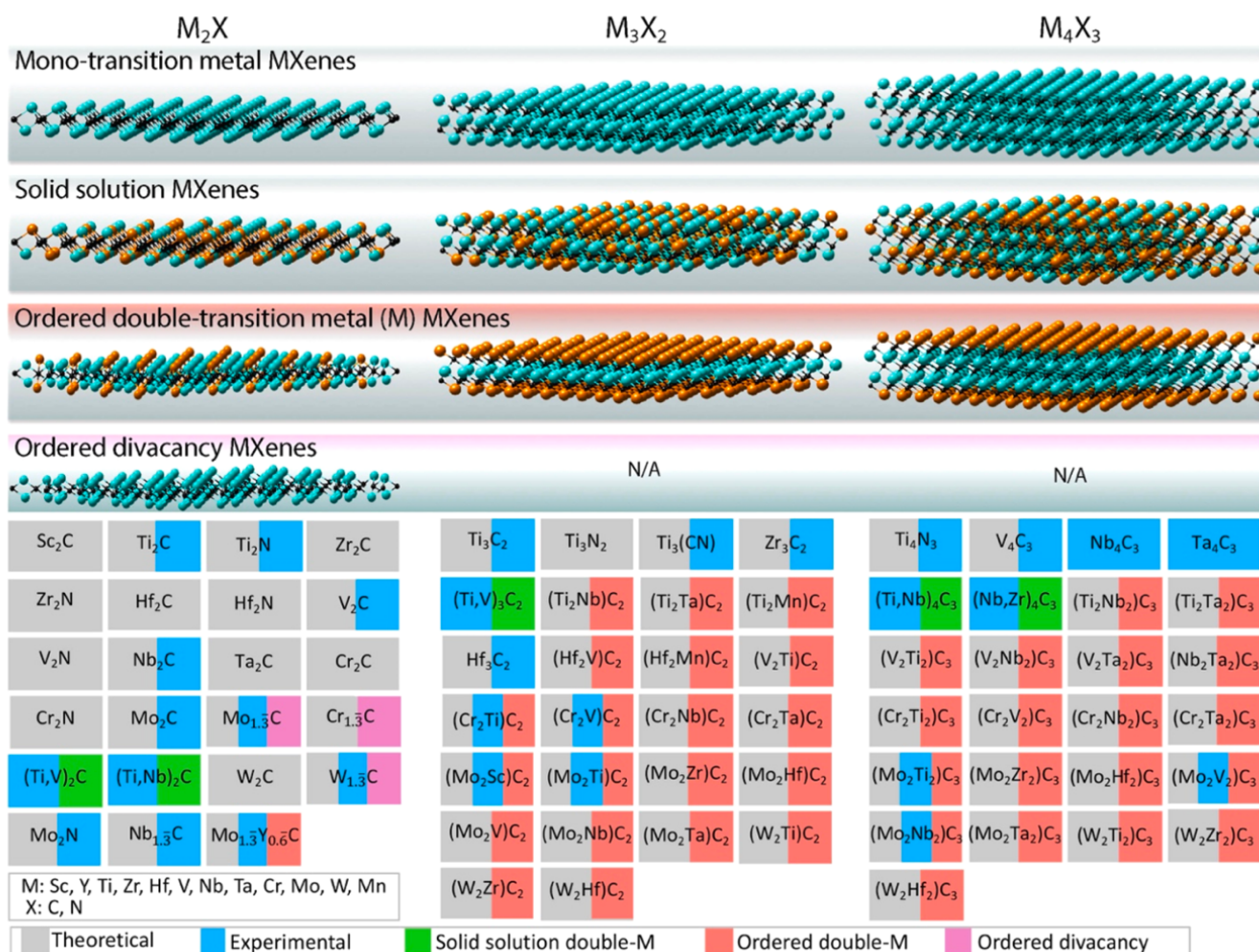
Figure 3.1.2. Possible MXene structures were reported experimentally and theoretically. Image taken from ref (Gogotsi & Anasori, 2019).

Following solution-based etching routes, the surface functional groups (T_z) are mainly fluorine (-F), hydroxyl (-OH), chlorine (-Cl), and/or oxygen (=O) moieties. The ones synthesized using acidic fluoride-containing solutions have a mixture of -H, =O, and -F terminations, while the ones coming from derivative salts can contain also -Cl terminations. However, etching routes containing molten salts, different than fluorine and halogen-based solutions, have produced terminations (T_z) such as -Br, -I, or -NH, -S, -Se, -Te, and else (Jawaid et al., 2021; M. Li et al., 2019; Y. Li et al., 2020; H. Shi et al., 2021).

DFT studies have predicted that the choice of MXene surface terminations can affect its electronic and magnetic properties (S. Bae et al., 2021; Khazaei, Mishra, Venkataramanan, Singh, & Yunoki, 2019), therefore the study of their presence and uniformity is essential for final applications and needs further investigation. Almost all experimental studies on MXenes have a mixture of different surface terminations, whose presence and quantification imply instrumental characterization. However, in 2020 V. Kamysbayev et al. achieved MXenes modifications with uniform terminations (Kamysbayev et al., 2020).

3.1.4.   The synthesis route for MXenes

The challenges in MXene synthesis are many, but mainly rely on the mechanistic understanding of how to control the production of larger-area of single-layer flakes, how to obtain a chemically safe synthesis with the aim of greener chemistry, and how to control surface chemistry by the quantification of the termination elements. The synthesis procedure starts with the selection of the MXene precursor, the selective A-atom layers etching, and ends with the delamination of the multilayers (K. R. G. Lim et al., 2022). On these guidelines, this section will explain the traditional and the newest insights on the selective etching of the MAX phases and the parameter control in the delamination and intercalation process.

As mentioned in the definition section, MAX phases are usually MXene precursors. A highly selective etching of the atomic layers is the key to making them, which is possible because M-A bonds are more chemically active than the M-X bonds. Nevertheless, from more than 10 different A elements (selected in red in Figure 3.1.1. b) 1A has been mainly used to successfully form MXenes. Table 3.1 summarizes the wide range of synthesis routes for possible Mxenes that are possible to use and their precursors. In this Thesis, a Ti_3AlC_2 was used due to its outstanding properties and ease of synthesis, as will be detailed in chapter 4.

As a predominant selective etch approach, fluoride-containing solutions have been used to remove the A-element layers from MAX phases to synthesize MXenes. Two main approaches are commonly used depending on the final desired properties and the application, either by using aqueous hydrofluoric acid HF (M Naguib, 2014) or *in situ* formation of HF. In the latter, the reaction of hydrochloric acid (HCl) and fluoride (e.g. LiF) (Ghidiu, Lukatskaya, Zhao, Gogotsi, & Barsoum, 2014) or ammonium hydrogen bifluoride and ammonium fluoride (J. Halim et al., 2014; Karlsson, Birch, Halim, Barsoum, & Persson, 2015; L. Wang et al., 2016) has been successfully applied for *in situ* HF formation to obtain titanium carbide. Still, new etching methods are constantly being published using bulk reactions, halogen-based solutions, and/or non-MAX phase precursors (Baig, Gul, Baig, & Shahzad, 2022; Ghidiu, Naguib, et al., 2014; Ghosh et al., 2022; Hong Ng et al., 2017; K. R. G. Lim et al., 2022; Jie Zhou et al., 2016).

As recent examples in literature, Mo_2CT_z is the first MXene to have been synthesized from a non-MAX phase precursor (Joseph Halim, Kota, et al., 2016; Meshkian et al., 2015). It comes from Mo_2Ga_2C, a phase that though similar to a MAX phase has A-element layers of Ga separating the carbide layers. Another example is $Zr_3C_2T_z$, coming from $Zr_3Al_3C_5$ as a non-MAX phase precursor (Jie Zhou et al., 2016) and etching aluminium carbide (Al_3C_3) from the layers. Where $Zr_3Al_3C_5$ belongs to example, removing Al-C units is energetically more favorable than just Al layers. Following this finding can enable the synthesis of new MXenes from non-MAX precursors.

Table 3.1.1. MXene synthesis conditions

Type	MXene	Precursor	Etchant	Concentration	Time (h)	T (ºC)	Comment	Ref
M₂X	Ti_2CT_z	Ti_2AlC	HF	10 wt.%	10	RT	Multilayer powder	(Michael Naguib et al., 2012)
	V_2CT_z	V_2AlC	HF	50 wt.%	90	RT	Multilayer powder	(Michael Naguib et al., 2013)
	Nb_2CT_z	Nb_2AlC	HF	50 wt.%	90	RT	Multilayer powder	(Michael Naguib et al., 2013)
	Mo_2CT_z	Mo_2Ga_2C	HF	25 wt.%	160	55	Delaminated via TBAOH intercalation, sonication in DI water	(Joseph Halim, Kota, et al., 2016)
			HCl-LiF	9M HCl-15mol LiF	72	35	Delaminated via sonication in DI water: 1mg/ml solution	(Seh et al., 2016)
	$(Ti,V)_2CT_z$	$(Ti,V)_2AlC$	HF	50 wt.%	19	RT	Multilayer powder	(M Naguib, 2014)
	$(Ti,Nb)_2CT_z$	$(Ti,Nb)_2AlC$	HF	50 wt.%	28	RT	Multilayer powder	(Michael Naguib et al., 2012)
M₃X₂	$Ti_3C_2T_z$	Ti_3AlC_2	HF	50 wt.%	2	RT	Multilayer powder	(Michael Naguib et al., 2012)
				10, 25 & 50 wt.%	24	RT	Delaminated via DMSO intercalation, sonication in DI water	(Ying et al., 2015)
				10 wt.%	24	RT	Multilayer powder	(H.-W. Wang, Naguib, Page, Wesolowski, & Gogotsi, 2015)
			HCl-LiF	6M HCl- 5mol LiF	45	40	Clay-like powder	(Ghidiu, Lukatskaya, et al., 2014)
				9M HCl- 5mol LiF	24	35	Delaminated via sonication in DI water	(Lipatov et al., 2016)
				6M HCl-7.5mol LiF	24	35	Delaminated via hand	(Lipatov et al., 2016;

						shaking (no sonication)	Shahzad et al., 2016
		NH$_4$OH	30 wt.%	18	RT	Multilayer powder	(H.-W. Wang et al., 2015)
		NH$_4$HF$_2$	1M	11	RT	Etched thin film of Ti$_3$AlC$_2$ (60 nm)	(J. Halim et al., 2014)
			1M	120	RT	Multilayer powder	(Karlsson et al., 2015)
(Ti, V)$_3$C$_2$T$_z$	(Ti, V)$_3$AlC$_2$	HF	50 wt.%	18	RT	Multilayer powder	(M Naguib, 2014)
Ti$_3$CNTz	Ti$_3$Al (C, N)$_2$	HF	30 wt.%	18	RT	Multilayer powder	(Michael Naguib et al., 2012)
Zr$_3$C$_2$T$_z$	Zr$_3$Al$_3$C$_2$	HF	50 wt.%	72	RT	Incomplete conversion	(Jie Zhou et al., 2016)
(Cr, V)$_3$C$_2$T$_z$	(Cr, V)$_3$AlC$_2$	HF	50 wt.%	69	RT	Multilayer powder	(Michael Naguib et al., 2012)
Cr$_2$TiC$_2$T$_z$	Cr$_2$TiAlC$_2$	HCl-LiF	6M HCl- 5mol LiF	42	55	Incomplete conversion	(Babak Anasori et al., 2015)
Mo$_2$TiC$_2$T$_z$	Mo$_2$TiAlC$_2$	HF	50 wt.%	48	55	Delaminated via DMSO or TBAOH intercalation and sonication in DI water	(B. Anasori et al., 2016; Babak Anasori et al., 2015)
		HF-HCl	10 wt.%- 10 wt.%	40	40		(Shahzad et al., 2016)
M$_4$X$_3$ Ti$_4$N$_3$T$_z$	Ti$_4$AlN$_3$	Molten salt LiF, NaF, KF		0.5	550	Molten salt etching in Ar atmosphere	(Urbankowski et al., 2016)
Nb$_4$C$_3$T$_z$	Nb$_4$AlC$_3$	HF	50 wt.%	90	RT	Multilayer powder	(Ghidiu, Naguib, et al., 2014)
(Nb, Ti)$_4$C$_3$T$_z$	(Nb, Ti)$_4$AlC$_3$	HF	50 wt.%	90	50	Multilayer powder	(J. Yang et al., 2016)
(Nb, Zr)$_4$C$_3$T$_z$	(Nb, Zr)$_4$AlC$_3$	HCl-LiF	12M HCl-10mol LiF	168	50	Multilayer powder	(J. Yang et al., 2016)
Ta$_4$C$_3$T$_z$	Ta$_4$AlC$_3$	HF	50 wt.%	72	RT	Multilayer powder	(Michael Naguib et al., 2012)
Mo$_2$Ti$_2$C$_3$T$_z$	Mo$_2$Ti$_2$AlC$_3$	HF	50 wt.%	96	55	Delaminated via DMSO or TBAOH intercalation and sonication in DI water	(B. Anasori et al., 2016; Babak Anasori et al., 2015)
		HF-HCl	10 wt.%- 10 wt.%	40	40		(Shahzad et al., 2016)

* HF, hydrofluoric acid; HCl, hydrochloric acid; LiF, lithium fluoride; NH$_4$OH, ammonium hydroxide; NH$_4$HF$_2$, ammonium bifluoride; NaF; sodium fluoride; KF,

potassium fluoride; RT, room temperature; TBAOH, tetrabutylammonium hydroxide; DMSO, dimethyl sulphoxide; DI water, deionized water.

**This table has been adapted from ref (Babak Anasori et al., 2017).

3.1.4.1. Selective Etching approaches

In top-down MXene synthesis, the A-atomic layer is selectively removed from the precursor, leaving $M_{n+1}X_n$ layers intact (K. R. G. Lim et al., 2022). The etching process involves the oxidation of the A-atom, because while in the MAX phase, the A-atom is in an oxidation state close to zero, while after the etching they are found with an increased oxidation state. A common example is seen in Eq.3.1.1 (M. Naguib, V. N. Mochalin, M. W. Barsoum, & Y. Gogotsi, 2014), where strong conditions are used, and HF is directly added. Theoretically, the performance of this reaction depends on the Gibbs free energy and stability of the final by-products. Therefore, the subsequent conversion of the A element to soluble salts or derivative compounds via ligation is crucial, as the etching process will immediately stop when the oxidized products or posterior hydrolysis of them restrict the etchant from accessing other precursor reaction sites. Another role of the etching solution is to remove the protective native oxide layer in the MAX phase surface.

$$Ti_3AlC_2(s) + 3H^+(aq) \rightarrow Ti_3C_2(s) + Al^{3+}(aq) + \frac{3}{2}H_2(g)$$
$$Al^{3+}(aq) + 3F^-(aq) \rightarrow AlF_3(aq) \&$$
$$Al^{3+}(aq) + 6F^-(aq) \rightarrow AlF_6^{3-}(aq)$$

$$Ti_3C_2(s) + 2HF(aq) \rightarrow Ti_3C_2F_2(s) + H_2(g)$$
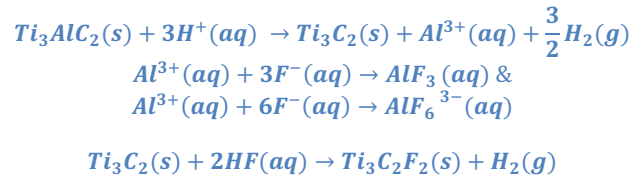
Equation 3.1.1. Ti₃AlC₂ etching in HF solutions.

Regarding fluoride-free routes, Al oxidation can also be performed by electrochemical etching (Eq.3.1.2) when coupled with -OH and -Cl ligands.

$$Ti_3AlC_2(s) \rightarrow Ti_3C_2(s) + Al^{3+}(aq) + e^-$$

Equation 3.1.2. Electrochemical Al etching.

In non-aqueous etching routes, similar analyses can be done. In the halogen-based etching approaches, the transition metals and halide ions act as oxidizing agents and ligands respectively (Jawaid et al., 2021; H. Shi et al., 2021). Meanwhile, in the molten salt route, the transition metal in the halide salt acts as the oxidizing agent and the halide ions as the ligands, e.g. the Cu^{+2} and the Cl^- in the $CuCl_2$ (Y. Li et al., 2020).

Bottom-up synthesis methods such as chemical vapor deposition (CVD) are also possible for synthesis. It has been reported, that α-Mo_2C orthorhombic 2D crystals were produced via CVD from methane on a bilayer of copper foil sitting

on Mo foil. However, using this method yields MXenes with large lateral size and few defects (C. Xu et al., 2015).

3.1.4.2. Intercalation & Delamination Mechanism

Forming individual 2D MXene sheets requires overcoming attractive forces between each stacked layer, and simple mechanical exfoliation provides a low yield of single layers. The presence of stronger intermolecular forces between layers increases the challenge of the process, thus, intercalation of different molecules and ions followed by sonication and/or agitation is widely used (Mashtalir et al., 2013).

The function of the intercalants is to expand the interlayer space and weaken interface interactions. Common examples include solvents, organic molecules, and ions. Successively, adding mechanical energy by agitation and/or sonication (in a suitable solvent) provides the energy to separate the intermolecular bonds between the multilayers into a stable colloidal solution of single or few-layered MXenes.

The solvent choice will directly depend on the MXene surface chemistry, if the termination groups are -F, OH, =O polar solvents can be used, e.g. water, DMSO, *N*-methyl-2-pyrrolidone (NMP), and dimethylformamide (DMF). As seen in Table 3.1, TBAOH or tetramethylammonium hydroxide (TMAOH) are effective in some cases. On the other hand, for MXenes prepared in the presence of HCl and fluoride ions, with -Cl termination groups, Li^+ ions are used for delamination (Alhabeb et al., 2017).

In these intercalation-delamination processes, the presence and attachment of intercalants between layers increases the c lattice parameter. Given this effect, during the washing, there is a swelling of the MXenes through water intercalation, and depending on how strong the intercalants could attach to the surface layers there would be colloidal stability on the flakes after the delamination and the extensive washing (Hart et al., 2019). Adding multivalent ions and removing adsorbed ions via acid treatments could result in flocculation and gelation. Altogether, these considerations rely on a fine-tuning of the intercalant ions and the surface termination groups, their stability and solubility are key for further development.

3.1.5. $Ti_2C_3T_z$

As the MXene that was first discovered, it is the one that presents more reports up to date (Kurtoglu, Naguib, Gogotsi, & Barsoum, 2012). Given this fact, this thesis will focus on this species $Ti_2C_3T_z$ and from now on whenever a MXene is mentioned it will refer to this one. This section will explore the particularities of the reported methods for the desired properties of the applications. As seen in Figure 3.1.3, there are dimensions and structural configurations that work better in different fields and applications.
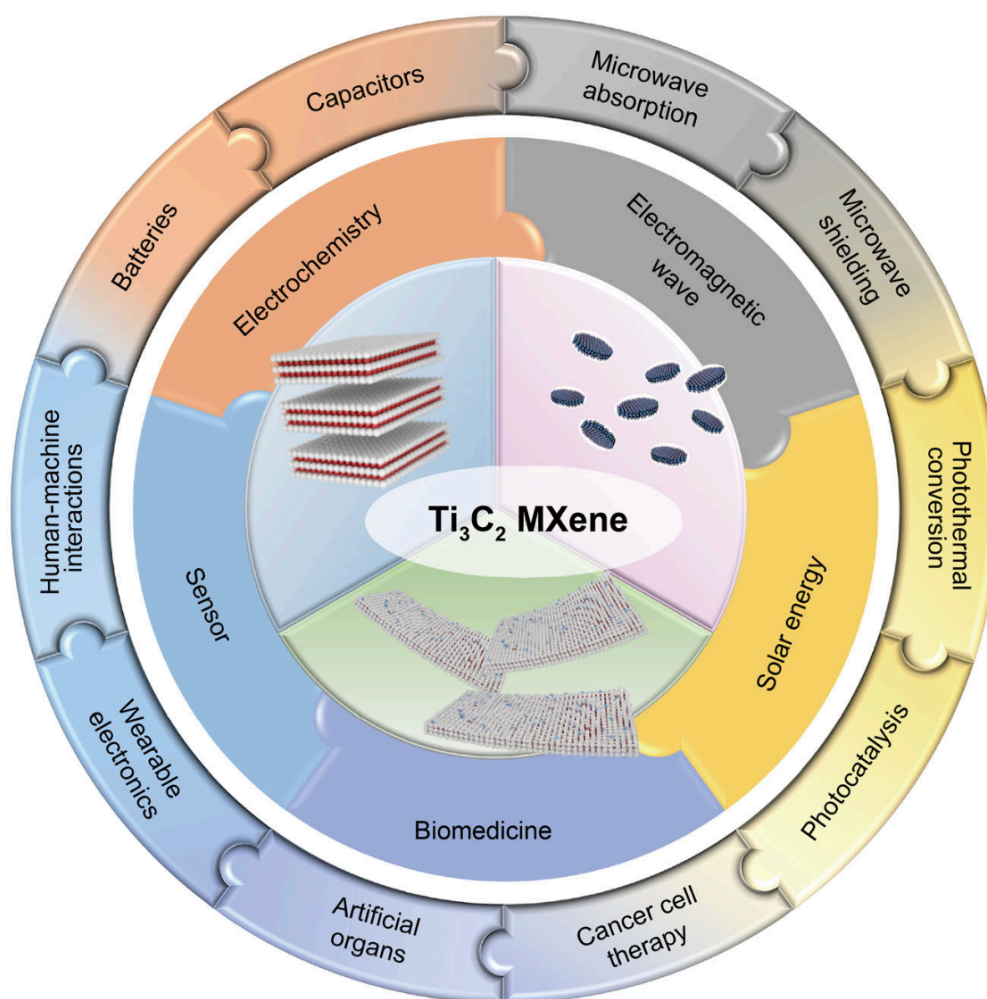
Figure 3.1.3. Schematic diagram of applications of different dimensional Ti3C2Tx MXene. Image taken from ref (W.-X. Huang et al., 2022).

3.1.5.1. Physicochemical Properties

The design and tuning of the synthesis methods convey a specific morphology, distribution, and surface chemistry in the MXene flakes. As seen in Table 3.1, where the main synthesis methods reported in the literature are displayed, these could affect the physical configuration and with it the physicochemical properties obtained, comprising the electrical conductivity, hydrophilicity, and mechanical stability.

Regarding the morphology, the macro- and micro-appearance of Ti_3AlC_2 will drastically be changed once etched into $Ti_3C_2T_z$, as seen in Figure 3.1.4 (a, b, c, and d). From the first, the dense black powder usually changes to dark purple or bright black, whereas, microscopically they exhibit a more compact layered structure after the etching. Nonetheless, after delamination, the multi-stacked MXenes turn into 2D single or few-layered nanosheets, as the ones schematically drawn in Figure 3.1.3.

For instance, monolayered flakes are prepared with strong corrosion methods including 40% HF aqueous solution, which usually breaks them down to nanometer lamellar size (100-400 nm) (Hong Ng et al., 2017). Meanwhile, those prepared on milder conditions such as LiF/HCl and NH_4Cl possess much larger sizes considering micrometer levels (S. Yang et al., 2018). Generally, the larger the lamellar sizes of nanosheets, the more active sites exposed; therefore, it is popular in electrochemistry, catalysis, and biomedical applications. Nevertheless, smaller flakes are also in demand due to their enhanced solubility, optical properties, and electromagnetic shielding applications (W.-X. Huang et al., 2022).
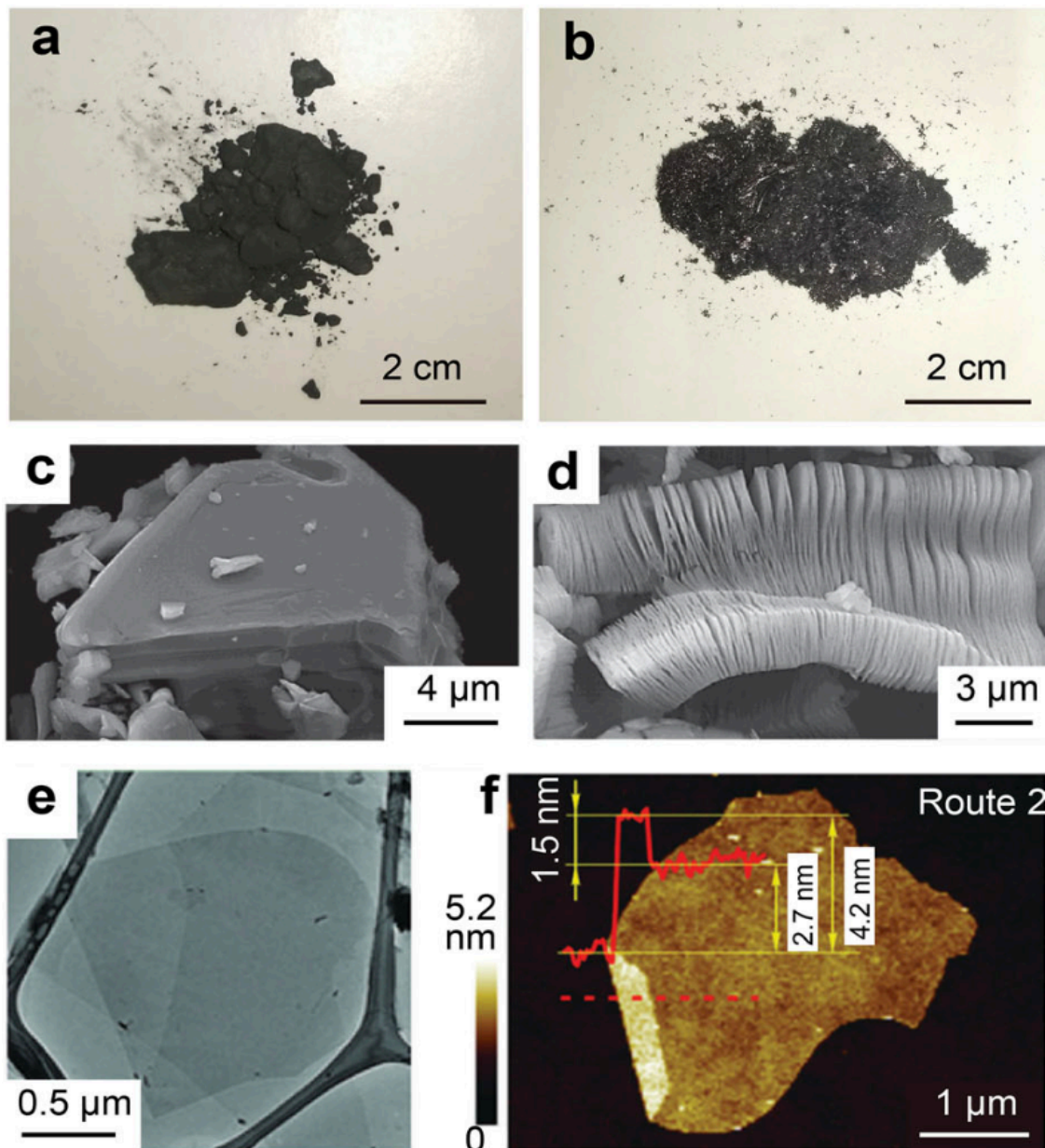
Figure 3.1.4. Morphology of Ti₃C₂ MXene. Photographs of the a) macro-appearance of Ti₃AlC₂ MAX phase and b) Ti₃C₂ MXene; SEM images of c) Ti₃AlC₂ and d) Ti₃C₂ accordion-like multilayers. Images were taken from ref (Babak Anasori et al., 2015). e) TEM and f) AFM images of 2D Ti₃C₂Tᵤ monolayers. Images were taken from ref (Lipatov et al., 2016).

3.1.5.2. Electrical conductivity

The most attractive property of MXenes is their electrical conductivity, even matchable in the 2D material field with graphene. In MXenes, the Fermi energy is located on the *d* metal bands that induce the metallic nature, and the *p* bands of carbon or nitrogen are located under the *d* bands, divided by small band gaps (Ravi Kumar et al., 2022). The conductive carbide core along with the transition metal oxide-like surfaces play a central role in their great performance as conductors (Lukatskaya et al., 2017). The Ti_3C_2 core enables a fast electron supply and favors their flow, providing electrochemically active sites. It has been reported that a pure MXene film with a thickness of 940 nm prepared by a scalable blade coating process with large-size flakes can exhibit an electrical conductivity of $1.5x10^4$ S/cm, i.e. of the same order of magnitude of graphene film conductivity (Jizhen Zhang et al., 2020).

This feature is influenced by factors such as the presence and elements of the terminal groups, interlamellar spacing, and temperature. Firstly, to shorten the conduction paths of electrons removing part of the termination groups by annealing in vacuum directly improves conductivity. Wang et al. (H. Wang et al., 2015) reported a three-time increment of the conductivity (up to. 2410 S/cm) for MXene nanosheets after exposing them at 600ºC for 1 h. Secondly, increasing the interlamellar spacing between flakes could increase electrical properties By delaminating multi-stacked MXenes conductivity can be increased by one order of magnitude (Lipatov et al., 2016). Moreover, the use of intercalants as Li^+ decreases resistance values from 41 to 10 Ω (Hart et al., 2019). Thirdly, a temperature decreases below 100 K increases resistivity, a phenomenon attributed to electron backscattering in 2D materials. Halim et al. (J. Halim et al., 2014) reported that this decrease in temperature increases resistivity in nanofilms from 4.8 to 6.2 $\mu\Omega.\,m$.

Improving electro-conductivity has been used in applications such as electromagnetic wave absorption and shielding, energy conversion, sensors, and catalysis.

3.1.5.3. Hydrophilicity and hydrophobicity

This property directly depends on the surface terminations, which are given according to the synthesis method chosen. The main synthesis methods for MXenes are made in aqueous solutions, providing the termination moieties derived from the reagents (mainly -OH, =O, -F & -Cl) & granting great hydrophilicity to final structure.. In this regard, application fields that take advantage of this feature are photocatalysis (R. Tang et al., 2020), pollutant degradation (Fang, Pan, Yin, & Pan, 2019), biomedicine (Soleymaniha, Shahbazi, Rafieerad, Maleki, & Amiri, 2019), and seawater desalination (Yin et al., 2021).

On the contrary, $Ti_3C_2T_z$ hydrophobic surfaces are achievable by surface modification with organic solvents or by its introduction to other functional materials to develop composites. This feature refers to specific applications such as developing textiles with heat endurance (Q.-W. Wang et al., 2019), or specific materials as platforms for applications such as electromagnetic interference-shielding (J. Liu et al., 2017).

Although the polar terminations grant great hydrophilicity, given this they have the proclivity to easily oxidize in air or water to form TiO_2 or oxycarbides, resulting in structure collapse and performance decrease in applications. This is a particular drawback for MXene development, however spontaneous oxidation can be managed under certain conditions such as vacuum storage, or even freezing in aqueous dispersions.

3.1.5.4. Mechanical stability

Titanium carbide mechanical properties depend directly on the interaction force between individual nanosheets and defect concentration inside the structures. Therefore, depending on the film thickness the material's tensile strength and flexibility varies. Zhang et al. studied that a film thickness of 940 nm can reach a tensile strength of 570 MPa and a Young Modulus in the vertical direction of 20.6 GPa (Jizhen Zhang et al., 2020). This property then allows their use in flexible functional devices and their application in the wearable electronic field (Ling et al., 2014). Furthermore, structural defects also affect this performance as the presence of defects results in up to a 17% of the elastic modulus (Ibrahim et al., 2020). It was also reported that the defect concentration in structures, from 2 to 8% can decrease the Ultimate Tensile Stress (UTS)from 21.6 to 18.9 GPa (Firestein et al., 2020).

3.1.6. MXene polymeric composites & 3D printing.

The inclusion of MXenes in a polymeric matrix can significantly increase the mechanical, thermal, and conductivity properties in comparison to neat polymers (L. Liu et al., 2021; D. Wang et al., 2021; K. Wang et al., 2023). For instance their incorporation can significantly improve (up to 155%) the tensile strength and (102%) the modulus, due to the microcracks bridging effect of evenly dispersed MXene particles in the matrix (Hu et al., 2022). Additionally, composites with MXenes as fillers can target a thermal conductivity 141.3% higher than neat epoxy, and their presence could restrict polymer chain movement and improve also the storage modulus (Wazalwar, Tripathi, & Raichur, 2022). Meanwhile, their exceptional electrical properties make them an excellent filler for electrocatalytic applications and electronics, though their conductivity is directly affected by the composite loading, the surface groups, particle size, defect concentration, and contact resistance between flakes (M.-S. Cao et al., 2019).

Their use has been considered for 3D printing to give them a customizable architecture and major applicability, using techniques such as Direct Ink-Writing (DIW) for electromagnetic shielding and capacitors (Dai et al., 2022; W. Yang et al., 2019), DLP for their conductivity (Salas, Pazniak, et al., 2023), binder jet for applications such as energy storage (T. Li et al., 2022), or even CLIP for printing biosensors (B. Huang et al., 2021).

3.2. Semiconductor Photocatalysts (PhCN/TiO₂)

3.2.1. Historical Development

In the historical overview of TiO_2 for photocatalysis, Hashimoto & coworkers (Hashimoto, Irie, & Fujishima, 2005) pointed out that the oxide powders have been used for millennia as a white pigment, and that their activity under sunlight has been known since 1929 for paint deterioration & fabrics.

Yet scientific studies in photocatalysis started in Lyon, France with the concept of heterogenous catalysis at Université Claude Bernard in 1970 to describe the partial alkane oxidation and olefinic hydrocarbons in the presence of TiO_2 (Fujishima & Honda, 1972; Steinbach, 2006). Then, Teichner reports the behavior of TiO_2 under UV irradiation in ambient conditions and found that when the metal oxide was irradiated and evacuated (to 10^{-6} torr) the white powdered particles turned blue because of losing a fraction of its surface oxygen. Exposing the blue particles to oxygen again restored them to their initial color. Successively, in 1972 other studies reported the first results on water splitting using TiO_2 electrodes by Fujishima and Honda (Fujishima & Honda, 1972). After this, publications in photocatalysis bloomed.

Nowadays, the development in photocatalysis regards the studies of new materials with higher efficiency. Different approaches are used to overcome technical limits and to take advantage of the visible component in light absorption, mainly from solar emissions. The strategies that have been utilized to overcome this issue include lowering the material band gaps, using the doping process for new energetic levels, and the use of heterostructures with increased charge separation.

3.2.2. Basic Principles & Definition

A photocatalytic process occurs when light interacts with a semiconductor surface (the photocatalyst) allowing a redox process. At this point, two reactions occurred simultaneously, oxidation from the photogenerated holes and reduction from the photogenerated electrons (see Figure 3.2.1.).

The process can be divided into four fundamental steps: (I) light absorption to generate electron-hole pairs, (II) excited charges separation, (III) transfer of electrons and holes to the photocatalyst surface, (IV) charges utilization on the surface for redox reactions (Ren et al., 2022). The holes left in the valence band have high oxidizing power and, reacting with water, generate hydroxyl radicals responsible for pollutant degradation. Meanwhile, the electrons in the conduction band, via reaction with dissolved oxygen for superoxide ions promote the reduction process.

A good photocatalyst, on the other hand, should promote electrons just by exposure to light, from the valence band (VB) to the conduction band (CB), leaving positive holes (h^+) in the VB. Also, for the efficient photogeneration of the e^-/h^+ pairs, the incident light energy (hv) must overcome the band gap. Both e^- and h^+ can initiate redox processes on the substances present in the surrounding media (K. Rokesh et al., 2021). Therefore, its efficiency depends on features like suitable band edge position, narrow band gap energy, reduced charge recombination, enhanced charge separation, transfer, and surface-active sites (Karuppannan Rokesh, Sakar, & Do, 2020). However, the whole process efficiency would depend on other factors such as photocatalyst morphology, size and surface area, reaction temperature, pH, light intensity, photocatalyst amount, and quantity of organic catalyzed product.
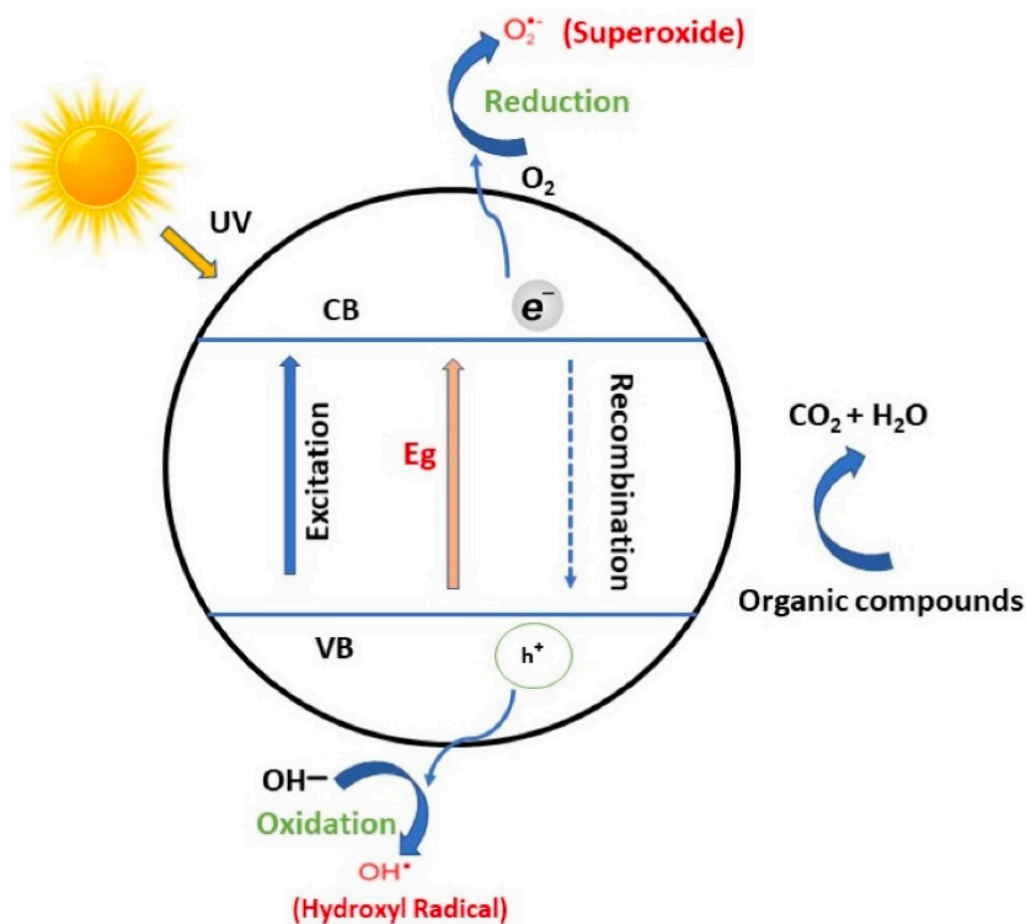
Figure 3.2.1.Schematic diagram of a semiconductor-mediated photocatalytic mechanism. Image taken from ref (Aslam et al., 2022).

3.2.3.   Semiconductor Photocatalysts

As mentioned, photocatalysis is the process of activation and/or acceleration of a chemical reaction driven by light irradiation by means of photoactive materials (Aguirre-Cortés et al., 2023). Semiconductors(SC) are defined as a materials that have a crystalline structure and peculiar electronic characteristic i.e. they have very few mobile electrons at room temperature, which anyway can be promoted, generating electron/hole pairs providing energy, which can be electrical, photonic, thermal,… (Rahman, 2014).Their use for as photocatalysts is reported in several papers (Asahi, Morikawa, Ohwaki, Aoki, & Taga, 2001; Porcu, Castellino, et al., 2020; K. Zhang et al., 2017). SC-based photocatalysts can absorb photons to generate electron-hole pairs that are used for further oxidation or reduction or for photodegradation. These materials have a moderate band gap (E_g<3.5 eV), meaning the energy difference between the valence band (VB) and the conduction band (CB) in its electronic structure (Aguirre-Cortés et al., 2023).

Metal oxides are considered the most efficient materials in this context, while selenides and sulfides are less considered due to their toxicity and poor stability. Currently, the most attractive ones, are n-type SC like TiO_2, WO_3, and Fe_2O_3, because of their stability and CB edge with a potential level negative enough that allows photon reduction without additional electric bias (Kay, Cesar, & Grätzel, 2006; Palmas et al., 2016). The general photocatalytic mechanism is reported in the Eq.3.2.1.

$$SC + Light\ energy \rightarrow\ SC\ (e_{CB}^- + h_{VB}^+)$$
$$Dye + SC\ (h_{VB}^+) \rightarrow Oxidation\ process$$
$$SC\ (h_{VB}^+) + H_2O \rightarrow SC + H^+ + OH^-$$
$$SC\ (h_{VB}^+) + OH^- \rightarrow SC + OH^{\cdot}$$
$$Dye + SC\ (e_{CB}^-) \rightarrow Reduction\ Process$$
$$SC\ (e_{CB}^-) + O_2 \rightarrow SC + O_2^-$$
$$O_2^- + H^+ \rightarrow HO_2^{\cdot}$$
$$HO_2^{\cdot} + HO_2^{\cdot} \rightarrow H_2O_2 + O_2$$
$$Dye + OH^{\cdot} \rightarrow Degrdation\ Products$$
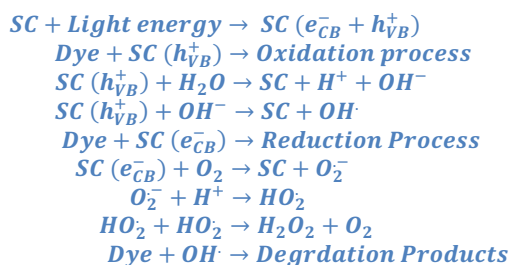
Equation 3.2.1. The photocatalytic mechanism for dye degradation

The main drawbacks of n-type SC are their high recombination rates and negligible light harvesting in the visible range, therefore, strategies such as surface modification, facet engineering, morphology control, doping, and the addition of oxidants have been explored (Nakata & Fujishima, 2012; C. C. Nguyen, Vu, & Do, 2015; Porcu, Secci, & Ricci, 2022; Preethi, Antony, Mathews, Walczak, & Gopinath, 2017; Serpone & Emeline, 2012; Steinbach, 2006; Juan Wang, Wang, Cheng, Yu, & Fan, 2021).

On the other hand, organic SC are preferred due to their abundance in earth constituents, and their optical and structural properties, and particularly because of their tunable energy levels. They can be divided into two categories: polymers and

small molecules. Where the definition of a polymeric SC stands as macro-molecules based on *sp2* hybridized carbon atoms, with the alternation of singles and double bonds along their building block (Porcu et al., 2022) as seen in Figure 3.2.2.

Despite the polymer's versatility, their efficiency can be hampered by the low thermal and short-time structural stability. Therefore, their conjugations can encompass covalent organic frameworks (COFs), metal-organic frameworks (MOFs), or polymeric carbon nitrides (CN). Given the scope of this thesis, CNs are in the limelight in this proceeding, by the use of phenyl carbon nitride (PhCN).
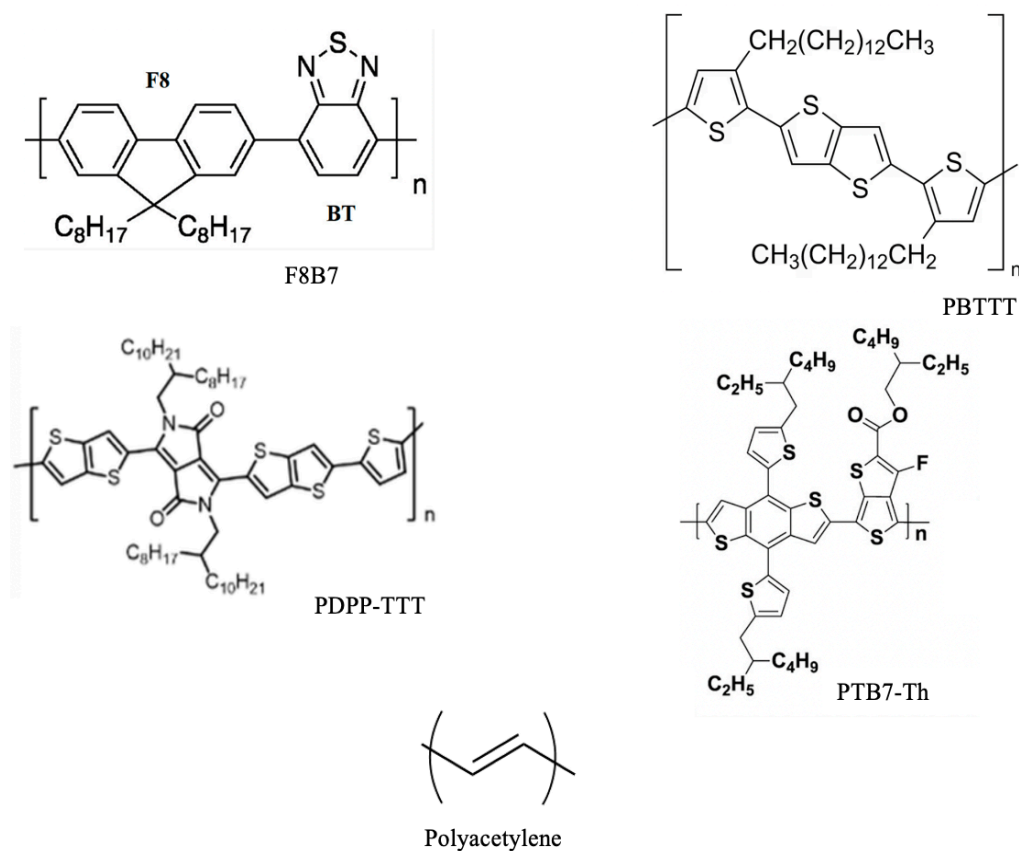
Figure 3.2.2. Chemical structures of SC-polymers. Image taken from ref (Porcu et al., 2022)

Polymeric carbon nitride has emerged as a metal-free photocatalyst. Kroke et al., using density functional theory (DFT) methods, proposed a system based on two-dimensional heptazine-units polymer as the most thermodynamically stable structure (Kroke et al., 2002). Given its graphitic-like structure, it was called graphitic carbon nitride (g-C_3N_4), a layered material in which van der Walls forces hold the stacking layers (C-N bonds), and each layer is composed of the heptazine units, bridged by tertiary amino groups with high condensation degree.

The appealing properties of this molecule include its thermal and chemical stability, biocompatibility, eco-friendly, planar configuration with a π-conjugated system, and moderate bandgap workable in the solar spectrum (Ong et al., 2017;

Porcu, Secci, Abdullah, & Ricci, 2021; Zheng, Lin, Wang, & Wang, 2015). Nevertheless, the efficiency of g-C$_3$N$_4$ by itself is diminished by low quantum efficiency and high recombination rate for electron-hole pair photogeneration (Y. Zhang et al., 2013). Recent studies report that by controlling the morphology and surface properties, an enhancement of the photoreduction can be observed. Particularly, Porcu et. al studied a new polymer of the CN-polymers with enhanced absorption in the solar spectrum (Porcu, Castellino, et al., 2020). The authors exfoliated phenyl-doped carbon nitride for 4-nitrophenol reduction as seen in Figure 3.2.3.
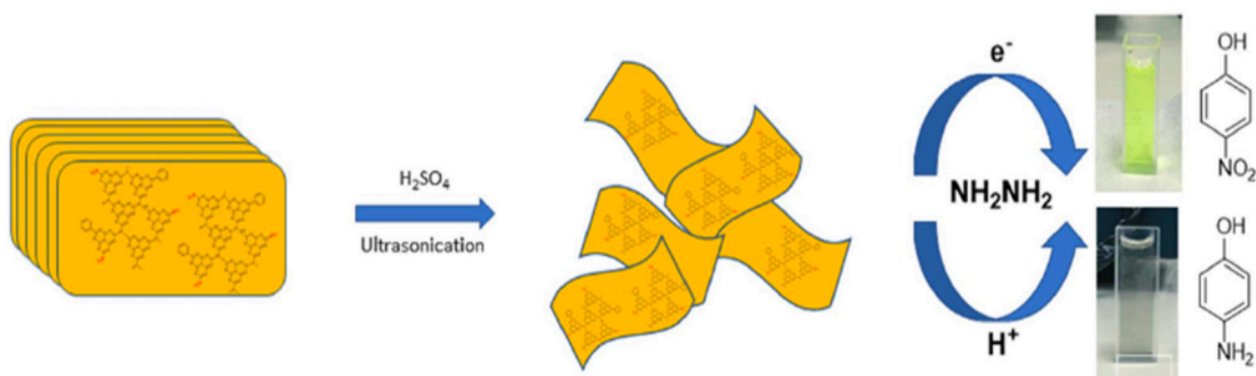
Figure 3.2.3. 4-Nitrophenol photoreduction by phenyl carbon nitride (PhCN). Image taken from ref (Porcu et al., 2021)

3.2.3.1. Heterostructures

The design of heterojunction systems can improve the photocatalytic efficiency of SC materials. General designs include combinations such as SC-SC heterojunction, SC-metal heterojunction, SC-carbon heterojunction, and the multicomponent heterojunction (H. Wang et al., 2014). These are defined by the coupling of two SC-photocatalysts to take advantage of their relative band structure (Xin Li, Yu, Jaroniec, & Chen, 2019). This coupling has been classified into Type I, Type II, Z, and S-scheme photocatalysts, as mirrored in Figure 3.2.4.
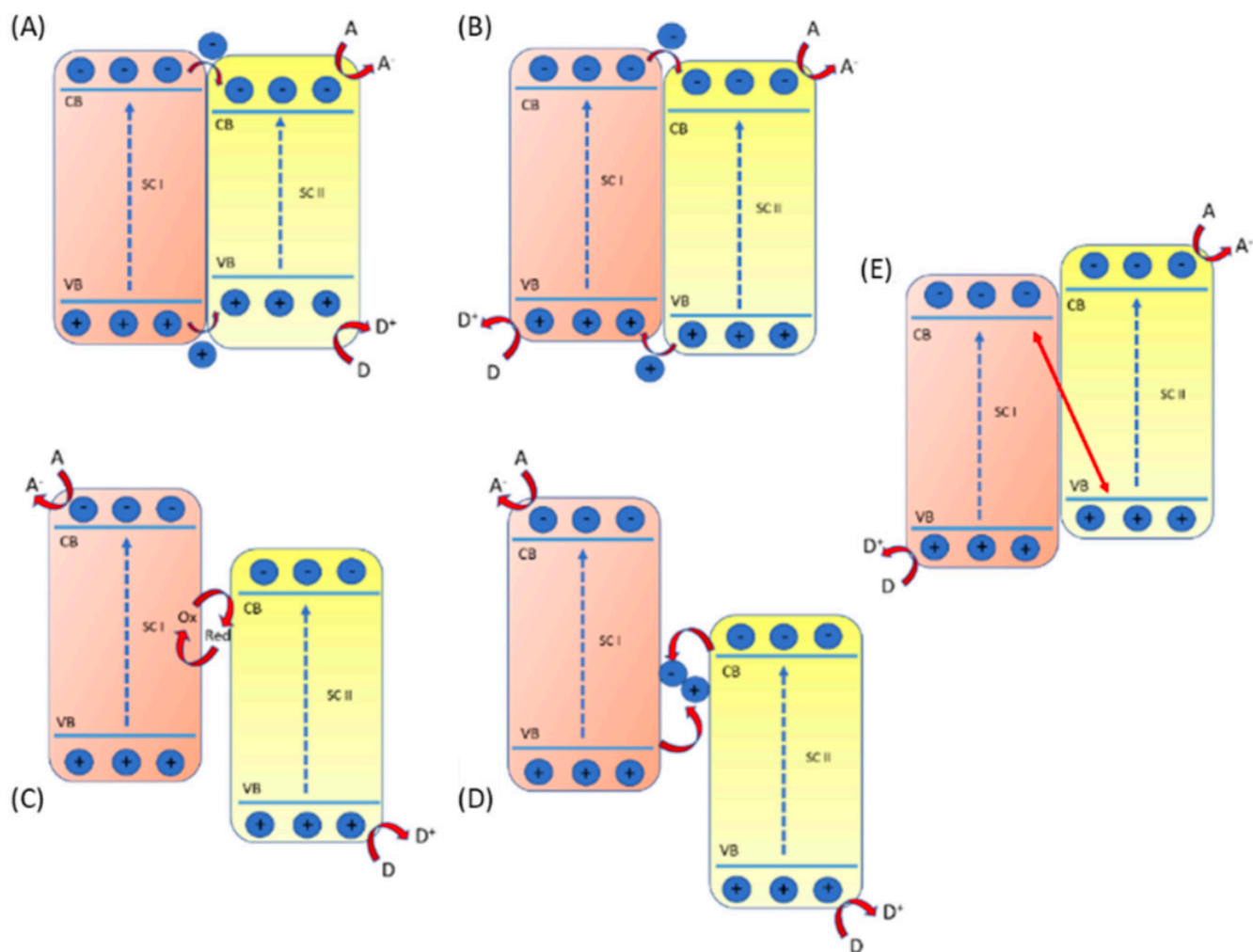
Figure 3.2.4. Heterojunction systems, (A) Type I, (B) Type II, (C) Z-scheme redox mediator, (D) all solid Z-scheme and (E) S-scheme. Taken from ref (Porcu et al., 2022)

The S-scheme has been used to understand the mechanism between hybrid organic-inorganic heterostructure, which will be recalled next.

3.2.3.2. Organic/Inorganic Heterostructure

The formation of hybrid materials by coupling organic-inorganic SC permits to obtain a new class of material with tunable properties. There are three main types of synthesis methods between these systems: sol-gel, solvothermal and/or hydrothermal, and solid state. According to the bond formation between both SC, stability and efficiency are given in the system. On the one hand, the stability of the system can be provided by physical interactions such as hydrogen bonding, van der Waals, or ionic interactions, where proper functional groups are necessary to stabilize the structure. On the other hand, it can be defined by stronger interactions generated by chemical bonding, making it a very stable material with a fast charge transfer process.

The organic part of the hybrid system can act as a photocatalyst in synergy or a photosensitizer. As a photosensitizer, it will absorb a photon with a suitable wavelength on the surface and pass it to an excited state, then, the photoexcited carriers are injected into the excited inorganic band (following the S-scheme and/or Z-scheme in Figure 3.2.4 (c, d & e). The sensitizer's role is at this point to overcome physical limitations by lowering the absorption bands. Section 3.2.3.4 contains different examples of this type of system.

3.2.3.3. Organic/Inorganic Heterostructure example & applications

As a promising technology, the photocatalysis process can be applied for the fabrication of fuel cells (Bhunia & Dutta, 2020), solar conversion (C. C. Nguyen et al., 2015), healthy treatments (K. Rokesh et al., 2021), and environmental radiation (S. Bagheri, TermehYousefi, & Do, 2017), see Figure 3.2.5.
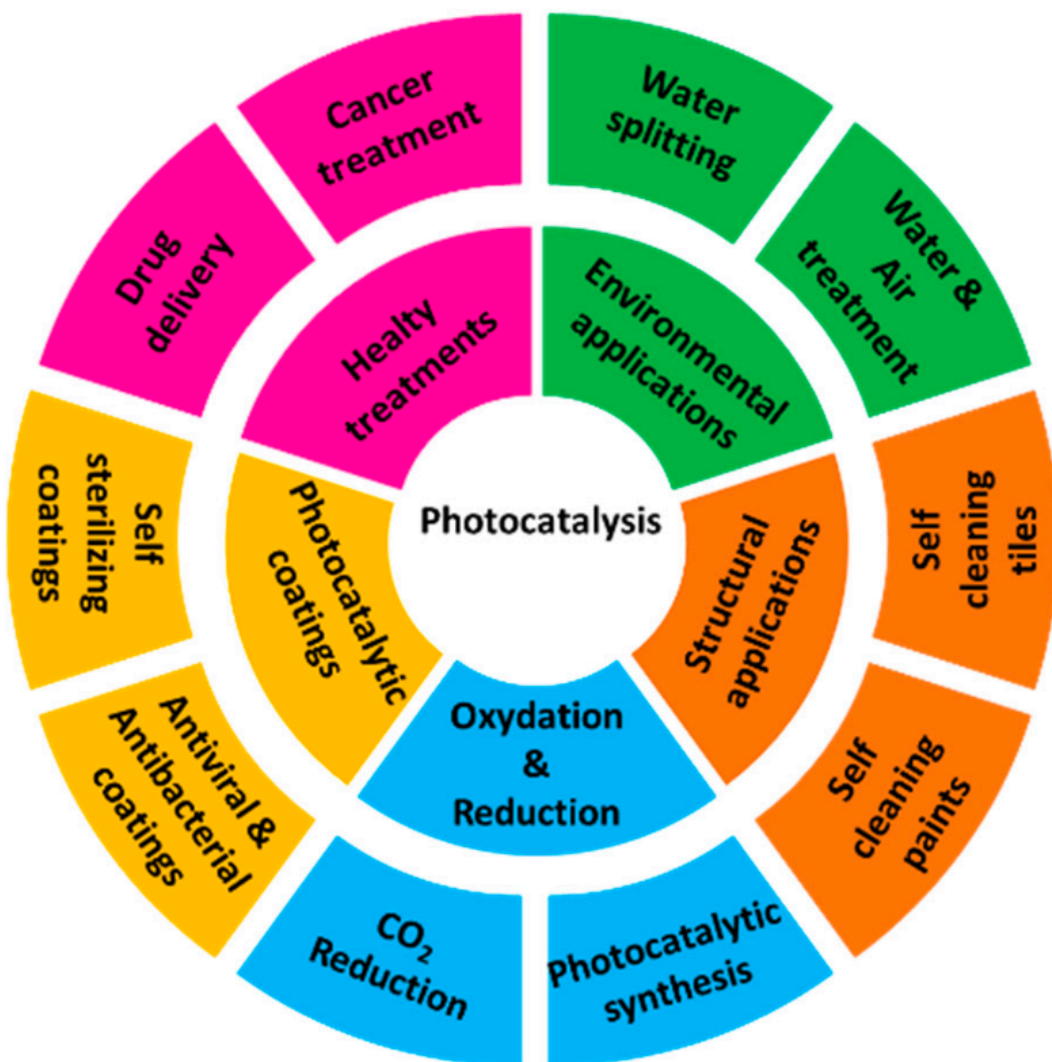
Figure 3.2.5.Application fields of photocatalysis. Image taken from ref(Porcu et al., 2022)

As an example of its use, photocatalysis has been employed to degrade several organic waste types, such as dyes (Porcu, Castellino, et al., 2020), phenolic compounds (Mohamed et al., 2020), organohalides (Gusain, Khan, & Khatri, 2020), and petroleum hydrocarbons (Gusain et al., 2020), but also for heavy metal removal (Nakata & Fujishima, 2012). This technique has also been used for the degradation of pharmaceutical compounds in water and soils (Duy, Bui, & Hien, 2020), as displayed in Table 3.2.1.

3.2.3.4. Compositions & Targeted Application

The next table summarizes examples of different published organic/inorganic heterostructures with targeted application and efficiency. Table 3.2.1 was used to exemplify different Hybrid organic/inorganic System (HS) found in literature and used as photocatalysts for the degradation of organic pollutants, however, as PhCN/TiO$_2$ is the HS used in the thesis, section 3.2.4 is completely dedicated to detail its mechanism and applications.

Table 3.2.1. Reported Organic/Inorganic Heterostructures & applications.

Application	Photocatalyst	Target Contaminant	Light Source	Efficiency	Ref.
Degradation of organic pollutants	Citric acid/CeO_2	50 ppm glyphosate	UV lamp 800 W/m^2, 365 nm and visible lamp 1800 W/m^2, 400–800 nm	100%	(H. Wu et al., 2021)
	Perylene imide/Bi_2WO_6	50 mL Bisphenol A 10 ppm	300 W Xe lamp cold light source	100%	(J. Han et al., 2021)
	Ag_3PO_4/PDI	20 ppm tetracycline hydrochloride	300 W xenon lamp with a cut filter (>420 nm)	82%	(Cai et al., 2020)
	WO_3/Cu/PDI	20 ppm tetracycline hydrochloride	300 W Xe lamp with a cut-off filter (λ > 420 nm)	75%	(Zeng et al., 2020)
	ZnSe/Polyaniline	10 ppm tetracycline hydrochloride	LED with 50 W powers and 4300 LM as a visible-light source	90%	(Shirmardi et al., 2018)
	g-C_3N_4/TiO_2	200 mL Bisphenol A, Brilliant green and mixed dyes 20 ppm	Direct sunlight	95%	(Sutar, Barkul, Delekar, & Patil, 2020)
	PhCN/TiO_2	50 mL RhB/MB 10 ppm	white LED Philips 13 W with optical power 100 mW	98%	(Porcu, Castellino, et al., 2020)
	S-doped g-C_3N_4/TiO_2	100 mL Congo Red 50 ppm	300 W Xenon lamp	>90%	(J. Wang et al., 2021)
Hydrogen evolution	Polyaniline/ZnO	H_2O	Xe lamp	9.4 mmolh^{-1} g^{-1} H_2	(Hamdy et al., 2021)

	Cds/TCP	H_2O	300 W Xe-lamp UV cut-off filter $\lambda \geq 420$ nm	104.51 mmolh^{-1} g^{-1} H_2	(Liang et al., 2019)
	Pyrene/MoS$_2$	H_2O	A 300 W Xeon lamp with a working current of 15 A	2.7 mmolh^{-1} g^{-1} H_2	(Zang, Zhang, Lan, Zheng, & Wang, 2019)
	Ti-phosphonate/MOF	H_2O	visible-light irradiation ($\lambda > 400$ nm)	1260 mmolh^{-1} g^{-1} H_2	(Zhu et al., 2020)
	g-C$_3$N$_4$/TiO$_2$/Ti$_3$C$_2$	H_2O	simulated visible light (Xe 300 W lamp)	2592 μmolh^{-1} g^{-1} H2	(Hieu et al., 2021)
CO2 reduction	InVO$_4$ /g-C$_3$N$_4$	CO_2 and H_2O	visible light irradiation ($\lambda > 420$ nm)	69.8 mmolh^{-1} g^{-1} CO	(S. Gong et al., 2021)
	Graphydine/Bi$_2$WO$_6$	CO_2 and H_2O	simulated sunlight irradiation	2.13 mmolh^{-1}g^{-1} CH3OH	(Ruiqi Yang et al., 2021)
	Zr(IV)/MOF/Co	CO_2 and H_2O	visible-light irradiation	70.8 mmolh^{-1} g^{-1} CH$_4$	(Kong et al., 2021)
	SnNb$_2$O$_6$ /CdSe-DETA	CO_2 and H_2O	visible-light irradiation	36.16 mmolh^{-1} g^{-1} CO	(Ke, Zhang, Dai, Fan, & Liang, 2021)
	g-C$_3$N$_4$ /TiO$_2$	CO_2 and H_2O	($\lambda > 400$nm) 8 W UV-light lamp	56.2 μmolh^{-1} g^{-1} CO	(H. Wang et al., 2020)
Sterilization	CeO$_2$/polymeric CN	*Staphylococcus aureus*	visible-light irradiation Sn	88%	(Xia et al., 2020)
	a-Fe$_2$O$_3$/g-C$_3$N$_4$	*Escherichia coli*	300 W Xe-lamp UV cut-off filter $\lambda \geq 420$ nm	>80%	(H. Yang et al., 2022)

	P-doped MoS$_2$/g-C$_3$N$_4$	_Escherichia coli_	Visible light	100%	(X. Zhang et al., 2022)
	Sn$_3$O$_4$/PTCDI	_Staphylococcus aureus & Escherichia coli_	Simulated sunlight	>90%	(Ruiqi Yang et al., 2021)
Reduction of heavy metals	TiO$_2$/WO$_3$/PANI	Cr(VI) 10 ppm	400 W visible lamp	68%	(Rathna, PonnanEttiyappan, & D, 2021)
	PVP/Bi$_2$S$_3$	Cr(VI) 10 ppm	visible light	95%	(Shen et al., 2020)
	PW$_{12}$/CN/Bi$_2$WO$_6$	Cr(VI) 10 ppm	1 KW Xe Lamp	98%	(Ruixiang Yang, Zhong, Zhang, & Liu, 2020)

*Table adapted from ref (Porcu et al., 2022)

3.2.4.   PhCN/TiO$_2$
3.2.4.1. Applied Mechanism for Photocatalytic Dye Degradation

PhCN/TiO$_2$ as a hybrid nanocomposite offers an enhanced surface and catalytic action with an extended photo absorbance reachable up to the visible level, higher charge generation, improved interfacial charge separation, and strong redox properties (Porcu, Castellino, et al., 2020; Porcu et al., 2021). TiO$_2$ is widely studied among SC photocatalysts, though its high band gap (3.2 eV) makes it negligible for light harvesting in the visible range (Nakata & Fujishima, 2012). Therefore, the use of photogenerated charge carriers capable of excitation through the absorption of UV light has been reported in synergy with TiO$_2$ (C. Peng et al., 2016), to increase its photoactivity towards a visible light range.

Particularly, organic-inorganic hybrid systems coupling TiO$_2$ with delocalized conjugated structures with lower band gaps such as graphitic carbon nitride (g-C$_3$N$_4$) (Yan, Li, & Zou, 2009) and phenyl-carbon nitride (PhCN) (Porcu, Castellino, et al., 2020) have been proven efficient. Nonetheless, PhCN offers a superior performance given its capacity to utilize a larger portion of the visible solar spectrum. Its lower band gap (2.0 eV) and slower recombination rate demonstrate that the synthesis of the heterojunction PhCN/ TiO$_2$ system works efficiently, as seen in Figure 3.2.6. The last figure, explains the transfer process of photoexcited electrons from the LUMO state in PhCN to the almost resonant CB in TiO$_2$, facilitating the charge transfer from the organic part to the inorganic one. While the holes remain in the HOMO state of PhCN, it further increases the charge separation of the photogenerated electron-hole pairs. Then the e^-/h^+ pairs will later oxidize species in solution that will further degrade Rhodamine B (RhB).
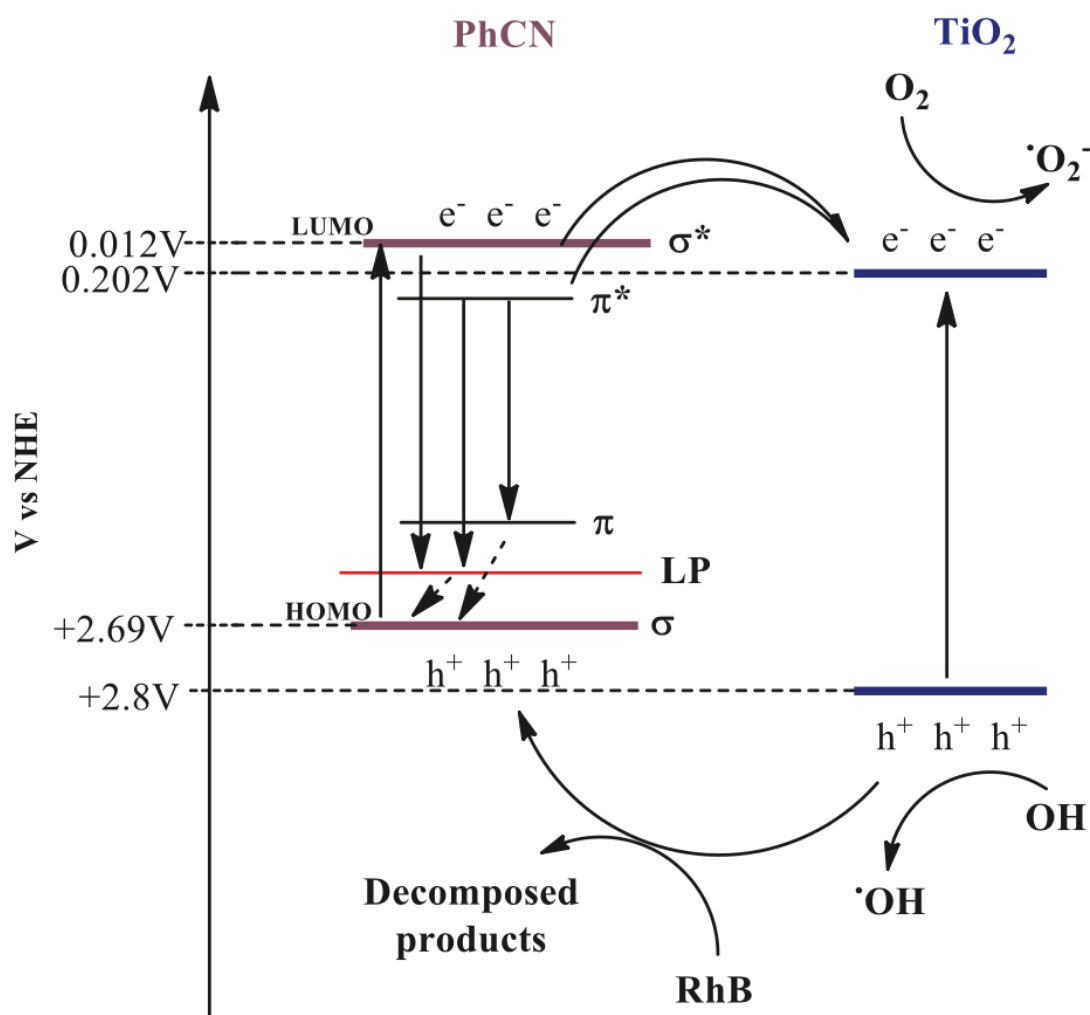
Figure 3.2.6. Schematic representation of the transfer process of photoexcited electron from the LUMO state of PhCN to TiO₂ CB. Image taken from ref (Porcu, Castellino, et al., 2020)

3.2.4.2. PhCN/TiO₂ in 3D nanocomposites for photocatalytic applications

PhCN/TiO₂ is a recently developed hybrid material by S.Porcu et al. its applications are published so far in hybrid composites by surface modifications. The inclusion of this material for additive manufacturing applications and specifically for 3D printing was explored during this thesis in the last chapter. This research includes its use as a hybrid coating material, using a sol-gel process and dip-coating and its inclusion as a filler in vat photopolymerization 3D printing. Further investigations were pursued without success by its inclusion in glassy polymers, though there seemed to be material degradation in the thermal treatments explored.

Chapter 4

4. Development of polymeric/MXene composite inks toward 3D printable electronics

This chapter was written based on the published article (Salas, Pazniak, et al., 2023).

4.1.   Introduction

2-Dimensional materials based on transition metal carbides carbonitrides, and nitrides, known as MXenes, have recently attracted large research interest due to their properties, such as high electrical conductivity (Michael Naguib, Vadym N. Mochalin, Michel W. Barsoum, & Yury Gogotsi, 2014; Q. Tang, Zhou, & Shen, 2012), volumetric capacitance (Ghidiu, Lukatskaya, et al., 2014; Ling et al., 2014; Lukatskaya et al., 2017), hydrophilicity (M. Han et al., 2020), and high thermal endurance (Kang et al., 2019; Z. Li et al., 2015; R. Liu & Li, 2018; Pan et al., 2019). Such characteristics envisage promising performances in different fields like energy storage (Shanto et al., 2022), electromagnetic shielding (Wan, Liu, Tang, Wen, & Xiao, 2021), photodetectors (Tao et al., 2019), sensors (Chia et al., 2020) and electrocatalysis (H.-J. Liu & Dong, 2021). MXenes are obtained from layered precursors known as the MAX phase, as mentioned in the previous chapter. They are then produced by selective chemical etching of the A-element, in fluorine (F) or halogen (Cl, Br, etc.)-based environments. This process induces in the MXenes the presence of surface functional groups inherited from the etchants. After which, the formula of MXenes is $M_{n+1}X_nT_z$, where T_z comes from the terminations given by the acid solution or melts, typically =O, -OH, -F, and -Cl (Carey & Barsoum, 2021; Y. Li et al., 2020).

These termination groups determine the physicochemical properties such as their solubility and particularly the conductivity, and also allow better interaction with polymeric matrices, enabling the fabrication of MXenes-based composites (V. Chaudhary et al., 2022; Jasim et al., 2022; Luo et al., 2022). These materials can combine the properties of polymers, such as good mouldability and processing, with

the outstanding properties of MXenes such as the electrical and thermal response (Naik, Singh, & Sharma, 2022). The interest in them is reflected in the number of published research articles, around 800 articles just in 2022 (source Scopus). For example, Qin L. *et al*. used the electrochemical polymerization process to develop MXene/composite films (Qin et al., 2019) for micro-supercapacitors. Shamsabadi, A.A. *et al.* developed membranes for CO_2 separation by embedding 2D $Ti_3C_2T_x$ nanosheets in Pebax®-1657 copolymer (Shamsabadi et al., 2020).

Beyond conventional manufacturing processes, additive manufacturing (AM) techniques, known as 3D printing, can be used to develop MXene-based architectures (Cui, Zhu, Tong, & Zou, 2023). This combination permits overcoming conventional 2D application of MXenes, achieving complexity in designs, accuracy, and fabrication of 3D objects from CAD data, via layer-by-layer processes (Gross, Erkal, Lockwood, Chen, & Spence, 2014). AM technology has been used to print MXene-based micro-supercapacitors (C. J. Zhang et al., 2019), electrodes (J. Zhang et al., 2019) and others (Fu et al., 2022). Furthermore, polymeric composites containing MXenes were also employed in 3D printing (Aakyiir et al., 2022; T. Li et al., 2022).

Among the different 3D printing technologies, Digital Light Processing (DLP) and Stereolithography (SLA) (Goyanes, Det-Amornrat, Wang, Basit, & Gaisford, 2016) are known to be particularly suitable for the development of functional materials (Fu et al., 2022; Gonzalez et al., 2022; Lantean, Roppolo, Sangermano, Pirri, & Chiappone, 2018). For what concerns this investigation, few works are present in the literature related to light-induced 3D printing for MXenes-based inks, due to some intrinsic limitations. In fact, it is necessary to maintain the uniform distribution of the particles in the photocurable formulation during the printing process, avoiding sedimentation or aggregation which can affect the final properties and enhance the contact between MXenes and outside stimuli (Lantean et al., 2019; Lantean et al., 2022). Meanwhile, increasing the content of the nanoparticles may interfere with the photopolymerization since they compete with the photoinitiator in absorbing the incident light irradiation (B. Huang et al., 2021) and increasing the viscosity (Greaves, Mende, Wang, Yang, & Barg, 2021). So far in previous works, 3D MXene-based structures have been printed either in particular conditions (Tetik et al., 2022), with limited resolution (B. Huang et al., 2021) or in simple squared patterns for electrodes (J. Zhang et al., 2019). In this context, to the best of our knowledge only Fu. J *et al* have achieved SLA printing with MXenes for scaffolds (Fu et al., 2022) and Huang *et al*. have achieved CLIP (B. Huang et al., 2021) for multifunctional gels while studies with DLP are not reported.

In this work, we aimed to develop 3D printable MXene-based ink via DLP photopolymerization. Hence, we embedded MXenes in the printable formulations, to obtain complex and precise 3D geometries. The MXene composition used in this study is $Ti_3C_2T_z$ prepared by chemical etching of Ti_3AlC_2 in hydrofluoric acid (HF). These were later introduced into a monomer formulation of Bisphenol A dimethacrylate (BPA-dma) and Trimethylolpropane triacrylate (TMPTA), whose reactions kinetics was studied by photorheology. Chemical characterization of the

material and the resolution analysis of the printed structures through 3D scanning were performed. The choice of these monomers was based on their compatibility with an annealing post-process, which was further exploited to increase the electric conductivity of the 3D structures.

4.2. Materials & Methodology

The next section contains the procedures for the development of the materials used for the preparation of the ink, the printing parameters, and the characterizations applied to determine its properties.

4.2.1. MAX phase precursor

Ti_3AlC_2 MAX phase powders were synthesized from their elemental constituents by solid-liquid state reaction. Titanium (d50 = 24.8 μm, 99.0% pure), aluminum (d50 = 9.1 μm, 99.5% pure), and graphite (d50 = 6.9 μm, 99.0% pure) powders (all from Alfa Aesar) were used as starting materials and mixed in a molar ratio 3.0:1.1:2.0, respectively. An extra 10 wt. % of the aluminum was added to compensate for its loss during the synthesis process at high temperatures. The mixture was heated up to 1350°C for 3 h under an argon atmosphere to avoid oxidation. The synthesized Ti_3AlC_2 sample was ground in an agate mortar and milled in a planetary milling at 200 rpm in ethanol with zirconia balls (5 mm diameter) for 2 h. The resultant Ti_3AlC_2 powder presented a unimodal particle size distribution (d10 = 3.6 μm, d50 = 6.2 μm and d90 = 10.1 μm).

4.2.2. MXenes Synthesis

The Ti_3AlC_2 MAX phase was etched under 49% HF (2.44 M), where 2 g (0.0103 mol) of the powder was added slowly into a Teflon beaker containing 10 ml of the stirring acid. Therefore, the proportion of MAX phase per acid was 1:24.4. The mixture was kept for 5 h at room temperature with continuous stirring. The obtained solution was then transferred into a 50 mL falcon and repeatedly diluted with deionized (DI) water, centrifuged at 3500 rpm for 3 min until the supernatant reached a neutral pH. The intercalation of the multi-layered structures was performed by adding 2 mL of 40% TBAOH (Tetrabutylammonium hydroxide) to the etched product and left stirring for 24 h. The delaminated suspension was washed in ethanol several times to get rid of the residual TBAOH until the neutral pH was reached. The $Ti_3C_2T_z$ MXenes were collected onto a polyvinylidene fluoride (PVDF) membrane (0.22 μm pore size) by vacuum filtration and left overnight on a vacuum dryer. Before using, MXene powder was dispersed in DI water and additionally sonicated at 49 kHz for 50 min in an ice bath under nitrogen bubbling. Then MXenes were collected by centrifugation at 3500 rpm for 30 min, recovering the supernatant, which was further used to prepare the ink.

4.2.3. Ink Preparation for the printable composites.

The formulations were prepared by mixing the monomers (BPA-dma and TMPTA), the photoinitiator (BAPO), solvent (ACN), and by adding the MXenes, in the quantities reported in Table 4.1, followed by bath sonication for 5 min. The percentages refer to the relative amount of each component in the final formulation.

Regardless the global attention to the materials containing BPA (Bonefeld-Jørgensen, Long, Hofmeister, & Vinggaard, 2007) (BPA-dma), it present standard acylates hazards. Furthermore, its use was envisaged due to the high aromatic content, which will be later exploited in the carbonization process.

Table 4.1.Formulations

Formulation	BPA-dma [wt.%]	TMPTA [wt.%]	MXenes [wt.%]	ACN [wt.%]	BAPO [phr]
BPA-dma: TMPTA	17	33	0	50	1
MXenes 1%	16	33	1	49	1
MXenes 2%	16	32	2	48	1
MXene 5%	16	31	5	47	1

4.2.4. 3D Printing Parameters

The 3D Printing of the nanocomposites was performed on an ASIGA UV-MAX DLP printer with LED light source emitting at 385 nm. During the printing, the layer thickness was fixed at 50 μm for the burn-in and 70 μm for the successive layers, with the light intensity at 37 mW.cm^{-2}. The exposure time was 21 s for the BPA-dma: TMPTA composite, and for the other composites 25, 30 and 35 s increasing the time with the MXene concentration.

Finally, the post-curing process was performed on the printed samples. They were first washed with acetone to remove residual formulation and then exposed under a UV lamp (from Robot Factory) for 2 min, with a light intensity of 12 mW·cm^{-2}.

4.2.5. Post Treatments: Annealing

Two types of thermal treatment were tested to evaluate the annealing process, one under inert conditions and the other under reductive ones. The first one involved heating for 5 h at 900°C at a heating rate of 3°C/min under an argon atmosphere with >50 ml/min gas flow in a tubular furnace using pure Ti metal as the oxygen

getter. The same protocol was used for the reductive environment but under a 5% hydrogen and argon atmosphere.

4.2.6. Characterization Techniques:
4.2.6.1. Evaluation of 3D printability: Photorheology

The investigation of the kinetics of the photocurable formulations was done by photorheology using an Anton PAAR Modular Compact Rheometer (Physica MCR 302) in parallel-plate mode, equipped with a UV-light source (Hamamatsu LC8 lamp 15 mW·cm^{-2}) under the glass bottom plate, with a settled distance of 50 mm. The measurements were performed under isothermal conditions (25°C) with a constant shear angular frequency (10 rad·s^{-1}). The photo-reactivity was investigated by following the changes in the storage moduli (G') during UV-light irradiation. The light was switched on after 60 s to stabilize the system before the polymerization onset. Meanwhile, the viscosity curve was performed on the same equipment changing to a rheometer modulus with shear rates in the range 0.001-100000 s^{-1}.

4.2.6.2. Detecting Absorbance & Visible Spectra

The UV-visible spectra were recorded by a Synergy™ HTX Multi-Model Microplate Reader Instrument (Biotek, Winooski, VM, USA) set in spectrum mode between 330 and 700 nm at a scan step of 1 nm. The experiments were performed on solid films of 200 nm, using a 24-well plate.

4.2.6.3. Measuring polymeric conversion: FTIR Analysis

The Fourier-transform infrared spectroscopy (FTIR) spectra were collected using a Tensor 27 FTIR Spectrometer (Bruker) equipped with an ATR (Attenuated Total Reflectance) tool. The average signal collected was in the range of 4000-500 cm^{-1} with a resolution of 4 cm^{-1}. For each sample, a background measurement was run before the analysis was performed on the liquid formulation (t=0) and the solid films (t=t$_\infty$). The conversion of the acrylate double bonds was calculated following the decreased area of specific peaks.

4.2.6.4. Thermal Simulation, morphological & oxidation profile after annealing

The morphology of the prepared composites was investigated by a Zeiss Supra 40 FESEM, equipped with a GEMINI II column and EDS analyser, where a probe

current of 1200 pA and an accelerating voltage between 5.00 and 15.00 kV were used. On the other hand, the surface composition was analysed by a PHI 5000 Versaprobe Scanning X-ray Photoelectron Spectrometer (monochromatic Al K-a X-ray source with 1486.6 eV energy). The sample size was 100 μm for the high-resolution shift, exploiting 23.5 eV for these peaks. To reduce the charging effect during measurements, all samples were analysed with a combined electron Ar-ion gun neutralizer system. All core level peak energies were referred to C 1s peak at 284.5 eV, and the background contribution, in HR scans, was subtracted by means of a Shirley function.

X-ray diffraction (XRD) was used (Panalytical X'Pert Pro X-ray diffractometer) in Bragg/Brentano configuration with Cu Ka as an X-ray source to examine the crystalline structures. Finally, the Thermal Gravimetric Analysis (TGA) was performed to determine the degradation temperature in an inert environment, using a Mettler Toledo TGA with STARe software and placing the samples on alumina crucibles (70 μL). The temperature in the TGA started from RT to 900ºC, with a heating rate of 10 K/min.

4.2.6.5. Evaluation of mechanical properties

The mechanical properties were evaluated through a Tritec 2000 DMA (Triton Technology Ltd, London UK). The measurements were conducted at 26ºC in a stress/strain setup with a target force of 5 N, force ramp rate of 0.5 N/s on 3D printed samples of 10*10*1 mm^3, while the annealed shrunk versions were 5x5x2 mm^3.

4.2.6.6. Materials electrical resistance

The resistance was measured at 25 ºC through a voltage linear sweep method from -10 V to 10 V with compliance of 0.021 A using a Keithley 4200A SCS Parameter Analyzer. In each measurement, was performed with a 2-probe (tweezer) system, with a direct CVU path.

4.2.6.7. 3D Scanning, Shrinkage, & Resolution

It was performed to evaluate print resolution compared to the original CAD file, using a 3D optical scanner (E3, 3Shape). This scanner includes 2 cameras of 5 MP, an accuracy of 7 μm (ISO 12836) with a scan speed of 18 s. The scanned data and the reference model were aligned before the statistical comparison, and the analysis is displayed as a colored 3D heatmap displaying the geometrical deviation. The same software was used to measure and compare samples before and after annealing, to determine the surface area exposed and the volume of the printed samples.

4.3. Results & Discussion

This section contains results and their corresponding explanations as a consequence of the characterization activities, comparing them with the preceding literature.

4.3.1. Evaluation of 3D Printability

To investigate the 3D printability of MXene inks based on acrylate monomers, photopolymerization's kinetics was initially evaluated. Figures 4.1(a-d) show the schematic representation of the process. $Ti_3C_2T_z$ MXenes have a broad light absorption in UV-Vis range which overlaps the BAPO photoinitiator absorption (band from 350-430 nm (G. Gonzalez et al., 2020)), as inferable from the UV-visible spectra in Figure 4.3. This may reflect a decrease in the efficiency of the photopolymerization mechanism, due to a competitive absorption of incident light (Salas, Zanatta, et al., 2023). This effect was investigated using photorheology, following the change of viscoelastic properties after irradiation. Figure 4.1 e) shows the changes in *G'* modulus (elastic modulus) for the different tested formulations. The photorheology demonstrates that formulations with higher concentrations of $Ti_3C_2T_z$ showed a slight delay after the start of the photopolymerization (see inset in Figure 4.1 e)). Nevertheless, they showed similar *G'* values at the end of the reaction and stability at this stage, confirming their suitability for 3D printing. The presence of MXenes in the BPA-dma: TMPTA resin slows the reactivity of the photopolymerization, which confirms their photo-blocker activity (B. Huang et al., 2021); in 3D printing this usually translates into longer layer exposure. The photo-blocker effect is like the UV-shielding effect already measured for CNTs (Cortés et al., 2021; Gonzalez et al., 2017; Marco Sangermano, Pegel, Pötschke, & Voit, 2008).

In Figure 4.1 f) viscosities of the different formulations are reported. As expected, all the formulations showed a shear-thinning behavior and an increase in viscosity with the increasing amount of MXenes. In standard DLP 3D printing, usually, viscosity below 50 Pa·s is requested (Tetik et al., 2022), thus formulations containing 5% of MXene can be critical in the next investigation step.
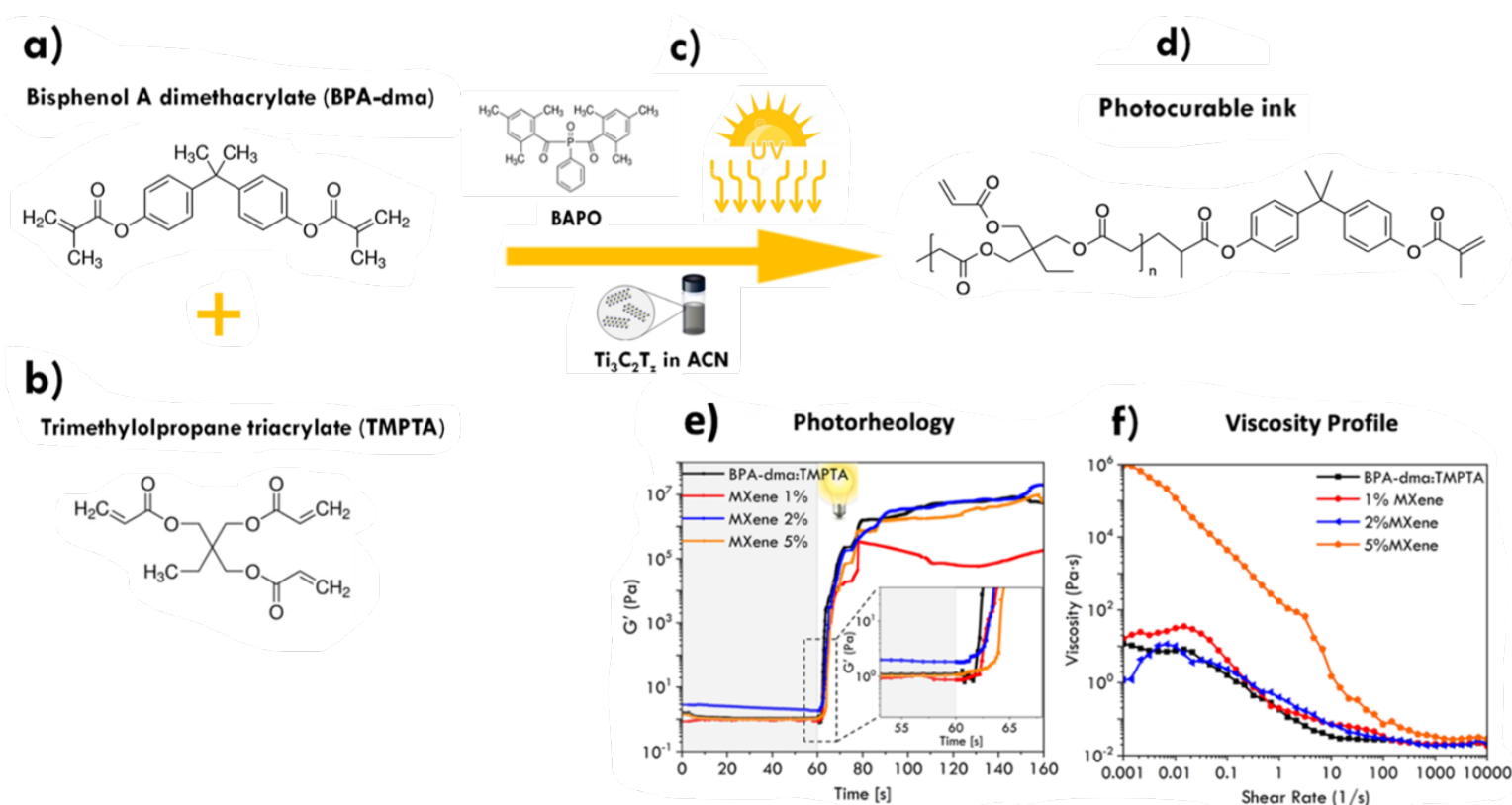
Figure 4.1 Chemical formula of a) BPA-dma and b) TMPTA, c) BAPO chemical formula and the schematic representation of the preparation process, d) representation of the final polymer, e) photorheology and f) viscosity profile of the given formulations. Image taken from ref (Salas, Pazniak, et al., 2023)

Once stable formulations were developed (Figure 4.1 e) and their behavior under irradiation was investigated, these were used to produce 3D printed structures like the one shown in Figure 4.2 b) and Figure 4.2 c). Each formulation required an optimization of the printing parameters, as reported in the method section. As expected after photorheology tests, longer layer irradiation times are necessary for the formulations containing the fillers. Figure 4.2 (b and c) demonstrates the good CAD fidelity of formulations with 2 wt.%. MXenes and for 5 wt.%. Therefore, complex MXenes-based architectures can be printed showing a good resolution, and exemplary structures like lattice cube and honeycomb were reproduced. Such complex geometries can be then envisaged and designed for advanced electronic applications. Nevertheless, to this perspective also electric and electronic performance must be evaluated.

In the present case, a further increase in the content of MXenes will have the previously mentioned limitations in terms of printability. So, our strategy focuses first on 3D printing using an ink that includes monomers, like TMPTA and BPA-dma, with a low amount of oxygen for later, as a second step, inducing annealing. Accordingly, the MXenes content should increase in the final composites, with further conductivity enhancement. The thermal treatments were performed either under an inert or reductive atmosphere, and those were compared in terms of material characteristics and shrinkage of the structures.
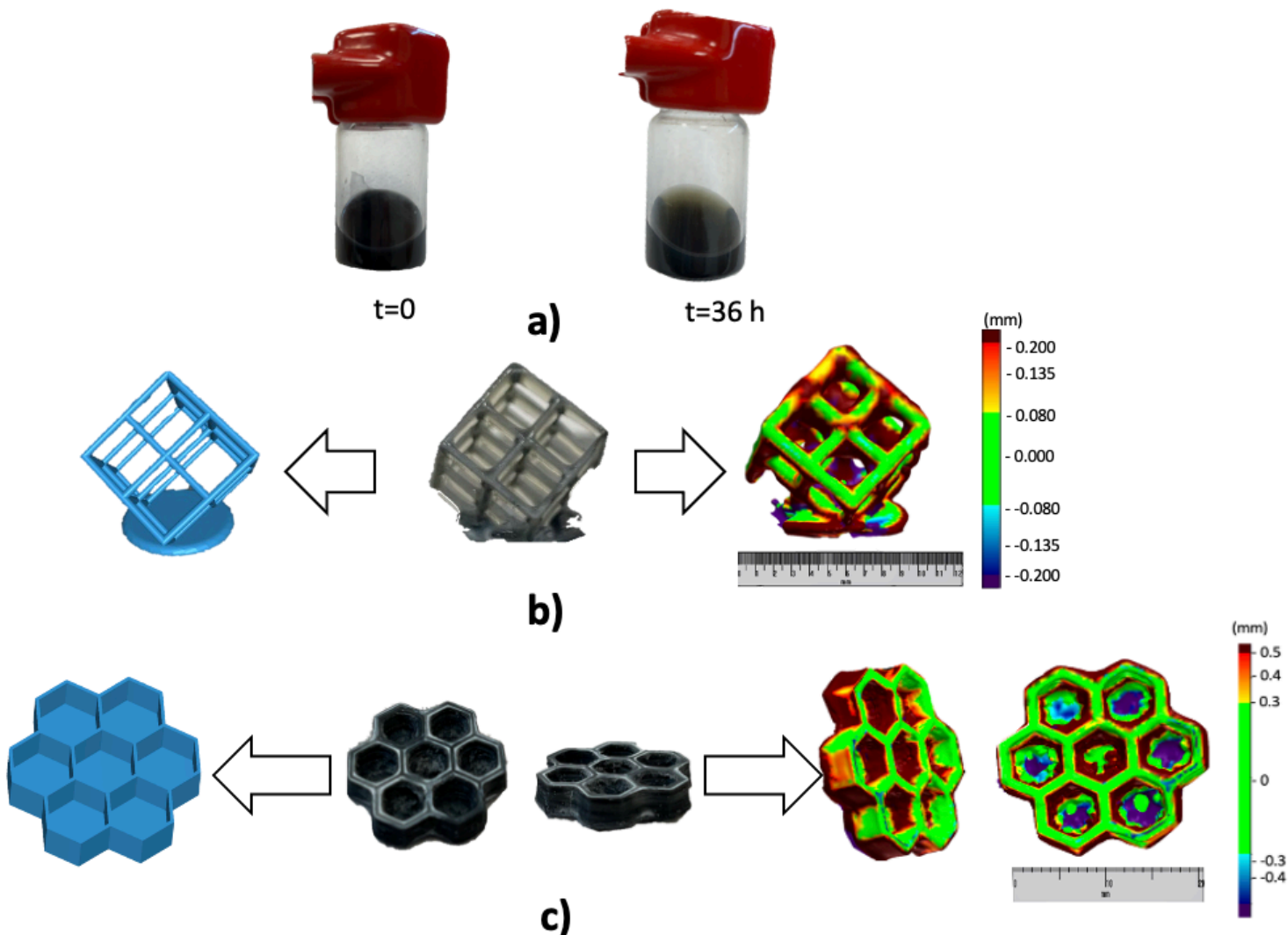
Figure 4.2. a) Stability of the liquid formulation up to 36 h and b) figure from the CAD to the printed structure (MXene 2%) and its 3D scanning, c) Printed honeycomb (MXene 5%) from the CAD up to the 3D Scanning image. Image adapted from ref (Salas, Pazniak, et al., 2023)

4.3.2. Detecting Absorbance & Visible Spectra: The Photoblocker Effect

The presence of MXenes can also be beneficial for 3D printing, acting similarly to functional dyes. In transparent resins the control of light penetration can be problematic, causing uncontrolled polymerization and consequently poor resolution of printed structures (Annalisa Chiappone et al., 2017). In DLP 3D printing, a dye is often used for limiting light diffusion. So far, in the literature, organic functional

dyes have been reported (Gastaldi et al., 2020) to add properties likewise, but also inorganic materials were exploited such as silver nanoparticles (Fantino, Chiappone, Roppolo, et al., 2016), graphene oxide (Annalisa Chiappone et al., 2017), and others. In this case, MXenes, can also play a role in this direction, since they give a blackish pigmentation, limiting also light penetration and allowing better control of the reaction.

Figure 4.3 shows the spectra from 330 to 700 nm of the printed polymeric composites, without and with the corresponding MXene concentrations. In the polymeric spectra, which corresponds to the neat polymeric matrix, two subtle peaks are visible at 370 nm and 395 nm related to the BAPO photoinitiator (Frascella et al., 2018). Those peaks are less evident in in the composites with MXene, since the presence of this filler provides a blackish pigmentation. In this regard, as expected, it is also visible that by increasing the MXene concentration in the composite the absorbance tends to increase, which is noticeable as the higher concentrations have a broader decrease from 330-500 nm(Satheeshkumar et al., 2016). Xu and coworkers identified that exfoliated $Ti_3C_2T_z$ MXenes have a particular broad peak from 275-400 nm which can be the influence for this broad decrease when increasing the MXene concentrations (X. Xu et al., 2020). Noteworthy, the film with 1% of MXene appears considerably with a similar absorbance with the polymeric matrix, however this can be related to a slightly lower thickness of the film, which can be related to human error. In this context it is important to highlight again that t MXene particles compete for light absorption with BAPO, whichcan be translated towards its printability, as the BAPO peaks seem subtly disappear from the MXene curves. In literature this photoblocker effect is also seen by Huang et al (B. Huang et al., 2021) when using MXenes in hydrogel for CLIP printing. In the present case it appears particularly evident in the sample with 3% and 5% of MXenes, which curves are constantly above neat polymer.
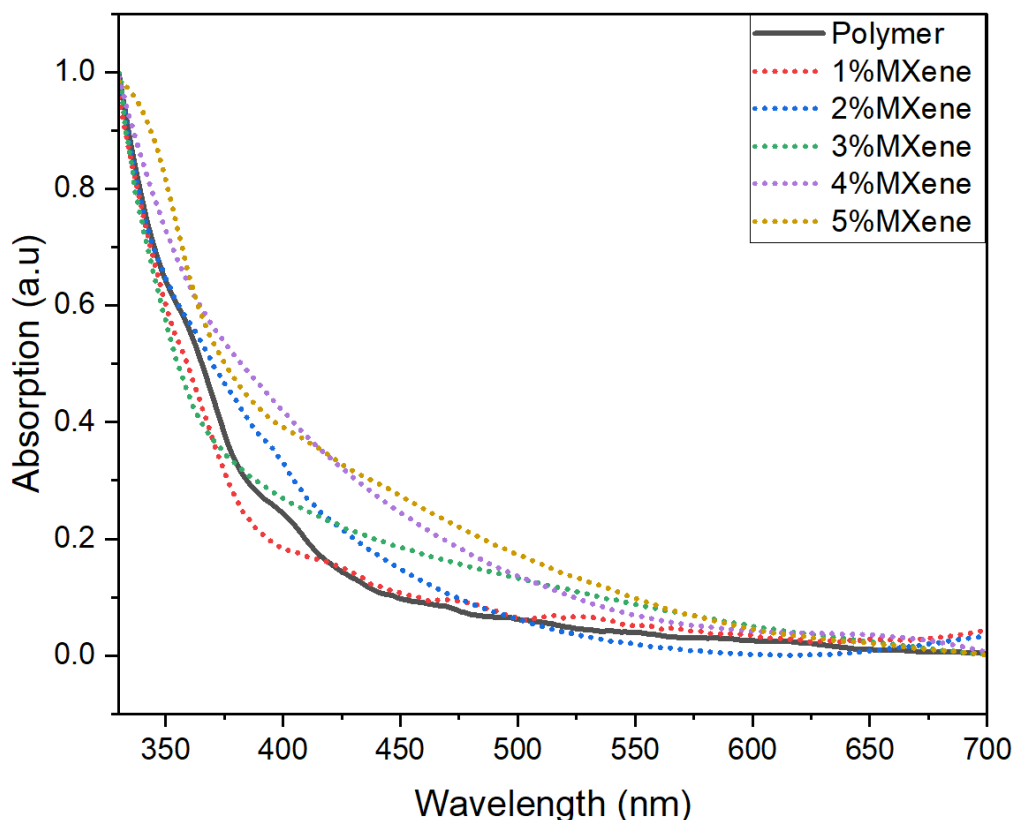
Figure 4.3.UV-Vis performed on thin films (200 μm)

4.3.3. Measuring polymeric conversion: FTIR

The effect on photopolymerization of polymeric MXene formulations can also be observed in the double bond conversion in the FTIR spectra (Figure 4.4) with a consistent decrease at the higher filler concentrations. The main peaks of each structure are also signalled in each correspondent graph, using mainly the acrylate peak at 875 cm^{-1}. The calculated % conversion degree (%CD) is seen in Table 4.2, which was calculated by measuring the peak areas from the formulation without crosslinking and the crosslinked ones. It is evidently seen that the formulations with higher MXene concentration, have less polymeric conversion, as a consequence of the photoblocker effect and the increased viscosity.
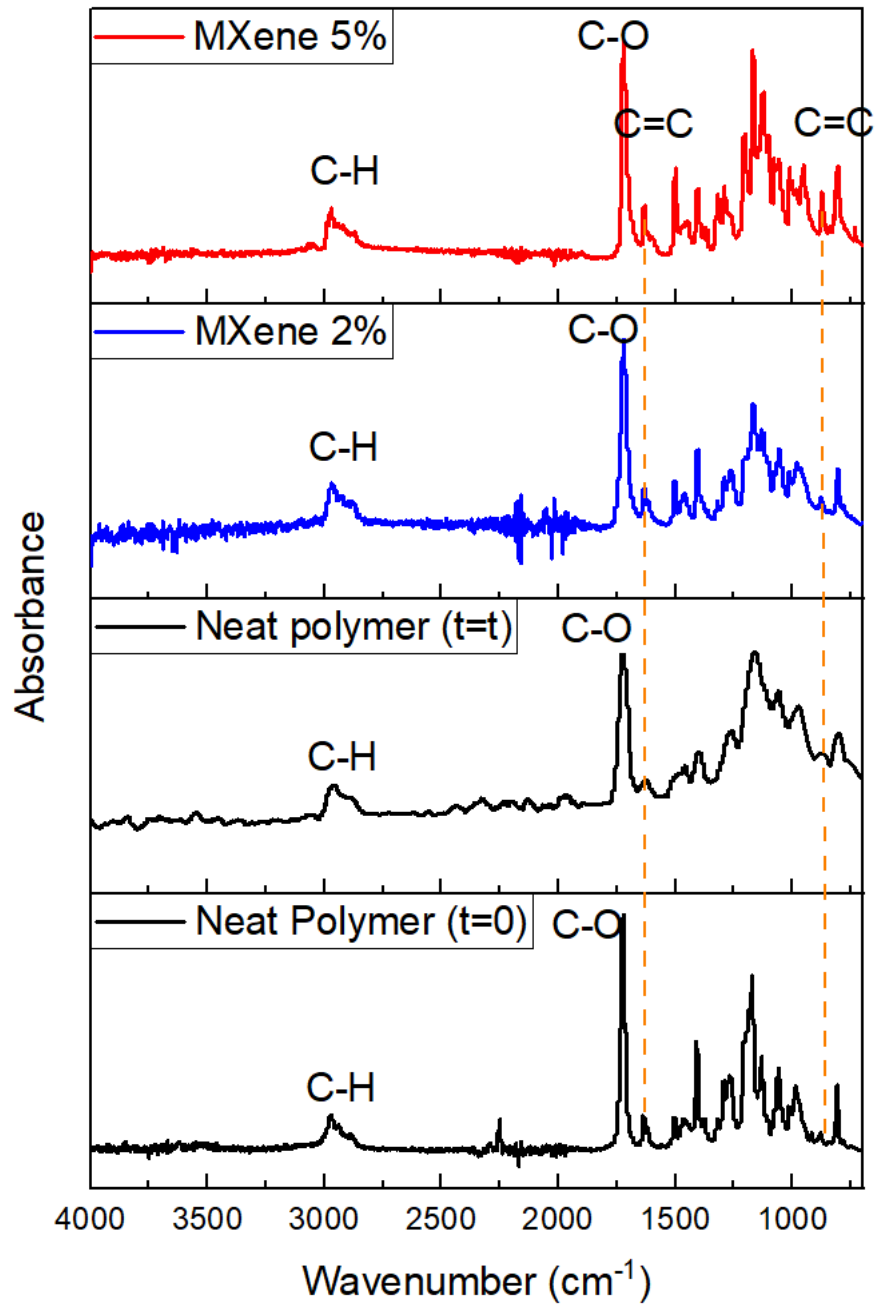
Figure 4.4.FTIR spectra of the formulations, before (t_0), after polymerization (t_∞) and polymerized (t_∞) with MXenes (2% and 5%).

Table 4.2.Photopolymerization conversion degree (%CD)

Sample\Wavenumber (cm^{-1})	$A_{(C=C(t_0))}$	$A_{(C=C(t_\infty))}$	$A_{(C=C(t_\infty))}/A_{(C=C(t_\infty))}$	%CD
TMPTA: BPA-dma\ 875 cm^{-1}	0.84	0.19	0.22	77%
TMPTA:BPA-dma (MXene 2%)\ 875 cm^{-1}	0.84	0.6	0.71	29%
TMPTA:BPA-dma (MXene 5%)\ 875 cm^{-1}	0.84	0.7	0.83	17%

4.3.4. Thermal simulation, morphological & oxidation profile after annealing

TGA measurements (Figure 4.5 (a)) were initially performed in an inert atmosphere, to simulate the thermal process in the oven. As can be observed, the polymeric matrix undergoes thermal degradation with a consistent mass loss between 400°C and 500°C, while the mass of MXenes is almost constant for the whole thermal process as seen on the black curve and the respective composites. However, the presence of the MXenes seemed to slightly delay the degradation towards higher temperatures. Most importantly, a certain residue can be measured at the end of the process, which in the case of the pure polymeric matrix was around 3 wt.% of the initial mass, and with MXenes is higher than 10 wt.% This can be consistent with a barrier effect of MXenes towards volatilization of degradation by-products during the thermal process, which leads to carbonization. On the other hand, TGA measurements cannot provide information on the structural modifications of the materials, and to this aim, XRD, XPS, and FESEM experiments were performed.

The results of the XRD analysis on the polymeric matrix, the pure $Ti_3C_2T_z$ MXenes obtained from the Al removal in the MAX phase, and the materials inserted in the composite are shown in Figure 4.5 c). The polymeric matrix (Figure 4.5 c), black curve) shows the expected amorphous behavior around 15°.

Concerning pure MXenes, yellow and green curves in Figure 4.5 c) show the spectra after synthesis and after thermal treatment in an inert atmosphere at a temperature of 600 °C respectively. Typical (002), (004), and (006) peaks from the lamellar structure are detectable in both spectra, while the corresponding picture of this structure is reported in Figure 4.6 a). Furthermore, traces of oxidation are present. According to Li. Z et al. (Z. Li et al., 2015), the first oxidation stage involves the oxidation of the MXenes surface layers, where the TiO_2 anatase form appears first, as evident in the yellow curve. Despite the inert atmosphere, thermal treatment at 600 °C in an inert atmosphere causes an evolution of the Ti oxidation process toward the formation of titanium dioxide in rutile crystallographic form. These newly formed nanocrystals are attached to the outer sheets and limit the contact of unreacted sheets with O_2, which in turn slows further oxidation and hinders the release of CO_2 produced by titanium carbide degradation.

Figure 4.5 c) also shows the XRD spectra of composite materials at different concentrations (2 wt.% MXene, blue curve, and 5 wt.% MXene, orange curve). The fillers are embedded into the polymer matrix, as confirmed by the characteristic (002) and (004) peaks related to the lamellar MXene structure. Figure 4.5 b) shows a schematic interaction between the polymer and the MXene in the composite. In this case, the material shows an increase in the interplanar distance, witnessed by the shift of the (002) peak towards smaller angles. This phenomenon is compatible with the typical behavior of lamellar materials reported in the literature (Pan et al., 2019; J. Wei et al., 2020) and it is accentuated by the thermal treatment. In literature,

it is also reported that at high temperatures. like 900 °C in an inert atmosphere, moieties including -F, -OH groups are eliminated without affecting the layered structure and maintaining the conductivity (Rakhi, Nayak, Xia, & Alshareef, 2016). However, when embedded in a polymeric matrix, despite the inert atmosphere, the degradation of the polymeric matrix induces the generation of oxygen and hydroxyl radicals, which in turn can lead to MXenes oxidation as evidenced by the XRD patterns (Figure 4.5 b), light blue curve).

Moreover, high-temperature annealing treatments at 900 °C of the composite material in a reducing environment have been carried out and the spectral characteristics are reported in Figure 4.5 b) (red curve). Also in this case, the characteristic peaks of the MXenes are no longer detectable, showing that the long-range order of the crystalline structure is lost during the treatment.
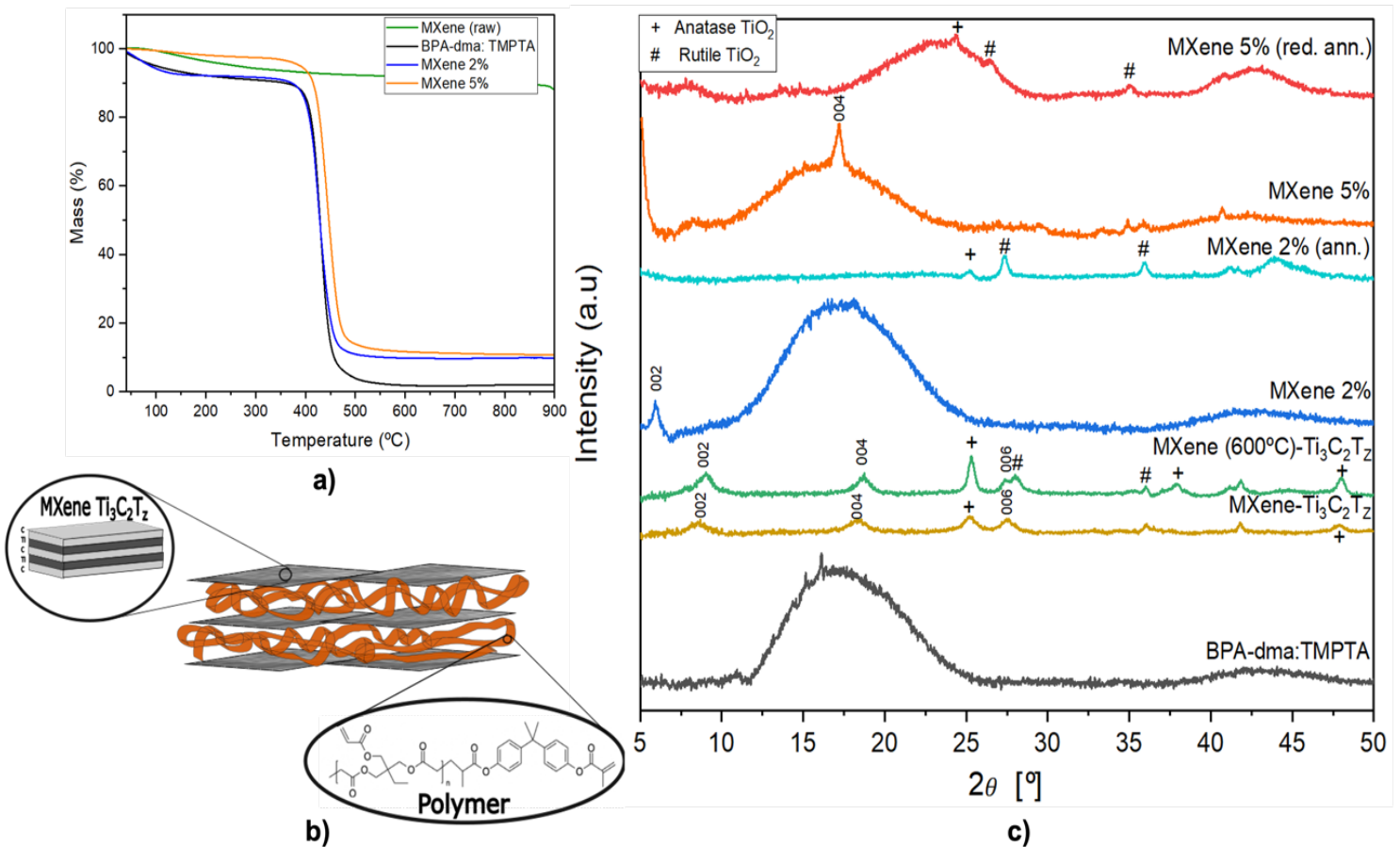
Figure 4.5. (a) TGA in N2 of the pristine MXenes sample (green), the composite BPA-dma: TMPTA (black), composite at 2 wt.% (blue) and 5wt.% MXenes (orange) content. (b) Schematic representation of the interaction between polymeric matrix & Ti3C2Tz-MXene. (c) XRD patterns of the BPA-dma: TMPTA (black), MXenes sample before annealing (yellow), after annealing (green), MXenes/composite at 2 wt.% (blue), annealed MXene/composite 2 wt.% (light blue), MXene/composite 5 wt.% (orange) before annealing and after reductive annealing (red). (JCPDS cards: TiO2 anatase: 89-4921; TiO2 rutile: 89-4920)

Figure 4.6 a) shows the pristine $Ti_3C_2T_Z$ morphology, with a delaminated structure whose chemical nature and structure were also confirmed by XRD (Figure 4.5 c)-yellow curve) and XPS (Figure 4.7 A). Figure 4.6 (b, c, and d) shows MXenes

in the composite under different conditions. Figure 4.6 b) shows an aggregation of MXenes sheets on the cross-section of the 3D-printed polymeric composite, where some stacking is still preserved though the MXene flakes seem broken. Figures 4.6 (c and d) were taken after the different types of thermal treatments performed on the composites (reducing and inert environment respectively), where the morphology of the MXenes is no longer preserved and appears to be dispersed on the rough surface.
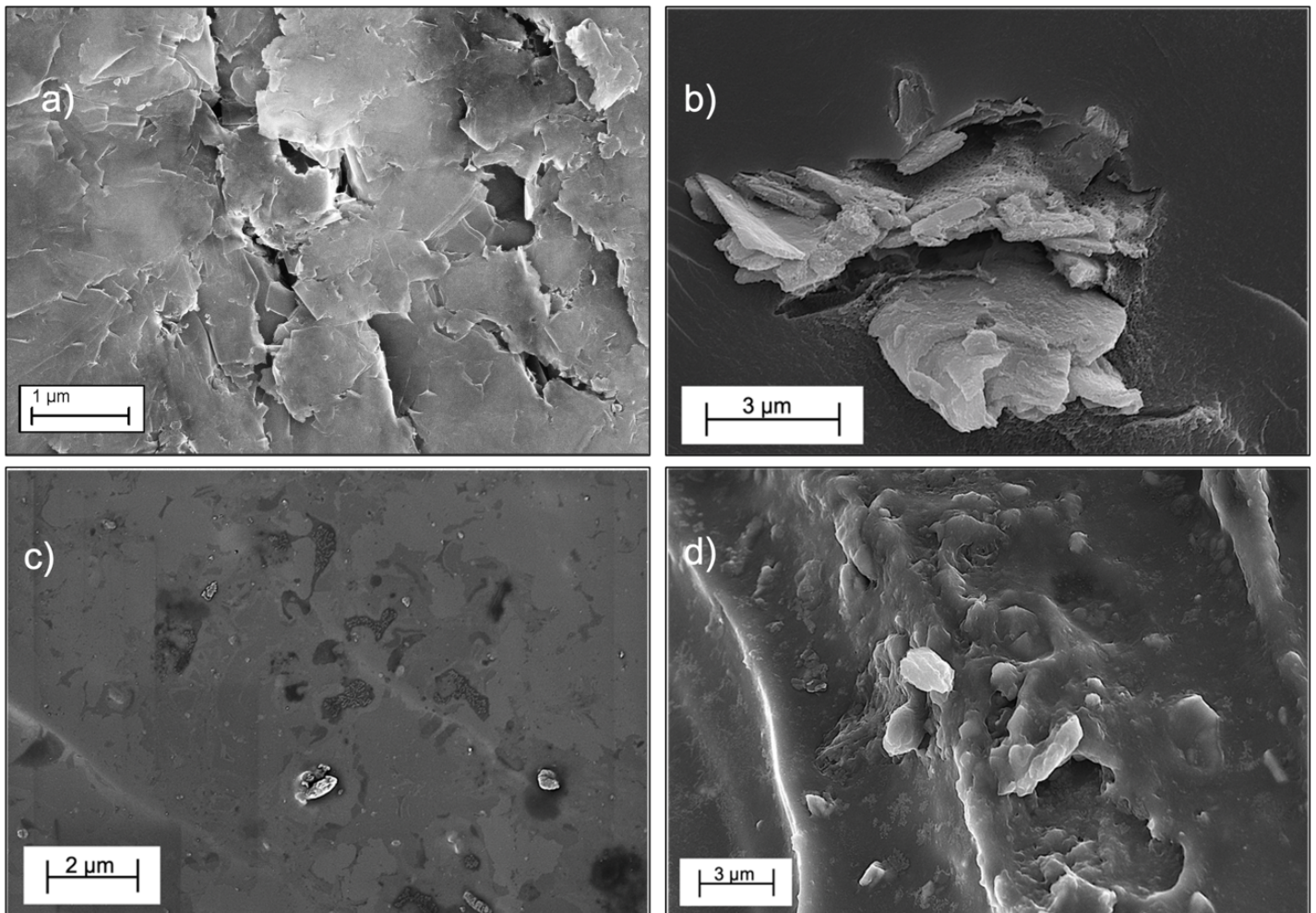
Figure 4.6. FESEM images of: a) pure MXenes (Ti3C2Tz) delaminated sample; b) 5 wt.% MXenes/composite before annealing; c) 5 wt.% MXenes/composite annealed in a reductive environment; d) 5 wt.% MXenes/composite annealed in an inert environment.

XPS was also used to better characterize the composites. High Resolution (HR) Ti2p and C1s spectra are collected and compared in Figure 4.7: concerning the HR Ti2p spectra, in the pure MXenes sample two main components are observed. The highest belongs to the Ti-C bond (constituted by a doublet at 455.7 eV and at around 462 eV), while the second and lower peak belongs to the TiO_2 at 460 eV. This second peak represents the different possible forms of Ti oxycarbides present on the surface given by the sample oxidation (Joseph Halim, Cook, et al.,

2016; R. Liu & Li, 2018; C. Peng et al., 2016). Differently, the printed composite shows a very low Ti-C signal with great dispersion at 455.6 eV, due to the low concentration of reduced Ti at the surface and the presence of TiO_2, evidenced by the 459.3 eV peak. This may suggest that MXenes are mainly embedded and not present on the composite surface. Meanwhile, the Ti bonds can be easily detected on the composite's annealed version, since most of the organic phase was thermally degraded, giving less dispersion and sharper peaks. On the other hand, the Ti-O peak presence, also observed from XRD, indicates a certain degree of oxidation of MXenes on the composite surface and after annealing, higher than in the pure MXenes phase (Figure 4.7 c). This can be related to spontaneous surface oxidation of $Ti_3C_2T_Z$MXenes, under environmental conditions.
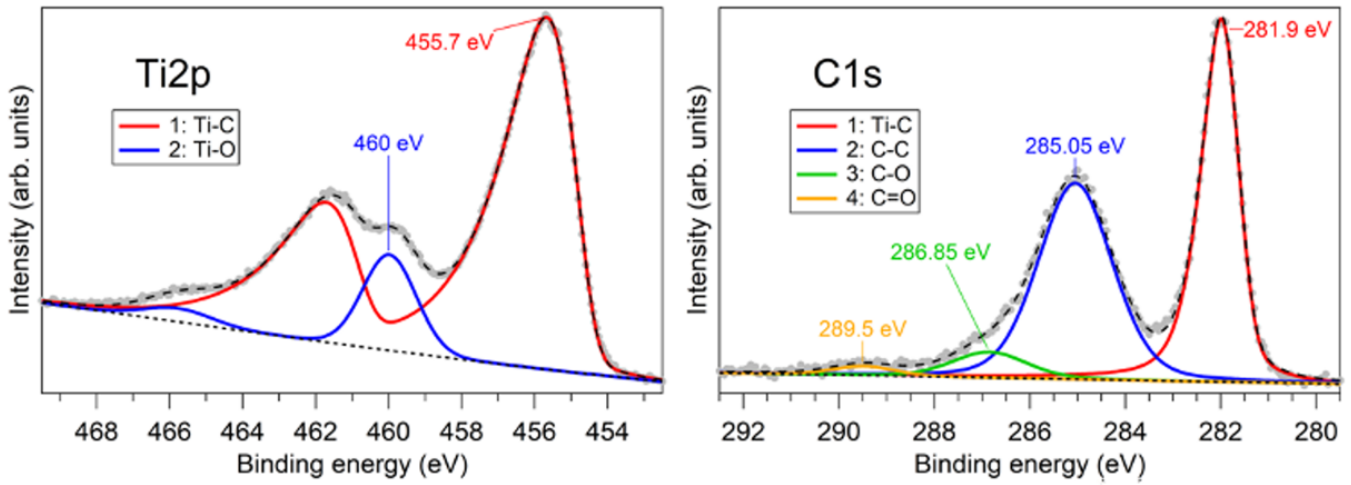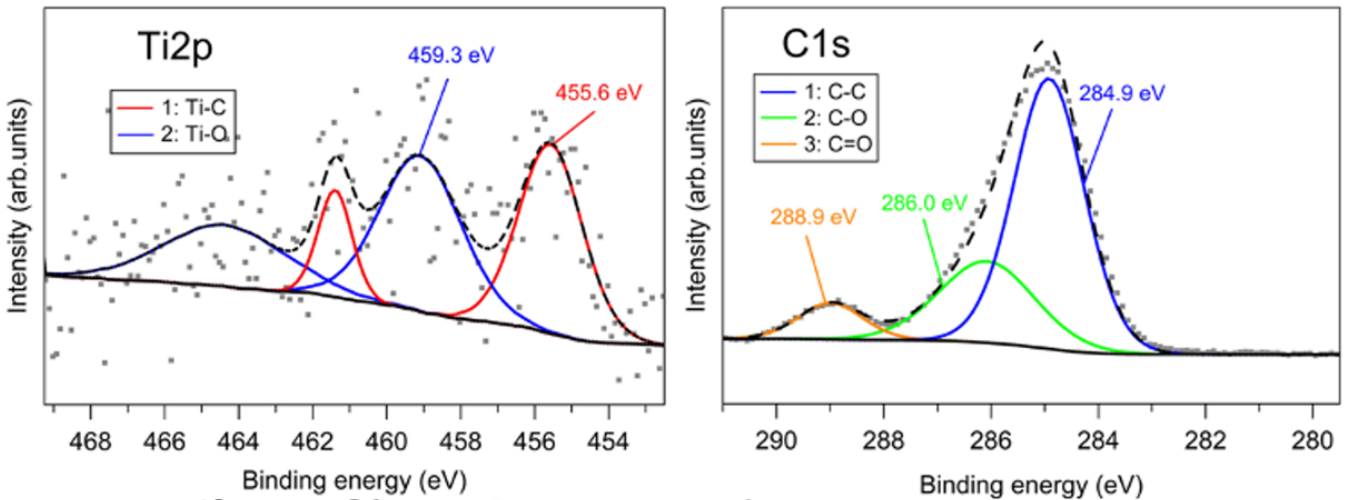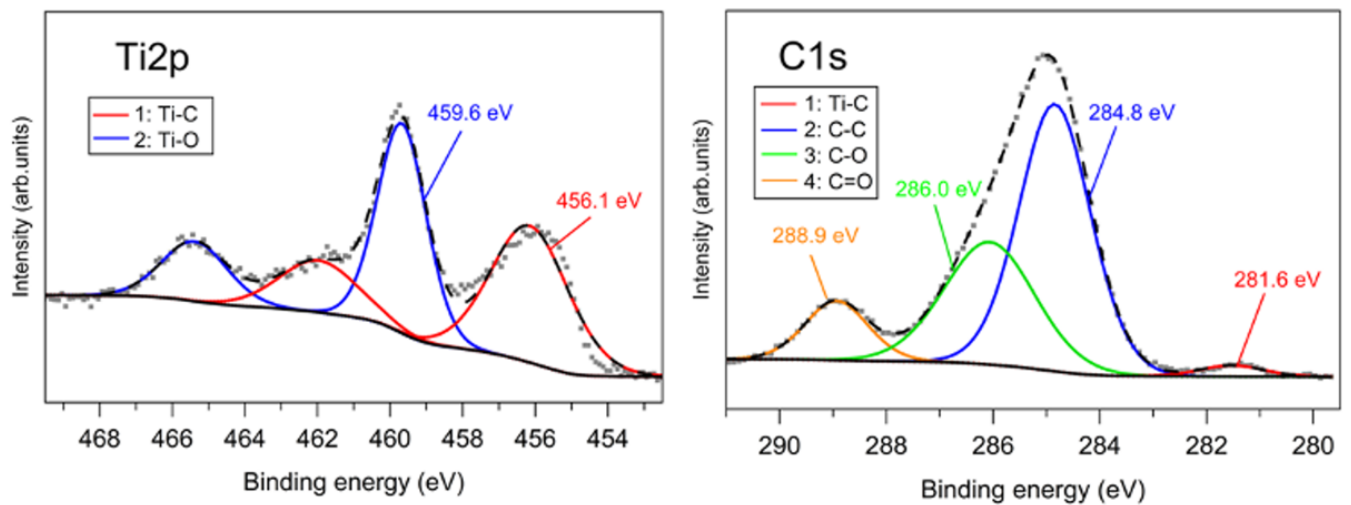
Figure 4.7. XPS High-resolution spectra A) Pure MXenes sample, B) 5 wt.%MXenes/composite and C) the annealed 5 wt.%MXenes/composite. Each bond is represented in a specific color line shown on the legends.

Regarding C1s spectra, on the pure MXenes sample (Figure 4.7 A) the Ti-C at 281.9 eV is the most relevant component, reflecting the (Ti_3C_2) bonds. Other components are also present at 285 eV, 286.8 eV and 289.5 eV, which were attributed to C-C, C-O and C=O bonds respectively (Joseph Halim, Cook, et al., 2016; C. Peng et al., 2016; Rakhi et al., 2015). In contrast, in the composite samples (Figure 4.7 B)) the Ti-C was not detected, while peaks related to C-C, C-O and C=O were evidenced. The presence of those peaks is consistent with the observation of the polymeric matrix, supporting the description above mentioned on the low surface exposure of MXenes in this sample. Finally, in the annealed sample, the Ti-C peak is again observed, in good agreement with the other XPS measurements.

4.3.5.   Evaluation of the mechanical properties

Table 4.3. Young's Modulus [GPa]

Sample	Young 's Modulus [GPa]
BPA-dma: TMPTA	0.08 ± 0.03
MXene 5%	0.3 ± 0.1
BPA-dma: TMPTA (ann.)	2 ± 0.2
MXene 5% (red. ann.)	2.1 ± 0.3

In Table 4.3 all the available parameters are summarised. As expected, the presence of MXenes increases the Elastic Modulus of the composite (from 80 MPa to 300 MPa with 5% MXenes), while it has a lower effect after thermal treatment, with the mechanical behavior that is mostly determined by the carbonization process. In fact, the Young's Modulus value after thermal annealing for the neat polymeric matrix is 2 GPa, and 2.1 GPa in the presence of MXenes due to their high thermal endurance (Y. Cao et al., 2017). These values, like polymers such as polycarbonate or polypropylene, may suggest the use of annealed 3D printed parts also for not-demanding structural applications beyond the functional one.

4.3.6.   Material Electrical Resistance
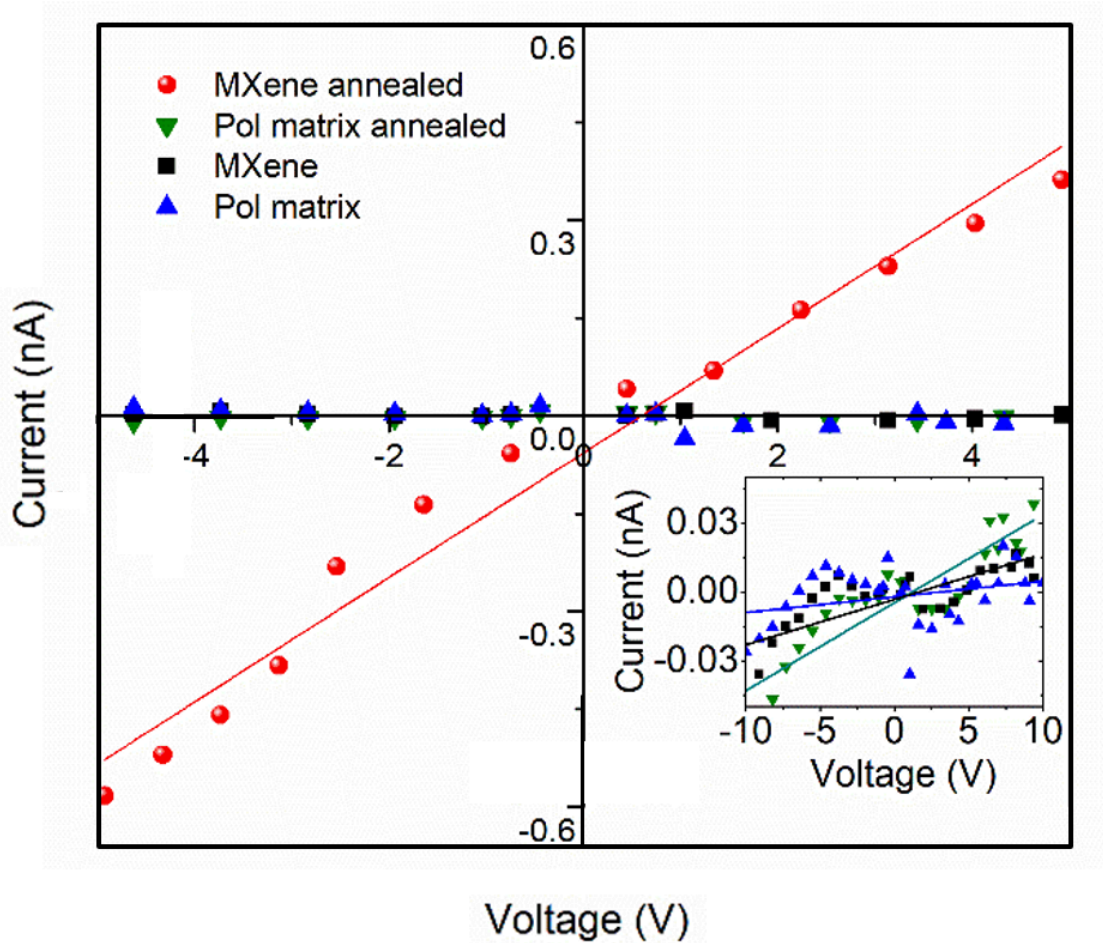
Figure 4.8. I-V Measurements of the determined samples

Table 4.4. Resistance Measurements

Sample	Resistance (GΩ)
Polymer Matrix (BPA-dma: TMPTA)	1468.4
Polymer Matrix (carb.)	261.8
MXene composite 5 wt.%	507.6
MXene composite 5 wt.% (carb.)	10.5

Hosting polymeric matrix is an insulating material and the presence of MXenes decreases resistance from 1468.4 to 507.6 GΩ (see Table 1.4), however, those 3D printed structures are still not suitable for an electronic application. To obtain conductive structures should be thus necessary to increase considerably the content of MXenes as well as the conductivity of the hosting matrix. For this aim, Tetik. H *et al.* exploited direct inkjet printing and freeze casting (Tetik et al., 2022), while Yang. W *et al.* (W. Yang et al., 2019) used extrusion-based 3D printing and freeze-drying to withhold MXenes architectures with good conductivity.

The I-V measurements carried out on the printed samples are shown in Figure 4.8. As evident, the MXenes-containing composite after the reducing carbonization treatment is characterized by larger conductivity with respect to the other samples, which display similar low current values. It is reported that when MXenes are exposed to up to 900ºC, terminal groups such as -O and-OH can be eliminated without affecting their layered structure and maintaining their conductivity (Ji et al., 2020) which contributes to this finding.

Moreover, it is important to highlight that the carbonization treatment is beneficial also to increase the conductivity of the bare polymeric matrix, as shown in the inset of Figure 4.8. The temperature helps removing various carbon-derived species from the surface, which leaves Ti-C bonds exposed or increases their exposure as seen on the XPS.

The obtained I-V curves were fitted with straight lines to calculate their slope, and consequently, to evaluate the resistances of the different samples, which otherwise, would have been difficult to obtain because of the very noisy values due to the low conductivity of the samples by themselves. The obtained resistance values demonstrate that the addition of the MXenes to the polymeric matrix has effectively increased its conductivity, which also became one order of magnitude larger after the thermal treatment.

4.3.7.   3D Scanning, Shrinkage & Resolution
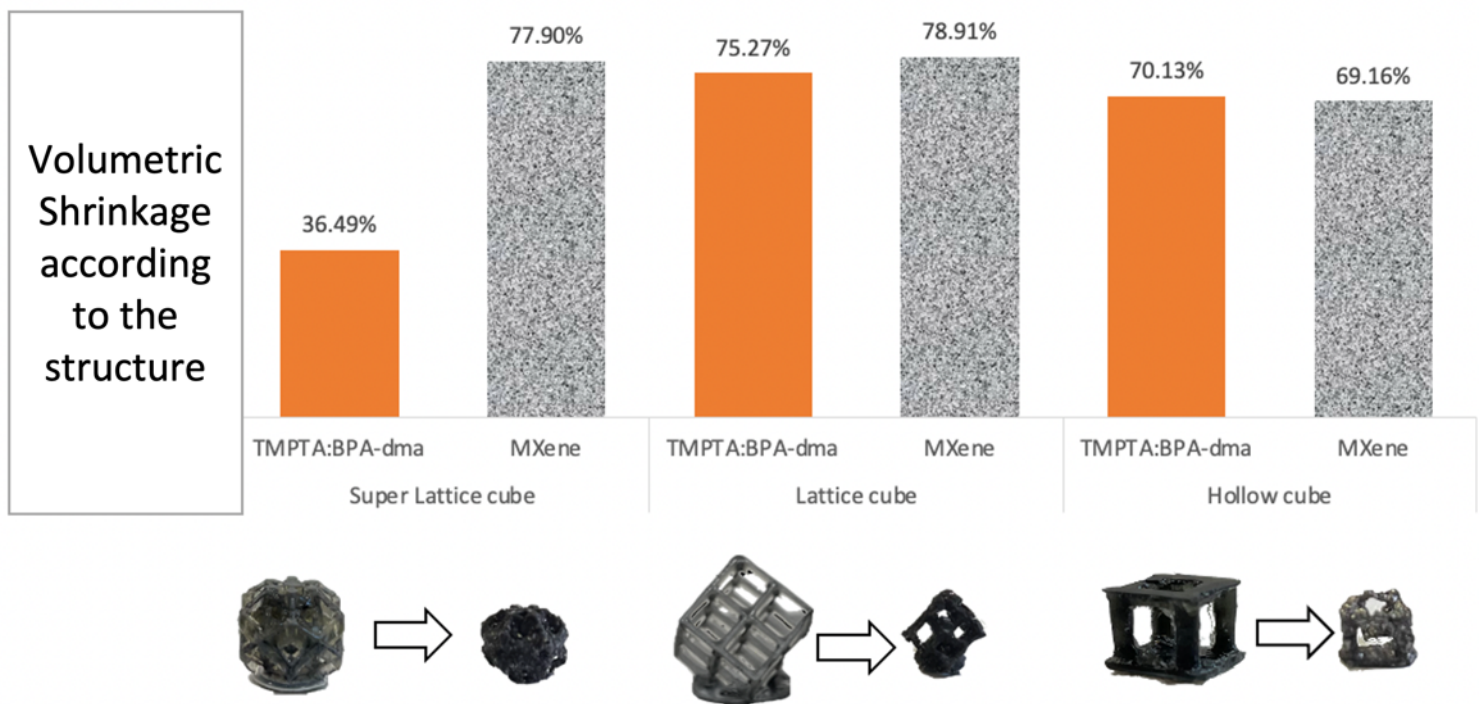
Figure 4.9. Bar chart representation of the volumetric shrinkage of the structures with and without MXenes, with printed structures of the nanocomposite showing the results.

After the annealing was performed on 3D printed structures, as expected for a thermal process, an evident shrinkage in the components was observed, which was measured by comparing the volume of the structures before and after the thermal treatment. The volume was measured by the 3D scanner and then the percentage of shrinkage was calculated. Figure 4.9 shows shrinkage percentage in various structures with and without MXenes and the 3D structures with MXenes and their corresponding annealed counterparts. The shrinkage varies according to the 3D structure, but it was measured at around 75% for the structures with MXenes. In this regard, these measurements suggest that the CAD design and thus the printing should be adjusted according to the volume of the final required device.

4.4.   Conclusions

In this work, the fabrication of printable MXenes nanocomposite polymers using DLP 3D printing is reported based on photocurable acrylate resins and containing Ti_3C_2Tz as a nanofiller. During the printing, higher light intensity and longer slicing time were needed due to the photo blocker activity of the MXenes, but the structures were achieved with high fidelity. However, nanocomposites did not show significant improvement in electrical properties compared to the neat polymeric matrix, thus the carbonization process was performed on 3D-printed structures. This increases the relative amount of MXenes in the 3D printed structures without affecting the quality of the fillers, as witnessed by XRD, XPS, and electronic microscopy measurements. After carbonization, the 3D-printed structures maintained their complex shape, despite, a shrinkage of about 75% measured. This requires that careful design of CAD should be performed to obtain objects with the desired final shape. Finally, electrical measurements were performed to measure the capability for electronic application. Even if the resistance was decreased by one order of magnitude, these 3D printed MXenes/composites still need an improvement of their electric properties. To this end, the feasibility of 3D printing with this material on DLP suggests intriguing advancements in this technology, even if still a lot needs to be improved, especially in terms of electrical conductivity. The potential to develop 3D architectures through this method gives the possibility to create complex devices and further advanced electronic applications, achieving also good resolution, always considering proper compensation for the shrinkage of the material.

Chapter 5

5. Photopolymerizable 3D composites developed with PhCN/TiO$_2$ for photocatalytic applications.

5.1. Introduction

The development of photopolymerizable 3D composites with semiconductor (SC) materials has been studied for various applications, i.e. redox (K. Rokesh et al., 2021), catalysis (C.-C. Nguyen, Vu, Chabot, Kaliaguine, & Do, 2017; Chunping Xu, Ravi Anusuyadevi, Aymonier, Luque, & Marre, 2019), and photocatalysis (Aguirre-Cortés et al., 2023; S. Y. Lee, Kang, Jeong, Do, & Kim, 2020; Nakata & Fujishima, 2012). In literature, SC can be found in different species given their efficiency, like, in Rokesh et al. where CaBiO$_3$ was used to develope photocatalytic redox systems for antibiotic degradation, or in Nguyen et al. where Pt/TiO$_2$/C$_X$N$_Y$-triazine hybrid nanocomposites were employed as co-catalysts on carbon colloidal spheres for hydrogen generation and organic pollutant degradation. Consequently, those materials are appealing for a wide variety of research fields, as seen in Chapter 3, such as environmental (Cai et al., 2020; S. Y. Lee et al., 2020), pharmaceutics (Ruiqi Yang et al., 2021), and structural (Amorim et al., 2018).

The combination of composites containing SC and AM technology or 3D printing permits the design of 3D architectures enhancing the possible application, combining material properties with high-resolution complex structures (Taormina, Sciancalepore, Messori, & Bondioli, 2018), absorption (D. Nguyen et al., 2019), and resistance (S. Park, Shou, Makatura, Matusik, & Fu, 2022).

In particular, the combination of photocatalytic SC materials with 3D printing photopolymers has been reported, but mainly by adding them during the post-treatments (Aguirre-Cortés et al., 2023). For example, by using surface functionalization or deposition strategies, Mei et al. printed by stereolitography (SLA) a carbon-ceramic matrix and later by hydrothermal reaction deposited MoS$_2$ for RhB degradation (Mei et al., 2019). Another example in SLA printing is

reported in Wang et al. , that printed complex architectures with acrylate-based formulations, and then coated those with Cu- and Ni- structures by immersion deposition. (X. Wang et al., 2014). Moreover, other AM strategies for the development of photopolymerizable 3D composites for photocatalytic applications are reported, directly embedding the SC in the polymeric formulations. In this frame Medina et al. used SLA photoactive resins with hyper-porous carbons for the degradation of rhodamine B (RhB) (Medina et al., 2019). Alternatively,- Diaz-Marta et al. used direct ink-writing (DIW) to 3D print SiO_2 colloidal inks with an inorganic binder for Suzuki reactions (Díaz-Marta et al., 2018).

Among photocatalytic SC materials, organic-inorganic hybrid systems were explored for their superior performance due to their recombination rates,thermal and chemical stability (Porcu et al., 2021). These materials are particularly appealing because the formation of charge transfer complex at the interface between the organic donor and the inorganic acceptor allows to increment the charge separation and consequently photocatalytic performance. However, one of the main challenges of these compounds consists in controlling the range of light absorption, hopefully performing a red-shift to the working spectral range from UV to visible and NIR, to utilize a larger portion of the visible solar spectrum (Rehman, Ullah, Butt, & Gohar, 2009). In this context, the application of $PhCN/TiO_2$ as photocatalytic material has demonstrated high efficiency under visible light irradiation (Porcu, Castellino, et al., 2020). Introducing such catalysts in the AM field opens a wide range of possibilities for translating their applicability into customizable 3D architectures and taking advantage of their efficiency under visible light spectra for efficient catalytic photodegradation.

In this context, this research aims to introduce $PhCN/TiO_2$ to translate its photocatalytic activity into DLP-developed 3D printed composites.
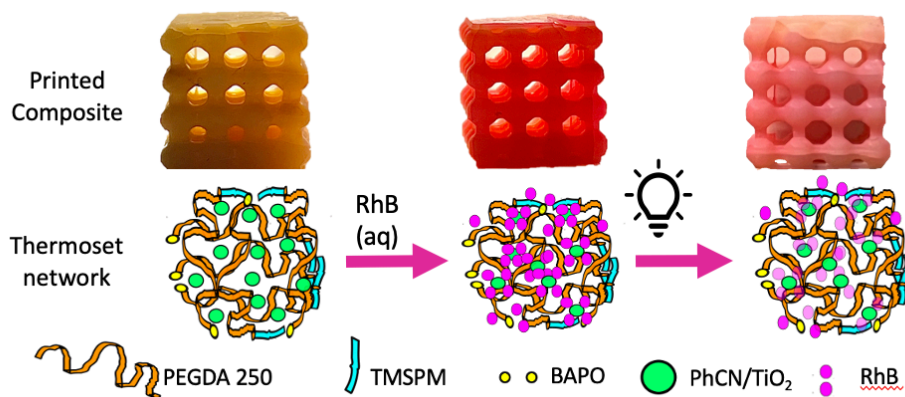
Figure 5.1. Translating photocatalytic activity towards 3D printing

The investigations performed pursued different strategies: the first aimed at testing this hybrid system (HS) for surface functionalization, employing dip-coating on 3D printed structures as a covering technique, optimizing the anchoring onto the polymer surface via an autoclave procedure, and finally testing photocatalytic

activity. The second consisted of using the HS as a filler in polymeric matrices, where the interaction between the HS and the polymeric matrix is explored by comparing rheology, photokinetics, and mechanical properties in the two polymeric matrixes, polyethylene glycol diacrylate (PEGDA with Mn 250) and an optimized ink/resin with PEGDA (Mn 250) and 3-(Trimethoxysilyl)propyl methacrylate (TMSPM). Chemical characterizations were performed on the polymeric matrix to evaluate polymeric conversion and surface morphology, while the material's printing resolution was determined by 3D scanning. Once the more suitable polymeric matrix for this filler was chosen, catalytic photodegradation tests of RhB were executed in solution, of the composite and the coated versions with the HS to compare the efficiency of the used approaches. Then, in the printed composite, solid photodegradation of the RhB was further evaluated.

On the other hand, embedding photocatalytic precursors in polymeric resins was already investigated (Porcu et al., 2022; Zhakeyev et al., 2021), which evidenced mainly two drawbacks. First, the interaction between catalyst and reagents decreased, due to hindered conditions, resulting in a decrease of efficiency (Amorim et al., 2018; S. Y. Lee et al., 2020). Secondly, the polymeric matrix was also affected by photocatalytic activity of the HS used, resulting in a degradation of the same polymer. In this context, the choice of utilizing TMPSM as a silane monomer had a two-fold purpose; the first one is because of its structural capacity, enhancing the crosslinking and stress resistance for the polymeric matrix (Amerio et al., 2008) given its exposure to radical species generated by the filler; and the second for its known use as coupling agent (Belon et al., 2011; Chemtob, Courtecuisse, Croutxé-Barghorn, & Rigolet, 2011; A. Chiappone et al., 2016; Malucelli et al., 2005) given the further possibility of performing a sol-gel reaction with Si-OCH$_3$ groups, and creating chemical bonds between the organic and the inorganic phase (Roppolo et al., 2012) (P. M. Ajayan, L. Schadler, & Braun, 2003). The sol-gel technique is defined as a two-step hydrolysis and condensation reaction (Comstock, 1995; Malucelli et al., 2005), where in this case the silane precursor starts the reaction and permits further condensation with a posterior addition of an inorganic phase component. In this context, the possibility of transforming the polymeric matrix into a glassy-like polymer was explored, aiming at optimizing the process for future SC embedding.

5.2.   Materials & Methodology

The next section contains the procedures for the development of the materials used for the preparation of the ink, the printing parameters, and the characterizations applied to determine its properties and efficiency in the photocatalytic degradation of RhB.

5.2.1. PhCN/TiO₂ (HS) Synthesis

PhCN/ TiO$_2$ hybrid system was prepared by a hydrothermal method followed by calcination, where 0.02 g of PhCN was dispersed in 15 mL of ethyl alcohol and stirred for 30 min. 0.075 g of ascorbic acid was then added to the suspension, after which, 0.5 mL TiCl$_4$ was added dropwise for 20 min while undergoing magnetic stirring. Subsequently, the solution was transferred to a 50 mL Teflon-lined autoclave and oven-heated to 180ºC for 8 h. Once cooled to room temperature, the product was 4 times washed with DI water and absolute alcohol followed by a 12 h drying procedure at 60ºC. The powder was later calcinated at 400ºC for 2 h to obtain white powders. The procedure was the same one followed by (Porcu, Castellino, et al., 2020).

5.2.2. Hybrid Ink preparation of printable Si-polymeric hybrid matrix

The synthesis of this polymer (PEGDA: TMSPM) was performed following the reaction in Figure 5.3 and according to Table 5.1 ratios. The exploited materials were: PEGDA M$_n$ 250 (Sigma-Aldrich), TMSPM (98% Sigma Aldrich), Phenylbis(2,4,6-trimethylbenzoyl) phosphine oxide (BAPO 97% Sigma-Aldrich).

Table 5.1.Chemical compositions of the PEGDA: TMSPM inks

Name	BAPO (phr)	TMSPM (wt. %)	PEGDA (wt. %)
PEGDA	1	0	100
50% TMSPM	1	50	50
52% TMSPM	1	52	48
58% TMSPM	1	58	42
80% TMSPM	1	80	20

5.2.3. PhCN/TiO₂ (HS) as coating

The hybrid system was used to coat 3D-printed structures to test the efficiency of these devices in photocatalytic degradation. Two main techniques were used for this: simple dip-coating and autoclave dip-coating. Both procedures were performed in the same size samples, which were printed with the chosen matrix and 15x5x5 mm dimensions and dipped in the same homogeneous solution of PhCN/TiO$_2$ with a concentration of 50 mg/ 25 mL DI- water.

Before dipping the pieces in the PhCN/TiO$_2$ solution, surface activation was performed, by submerging the printed matrixes in a solution of H$_2$O$_2$:H$_2$SO$_4$ (1:3).

5.2.4.   Dip-coating technique.

The technique was performed by constantly dipping the 3D parts in a stable PhCN/TiO$_2$ solution with a tweezer, and then letting air-drying. The latter was repeated three times to ensure the homogenous powder attachment to the surface.
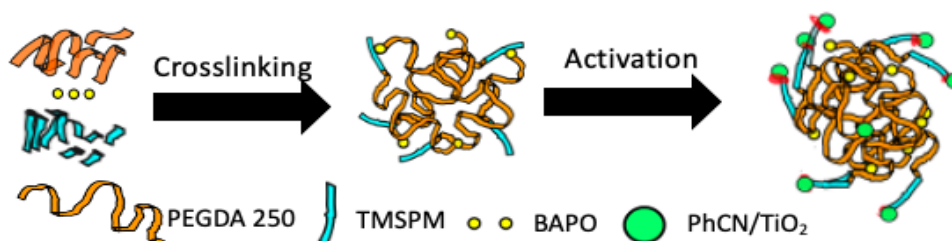
Figure 5.2. Schematic representation of the elaboration procedure.

5.2.5.   Autoclave+ Dip-coating

The technique was performed by dipping the 3D sample and letting it submerge in the PhCN/TiO$_2$ solution, then putting it in an autoclave at 180ºC for 5 hrs. Afterward, it was taken out and air-dried. This approach was studied aiming to establish whether the thermal treatment can be employed to create chemical bonds between the 3D printed structure and the HS, improving the adhesion without affecting the photocatalytic activity.

5.2.6.   PhCN/TiO$_2$ (HS) optimization as filler

Table 5.2 shows all the formulations used, with different filler loadings, for embedding strategy.

Name	BAPO (phr)	TMSPM (wt.%)	PEGDA (wt. %)	PhCN/TiO$_2$ (phr)
PEGDA	1	0	100	0
1% HS PEGDA	1	0	100	1
2%HS PEGDA	1	0	100	2
5% HS PEGDA	1	0	100	5
10% HS PEGDA	1	0	100	10
Hybrid Matrix (58% TMSPM)	1	58	42	0
1% HS	1	58	42	1
2% HS	1	58	42	2
5%HS	1	58	42	5
10% HS	1	58	42	10
15% HS	1	58	42	15

5.2.7. Optimization of the 3D printing parameters in MAX Asiga DLP printer & Anycubic Mono Photon SE

Table 5.3 shows the printing parameters in a MAX Asiga DLP (LED light source at 385 nm) printer for the obtained 3D structures with the respective polymeric matrix, 58% TMSPM formulation.

Table 5.3. 58% TMSPM & neat PEGDA printing parameters

	58% TMSPM (Hybrid Matrix)		PEGDA	
Parameter	Burn-in	1	Burn-in	1
Slicing time (s)	7	5	3	1
Light Intensity (mW/cm^2)	27	20	10	5
Layer Thickness (um)	50	75	50	100
Off time (s)	1.5	1.5	3	5
Print range (mm)	4	11	4	11

Since part of the experiments was conducted at Cagliari University, a different printer was also used for producing PhCN/TiO$_2$ loaded 3D composites (10% HS).

The printer used for this material Anycubic (LED light source of 405 nm) was Mono Photon SE and its parameters are reported in Table 5.4.

Table 5.4. 10% HS Printing Parameters with the chosen polymeric matrix & the PEGDA matrix

	58% TMSPM (Hybrid Matrix)		PEGDA	
Parameter	Burn-in	1	Burn-in	1
Slicing time (s)	15	14.5	15	10.5
Light Intensity (mW/cm²)	11.5	11.5	11.5	11.5
Layer Thickness (um)	100	75	100	75
Off time (s)	2	1.5	5	5
Print range (mm)	4	11	4	11

5.2.8. Post-treatment: Transforming the polymeric matrix into glassy polymers.

Once printed the 58% TMSPM formulation, the coated versions and the composite were both exposed to a thermal treatment submitting them to inert conditions in a tubular furnace, for 5 hrs at 400°C at a heating rate of 5°C/min under an Ar atmosphere with a >50 ml/min gas flow.

5.2.9. Characterization Techniques
5.2.9.1. Evaluation of the 3D printability: Photorheology

The photopolymerization kinetics between the TMSPM and PEGDA were measured through photorheology using an Anton PAAR Modular Compact Rheometer (Physica MCR 302) in parallel-plate mode, equipped with a UV-light source (Hamamatsu LC8 lamp 11 mW.cm^{-2}) under a crystal bottom plate, with a distance of 50 mm between the lamp and the plate. The measurements were performed in isothermal conditions at 25ºC with a constant shear angular frequency (10 rad.s^{-1}) following the changes in the storage modulus (G') without light for 60 s to stabilize the system before reaction, and upon UV light irradiation after that. The optimization of the filler loadings inside the resin was done on similar conditions, however, the light intensity applied was higher up to 25 mW.cm^{-2}. The amplitude sweep was done with an angular frequency of 10 rad/s from a strain of 0.01-1000 %. The viscosity profile was performed on the same equipment changing

to a rheometer modulus with shear rates in the range of 5-1000 s^{-1} in samples with filler loadings.

5.2.9.2. 3D Scanning: Proving 3D printed resolution fidelity.

The same equipment as for the previous chapter was used to obtain a scanned reference model of the 3D printed objects, that were then compared to the original CAD file (optical scanner E3, 3Shape). This scanner includes 2 cameras of 5 MP, an accuracy of 7 μm (ISO 12836) with a scan speed of 18 s. After this, the scanned data and the reference model were aligned before the statistical comparison, and the analysis was displayed as a colored 3D heatmap displaying the geometrical deviation.

5.2.9.3. Mechanical Testing

The samples' tensile strength and elongation break were measured using an INSTRON 3366 electromechanical universal testing machine, equipped with a 500 N load cell. The tests were carried out on 3D-printed dumbbell-shaped specimens of 50 mm* 12.5mm* 2mm, with a tensile rate of 2 mm.min^{-1} replicated on 3 different samples before their breakage. During the tensile testing, the stress (measured through machine-recorded force) and strain (through the displacement based on the initial cross-section area and gauge length) were followed in real-time. At the same time, Young's modulus E was calculated based on the initial linear elasticity regime of the stress-strain curve.

5.2.9.4. Detecting functionalities & measuring polymeric conversion: FTIR

The Fourier-transform infrared spectroscopy (FTIR) spectra were collected using a Tensor 27 FTIR Spectrometer (Bruker) equipped with an ATR (Attenuated Total Reflectance) tool. The average signal collected was in the range of 3500-600 cm^{-1} with a resolution of 4 cm^{-1}. The analysis was performed on the liquid formulation (t=0) and the solid films of 0.2 mm (t=t$_\infty$) of both resins, PEGDA, 58% TSMPSM, and the films with the respective filler (PhCN/TiO$_2$) concentration. The conversion (%CD) was calculated by monitoring the decrease in the area A of the FTIR absorption band of the reactive functionality C=C, with a peak around 1638 cm^{-1}. The area was normalized by a constant signal in the spectra C=O with the peak around 1730 cm^{-1}. The following Equation 5.1 shows how the conversion was calculated.

$$\%CD = \left(1 - \frac{\left[\frac{A_{C=C}}{A_{C=O}}\right]_t}{\left[\frac{A_{C=C}}{A_{C=O}}\right]_{t=0}}\right) x100$$

5.2.9.5. Determining Surface Morphology: FESEM & EDS

The morphology of the prepared composites was investigated by a Zeiss Supra 40 FESEM, equipped with a GEMINI II column and EDS analyzer, where a probe current of 1200 pA and an accelerating voltage between 5.00 and 15.00 kV were used.

5.2.10. Photocatalytic Application: detecting RhB absorbance & photoluminescence (PL) to determine photocatalytic degradation.

The photocatalytic performance of the prepared samples was evaluated by monitoring the concentration changes in RhB aqueous solution under visible light irradiation. The photocatalytic performance was assessed using a white LED (white LED Philips 13 W with an optical power of 100 mW) as the light source.

5.2.10.1. Concentration Changes in Solution

Before light irradiation, both the solid 3D composite (10% HS) and RhB (50 mL, 10 mg·L^{-1})/MB (50 mL, 10 mg·L^{-1}) were stirred in the dark for 30 min to ensure absorption−desorption equilibrium between the catalyst and the dye. During the photodegradation process, 2 mL aliquots were collected every 60 min. The aliquots were then centrifuged and the residual concentrations of RhB were analyzed using the UV−Vis-NIR Agilent Technologies Cary 5000 spectrophotometer.

5.2.10.2. Concentration Changes in Solid

Measurements were performed by using a PbS solid-state photodetector. The reflection configuration measures the diffused reflection of the sample concerning a KBr reference that is considered to have 100% reflectivity. The Kubelka-Munck equation was applied to extract the absorption features (L. Yang & Kruse, 2004).

5.2.10.3. Photoluminescence (PL) Spectroscopy in solid samples

PL measurements were recorded by exciting samples with 200 fs pulses sourced from an optical parametric amplifier (Light Conversion TOPAS-C) pumped by a regenerative Ti: Sapphire amplifier (Coherent Libra-HE). The signal was recorded by a streak camera (Hamamatsu C10910) equipped with a grating spectrometer (Princeton Instruments Acton Spectra Pro SP-2300). All the measurements were collected in the front-face configuration to reduce inner filter effects. Proper emission filters were applied to remove the reflected contribution of the excitation light.

5.3. Results & Discussion

This section contains results and their corresponding description as a result of the characterization activities, comparing them with the preceding literature.

5.3.1. Determining ink-printability of Si-polymeric matrix and the inclusion of PhCN/TiO₂ as a filler and coating: Rheology, Photorheology & 3D Scanning Fidelity

The 3D printability of the different polymeric matrices was first explored with different oligomer quantities, as reported in Table 5.1, to evaluate the possible development of 3D printing inks. To this aim, the comparison of the photopolymerization kinetics using photorheology was performed and by amplitude sweep the Linear Visco Elastic region (LVE) of the main formulations was done too. Rheology was measured in these samples; however, as both reagents were liquid, with similar and low viscosity, it was disregarded as it did not interfere in the printing procedure, the viscosity of the liquid samples of the two main polymeric matrixesis shown in Figure SI-2.

Figure 5.3 shows the chemical reagents used, together with the amplitude sweep measurements performed on the representative samples (Figure 5.3.B), a table summarizing Storage modulus (G') values monitored in the photorheology measurement, the delay times for each reaction to initiate upon light irradiation, and a printed object with the chosen matrix. Figure 5.3 C) presents the photorheology of the settled formulations, from where the values of the attached table were obtained. The table reflects that by increasing the TMSPM monomer concentration, a longer delay time before the gel point is measured. This, in 3D printing terms, suggests longer printing times. The increase in the delay could be due to the effect of introducing a different reactive group with the same quantity of photoinitiator in solution (Roppolo et al., 2012), and even though TMPSM is a very reactive

molecule (Hadi Mohammed, Ahmad, Ibrahim, & Zainuddin, 2016) the presence of a trimethoxysilane group in the main chain aside from a carbonyl group might slower the photopolymerization reactivity in comparison to neat PEGDA in solution. Additionally, from the photorheology, it can be appreciated, that once the crosslinking is accomplished and solid structures are reached with light irradiation, the max G' is higher for the formulations with higher TMSPM content. Similar results were seen by Chiappone et al. when printing hybrid nanocomposites with the same silane monomer, even if she incorporated also tetraethyl orthosilicate (TEOS) (A. Chiappone et al., 2016) in the resins.
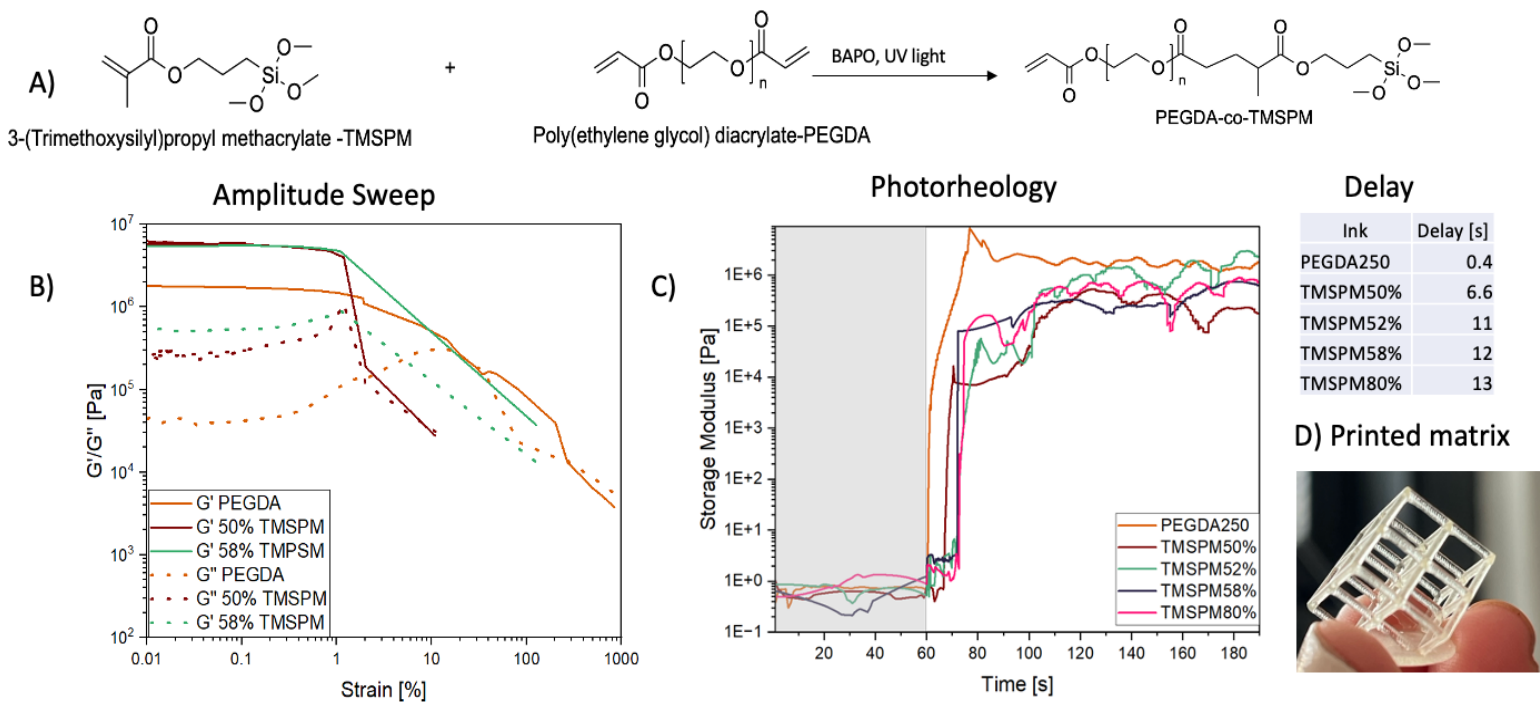
Figure 5.3. Resin-like behavior. A) Schematic representation of the chemical reaction. B) Amplitude sweep C) Photorheology and time-delay chart D) 3D printed structure of 58% TMSPM matrix.

Figure 5.3 B) shows that both the PEGDA and TMSPM (50% and 58%) formulations have similar LVE regions under increasing oscillating amplitude in the liquid phase, standing a strain value of up to 1 %. The PEGDA formulation has a smoother drop, indicating an easily flowing material, while formulations with TMSPM reflect brittle fracture behavior and a storage modulus almost one order of magnitude higher in comparison to PEGDA, due to strengthened networks. Regarding formulations with TMSPM, the 58% one shows a higher G" modulus and a more subtle drop once the yield point is reached, indicating a more gradual breakdown compared to the 50% resin. Therefore, by adding the silane monomer the G" slightly increases with the TMSPM concentration, also increasing flexibility which is observed by the gradual breakdown, given to its mono-functionality which at the polymeric network level decreases the crosslinking points (Pezzana, Melilli, Guigo, Sbirrazzuoli, & Sangermano, 2023; Yagci, 2006).

PEGDA is a well-known oligomer which has been used in photopolymerization and 3D printing (Goyanes et al., 2016; Simon & Dimartino, 2019; Warr et al., 2020). As a precursor of polymeric networks in 3D printing, it achieves great resolution (Y. Yang, Zhou, Lin, Yang, & Yang, 2020), its reactivity and mechanical properties depend on its molecular length (Rekowska et al., 2023) and its biocompatibility (Warr et al., 2020) makes it is a perfect oligomer for additive manufacturing, which is why it was chosen as first model for building composites with the HS. However, as seen, adding TMSPM in the formulations enhanced the polymeric matrix for a better withstanding of this filler.

Another advantage of the TMSPM formulations as printable inks is their transparency and the high resolutions obtained in 3D architectures. However, high concentrations of TMSPM in the formulation as TMPSM 80% were difficult to print as only bulk 3D (Figure SI-1) structures were possible to reproduce, while complex architectures cannot be achieved. Conversely, up to 58% of TMSPS in the formulation complex geometries, like the ones reported in Figure 5.3 D) or Figure 5.3, were fabricated. Given these indications, the chosen formulation containing TMSPM for testing the embedding of $PhCN/TiO_2$ was the TMSPM 58%. Figure 5.4 shows a CAD file and the heatmap of the scanned 3D-printed object. This heatmap shows a red zone on the flat part of the structure given to shrinkage, which means a higher deviation concerning the CAD file up to +/- 0.25 mm. On the contrary, the green zones present on the parts witness high CAD fidelity.
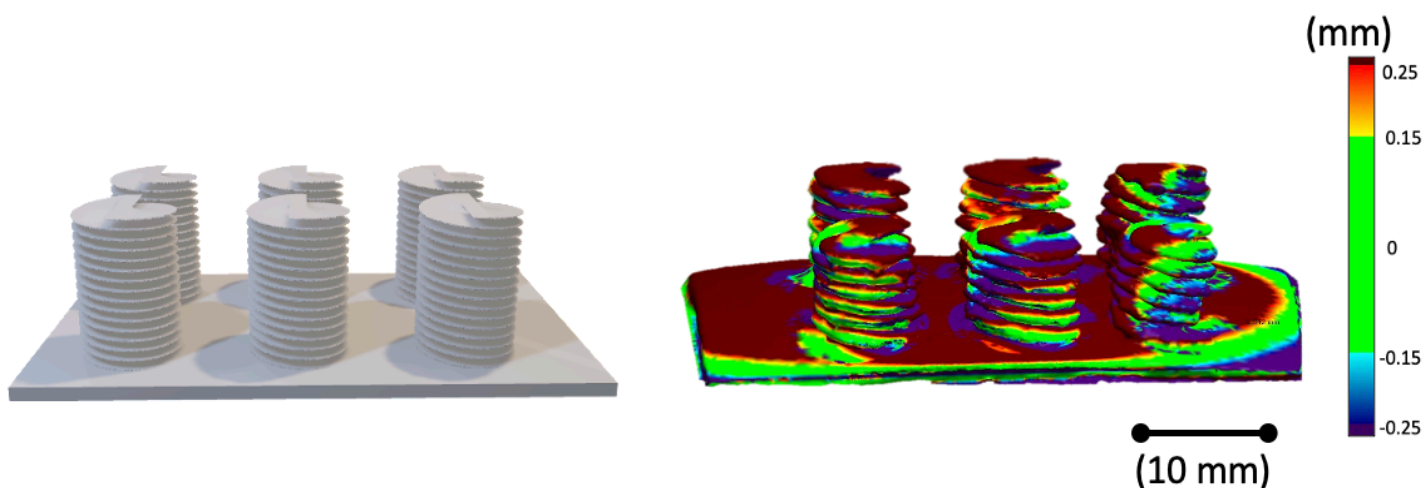
Figure 5.4. CAD file and 3D scanned product from the respective CAD with mm deviationheatmap.

Once chosen an efficient photoreactive resin, meaning short printing times and good G' as seen in Figure 5.3 C), the filler was added. Hence, an optimization of the process was performed, aiming at finding the maximum possible amount of HS fillers that can be introduced without affecting dramatically the printing process, but sufficient to further exploit the photocatalytic activity. As mentioned the HS is known for its photocatalytic activity in visible light (Porcu, Castellino, et al., 2020),

115

enabling the generation of radical species. In this case, this generation can be helpful for the photocuring process, even if the presence of fillers is well known for decreasing the photopolymerization process, both for absorbance and hindering effects (Gonzalez et al., 2017). Thus, different amounts of fillers were loaded in the two photocurable formulations, the 58%TMSPM and a PEGDA one, to compare the photoreactivity.

Figure 5.5 and Table 5.5 present the given optimization analysis for the 58% TMSPM, while Figure 5.5 A) is a schematic representation of the reagents, and the crosslinked networks with and without the filler. Observing data reported in Figure SI-2, it is evident that the resins show a Newtonian behavior within the shear-rate range explored and that increasing the concentration of the filler inside the resin strongly increases the viscosity. In standard DLP 3D printing, usually, a viscosity below 50 Pa·s is requested (Tetik et al., 2022), thus the obtained viscosities with this ink are optimal. However, with the 15% HS there was too much sedimentation and no stability of the powder and the solution, thus this concentration was not used for further investigation.

Meanwhile, the same optimization was performed for PEGDA formulation, as seen in Figure 5.6 and Table 5.6, where Figure 5.6 A) is a schematic representation of the reagents before and after crosslinking, and the version including the filler in it. The first graph shows the rheology where a shear thickening effect seems to appear when increasing the concentration of the filler at 10% in the resins. This phenomenon is attributed to the formation of hydrodynamic clusters formed by the aggregation of the filler inside the resin that interrupts the flow of the oligomers in solution (M. Wei, Sun, Qi, Chang, & Zhu, 2018).

116
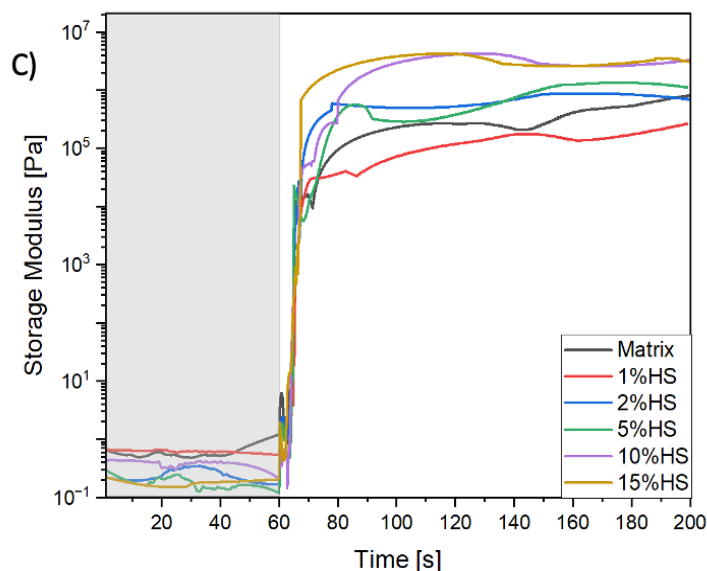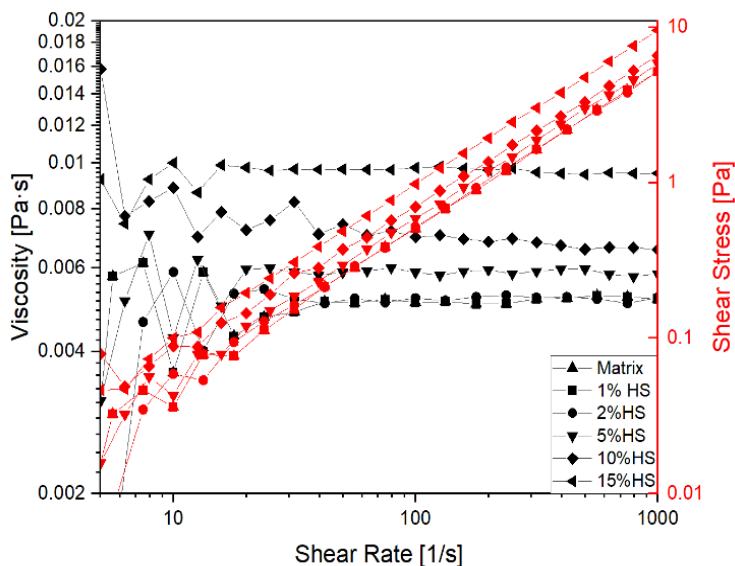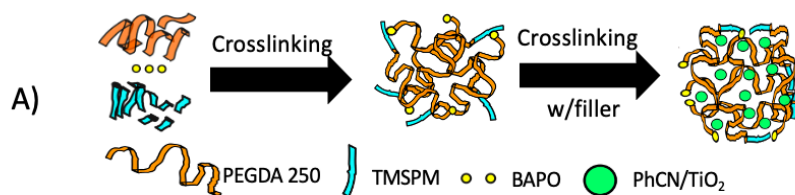
Figure 5.5. Filler optimization in TMSPM/PEGDA matrix. A) Schematic representation of the chemical reaction. B) Rheology profile C) Photorheology performed with different HS loadings

Table 5.5.Acquired values from photorheology (Delay, slope, and Max G') from Matrix formulations.

Formulation	Delay [s]	Slope [Mpa/s]	MAX (G') MPa at 144s
Matrix	3.8	2.42	0.21
1% HS	4.6	1.57	0.18
2%HS	4	1.47	0.77
5%HS	4.2	1.43	0.9
10%HS	4.2	1.09	2.7
15%HS	4.2	--	2.7

Tables 5.5 & 5.6 show the main kinetic parameters extrapolated from photorheology measurements. In both cases, the same effect is observed when increasing the concentration of the filler: the viscosity and shear stress of the formulations increase, and as a consequence the kinetic in the reaction decreases, showing longer delay times before the propagation phase, and lower slope values. As expected, PEGDA formulations showed better values compared to the 58% TMSPM one, with shorter delay time ranges at the beginning of the reaction which could be translated into shorter printing times afterward, and higher Max G' modulus achieving stiffer crosslinked networks. This property would be better

117

analysed with the mechanical tests on photopolymerized specimens. However, the reactivity of the PEGDA resin seems to decrease when loaded at 10% HS, showing a lower slope (meaning a slower photopolymerization kinetics) than the other polymeric formulation when using the same concentration of filler; this can be a consequence of the previously mentioned shear-thickening effect (M. Wei et al., 2018). Concerning the 58% TMSPM formulation, increasing the filler concentrations had a similar effect by diminishing the slope and increasing polymerization times.

Whereas, Figure 5.7 shows printed structures of the composite with 10% HS, and how the photoluminescence of the hybrid system is rendered to the printed 3D structure when exposed to UV light.
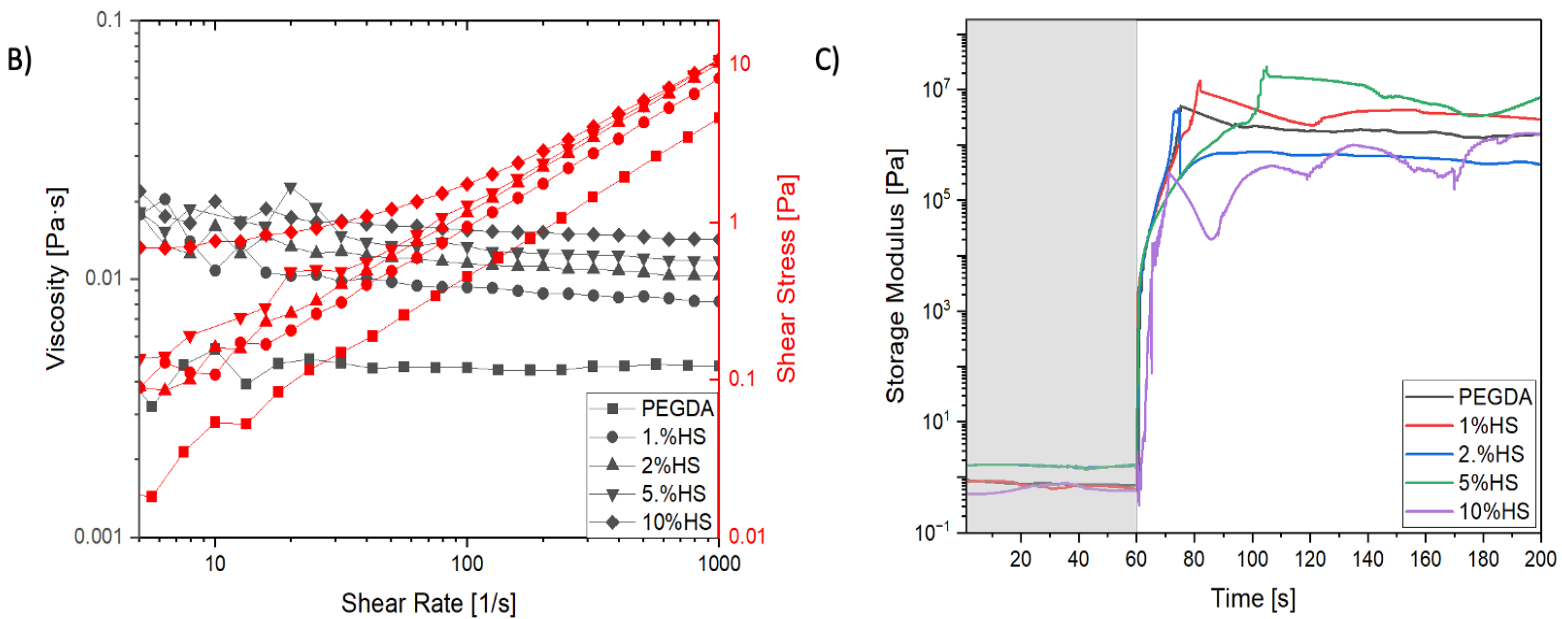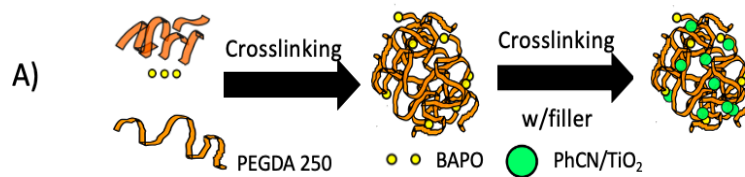
Figure 5.6. Filler optimization in PEGDA matrix. A) Schematic representation of the chemical reaction. B) Rheology profile C) Photorheology with different HS loadings

Table 5.6. Acquired values from photorheology (Delay, slope, and Max G') from PEGDA formulations.

Formulation	Delay [s]	Slope [MPa/s]	MAX (G') MPa at 144s
PEGDA	0.6	2.13	1.8
1% HS	0.2	1.28	4
2%HS	0.4	1.26	0.6
5%HS	0.4	1.21	11
10%HS	2.8	0.92	0.9
15%HS	--	--	--

(a)
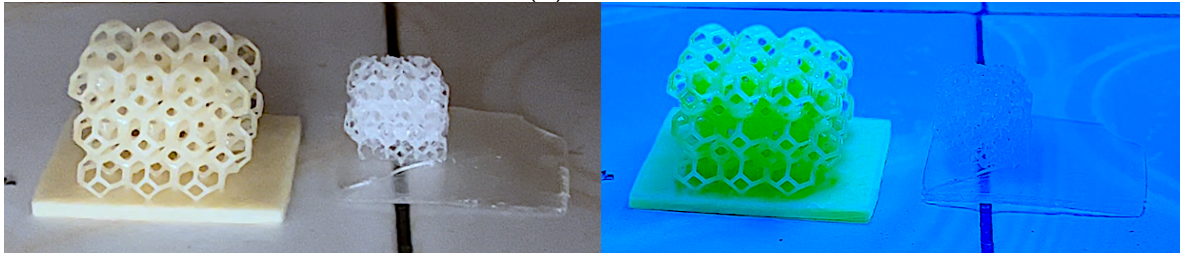
Figure 5.7. (a) 3D Printed PhCN/TiO$_2$ composite (b) PhCN/TiO$_2$ composite vs. Polymeric matrix at visible light (c) PhCN/TiO$_2$ composite vs. Polymeric matrix at 385 nm UV light.

5.3.1.1. Glassy Polymers

After the post-treatment, the shape and architecture of the printed objects are preserved as seen in Figure 5.8, though there is a noticeable shrinkage in the structures which is measured by the volumetric scanned comparison and calculated by Eq. 5.2. The attached Table 5.7 shows the calculated shrinkage of the respective formulations following the next equation.

$$Shrinkage\ (\%) = \frac{(initial\ volume - final\ volume)}{(iinital\ volume)} X100$$

Equation 5.2. Shrinkage Calculation

On the other hand, the photocatalytic efficiency was evaluated following the RhB degradation in solution, seen in section (5.3.5.1), at Figure 5.14 showing the different treatments done with the glassy polymers. The considered matrix was 58% TMSPM.

119

5hrs- 900 ºC Ar
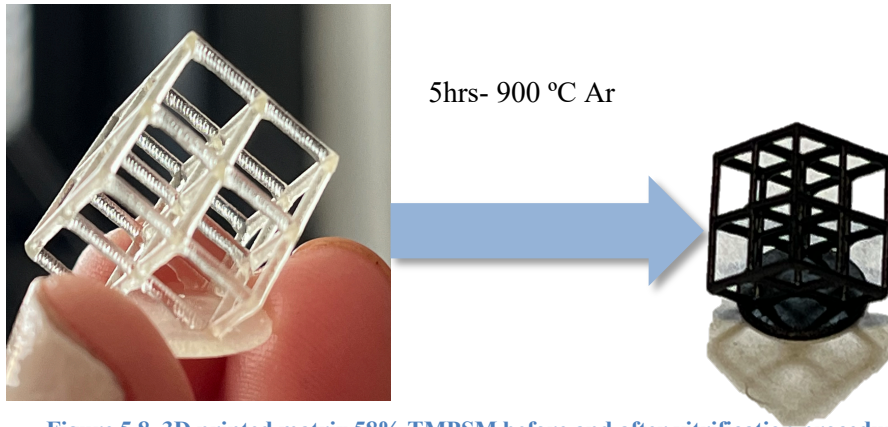
Figure 5.8. 3D printed matrix 58% TMPSM before and after vitrification procedure. The attached table represents the calculated shrinkage values respective to the scanned volume.

Table 5.7. Shrinkage results in the corresponding formulations

TMSPM (wt. %)	50	52	58
Shrinkage (%)	88.799	84.805	80.670

The development of an advanced matrix turning this composite into glass by a chemical vitrification (Oleinik, 1987) was thought initially to introduce them into extreme environments and induce photocatalytic degradation in extremely acidic conditions, or high temperatures. Once these advanced composites were introduced to the "piranha solution" they were able to withstand this environment, however, as mentioned, the photocatalytic activity of the HS was reduced to almost none, given the most probable degradation of the PhCN inside after the exposure to thermal treatment. In section 5.3.5.1.1, its photocatalytic activity is explored.

5.3.2.   Mechanical Testing

The mechanical properties of the photo-cured specimens were investigated by tensile tests, that were done on 3D-printed flat specimens (dumbbell shape formed) with a thickness of 1.4 mm. Young's Modulus E was obtained by the linear regime of the stress-strain curves, and it is shown with the elongation break in Table 5.7. In this case, the values measured resulted higher than the similar materials obtained by Chiappone et al. (A. Chiappone et al., 2016). This is due to the use of a PEGDA with lower Mn, which permits a higher crosslinking density and consequently higher stiffness.

Regarding Figure 5.8, which shows the stress-strain curve, the matrix formulation, which contains 58% TMSPM shows an increase of almost 50% in the E value, a lower Young's modulus, and a higher elongation, indicating lower stiffness and better elasticity compared to the neat PEGDA network. This is consistent with a decrease of the cross-link density induced using a monofunctional monomer, with synergistic positive effect of the presence of a precursor of an inorganic phase (silica), which can enhance mechanical performances. While samples, containing 10% HS present a notable decrease in the E value for both networks and a slightly higher Young's modulus, translating in the ability of the filler to influence the material stiffness. However, this effect is less pronounced in the polymer with TMSPM where it seems that the presence of Si-O-C bonds (seen in the XPS of printed matrix- Figure SI- 4) inside allows stronger interconnections and elasticity, also providing the matrix a further possibility of performing sol-gel reactions later on and functionalizing (Belon et al., 2011; Chemtob et al., 2011). The filler's insertion also seems to add fragility or a brittle behavior in crosslinked samples, as the elongation in samples with filler is shorter.
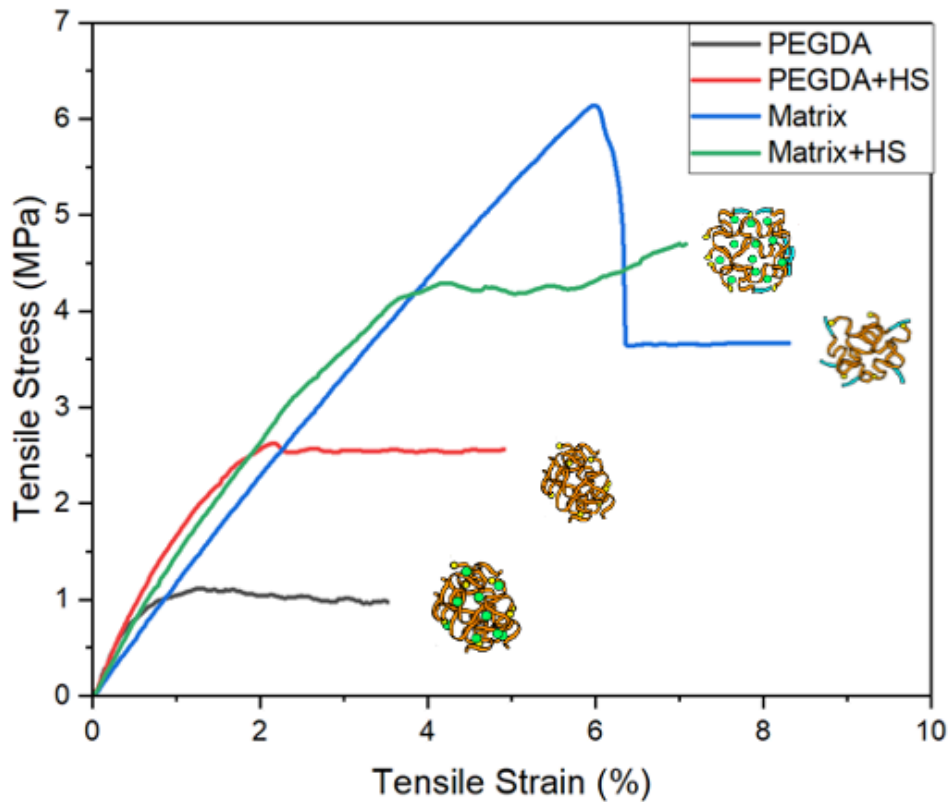
Figure 5.9. Stress-strain curves of PEGDA, PEGDA+HS, Matrix, and Matrix + HS networks

Table 5.8. Young's Modulus (MPa) and Elongation break (%) of the printed formulations

Parameter	PEGDA	PEGDA+HS	Hybrid Matrix	Hybrid Matrix+HS
Young's Modulus (Mpa)	1.5	1.8	1.1	1.2
Elongation break (%)	4.9	3.51	6.4	8.1

5.3.2.1. Introducing Glassy polymers into RhB solution for photodegradation

As mentioned before, the vitrification was performed by introducing the polymeric matrixes and composites to high temperatures and inducing them to slow cooling ramps, where the SiO_2 coming from the silane monomer is the main glass former by ionic-covalent systems (Persch et al., 2021). Figure SI-4, shows how after the thermal treatment, the Si derived peak is sharper which shows the tendency to glass formation.

The glassy polymer matrix (red line) by itself seems to have similar activity compared to the concentrated RhB solution degradation by itself, keeping a similar concentration as seen in Figure 5.10. The glassy versions of the composite (filler) and the coated systems had similar activity to the glassy matrix, though arriving at almost a 4 % in photodegradation, which indicates that the PhCN after being exposed to high temperatures degrades almost to completion and the photocatalytic system activity decreases, therefore, the HS is not able to absorb energy from visible light. At this point, TiO_2 should be the main component remaining from the HS and its photoabsorbance should be around 3.2 eV (Jańczyk, Krakowska, Stochel, & Macyk, 2006) negligible from the visible range.
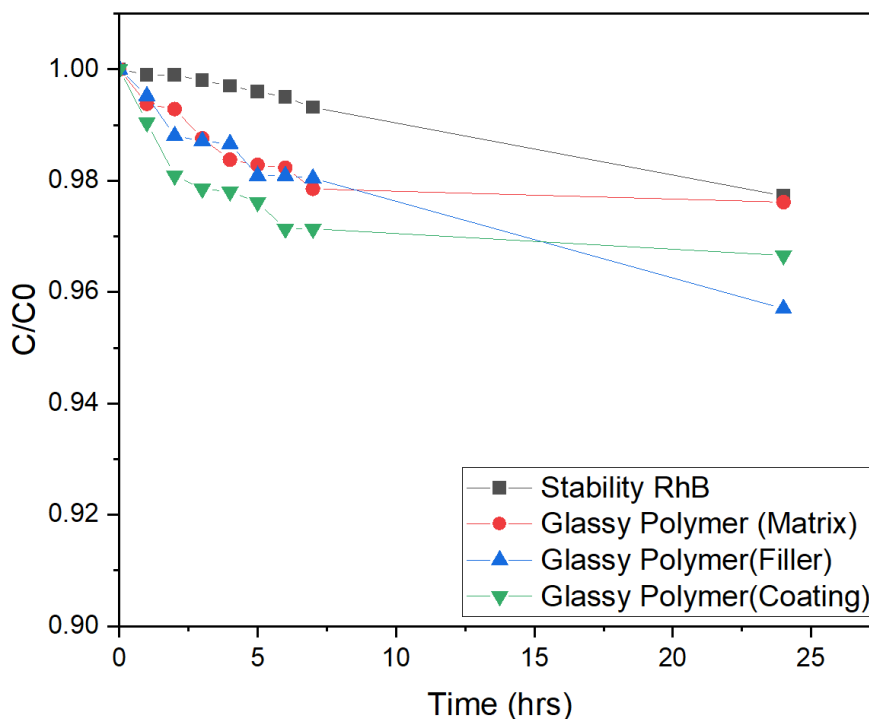
Figure 5.10. RhB photodegradation in solution of glassy polymers

5.3.3. FTIR characterization & polymeric conversion

FTIR characterization served to the identification of the respective bonds, and the posterior calculation of polymeric conversion for both photopolymerizable inks. The conversion was calculated by following the decrease of the band attributable to the C=C stretching vibrational mode at 1638 cm^{-1}, normalizing it with the simultaneous diminution of the C=O absorption band at 1720 cm^{-1} bonds that are present in both cases.

Figure 5.10 A) and B) show the obtained FTIR for the PEGDA and 58% TMSPM resins, comparing liquid formulations and 3D printed samples, with and without filler. In the PEGDA spectra, the main identifiable peaks correspond at 2876 cm^{-1} from the C-H stretching, 1445 cm^{-1} from C-H bending, and 1720 cm^{-1} from the C=O absorption band (Kianfar, Vitale, Dalle Vacche, & Bongiovanni, 2021). Before the polymerization the C=C peak at 1638 cm^{-1} is higher given its abundance in the oligomeric form. After the polymerization, given its reaction, there are less PEGDA molecules present with the C=C bond which would be the unreacted ones, while the changed ones turn into the C-C form, that is why conversion is usually measured by the decreased of the C=C bonds. Moreover, similar peaks were found in the 58% TMPSM matrix formulation. Given its PEGDA content also conversion is measured by the same formula with this formulation. Although, in the FTIR there is a characteristic silica point at 1100 cm^{-}

123

appreciated (Posthumus, Magusin, Brokken-Zijp, Tinnemans, & van der Linde, 2004), and peak correspondant to the Si-O-Si stretchingvisible at 1020 cm⁻¹ & other at 820 cm⁻¹ (Soloukhin et al., 2002).

Table 5.9 shows the %CD respecting both formulations and how the insertion of the filler affects its polymerization. As mentioned before, pristine PEGDA has better reaction kinetics in contrast to formulations with TMSPM added, in this case reflecting it in a higher %CD. While the filler presence significantly diminishes the conversion degree in both cases, this effect is more pronounced in neat PEGDA. The same effect has been seen in the chapter before when adding MXenes in the respective inks, and it is given to the increased viscosity in the resins that obstructs the oligomeric flow and collision/contact between them, which in the neat PEGDA is worsened due to the shear thickening at this concentration in the formulation.
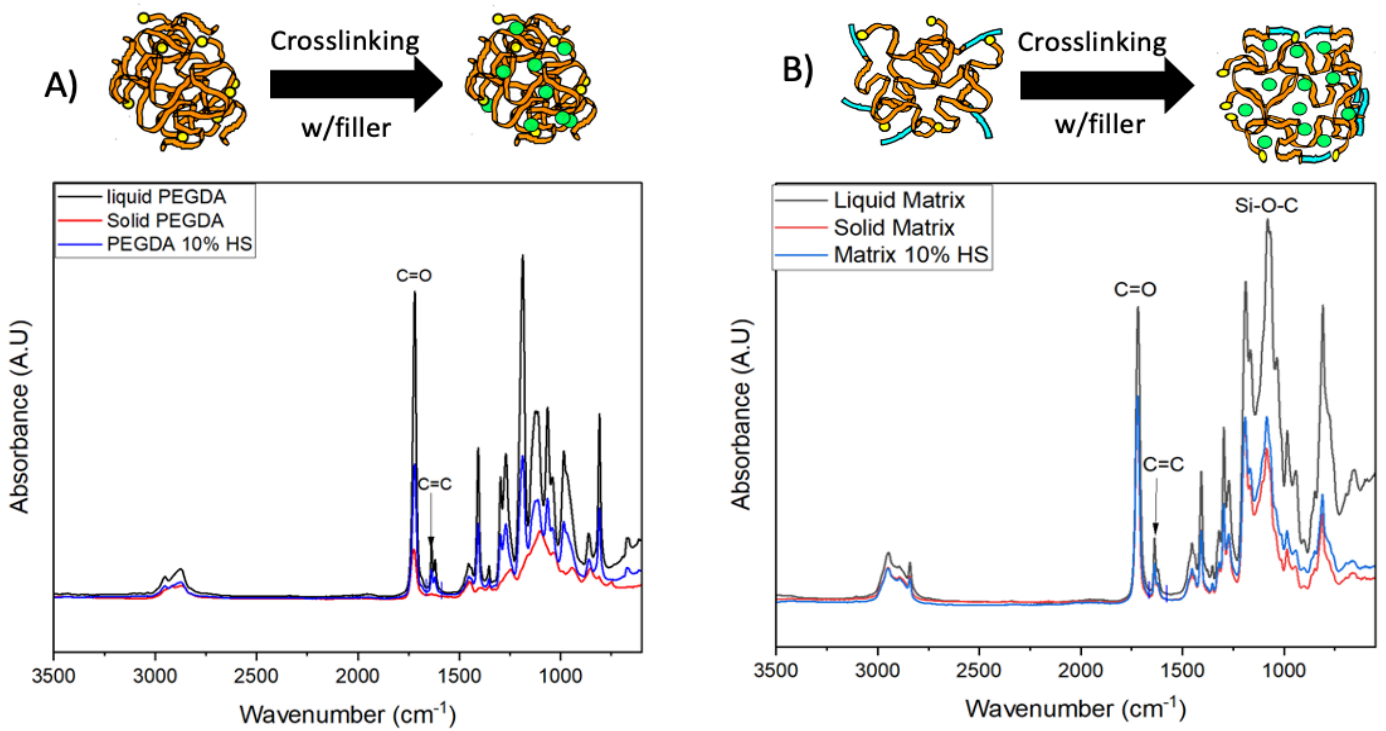
Figure 5.11. FTIR graphs, focusing on the C=C sign to measure polymeric conversion. A) PEGDA-ink system B) TMSPM/PEGDA-ink system.

Table 5.9. Polymeric conversion in PEGDA system and TMPSPM/PEGDA system

Sample	Wavenumber (cm^{-1})	$A_{(t=t)}$	$A_{(t=0)}$	$A_{(C=C)}/A_{(C=O)}$	%CD
PEGDA	1638 cm-1 (C=C)	0.39	7.07	0.10	78.59%
	1720 cm-1 (C=O)	3.79	14.71	0.48	
PEGDA+10%HS	1638 cm-1 (C=C)	1.58	4.5	0.22	26.95%
	1720 cm-1 (C=O)	7.07	14.71	0.31	
Hybrid Matrix	1638 cm-1 (C=C)	1.01	4.49	0.13	71.12%
	1720 cm-1 (C=O)	8.03	10.31	0.44	
Hybrid Matrix+10%HS	1638 cm-1 (C=C)	1.44	3.04	0.21	30.33%
	1720 cm-1 (C=O)	7.01	10.31	0.29	

5.3.4. Determining the Morphology of the polymeric composite

FESEM analysis was performed to determine the dispersion and morphology of the fillers inside both the polymeric networks. Figure 5.11 (A and B) represent neat PEGDA and the matrix networks respectively with homogenous surfaces, while Figure 5.11 (C-G) shows how the fillers are distributed on the surface of the composite, by randomly polydispersed agglomerations of less than 5μm each , whilst. The filler contains Ti, which has high electron reflectance, therefore it appears clearer in FESEM pictures. This result is good agreement with the data reported in S.Porcu et al., in which it was showed that PhCN/TiO$_2$ has a spheric shape (Figure 5.11 D), which is similar as the particles observed in Figure 5.11 C). As mentioned, Chiappone et al. (A. Chiappone et al., 2016) printed a similar network with a lower TMSPM concentration. In this work, similar morphologies were encountered in the surface of the polymer, chemical structures can be seen in Figure 5.13. In comparison, as expected, PEGDA network is fully homogenous.

Regarding the HS, Porcu et al. had already tested this HS, as seen in Figure 5.11.D), showing spherical shapes with micrometer scale dimensions of about 10 μm. (Porcu, Castellino, et al., 2020) FESEM images show that the fillers preserved their original shape in both composites. Furthermore, in both composite structures, the filler seems to be well-dispersed for this concentration and with little aggregations on the surface. However, in PEGDA networks these seem to have bigger particle sizes, because of the shear thickening effect seen in the rheology, while the matrix networks present smaller particle sizes generally. In VP, the presence of big clusters is undesirable when polymerizing, as printing can be severely affected. In particular, clusters larger than layer thickness may enable the printing process, due to incomplete reach of printing levels.

Elemental composition was evaluated by EDX of Figures 5.11 (C and E), and the gathered data is seen in Table 5.11. Nitrogen, which is usually present in the PhCN structures because of the carbonitride bonds, according to Porcu et al., could not be detected in these figures since the nitrogen present in the HS is 0.7% (Porcu, Castellino, et al., 2020) which is too low to be detectable under this technique, and also because of the low concentrations (10%) of the HS in the composite. The detection limit for EDX in composites, for elements inside is usuallt for them to be higher than 10% wt (Nasrazadani & Hassani, 2016). Furthermore, N band can be somehow hidden by C and O signals. Ti was detected in very low concentrations for both cases (0.97% and 0.19%) confirming the incorporation of anatase species inside the composite, which in the pure HS has a 15% concentration. Yet, PhCN presence is notable because of the structure's photoluminescence when irradiated, which is a particularity of this component (Ashfaq et al., 2021; Porcu, Castellino, et al., 2020; Porcu et al., 2021). Another particularity was P(phosphorous) presence in the composites regarding BAPO's presence inside the compositions and Si presence in TMSPM or the matrix structures, which is directly involved with its high concentrations in the formulations.
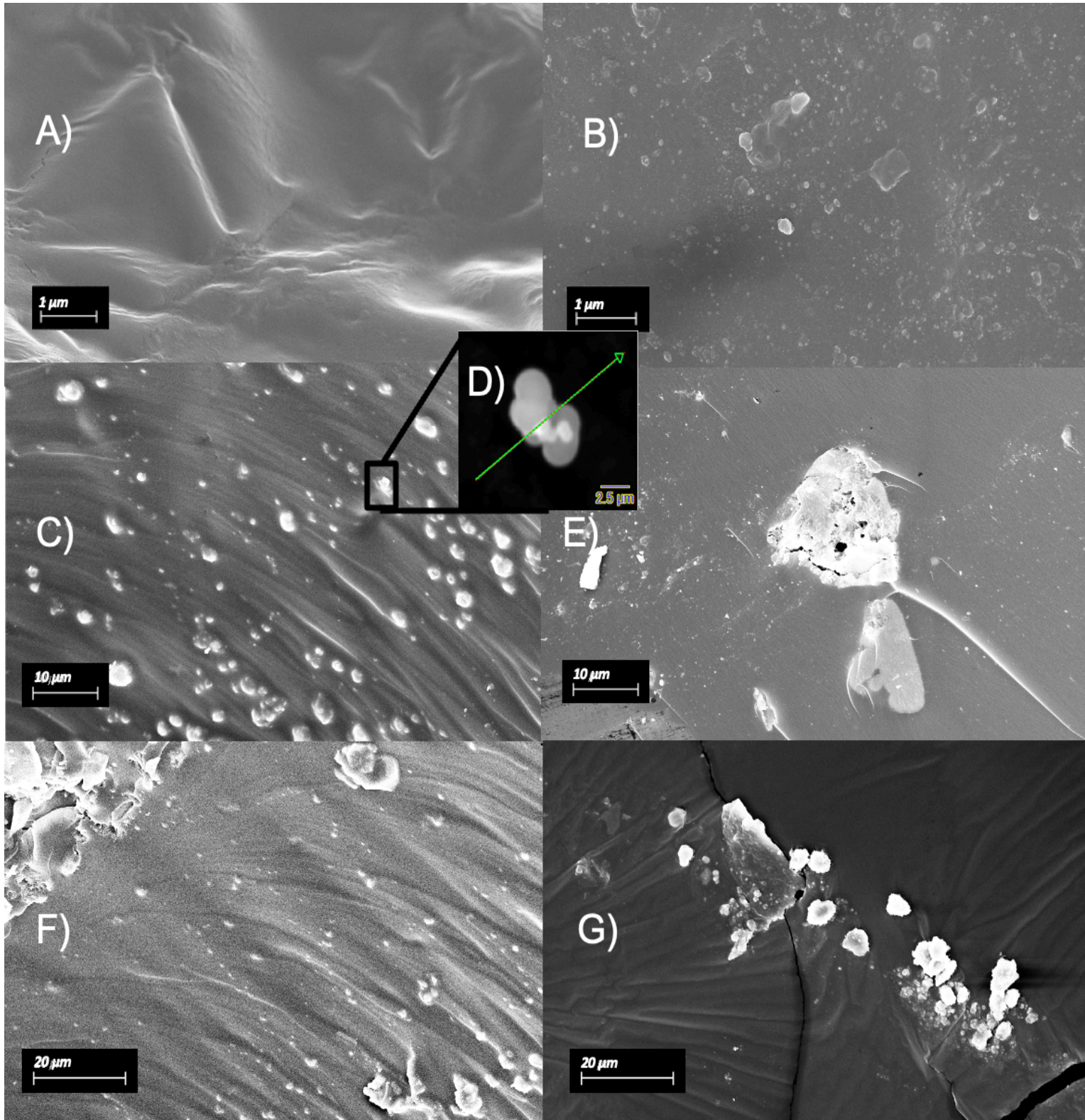
Figure 5.12. FESEM pictures. A) PEGDA printed formulation, B) 58% TMPSM printed formulation, C) and F) correspond to PEGDA (10% HS) cross-section, D) Image taken from Porcu et al. (Porcu, Castellino, et al., 2020) of the PhCN/TiO$_2$ and E) and G) to 58% TPMSM matrix at (10% HS) cross-section.

127

	Figure C		Figure E	
	Weight (%)	Atomic (%)	Weight (%)	Atomic (%)
C K	57.83	65.34	51.95	62.56
N K	0	0	0	0
O K	39.85	33.8	32.86	29.71
Si K	0	0	13.79	7.1
P K	1.35	0.59	1.22	0.57
Ti K	0.97	0.28	0.19	0.06
Totals	100		100	

5.3.5.   Photocatalytic Application Efficiency

This section reports the application efficiency of all the synthesized approaches, starting from the HS used at the beginning for coating applying the sol-gel technique and the HS inside the matrix network as fillers.

The first experiments refer to the measured photocatalytic efficiency in solution, while the second ones analyze the photocatalytic efficiency after being in solution, by leaving the same 3D printed composites exposed to light.

Posthumus et al. reported the reaction of TMSPM after a sol-gel reaction with oxide particles (tin oxide, antimony doped tin oxide, and silica particles), with the formation of bonds between the TMPSM-carbonyl and the oxide (Posthumus et al., 2004). The approach here studied envisage to apply the same strategy, exposing the surface of the 3D printed component to oxidizing solutions to promote the presence of surface hydroxyl groups that can be employed in a sol-gel reaction between the Si-O-H exposed moieties and the HS; Figure 5.13 mirrors the procedure and synthetic routes. Two routes were investigated: the simple dip-coating and the dip coating plus autoclave, to perform a temperature-aided condensation reaction. A full characterization of these processes was not reported in this Thesis due to lack of time, but for the sake of the project, photocatalytic efficiency in solution was tested, as reported in the following paragraph.
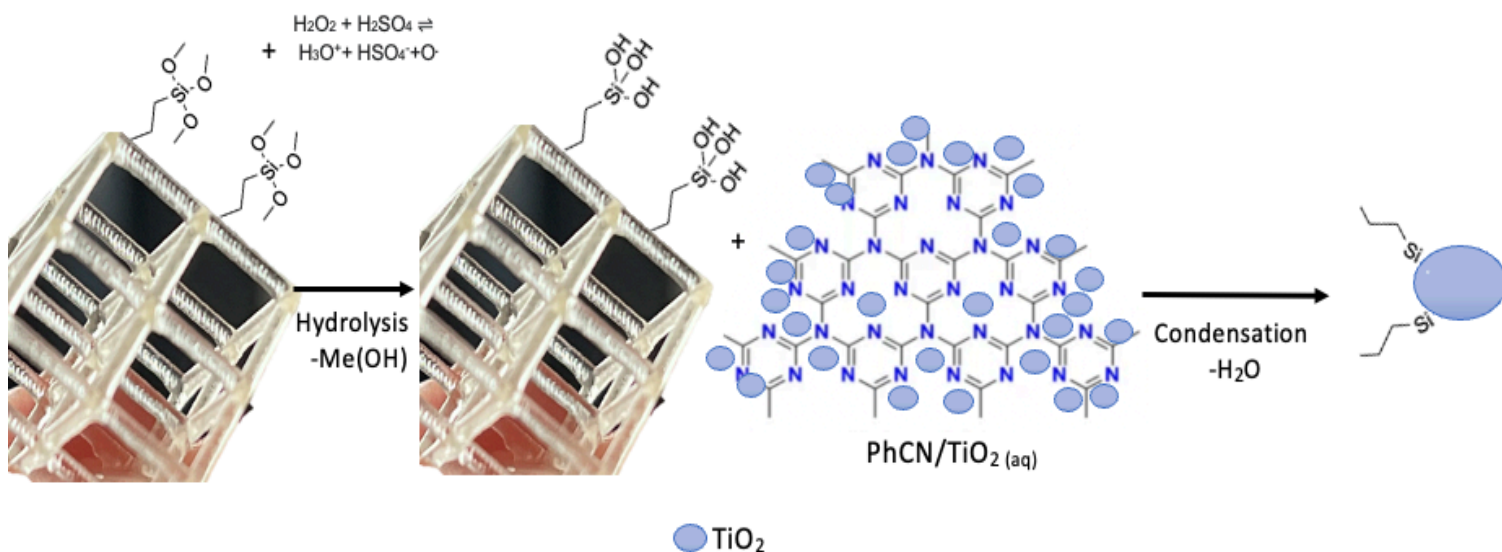
Figure 5.13.The sol-gel technique applied for the coating strategy with the HS over printed polymeric matrix.

5.3.5.1. RhB photodegradation in liquid solution

The hybrid matrix, hybrid matrix+10% HS, dip-coating Figure 5.14 A, and the dip-coating plus autoclave Figure 5.14 B) approaches were assessed for their catalytic performance in solution by RhB photodegradation under LED irradiation. Most of the light emitted from a LED source has an energy below 2.8 eV (Porcu et al., 2022), and it cannot be absorbed by the TiO_2 in the anatase phase, which requires an energy of 3.2 eV (Yuhan Li et al., 2017; Nakata & Fujishima, 2012). On the other hand, this light below 2.8 e.V can be efficiently absorbed by PhCN according to Porcu and coworkers who developed this hybrid material $PhCN/TiO_2$ (Porcu et al., 2021), once the light absorbed by the organic part, the photoexcited electrons from the LUMO state pass to the TiO_2 (the inorganic part) conduction band. Given their relative positions of PhCN valence band and TiO_2 conduction band, charge transfer is facilitated between the organic PhCN to the inorganic part. At the same time, holes remain in the HOMO state of PhCN, further increasing the charge separation of the electron-hole pairs (Porcu, Castellino, et al., 2020). Then, the electrons of the excited states react with the oxygen in the solution (RhB+ DI water) to create superoxide and hydroxyl radicals that photodegrade the RhB.

Figure 5.13 C) shows the normalized RhB concentration as a function of time for the studied approaches, compared with RhB stability in solution when exposed to light (black line). The RhB concentrations were calculated from the UV-Vis spectra shown in Figure SI-3. Regarding the composites approach (red line), when being immersed in the RhB solution it showed a similar behavior compared to the printed matrix (the blue line). This suggests that when tested in solution and exposed to light, the filler inside is not quietly exposed or remains unavailable for reacting with the pollutant in contact with the surface and consequently the decrease measured can be related to surface absorption or, in the best case, the diminished

catalytic activity of the surface groups. This is consistent with the coloration of the 3D printed structure, shown in Figure 5.13 c), the blue line.

Moreover, comparing the samples with HS on the surface as coated material, similar results were observed, with a degradation efficiency that reaches almost 70% of RhB degradation in both scenarios, namely the dip sample and the dip plus autoclave. In the dip-coating approach Figure 5.14 A), 70% of the RhB degradation was achieved, though some of the attached powder from the HS was subtly removed from the structure when agitating the solution during the experiment. As seen the HS maintained its original color over the surface, suggesting that there has been no modification in it. The detaching process could have avoided the light absorbance at the beginning, however, once a considerable amount of the HS powder was in solution the light absorbance could have increased given its increased surface exposure, increasing the photodegradation. In the dip plus autoclave Figure 5.14 B), there was better adhesion of the HS to the printed surface, which contributed to even RhB degradation though dependent on the surface being exposed to light. Though, as seen in the image, there is a slight change of color in the HS, which could suggest partial deterioration of the PhCN, even though, the results in the photocatalytic degradation on both coating strategies were similar. The color seen in this PhCN was similar to the one see by Porcu, et al (2020) thermally treated (Porcu, Roppolo, et al., 2020). Furthermore, no evident precipitation of HS was observed.

The HS by itself is evidently more efficient than when using the coating approach or another 3D printing approach so far, Porcu et al. reported shorter time ranges for RhB photodegradation, showing full degradation in less than 7 hours (Porcu, Castellino, et al., 2020; Porcu et al., 2021). Still, this approach avoids having to later separate the dispersed HS powder from the solution and provides practical structures which exposed surface could be modified to increase light exposure. The idea has already been applied with different materials by Seong et al., where he presents TiO_2 and Au-supported nanoparticles in a PDMS sponge for RhB photocatalytic degradation (S. Y. Lee et al., 2020).Zhan et al. presented inmobilized thin films of TiO_2 by inkjet printing for photocatalytic degradation of RhB, with similar degradation timings to the ones seen in these experiments (Zhan et al., 2020).
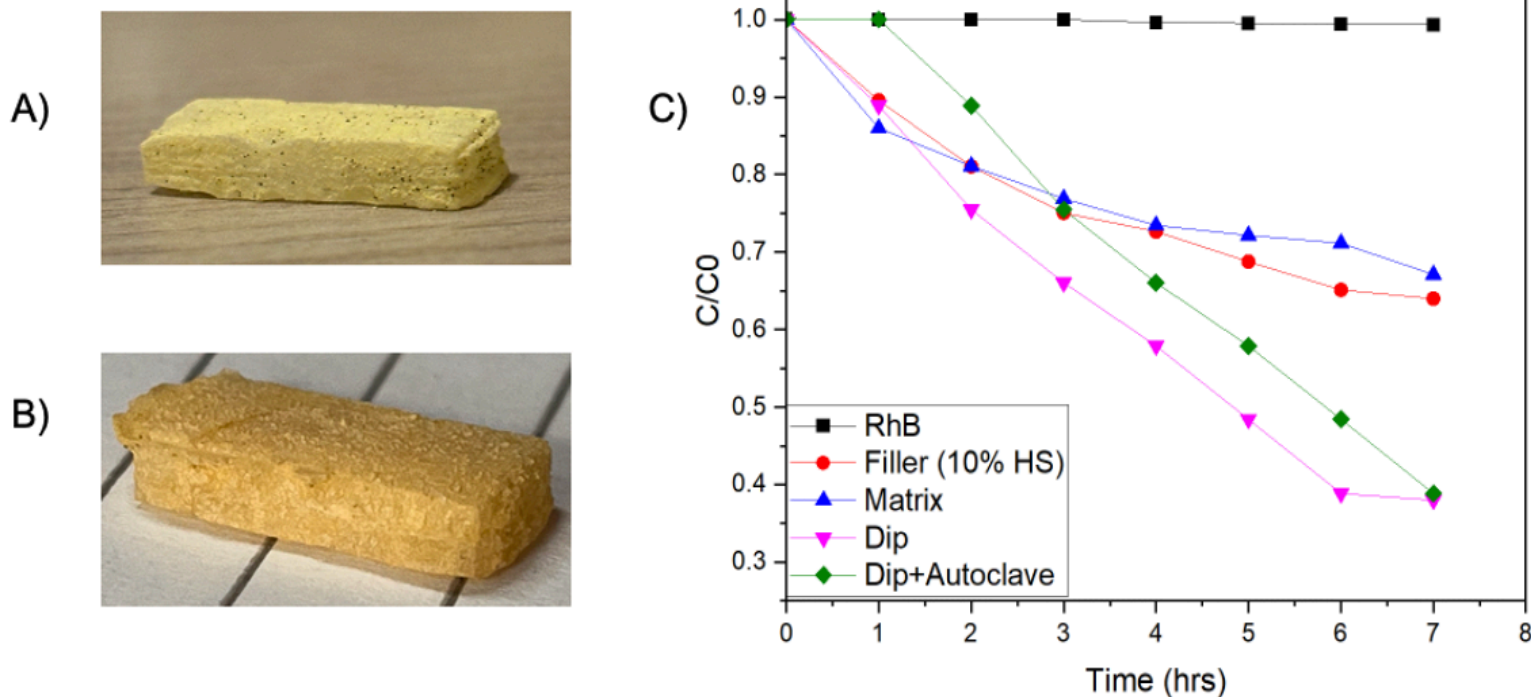
Figure 5.14. RhB photodegradation was performed using the different AM insertion approaches of PhCN/TiO$_2$. A) 3D printed object with Dip-coating technique (called "dip" in the graph). B) 3D Object with dip plus autoclave technique (called "dip+autoclave" in the graph). C) RhB photodegradation graph in solution with different approaches utilized for the photocatalytic reaction, the balck line corresponds to RhB autodegradation with lght by itself, the red line to the composite with the HS as filler in 10% concentration, the blue line is the control or the neat polymeric matrix, the purple line to the dip coated sample (Figure A), and the green line to the dip coated+autoclave (Figure B) .

5.3.5.2. RhB photodegradation in solid medium

Once removed from the RhB solutions, the composite structure was dried and exposed again to the LED light. Figure 5.15 A), shows the composite structures before and after being inserted into RhB solutions, while Figure 5.15 B), shows the normalized curve of the normalized RhB concentration inside the printed matrix alone and the composite. Inside the matrix, RhB remains stable in time, while, inside the composite, the photodegradation of the contaminant is appreciated in longer periods. Physically, RhB degradation is seen by the vanishing of its characteristic pink, as seen in Figure 5.15 C), and even its photoluminescence, as seen in Figure 5.17. Chemically, the PhCN/TiO$_2$ system needs a medium to react to create radicals that would later photodegrade the contaminant. Inside the composite, this medium could be provided by the remaining humidity of the immersion in RhB, remaining unconverted monomers, or by the polymeric matrix itself, though in these conditions the scavenger kinetics are very low. This is due to the low mobility of reactants in the solid structures and because more energy is needed for the generation of the radical molecules with these species, than for generating radicals with water. Cheng et al. reported the deethylation route by

photooxidation of RhB decomposition until the destruction of the chromophore structure (F. Chen, Zhao, & Hidaka, 2003). Similarly, here RhB is absorbed by TiO_2/SiO_2 particles where the amines in the RhB interact with the TiO_2/SiO_2 surface, constantly oxidizing and generating 4 different RhB intermediates before the chromophore destruction. This can be seen through the UV/Vis decrease of the maximum absorbance in time, meaning that RhB concentration is lowering (Figure 5.16).

(a)

(b)

(c)

After one week of being light-exposed
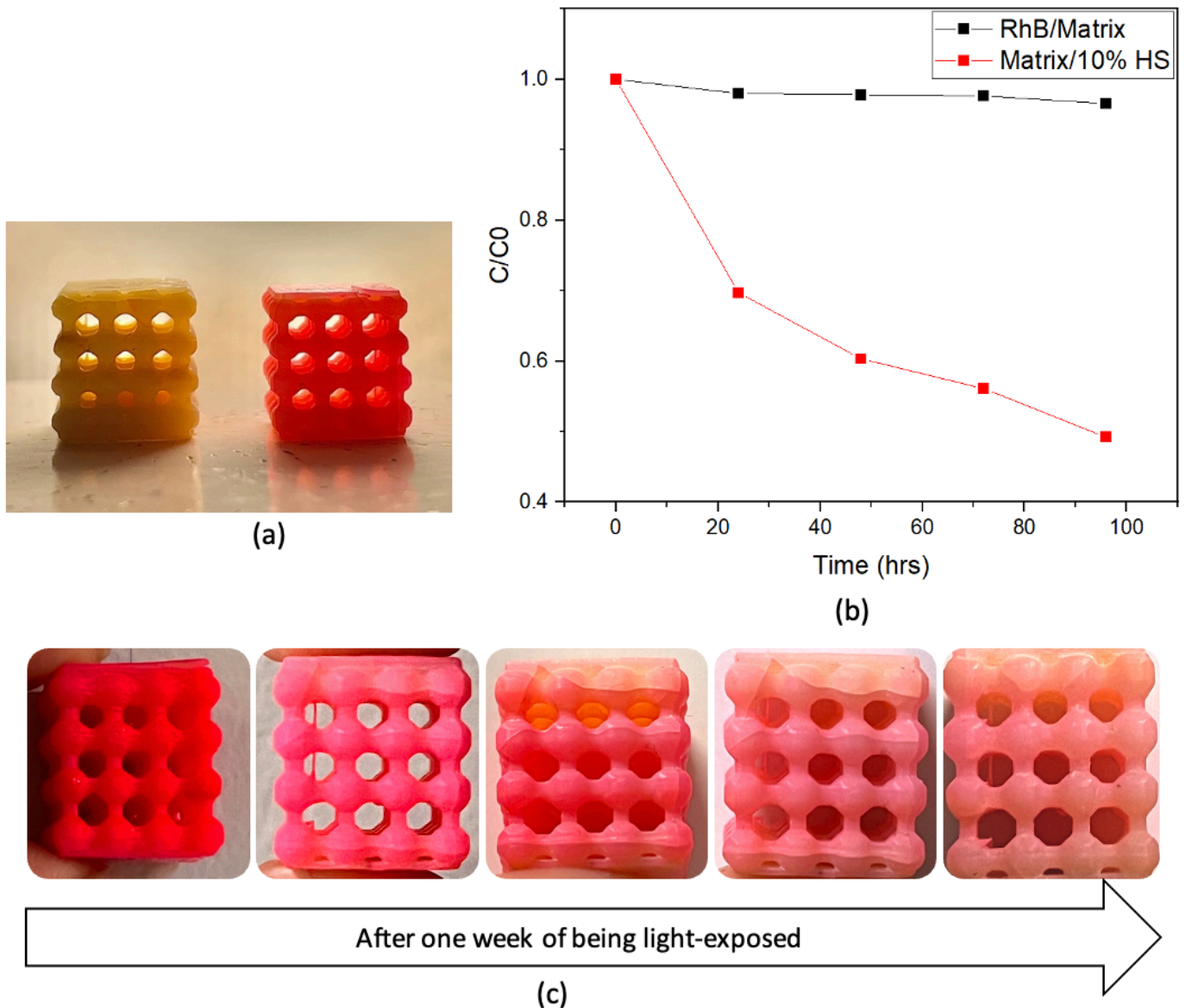
Figure 5.15. Printed 3D composite (10% HS). a) Before and after being submerged for 7 h in RhB. b) RhB degradation efficiency inside solid, c) Pictures of the 3D printed structure at each time of the efficiency curve.

5.3.6. Photoluminescence (PL) as consequence of RhB absorption

The PhCN has a band absorption around 350 nm, as mentioned by (Porcu et al., 2021). The HS has a UV-Vis absorption between the gaps 300-400 nm, which is reflected in the composite absorption also reported in Figure 5.16. The RhB has an absorption from 450-600 nm (Fang et al., 2019; Huoli Zhang et al., 2018), seen in the samples after exposure to RhB concentrated solutions. However, after light exposure and photodegradation in the composite, a slight decrease in the HS is reflected pairing the RhB decreased in its concentration, signaling a consumption of the HS after RhB photodegradation. The next Figure 5.17 follow the same effect measuring PL in the samples.

Figure 5.17 shows the PL spectra of the matrix, the composite, and the composite after RhB absorption. As seen in Figure 5.7, the printed matrix has no photoluminescence while the composite displays similar weak emissions as the HS by itself, as mentioned by Porcu et al. (Porcu, Castellino, et al., 2020). It has to be noted that the applied excitation energy is below the band gap of anatase, therefore the contribution of the inorganic component needs to be excluded and the main emission component regards the PhCN (Stagi, Carbonaro, Corpino, Chiriu, & Ricci, 2015).

Moreover, RhB has a strong photoluminescence emission between 550-700 nm within the printed structures that absorbed it. However, as proof of the HS performance, RhB maximum emission decreased after a 100-hour exposure of the composite to visible light, and with it also the HS emission, probably given to PhCN decomposition.
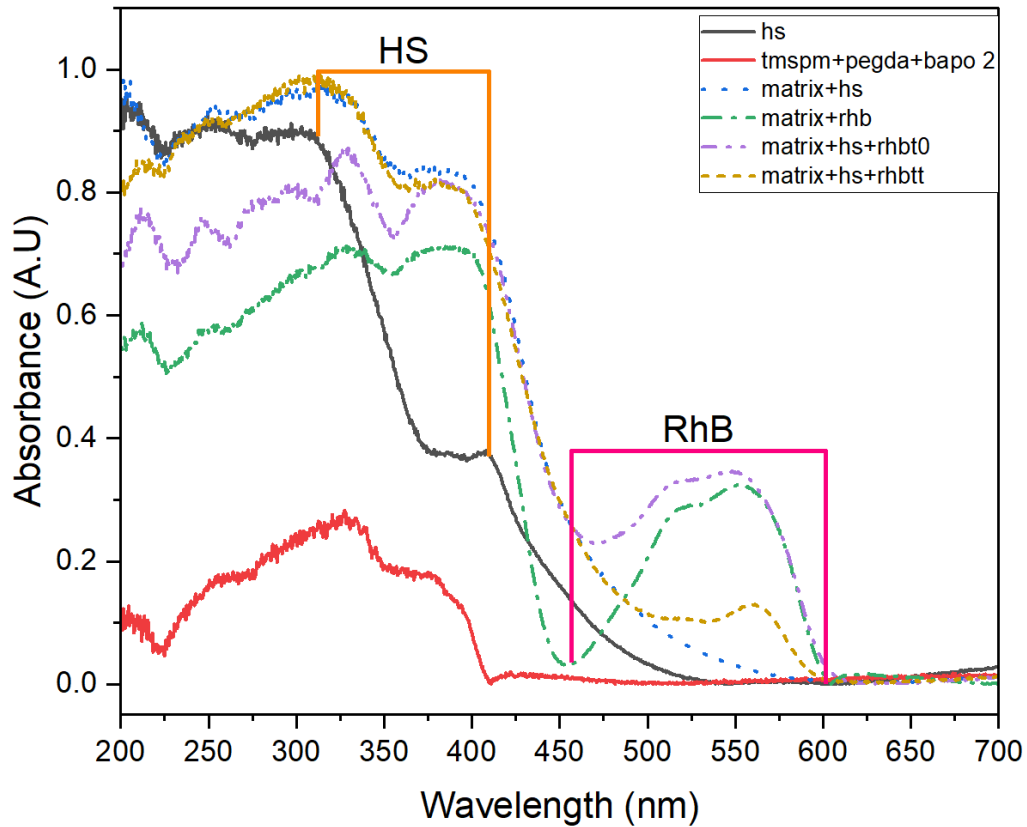
Figure 5.16. UV-Vis solid absorption of components in the settled polymeric the filler, the hybrid matrix, the composite, RhB+ Hybrid matrix, RhB(initial)+composite, RhB (after photodegradation)+composite.
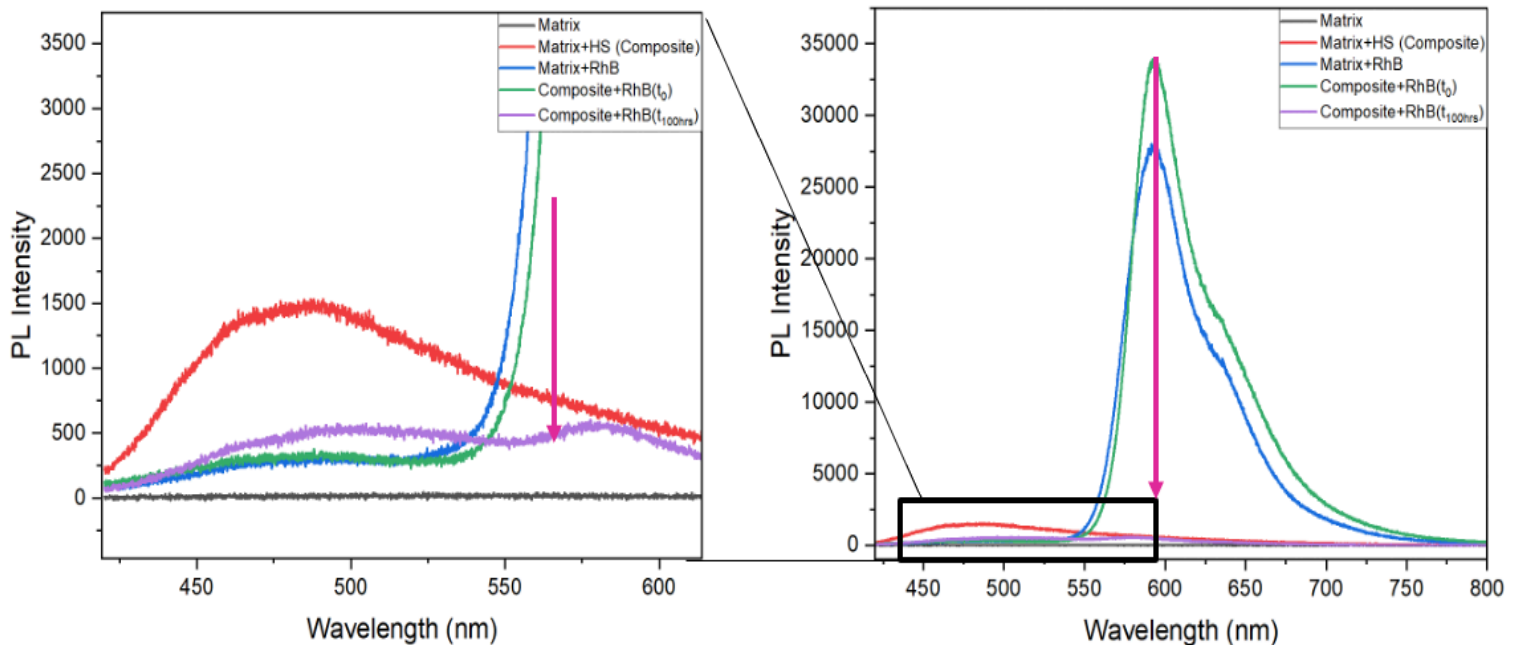
Figure 5.17. PL Spectroscopy of the Hybrid Matrix, the composite, the Hybrid matrix + RhB, RhB (initial) the composite, & RhB (after photodegradation) + the composite.

134

5.4.   Conclusions

In this part of the study, the insertion of PhCN/TiO$_2$ in VP 3D printing was explored utilizing different AM strategies, either grafting on the surface employing a post-treatment coating or embedding it as filler inside the photocured resins. The evaluation of both strategies was performed by measuring the photocatalytic degradation efficiency of RhB when using the material, and how it was affected when translating its applicability toward 3D printed structures.

In the first strategy, a good performance was achieved reaching a 70% degradation of the RhB in the dip coating treatment, and up to the same point when adding the autoclave treatment. In the latter, a more homogenous degradation rate was observed assuming a better attachment of the HS to the system, however, the effectiveness of this application was dependent on the exposed area of the active surface to the light. Therefore, for an optimization of the activity of the material utilizing this AM approach, 3D structures with increased exposed surface area are needed, or increasing the light irradiation angles over the structures. As a polymeric matrix, a formulation with an optimized quantity of TMSPM and PEGDA was used, where the silane bonds from the TMSPM were used as the coupling agent of the coating material and the matrix for assuring a better attachment. To ensure this scope more chemical characterizations are needed, like XPS or FESEM to prove the sol-gel reaction on the surface.

In the second strategy, we introduced the hybrid system inside a resin whose mechanical properties would not be affected as much when crosslinked and can withstand the photocatalytic degradation of RhB inside its structures. For the elaboration of the resin, PEGDA was used as the main oligomer for its great printability, and TMPSM for providing support, diminishing viscosity, and permitting stronger crosslinked bonds. To do this, an evaluation of rheology, photorheology and mechanical properties was done on both formulations to assess the effect of the filler in the photopolymerization. Then a formulation containing 58% TMSPM with a 10% HS or PhCN/TiO$_2$ concentration was selected, and the applicability of this material was evaluated. Where in solution, there was almost no RhB degradation but a great absorption of the colorant inside the structure, achieving a 30% of RhB in a 10 mg.L^{-1} environment. The photodegradation came later however, when left to the visible light for long time periods (100 h) achieving a 50% RhB degradation of the absorbed dye in the previous experimentation, proving that the system is still efficient though with slow kinetic when introduced inside a polymeric network.

General Conclusions

In this Thesis, different approaches for obtaining customized functional structures by optimizing photopolymerizable inks in VAT 3D printing were studied. Also, the suitable post-processing procedures for enhancing their applicability.

In the first chapters of the thesis a general introduction is reported, recalling AM techniques, polymeric composites for VP 3D printing, and the specific fillers used throughout this thesis for the translation of their most representative properties to a printed device.

In the first experimental part, Chapter 4, acrylate-based monomers with low-oxygen content in their molecular composition were used to fabricated 3D printed structures, adding a novel conductive material as filler, MXenes. For the MXene introduction in the resins, $Ti_3C_2T_z$ species was utilized, where its production was based on a strong etching approach with further delamination, to obtain smaller, better conductive and more stable flakes in comparison to other forms obtained by different synthesis methods. This method allowed better dispersibility inside the resin. As when printed in the polymeric composites, the conductivity reached was relatively low, a thermic post-treatment was included to increase the MXene concentration in the structures, and its exposition at the surface. The use of low-oxygen monomers was envisaged to diminish internal degradation on the 3D-printed objects to maintain the original structures even after the thermal post-treatment. Such procedure was also performed in an inert environment to avoid posterior MXene oxidation and maintain its conductive properties. Furthermore, chemical characterization was performed to evaluate its inclusion and the optimization of its concentration inside the photopolymerizable resin without compromising its printability with the DLP methodology. At this point, a photoblocker effect was observed, and an increase in the resin viscosity limited its concentration inside the resins. Then, a follow-up of the material evolution when submitted to extreme temperatures, where a little oxidation was seen in the MXenes, however, its conductive properties were maintained as this treatment did decrease the electrical resistance of the composite. The inclusion of 5 % MXene to the polymer decreased the electrical resistance from 1468 GΩ to 507 GΩ, while, after the post-treatment it decreased even more to 10.5 GΩ.

In the second experimentation part, a different filler material was employed, a photocatalytic semiconductor hybrid material, $PhCN/TiO_2$. This filler was used either as coating on 3D printed structures or as filler embedded within those, aiming at translating the photocatalytic degradation activity in 3D printed structures. In the

coating approach, first dip-coating was tested on a 3D printed part with 58% TMPSM/PEGDA composition. However, due to poor adhesion, an autoclave step was also added to enhance the attachment between the polymeric matrix and PnCN/TiO$_2$. In fact, by using TMPSM monomer in the formulation, a sol-gel chemical bonding can be enabled by using the silane monomer as a coupling agent between the organic matrix and the inorganic phase of the hybrid material. With dip-coating in both strategies it was possible to achieve results up to 70% RhB degradation in 7 hours, while the enhanced adhesion ensured a more homogenous photocatalytic behavior.

Whereas, as a second approach and the main scope of this part of the work, the photocatalytic material was included as a filler. For this part of the work, a comparison between the PEGDA matrix, and the 58% TMPSM matrix was done in terms of printability and mechanical properties and how the filler inclusion affected these properties. The optimization of the filler concentration was also accomplished on both resins, arriving at a 10% filler quantity respectively as the maximum without compromising printing times, polymeric conversion, resolution, and mechanical properties. We choose to proceed with the TMPSM matrix, given its ability to better withstand the filler from a mechanic point of view. Hereafter, the next part of the work was to translate the photocatalytic properties of the material into a composite printed structure. Regarding the efficiency in solution, unfortunately the composite showed negligible photocatalytic activity when submerged in the RhB solution, as its activity was comparable with the neat matrix, though an observable amount of RhB was absorbed by the printed composite (30% RhB in solution). Once dried the composite was left at light exposure, and then the photocatalytic activity was appreciated on the light-exposed surfaces of the solid. At this point, photoluminescence characterizations and solid UV were performed to evaluate the RhB photodegradation inside the solid, achieving almost up to a 53% degradation in a 100h time period.

References

Aakyiir, M., Tanner, B., Yap, P. L., Rastin, H., Tung, T. T., Losic, D., . . . Ma, J. (2022). 3D printing interface-modified PDMS/MXene nanocomposites for stretchable conductors. *J. Mater. Sci. Technol., 117*, 174-182. doi:10.1016/j.jmst.2021.11.048

Aguirre-Cortés, J. M., Moral-Rodríguez, A. I., Bailón-García, E., Davó-Quiñonero, A., Pérez-Cadenas, A. F., & Carrasco-Marín, F. (2023). 3D printing in photocatalysis: Methods and capabilities for the improved performance. *Appl. Mater. Today, 32*. doi:10.1016/j.apmt.2023.101831

Ahmad, I., Zou, Y., Yan, J., Liu, Y., Shukrullah, S., Naz, M. Y., . . . Khalid, N. R. (2023). Semiconductor photocatalysts: A critical review highlighting the various strategies to boost the photocatalytic performances for diverse applications. *Adv. Colloid Interface Sci., 311*, 102830. doi:https://doi.org/10.1016/j.cis.2022.102830

Ahn, D., Stevens, L. M., Zhou, K., & Page, Z. A. (2020). Rapid High-Resolution Visible Light 3D Printing. *ACS Cent Sci, 6*(9), 1555-1563. doi:10.1021/acscentsci.0c00929

Al Mousawi, A., Poriel, C., Dumur, F., Toufaily, J., Hamieh, T., Fouassier, J. P., & Lalevée, J. (2017). Zinc Tetraphenylporphyrin as High Performance Visible Light Photoinitiator of Cationic Photosensitive Resins for LED Projector 3D Printing Applications. *Macromol., 50*(3), 746-753. doi:10.1021/acs.macromol.6b02596

Al Rashid, A., Khan, S. A., G. Al-Ghamdi, S., & Koç, M. (2020). Additive manufacturing: Technology, applications, markets, and opportunities for the built environment. *Autom. Constr., 118*. doi:10.1016/j.autcon.2020.103268

Alhabeb, M., Maleski, K., Anasori, B., Lelyukh, P., Clark, L., Sin, S., & Gogotsi, Y. (2017). Guidelines for Synthesis and Processing of Two-Dimensional

Titanium Carbide (Ti$_3$C$_2$Tx MXene). *Chem Mater, 29*(18), 7633-7644. doi:10.1021/acs.chemmater.7b02847

Alves, D. C. d. S., de Farias, B. S., Breslin, C., Pinto, L. A. d. A., & Cadaval, T. R. S. A. (2022). Chapter 18 - Carbon nanotube-based materials for environmental remediation processes. In D. Giannakoudakis, L. Meili, & I. Anastopoulos (Eds.), *Advanced Materials for Sustainable Environmental Remediation* (pp. 475-513): Elsevier.

Amerio, E., Fabbri, P., Malucelli, G., Messori, M., Sangermano, M., & Taurino, R. (2008). Scratch resistance of nano-silica reinforced acrylic coatings. *Prog. Org. Coat., 62*(2), 129-133. doi:10.1016/j.porgcoat.2007.10.003

Amorim, S. M., Suave, J., Andrade, L., Mendes, A. M., José, H. J., & Moreira, R. F. P. M. (2018). Towards an efficient and durable self-cleaning acrylic paint containing mesoporous TiO2 microspheres. *Prog. Org. Coat., 118*, 48-56. doi:https://doi.org/10.1016/j.porgcoat.2018.01.005

Anasori, B., & Gogotsi, Y. (2019). *2D Metal Carbides and Nitrides (MXenes) Structure, Properties and Applications Structure, Properties and Applications*.

Anasori, B., Lukatskaya, M. R., & Gogotsi, Y. (2017). 2D metal carbides and nitrides (MXenes) for energy storage. *Nat. Rev. Mater., 2*(2). doi:10.1038/natrevmats.2016.98

Anasori, B., Shi, C., Moon, E. J., Xie, Y., Voigt, C. A., Kent, P. R. C., . . . Gogotsi, Y. (2016). Control of electronic properties of 2D carbides (MXenes) by manipulating their transition metal layers. *Nanoscale Horiz, 1*(3), 227-234. doi:10.1039/c5nh00125k

Anasori, B., Xie, Y., Beidaghi, M., Lu, J., Hosler, B. C., Hultman, L., . . . Barsoum, M. W. (2015). Two-Dimensional, Ordered, Double Transition Metals Carbides (MXenes). *ACS Nano, 9*(10), 9507-9516. doi:10.1021/acsnano.5b03591

Andrzejewska, E. (2001). Photopolymerization kinetics of multifunctional monomers. *Prog. Polym. Sci., 26*(4), 605-665. doi:https://doi.org/10.1016/S0079-6700(01)00004-1

Angelopoulos, P. M., Samouhos, M., & Taxiarchou, M. (2021). Functional fillers in composite filaments for fused filament fabrication; a review. *Mater. Today: Proceed., 37*, 4031-4043. doi:10.1016/j.matpr.2020.07.069

Appuhamillage, G. A., Chartrain, N., Meenakshisundaram, V., Feller, K. D., Williams, C. B., & Long, T. E. (2019). 110th Anniversary: Vat Photopolymerization-Based Additive Manufacturing: Current Trends and Future Directions in Materials Design. *Ind. Eng. Chem. Res., 58*(33), 15109-15118. doi:10.1021/acs.iecr.9b02679

Asahi, R., Morikawa, T., Ohwaki, T., Aoki, K., & Taga, Y. (2001). Visible-light photocatalysis in nitrogen-doped titanium oxides. *Sci, 293*(5528), 269-271. doi:10.1126/science.1061051

Ashfaq, A., Ikram, M., Haider, A., Ul-Hamid, A., Shahzadi, I., & Haider, J. (2021). Nitrogen and Carbon Nitride-Doped TiO(2) for Multiple Catalysis and Its Antimicrobial Activity. *Nanoscale Res Lett, 16*(1), 119. doi:10.1186/s11671-021-03573-4

Aslam, M., Fazal, D. B., Ahmad, F., Fazal, A. B., Abdullah, A. Z., Ahmed, M., . . . Rafatullah, M. (2022). Photocatalytic Degradation of Recalcitrant Pollutants of Greywater. *Catalysts, 12*(5), 557. Retrieved from https://www.mdpi.com/2073-4344/12/5/557

Bae, C.-J., Ramachandran, A., Chung, K., & Park, S. (2017). Ceramic Stereolithography: Additive Manufacturing for 3D Complex Ceramic Structures. *J. Korean Ceram. Soc., 54*(6), 470-477. doi:10.4191/kcers.2017.54.6.12

Bae, S., Kang, Y. G., Khazaei, M., Ohno, K., Kim, Y. H., Han, M. J., . . . Raebiger, H. (2021). Electronic and magnetic properties of carbide MXenes—the role of electron correlations. *Mater Today Adv., 9*. doi:10.1016/j.mtadv.2020.100118

Bagheri, A., & Jin, J. (2019). Photopolymerization in 3D Printing. *ACS Appl. Polym. Mater., 1*(4), 593-611. doi:10.1021/acsapm.8b00165

Bagheri, S., TermehYousefi, A., & Do, T.-O. (2017). Photocatalytic pathway toward degradation of environmental pharmaceutical pollutants: structure, kinetics and mechanism approach. *Catal. Sci. Technol, 7*(20), 4548-4569. doi:10.1039/C7CY00468K

Baig, M. M., Gul, I. H., Baig, S. M., & Shahzad, F. (2022). 2D MXenes: Synthesis, properties, and electrochemical energy storage for supercapacitors – A review. *JEAC 904*. doi:10.1016/j.jelechem.2021.115920

Barsoum, M. W. (2000). The $M_{N+1}AX_N$ phases: A new class of solids: Thermodynamically stable nanolaminates. *Prog. Solid. State Ch., 28*(1), 201-281. doi:https://doi.org/10.1016/S0079-6786(00)00006-6

Belon, C., Chemtob, A., Croutxé-Barghorn, C., Rigolet, S., Le Houérou, V., & Gauthier, C. (2011). A Simple Method for the Reinforcement of UV-Cured Coatings via Sol-Gel Photopolymerization. *Macromol. Mater. Eng. , 296*(6), 506-516. doi:10.1002/mame.201000350

Bertlein, S., Brown, G., Lim, K. S., Jungst, T., Boeck, T., Blunk, T., . . . Groll, J. (2017). Thiol–Ene Clickable Gelatin: A Platform Bioink for Multiple 3D Biofabrication Technologies. *Adv. Mater., 29*(44), 1703404. doi:https://doi.org/10.1002/adma.201703404

Beuermann, S., Paquet, D. A., McMinn, J. H., & Hutchinson, R. A. (1996). Determination of Free-Radical Propagation Rate Coefficients of Butyl, 2-Ethylhexyl, and Dodecyl Acrylates by Pulsed-Laser Polymerization. *Macromol., 29*(12), 4206-4215. doi:10.1021/ma960081c

Bhatt, P. M., Kabir, A. M., Peralta, M., Bruck, H. A., & Gupta, S. K. (2019). A robotic cell for performing sheet lamination-based additive manufacturing. *Addit. Manuf., 27*, 278-289. doi:10.1016/j.addma.2019.02.002

Bhunia, P., & Dutta, K. (2020). Photocatalysts and Photoelectrocatalysts in Fuel Cells and Photofuel Cells. In S. Rajendran, M. Naushad, L. C. Ponce, & E. Lichtfouse (Eds.), *Green Photocatalysts for Energy and Environmental Process* (pp. 19-55). Cham: Springer International Publishing.

Bonefeld-Jørgensen, E. C., Long, M., Hofmeister, M. V., & Vinggaard, A. M. (2007). Endocrine-disrupting potential of bisphenol A, bisphenol A dimethacrylate, 4-n-nonylphenol, and 4-n-octylphenol in vitro: new data and a brief review. *Environ Health Perspect, 115 Suppl 1*(Suppl 1), 69-76. doi:10.1289/ehp.9368

Cai, T., Zeng, W., Liu, Y., Wang, L., Dong, W., Chen, H., & Xia, X. (2020). A promising inorganic-organic Z-scheme photocatalyst Ag3PO4/PDI

supermolecule with enhanced photoactivity and photostability for environmental remediation. *Appl. Catal., B, 263*, 118327. doi:https://doi.org/10.1016/j.apcatb.2019.118327

Cao, M.-S., Cai, Y.-Z., He, P., Shu, J.-C., Cao, W.-Q., & Yuan, J. (2019). 2D MXenes: Electromagnetic property for microwave absorption and electromagnetic interference shielding. *J. Chem. Eng., 359*, 1265-1302. doi:10.1016/j.cej.2018.11.051

Cao, Y., Deng, Q., Liu, Z., Shen, D., Wang, T., Huang, Q., . . . Yu, J. (2017). Enhanced thermal properties of poly(vinylidene fluoride) composites with ultrathin nanosheets of MXene. *RSC Adv, 7*(33), 20494-20501. doi:10.1039/c7ra00184c

Carey, M., & Barsoum, M. W. (2021). MXene polymer nanocomposites: a review. *Mater. Today Adv., 9*. doi:10.1016/j.mtadv.2020.100120

Chaudhary, R. (2022). *Additive Manufacturing by Digital Light Processing (DLP).* (Ph.D. in Materials Science and Nanotechnology). UNIVERSITÀ DEGLI STUDI DI MILANO-BICOCCA, Milano.

Chaudhary, V., Ashraf, N., Khalid, M., Walvekar, R., Yang, Y., Kaushik, A., & Mishra, Y. K. (2022). Emergence of MXene–Polymer Hybrid Nanocomposites as High-Performance Next-Generation Chemiresistors for Efficient Air Quality Monitoring. *Adv. Funct. Mater., 32*(33). doi:10.1002/adfm.202112913

Chemtob, A., Courtecuisse, F., Croutxé-Barghorn, C., & Rigolet, S. (2011). Simultaneous sol–gel and anionic photopolymerization of 3-(glycidyloxypropyl)trimethoxysilane via photobase catalysis. *New J Chem, 35*(9). doi:10.1039/c1nj20320g

Chen, F., Zhao, J., & Hidaka, H. (2003). Highly selective deethylation of rhodamine B: Adsorption and photooxidation pathways of the dye on the TiO_2/SiO_2 composite photocatalyst. *Int. J. Energy Res., 5*, 674957. doi:10.1155/S1110662X03000345

Chen, L., Zhang, Y., Ye, H., Duan, G., Duan, H., Ge, Q., & Wang, Z. (2021). Color-Changeable Four-Dimensional Printing Enabled with Ultraviolet-Curable and Thermochromic Shape Memory Polymers. *ACS Appl Mater Interfaces, 13*(15), 18120-18127. doi:10.1021/acsami.1c02656

Chia, H. L., Mayorga-Martinez, C. C., Antonatos, N., Sofer, Z., Gonzalez-Julian, J. J., Webster, R. D., & Pumera, M. (2020). MXene Titanium Carbide-based Biosensor: Strong Dependence of Exfoliation Method on Performance. *Anal. Chem., 92*(3), 2452-2459. doi:10.1021/acs.analchem.9b03634

Chiappone, A., Fantino, E., Roppolo, I., Lorusso, M., Manfredi, D., Fino, P., . . . Calignano, F. (2016). 3D Printed PEG-Based Hybrid Nanocomposites Obtained by Sol-Gel Technique. *ACS Appl Mater Interfaces, 8*(8), 5627-5633. doi:10.1021/acsami.5b12578

Chiappone, A., Roppolo, I., Naretto, E., Fantino, E., Calignano, F., Sangermano, M., & Pirri, F. (2017). Study of graphene oxide-based 3D printable composites: Effect of the in situ reduction. *Compos. B. Eng., 124*, 9-15. doi:10.1016/j.compositesb.2017.05.049

Choi, J. W., Wicker, R. B., Cho, S. H., Ha, C. S., & Lee, S. H. (2009). Cure depth control for complex 3D microstructure fabrication in dynamic mask projection microstereolithography. *Rapid Prototyp. J., 15*(1), 59-70. doi:10.1108/13552540910925072

Chou, W. H., Gamboa, A., & Morales, J. O. (2021). Inkjet printing of small molecules, biologics, and nanoparticles. *Int J Pharm, 600*, 120462. doi:10.1016/j.ijpharm.2021.120462

Colebatch, A. L., & Weller, A. S. (2019). Amine-Borane Dehydropolymerization: Challenges and Opportunities. *Chem, 25*(6), 1379-1390. doi:10.1002/chem.201804592

Comstock, M. J. (1995). *Hybrid Organic-Inorganic Composites.*

Cook, C. C., Fong, E. J., Schwartz, J. J., Porcincula, D. H., Kaczmarek, A. C., Oakdale, J. S., . . . Shusteff, M. (2020). Highly Tunable Thiol-Ene Photoresins for Volumetric Additive Manufacturing. *Adv. Mater., 32*(47), 2003376. doi:https://doi.org/10.1002/adma.202003376

Corrigan, N., Xu, J., & Boyer, C. (2016). A Photoinitiation System for Conventional and Controlled Radical Polymerization at Visible and NIR Wavelengths. *Macromol., 49*(9), 3274-3285. doi:10.1021/acs.macromol.6b00542

Cortés, A., Cosola, A., Sangermano, M., Campo, M., González Prolongo, S., Pirri, C. F., . . . Chiappone, A. (2021). DLP 4D-Printing of Remotely, Modularly, and Selectively Controllable Shape Memory Polymer Nanocomposites Embedding Carbon Nanotubes. *Adv. Funct. Mater., 31*(50). doi:10.1002/adfm.202106774

Cortés-Guzmán, K. P., Parikh, A. R., Sparacin, M. L., Johnson, R. M., Adegoke, L., Ecker, M., . . . Smaldone, R. A. (2023). Thermal annealing effects on the mechanical properties of bio-based 3D printed thermosets. *Polym. Chem., 14*(22), 2697-2707. doi:10.1039/D3PY00200D

Cosola, A., Conti, R., Grützmacher, H., Sangermano, M., Roppolo, I., Pirri, C. F., & Chiappone, A. (2020). Multiacrylated Cyclodextrin: A Bio-Derived Photocurable Macromer for VAT 3D Printing. *Macromol. Mater. Eng. , 305*(9), 2000350. doi:https://doi.org/10.1002/mame.202000350

Crivello, J. V., & Reichmanis, E. (2014). Photopolymer Materials and Processes for Advanced Technologies. *Chem. Mater., 26*(1), 533-548. doi:10.1021/cm402262g

Cui, Y., Zhu, J., Tong, H., & Zou, R. (2023). Advanced perspectives on MXene composite nanomaterials: Types synthetic methods, thermal energy utilization and 3D-printed techniques. *iScience, 26*(1), 105824. doi:10.1016/j.isci.2022.105824

Dadashi Firouzjaei, M., Karimiziarani, M., Moradkhani, H., Elliott, M., & Anasori, B. (2022). MXenes: The two-dimensional influencers. *Mater Today Adv., 13*. doi:10.1016/j.mtadv.2021.100202

Dai, Y., Wu, X., Li, L., Zhang, Y., Deng, Z., Yu, Z.-Z., & Zhang, H.-B. (2022). 3D printing of resilient, lightweight and conductive MXene/reduced graphene oxide architectures for broadband electromagnetic interference shielding. *J. Mater. Chem. A, 10*(21), 11375-11385. doi:10.1039/D2TA01388F

de Beer, M. P., van der Laan, H. L., Cole, M. A., Whelan, R. J., Burns, M. A., & Scott, T. F. (2019). Rapid, continuous additive manufacturing by volumetric polymerization inhibition patterning. *Sci. Adv., 5*(1), eaau8723. doi:doi:10.1126/sciadv.aau8723

Demchenko, A. P. (2020). Photobleaching of organic fluorophores: quantitative characterization, mechanisms, protection*. *Methods Appl. Fluoresc., 8*(2), 022001. doi:10.1088/2050-6120/ab7365

Deng, H., Bilotti, E., Zhang, R., Loos, J., & Peijs, T. (2010). Effect of thermal annealing on the electrical conductivity of high-strength bicomponent polymer tapes containing carbon nanofillers. *Synth. Met., 160*(5-6), 337-344. doi:10.1016/j.synthmet.2009.11.001

Díaz-Marta, A. S., Tubío, C. R., Carbajales, C., Fernández, C., Escalante, L., Sotelo, E., . . . Coelho, A. (2018). Three-Dimensional Printing in Catalysis: Combining 3D Heterogeneous Copper and Palladium Catalysts for Multicatalytic Multicomponent Reactions. *ACS Catalysis, 8*(1), 392-404. doi:10.1021/acscatal.7b02592

Dietlin, C., Schweizer, S., Xiao, P., Zhang, J., Morlet-Savary, F., Graff, B., . . . Lalevée, J. (2015). Photopolymerization upon LEDs: new photoinitiating systems and strategies. *Polym. Chem., 6*(21), 3895-3912. doi:10.1039/c5py00258c

Dinita, A., Neacsa, A., Portoaca, A. I., Tanase, M., Ilinca, C. N., & Ramadan, I. N. (2023). Additive Manufacturing Post-Processing Treatments, a Review with Emphasis on Mechanical Characteristics. *Materials (Basel), 16*(13). doi:10.3390/ma16134610

Duy, N., Bui, H., & Hien, N. (2020). Heterogeneous photocatalysis for the removal of pharmaceutical compounds. In (pp. 161-183).

Enders, A., Siller, I. G., Urmann, K., Hoffmann, M. R., & Bahnemann, J. (2019). 3D Printed Microfluidic Mixers—A Comparative Study on Mixing Unit Performances. *Small, 15*(2), 1804326. doi:https://doi.org/10.1002/smll.201804326

Erkoc, P., & Ulucan-Karnak, F. (2021). Nanotechnology-Based Antimicrobial and Antiviral Surface Coating Strategies. *Prosthesis, 3*(1), 25-52. doi:10.3390/prosthesis3010005

Esmaili, M., Eldeeb, M. A., & Moosavi-Movahedi, A. A. (2021). Current Developments in Native Nanometric Discoidal Membrane Bilayer Formed by Amphipathic Polymers. *Nanomaterials (Basel), 11*(7). doi:10.3390/nano11071771

Fang, H., Pan, Y., Yin, M., & Pan, C. (2019). Enhanced visible light photocatalytic activity of CdS with alkalized Ti3C2 nano-sheets as co-catalyst for

degradation of rhodamine B. *J Mater Sci Mater Electron., 30*(16), 14954-14966. doi:10.1007/s10854-019-01868-y

Fantino, E., Chiappone, A., Calignano, F., Fontana, M., Pirri, F., & Roppolo, I. (2016). In Situ Thermal Generation of Silver Nanoparticles in 3D Printed Polymeric Structures. *Materials (Basel), 9*(7). doi:10.3390/ma9070589

Fantino, E., Chiappone, A., Roppolo, I., Manfredi, D., Bongiovanni, R., Pirri, C. F., & Calignano, F. (2016). 3D Printing of Conductive Complex Structures with In Situ Generation of Silver Nanoparticles. *Adv. Mater., 28*(19), 3712-3717. doi:10.1002/adma.201505109

Firestein, K. L., von Treifeldt, J. E., Kvashnin, D. G., Fernando, J. F. S., Zhang, C., Kvashnin, A. G., . . . Golberg, D. (2020). Young's Modulus and Tensile Strength of Ti(3)C(2) MXene Nanosheets As Revealed by In Situ TEM Probing, AFM Nanomechanical Mapping, and Theoretical Calculations. *Nano Lett, 20*(8), 5900-5908. doi:10.1021/acs.nanolett.0c01861

Fischer, H., & Radom, L. (2001). Factors Controlling the Addition of Carbon-Centered Radicals to Alkenes—An Experimental and Theoretical Perspective. *Angew. Chem. Int. Ed., 40*(8), 1340-1371. doi:https://doi.org/10.1002/1521-3773(20010417)40:8<1340::AID-ANIE1340>3.0.CO;2-#

Fors, B. P., & Hawker, C. J. (2012). Control of a Living Radical Polymerization of Methacrylates by Light. *Angew. Chem. Int. Ed., 51*(35), 8850-8853. doi:https://doi.org/10.1002/anie.201203639

Fouassier, J., & Lalevée, J. (2012). *Photoinitiators for Polymer Synthesis: Scope, Reactivity and Efficiency*.

Fouassier, J.-P. (1995). *Photoinitiation, photopolymerization, and photocuring : fundamentals and applications*. Munich, New York: Hanser ; Distributed by Hanser/Gardner Publications Munich, New York.

Fouassier, J. P., Allonas, X., & Burget, D. (2003). Photopolymerization reactions under visible lights: principle, mechanisms and examples of applications. *Prog. Org. Coat., 47*(1), 16-36. doi:10.1016/s0300-9440(03)00011-0

Frascella, F., Gonzalez, G., Bosch, P., Angelini, A., Chiappone, A., Sangermano, M., . . . Roppolo, I. (2018). Three-Dimensional Printed Photoluminescent Polymeric Waveguides. *ACS Appl Mater Interfaces, 10*(45), 39319-39326. doi:10.1021/acsami.8b16036

Fu, J., Taher, S. E., Abu Al-Rub, R. K., Zhang, T., Chan, V., & Liao, K. (2022). Engineering 3D-Architected Gyroid MXene Scaffolds for Ultrasensitive Micromechanical Sensing. *Adv. Eng. Mater.* doi:10.1002/adem.202101388

Fujishima, A., & Honda, K. (1972). Electrochemical photolysis of water at a semiconductor electrode. *Nature, 238*(5358), 37-38.

Gao, H., An, J., Chua, C. K., Bourell, D., Kuo, C.-N., & Tan, D. T. H. (2023). 3D printed optics and photonics: Processes, materials and applications. *Mater. Today 69*, 107-132. doi:https://doi.org/10.1016/j.mattod.2023.06.019

Garcia, C., Gallardo, A., López, D., Elvira, C., Azzahti, A., Lopez-Martinez, E., . . . Rodríguez-Hernández, J. (2018). Smart pH-Responsive Antimicrobial Hydrogel Scaffolds Prepared by Additive Manufacturing. *ACS Appl. Bio Mater., 1*(5), 1337-1347. doi:10.1021/acsabm.8b00297

Garra, P., Fouassier, J. P., Lakhdar, S., Yagci, Y., & Lalevée, J. (2020). Visible light photoinitiating systems by charge transfer complexes: Photochemistry without dyes. *Prog. Polym. Sci., 107*. doi:10.1016/j.progpolymsci.2020.101277

Gastaldi, M., Cardano, F., Zanetti, M., Viscardi, G., Barolo, C., Bordiga, S., . . . Roppolo, I. (2020). Functional Dyes in Polymeric 3D Printing: Applications and Perspectives. *ACS Mater. Lett., 3*(1), 1-17. doi:10.1021/acsmaterialslett.0c00455

Ghidiu, M., Lukatskaya, M. R., Zhao, M. Q., Gogotsi, Y., & Barsoum, M. W. (2014). Conductive two-dimensional titanium carbide 'clay' with high volumetric capacitance. *Nature, 516*(7529), 78-81. doi:10.1038/nature13970

Ghidiu, M., Naguib, M., Shi, C., Mashtalir, O., Pan, L. M., Zhang, B., . . . Barsoum, M. W. (2014). Synthesis and characterization of two-dimensional Nb_4C_3 (MXene). *Chem Commun (Camb), 50*(67), 9517-9520. doi:10.1039/c4cc03366c

Ghosh, A., Pal, H., Das, T., Chatterjee, S., & Das, A. (2022). Synthesis and Characterization of MXene from MAX phase. *Mater. Today: Proc., 58*, 714-716. doi:10.1016/j.matpr.2022.02.253

Gogotsi, Y., & Anasori, B. (2019). The Rise of MXenes. *ACS Nano, 13*(8), 8491-8494. doi:10.1021/acsnano.9b06394

Gong, H., Bickham, B. P., Woolley, A. T., & Nordin, G. P. (2017). Custom 3D printer and resin for 18 μm × 20 μm microfluidic flow channels. *Lab on a Chip, 17*(17), 2899-2909. doi:10.1039/C7LC00644F

Gong, H., Woolley, A. T., & Nordin, G. P. (2018). 3D printed high density, reversible, chip-to-chip microfluidic interconnects. *Lab on a Chip, 18*(4), 639-647. doi:10.1039/C7LC01113J

Gong, K., Zhou, K., Qian, X., Shi, C., & Yu, B. (2021). MXene as emerging nanofillers for high-performance polymer composites: A review. *Compos. B. Eng., 217*. doi:10.1016/j.compositesb.2021.108867

Gong, S., Teng, X., Niu, Y., Liu, X., Xu, M., Xu, C., . . . Chen, Z. (2021). Construction of S-scheme 0D/2D heterostructures for enhanced visible-light-driven CO2 reduction. *Appl Catal B: Environm., 298*, 120521. doi:https://doi.org/10.1016/j.apcatb.2021.120521

Gonzalez, G., Baruffaldi, D., Martinengo, C., Angelini, A., Chiappone, A., Roppolo, I., . . . Frascella, F. (2020). Materials Testing for the Development of Biocompatible Devices through Vat-Polymerization 3D Printing. *Nanomaterials, 10*(9). doi:10.3390/nano10091788

Gonzalez, G., Chiappone, A., Dietliker, K., Pirri, C. F., & Roppolo, I. (2020). Fabrication and Functionalization of 3D Printed Polydimethylsiloxane-Based Microfluidic Devices Obtained through Digital Light Processing. *Adv. Mater. Technol.* doi:10.1002/admt.202000374

Gonzalez, G., Chiappone, A., Roppolo, I., Fantino, E., Bertana, V., Perrucci, F., . . . Sangermano, M. (2017). Development of 3D printable formulations containing CNT with enhanced electrical properties. *Polymer, 109*, 246-253. doi:10.1016/j.polymer.2016.12.051

Gonzalez, G., Roppolo, I., Pirri, C. F., & Chiappone, A. (2022). Current and emerging trends in polymeric 3D printed microfluidic devices. *Addit. Manuf., 55*. doi:10.1016/j.addma.2022.102867

Gonzalez-Julian, J. (2020). Processing of MAX phases: From synthesis to applications. *J. Am. Ceram. Soc., 104*(2), 659-690. doi:10.1111/jace.17544

Goyanes, A., Det-Amornrat, U., Wang, J., Basit, A. W., & Gaisford, S. (2016). 3D scanning and 3D printing as innovative technologies for fabricating personalized topical drug delivery systems. *J. Control Release, 234*, 41-48. doi:10.1016/j.jconrel.2016.05.034

Greaves, M., Mende, M., Wang, J., Yang, W., & Barg, S. (2021). Investigating the rheology of 2D titanium carbide (MXene) dispersions for colloidal processing: Progress and challenges. *J. Mater. Res., 36*(22), 4578-4600. doi:10.1557/s43578-021-00282-7

Gross, B. C., Erkal, J. L., Lockwood, S. Y., Chen, C., & Spence, D. M. (2014). Evaluation of 3D printing and its potential impact on biotechnology and the chemical sciences. *Anal. Chem., 86*(7), 3240-3253. doi:10.1021/ac403397r

Gusain, R., Khan, A., & Khatri, O. P. (2020). Fatty acid-derived ionic liquids as renewable lubricant additives: Effect of chain length and unsaturation. *J. Mol. Liq., 301*. doi:10.1016/j.molliq.2019.112322

Hadi Mohammed, A., Ahmad, M., Ibrahim, A., & Zainuddin, N. (2016). SYNTHESIS AND MONOMER REACTIVITY RATIOS OF [3-(TRIMETHOXYSILYL) PROPYL METHACRYLATE/N-VINYL PYRROLIDONE] COPOLYMER. 2279-2291.

Halim, J., Cook, K. M., Naguib, M., Eklund, P., Gogotsi, Y., Rosen, J., & Barsoum, M. W. (2016). X-ray photoelectron spectroscopy of select multi-layered transition metal carbides (MXenes). *Appl. Surf. Sci., 362*, 406-417. doi:10.1016/j.apsusc.2015.11.089

Halim, J., Kota, S., Lukatskaya, M. R., Naguib, M., Zhao, M.-Q., Moon, E. J., . . . Barsoum, M. W. (2016). Synthesis and Characterization of 2D Molybdenum Carbide (MXene). *Adv. Funct. Mater., 26*(18), 3118-3127. doi:https://doi.org/10.1002/adfm.201505328

Halim, J., Lukatskaya, M. R., Cook, K. M., Lu, J., Smith, C. R., Naslund, L. A., . . . Barsoum, M. W. (2014). Transparent Conductive Two-Dimensional Titanium Carbide Epitaxial Thin Films. *Chem Mater, 26*(7), 2374-2381. doi:10.1021/cm500641a

Hamdy, M. S., Abd-Rabboh, H. S. M., Benaissa, M., Al-Metwaly, M. G., Galal, A. H., & Ahmed, M. A. (2021). Fabrication of novel polyaniline/ZnO heterojunction for exceptional photocatalytic hydrogen production and degradation of fluorescein dye through direct Z-scheme mechanism. *Opt. Mater, 117*, 111198. doi:https://doi.org/10.1016/j.optmat.2021.111198

Han, J., Deng, Y., Li, N., Chen, D., Xu, Q., Li, H., . . . Lu, J. (2021). A π-π stacking perylene imide/Bi2WO6 hybrid with dual transfer approach for enhanced photocatalytic degradation. *J. Colloid Interface Sci, 582*, 1021-1032. doi:https://doi.org/10.1016/j.jcis.2020.09.013

Han, M., Maleski, K., Shuck, C. E., Yang, Y., Glazar, J. T., Foucher, A. C., . . . Gogotsi, Y. (2020). Tailoring Electronic and Optical Properties of MXenes through Forming Solid Solutions. *J Am Chem Soc, 142*(45), 19110-19118. doi:10.1021/jacs.0c07395

Hart, J. L., Hantanasirisakul, K., Lang, A. C., Anasori, B., Pinto, D., Pivak, Y., . . . Taheri, M. L. (2019). Control of MXenes' electronic properties through termination and intercalation. *Nat Commun, 10*(1), 522. doi:10.1038/s41467-018-08169-8

Hashimoto, K., Irie, H., & Fujishima, A. (2005). TiO2 Photocatalysis: A Historical Overview and Future Prospects. *JJAP, 44*(12R). doi:10.1143/jjap.44.8269

Hieu, V. Q., Lam, T. C., Khan, A., Thi Vo, T.-T., Nguyen, T.-Q., Doan, V. D., . . . Tran, V. A. (2021). $TiO_2/Ti_3C_2/g-C_3N_4$ ternary heterojunction for photocatalytic hydrogen evolution. *Chemosphere, 285*, 131429. doi:https://doi.org/10.1016/j.chemosphere.2021.131429

Hong, B. M., Park, S. A., & Park, W. H. (2019). Effect of photoinitiator on chain degradation of hyaluronic acid. *Biomater Res, 23*, 21. doi:10.1186/s40824-019-0170-1

Hong Ng, V. M., Huang, H., Zhou, K., Lee, P. S., Que, W., Xu, J. Z., & Kong, L. B. (2017). Recent progress in layered transition metal carbides and/or nitrides (MXenes) and their composites: synthesis and applications. *J. Mater. Chem. A., 5*(7), 3039-3068. doi:10.1039/C6TA06772G

Hoyle, C. E., & Bowman, C. N. (2010). Thiol–Ene Click Chemistry. *Angew. Chem., Int. Ed. , 49*(9), 1540-1573. doi:https://doi.org/10.1002/anie.200903924

Hu, Y., Pang, S., Yang, G., Yao, X., Li, C., Jiang, J., & Li, Y. (2022). MXene modified carbon fiber composites with improved mechanical properties based on electrophoretic deposition. *Mater. Res. Bull, 150*. doi:10.1016/j.materresbull.2022.111761

Huang, B., Zhou, Z., Wei, L., Song, Q., Yu, W., Zhou, Y., . . . Lu, C. (2021). $Ti_3C_2T_x$ MXene as a novel functional photo blocker for stereolithographic

150

3D printing of multifunctional gels via Continuous Liquid Interface
Production. *Compos. B. Eng., 225*.
doi:10.1016/j.compositesb.2021.109261

Huang, W.-X., Li, Z.-P., Li, D.-D., Hu, Z.-H., Wu, C., Lv, K.-L., & Li, Q. (2022).
Ti_3C_2 MXene: recent progress in its fundamentals, synthesis, and
applications. *Rare Metals, 41*(10), 3268-3300. doi:10.1007/s12598-022-
02058-2

Ibrahim, Y., Mohamed, A., Abdelgawad, A. M., Eid, K., Abdullah, A. M., &
Elzatahry, A. (2020). The Recent Advances in the Mechanical Properties
of Self-Standing Two-Dimensional MXene-Based Nanostructures: Deep
Insights into the Supercapacitor. *Nanomaterials (Basel), 10*(10).
doi:10.3390/nano10101916

Ikemura, K., & Endo, T. (2010). A review of the development of radical
photopolymerization initiators used for designing light-curing dental
adhesives and resin composites. *Dent Mater J, 29*(5), 481-501.
doi:10.4012/dmj.2009-137

Ikuta, K., & Hirowatari, K. (1993, 10-10 Feb. 1993). *Real three dimensional
micro fabrication using stereo lithography and metal molding.* Paper
presented at the Proc. IEEE Int. Conf. Micro Electro Mech. Syst.
(MEMS).

International, A. (2012). Standard Terminology for Additive Manufacturing
Technologies. In *ASTM F2792-12a*. West Conshohocken, PA.

Jańczyk, A., Krakowska, E., Stochel, G., & Macyk, W. (2006). Singlet Oxygen
Photogeneration at Surface Modified Titanium Dioxide. *JACS, 128*(49),
15574-15575. doi:10.1021/ja065970m

Jasim, S. A., Hadi, J. M., Opulencia, M. J. C., Karim, Y. S., Mahdi, A. B.,
Kadhim, M. M., . . . Falih, K. T. (2022). MXene/metal and polymer
nanocomposites: Preparation, properties, and applications. *J. Alloys
Compd., 917*. doi:10.1016/j.jallcom.2022.165404

Jauk, S., & Liska, R. (2005). Photoinitiators with Functional Groups, 8.
Macromol. Rapid Commun., 26(21), 1687-1692.
doi:https://doi.org/10.1002/marc.200500507

Jawaid, A., Hassan, A., Neher, G., Nepal, D., Pachter, R., Kennedy, W. J., . . . Vaia, R. A. (2021). Halogen Etch of Ti(3)AlC(2) MAX Phase for MXene Fabrication. *ACS Nano, 15*(2), 2771-2777. doi:10.1021/acsnano.0c08630

Jeitschko, W., Nowotny, H., & Benesovsky, F. (1963). Kohlenstoffhaltige ternäre Verbindungen (H-Phase). *Monatsh. Chem., 94*, 672-676.

Ji, B., Fan, S., Ma, X., Hu, K., Wang, L., Luan, C., . . . Zhang, L. (2020). Electromagnetic shielding behavior of heat-treated Ti3C2TX MXene accompanied by structural and phase changes. *Carbon, 165*, 150-162. doi:10.1016/j.carbon.2020.04.041

Jia, H., Kong, Q.-Q., Liu, Z., Wei, X.-X., Li, X.-M., Chen, J.-P., . . . Chen, C.-M. (2020). 3D graphene/ carbon nanotubes/ polydimethylsiloxane composites as high-performance electromagnetic shielding material in X-band. *Compos. - A: Appl. Sci. Manuf., 129*. doi:10.1016/j.compositesa.2019.105712

Jiang, C.-c., Cao, Y.-k., Xiao, G.-y., Zhu, R.-f., & Lu, Y.-p. (2017). A review on the application of inorganic nanoparticles in chemical surface coatings on metallic substrates. *RSC Adv, 7*(13), 7531-7539. doi:10.1039/c6ra25841g

Jun, J.-B., Hong, J.-K., Park, J.-G., & Suh, K.-D. (2003). Preparation of Monodisperse Crosslinked Organic-Inorganic Hybrid Copolymer Particles by Dispersion Polymerization. *Macromol. Chem. Phys., 204*(18), 2281-2289. doi:https://doi.org/10.1002/macp.200300015

Juskova, P., Ollitrault, A., Serra, M., Viovy, J. L., & Malaquin, L. (2018). Resolution improvement of 3D stereo-lithography through the direct laser trajectory programming: Application to microfluidic deterministic lateral displacement device. *Anal Chim Acta, 1000*, 239-247. doi:10.1016/j.aca.2017.11.062

Kaczynski, J. B. (1989, June 28, 2000). What is the 3DPTM Process? Copyright 1989-2000, 3DPTM Laboratory, MIT. Retrieved from https://www.mit.edu/~tdp/whatis3dp.html

Kamysbayev, V., Filatov, A. S., Hu, H., Rui, X., Lagunas, F., Wang, D., . . . Talapin, D. V. (2020). Covalent surface modifications and superconductivity of two-dimensional metal carbide MXenes. *Sci., 369*(6506), 979-983. doi:10.1126/science.aba8311

152

Kang, R., Zhang, Z., Guo, L., Cui, J., Chen, Y., Hou, X., . . . Yu, J. (2019). Enhanced Thermal Conductivity of Epoxy Composites Filled with 2D Transition Metal Carbides (MXenes) with Ultralow Loading. *Sci Rep, 9*(1), 9135. doi:10.1038/s41598-019-45664-4

Karlsson, L. H., Birch, J., Halim, J., Barsoum, M. W., & Persson, P. O. (2015). Atomically Resolved Structural and Chemical Investigation of Single MXene Sheets. *Nano Lett, 15*(8), 4955-4960. doi:10.1021/acs.nanolett.5b00737

Kay, A., Cesar, I., & Grätzel, M. (2006). New Benchmark for Water Photooxidation by Nanostructured α-Fe2O3 Films. *J. Am. Chem. Soc., 128*(49), 15714-15721. doi:10.1021/ja064380l

Ke, X., Zhang, J., Dai, K., Fan, K., & Liang, C. (2021). Integrated S-Scheme Heterojunction of Amine-Functionalized 1D CdSe Nanorods Anchoring on Ultrathin 2D SnNb2O6 Nanosheets for Robust Solar-Driven CO2 Conversion. *Solar RRL, 5*(4), 2000805. doi:https://doi.org/10.1002/solr.202000805

Khazaei, M., Mishra, A., Venkataramanan, N. S., Singh, A. K., & Yunoki, S. (2019). Recent advances in MXenes: From fundamentals to applications. *Curr. Opin. Solid State Mater. Sci., 23*(3), 164-178. doi:10.1016/j.cossms.2019.01.002

Kianfar, P., Vitale, A., Dalle Vacche, S., & Bongiovanni, R. (2021). Enhancing properties and water resistance of PEO-based electrospun nanofibrous membranes by photo-crosslinking. *J. Mater. Sci. Technol., 56*(2), 1879-1896. doi:10.1007/s10853-020-05346-3

Kodama, H. (1980). Individual.

Kong, X.-J., He, T., Zhou, J., Zhao, C., Li, T.-C., Wu, X.-Q., . . . Li, J.-R. (2021). In Situ Porphyrin Substitution in a Zr(IV)-MOF for Stability Enhancement and Photocatalytic CO2 Reduction. *Small, 17*(22), 2005357. doi:https://doi.org/10.1002/smll.202005357

Kotsilkova, R., Petrova-Doycheva, I., Menseidov, D., Ivanov, E., Paddubskaya, A., & Kuzhir, P. (2019). Exploring thermal annealing and graphene-carbon nanotube additives to enhance crystallinity, thermal, electrical and tensile

properties of aged poly(lactic) acid-based filament for 3D printing. *Compos. Sci. Technol.*

, 181, 107712. doi:https://doi.org/10.1016/j.compscitech.2019.107712

Kroke, E., Schwarz, M., Horath-Bordon, E., Kroll, P., Noll, B., & Norman, A. D. (2002). Tri-s-triazine derivatives. Part I. From trichloro-tri-s-triazine to graphitic C3N4 structures. *New J Chem, 26*(5), 508-512. doi:10.1039/B111062B

Krongauz, V. V., & Trifunac, A. D. (2013). *Processes in Photoreactive Polymers*: Springer US.

Kruzelak, J., Kvasnicakova, A., Hlozekova, K., & Hudec, I. (2021). Progress in polymers and polymer composites used as efficient materials for EMI shielding. *Nanoscale Adv, 3*(1), 123-172. doi:10.1039/d0na00760a

Kurtoglu, M., Naguib, M., Gogotsi, Y., & Barsoum, M. W. (2012). First principles study of two-dimensional early transition metal carbides. *MRS Communications, 2*(4), 133-137. doi:10.1557/mrc.2012.25

Lai, H., Peng, X., Li, L., Zhu, D., & Xiao, P. (2022). Novel monomers for photopolymer networks. *Prog. Polym. Sci., 128*, 101529. doi:https://doi.org/10.1016/j.progpolymsci.2022.101529

Lakkala, P., Munnangi, S. R., Bandari, S., & Repka, M. (2023). Additive manufacturing technologies with emphasis on stereolithography 3D printing in pharmaceutical and medical applications: A review. *Int J Pharm X, 5*, 100159. doi:10.1016/j.ijpx.2023.100159

Lalevée, J., Fouassier, J., Graff, B., Zhang, J., & Xiao, P. (2018). Chapter 6. How to Design Novel Photoinitiators for Blue Light. In (pp. 179-199).

Lantean, S., Barrera, G., Pirri, C. F., Tiberto, P., Sangermano, M., Roppolo, I., & Rizza, G. (2019). 3D Printing of Magnetoresponsive Polymeric Materials with Tunable Mechanical and Magnetic Properties by Digital Light Processing. *Adv. Mater. Technol., 4*(11). doi:10.1002/admt.201900505

Lantean, S., Roppolo, I., Sangermano, M., Hayoun, M., Dammak, H., Barrera, G., . . . Rizza, G. (2022). Magnetoresponsive Devices with Programmable Behavior Using a Customized Commercial Stereolithographic 3D Printer. *Adv. Mater. Technol.* doi:10.1002/admt.202200288

Lantean, S., Roppolo, I., Sangermano, M., Pirri, C., & Chiappone, A. (2018). Development of New Hybrid Acrylic/Epoxy DLP-3D Printable Materials. *Inventions, 3*(2). doi:10.3390/inventions3020029

Layani, M., Wang, X., & Magdassi, S. (2018). Novel Materials for 3D Printing by Photopolymerization. *Adv. Mater., 30*(41), 1706344. doi:https://doi.org/10.1002/adma.201706344

Lee, M., Rizzo, R., Surman, F., & Zenobi-Wong, M. (2020). Guiding Lights: Tissue Bioprinting Using Photoactivated Materials. *Chem Rev, 120*(19), 10950-11027. doi:10.1021/acs.chemrev.0c00077

Lee, M. P., Cooper, G. J. T., Hinkley, T., Gibson, G. M., Padgett, M. J., & Cronin, L. (2015). Development of a 3D printer using scanning projection stereolithography. *Sci. Rep., 5*(1), 9875. doi:10.1038/srep09875

Lee, S. Y., Kang, D., Jeong, S., Do, H. T., & Kim, J. H. (2020). Photocatalytic Degradation of Rhodamine B Dye by TiO(2) and Gold Nanoparticles Supported on a Floating Porous Polydimethylsiloxane Sponge under Ultraviolet and Visible Light Irradiation. *ACS Omega, 5*(8), 4233-4241. doi:10.1021/acsomega.9b04127

Lewis, J. A., & Gratson, G. M. (2004). Direct writing in three dimensions. *Mater. Today, 7*(7-8), 32-39. doi:10.1016/s1369-7021(04)00344-x

Li, H., Fan, W., & Zhu, X. (2020). Three-dimensional printing: The potential technology widely used in medical fields. *J. Biomed. Mater. Res. Part A, 108*(11), 2217-2229. doi:https://doi.org/10.1002/jbm.a.36979

Li, M., Lu, J., Luo, K., Li, Y., Chang, K., Chen, K., . . . Huang, Q. (2019). Element Replacement Approach by Reaction with Lewis Acidic Molten Salts to Synthesize Nanolaminated MAX Phases and MXenes. *J Am Chem Soc, 141*(11), 4730-4737. doi:10.1021/jacs.9b00574

Li, N., Tong, K., Yang, L., & Du, X. (2022). Review of 3D printing in photocatalytic substrates and catalysts. *Mater. Today Ener., 29*. doi:10.1016/j.mtener.2022.101100

Li, T., Chen, T., Shen, X., Shi, H. H., Jabari, E., & Naguib, H. E. (2022). A binder jet 3D printed MXene composite for strain sensing and energy storage application. *Nanoscale Adv., 4*(3), 916-925. doi:10.1039/d1na00698c

Li, T., Jabari, E., McLellan, K., & Naguib, H. E. (2023). Review of additive manufacturing with 2D MXene: techniques, applications, and future perspectives. *Prog. Addit. Manuf., 8*(6), 1587-1617. doi:10.1007/s40964-023-00424-9

Li, X., Yu, J., Jaroniec, M., & Chen, X. (2019). Cocatalysts for Selective Photoreduction of CO2 into Solar Fuels. *Chem Rev, 119*(6), 3962-4179. doi:10.1021/acs.chemrev.8b00400

Li, X., & Zhitomirsky, I. (2020). Deposition of poly(methyl methacrylate) and composites containing bioceramics and bioglass by dip coating using isopropanol-water co-solvent. *Prog. Org. Coat., 148*, 105883. doi:https://doi.org/10.1016/j.porgcoat.2020.105883

Li, Y., Kankala, R. K., Chen, A. Z., & Wang, S. B. (2022). 3D Printing of Ultrathin MXene toward Tough and Thermally Resistant Nanocomposites. *Nanomaterials (Basel), 12*(16). doi:10.3390/nano12162862

Li, Y., Lv, K., Ho, W., Dong, F., Wu, X., & Xia, Y. (2017). Hybridization of rutile TiO2 (rTiO2) with g-C3N4 quantum dots (CN QDs): An efficient visible-light-driven Z-scheme hybridized photocatalyst. *Appl. Catal., B, 202*, 611-619. doi:https://doi.org/10.1016/j.apcatb.2016.09.055

Li, Y., Shao, H., Lin, Z., Lu, J., Liu, L., Duployer, B., . . . Huang, Q. (2020). A general Lewis acidic etching route for preparing MXenes with enhanced electrochemical performance in non-aqueous electrolyte. *Nat Mater, 19*(8), 894-899. doi:10.1038/s41563-020-0657-0

Li, Y., Wang, L., Yin, S., & Yang, F. (2013). Crystallization behavior of amorphous silicon nitride added with silicon powder. *Mater. Chem. Phys., 141*(2-3), 874-881.

Li, Y., Wang, W., Wu, F., & Kankala, R. K. (2023). Vat polymerization-based 3D printing of nanocomposites: A mini review. *Front. Mater., 9*. doi:10.3389/fmats.2022.1118943

Li, Z., Wang, L., Sun, D., Zhang, Y., Liu, B., Hu, Q., & Zhou, A. (2015). Synthesis and thermal stability of two-dimensional carbide MXene Ti_3C_2. *Mater. Sci. Eng. B, 191*, 33-40. doi:10.1016/j.mseb.2014.10.009

Lian, Q., Yang, F., Xin, H., & Li, D. (2017). Oxygen-controlled bottom-up mask-projection stereolithography for ceramic 3D printing. *Ceram. Internat., 43*(17), 14956-14961. doi:10.1016/j.ceramint.2017.08.014

Liang, Q., Cui, S., Liu, C., Xu, S., Yao, C., & Li, Z. (2019). Self-assembly of triptycene-based polymer on cadmium sulfide nanorod to construct core-shell nanostructure for efficient visible-light-driven photocatalytic H2 evolution. *Chem Eng J 364*, 102-110. doi:https://doi.org/10.1016/j.cej.2019.01.167

Ligon, S. C., Liska, R., Stampfl, J., Gurr, M., & Mulhaupt, R. (2017). Polymers for 3D Printing and Customized Additive Manufacturing. *Chem Rev, 117*(15), 10212-10290. doi:10.1021/acs.chemrev.7b00074

Lim, K. R. G., Shekhirev, M., Wyatt, B. C., Anasori, B., Gogotsi, Y., & Seh, Z. W. (2022). Fundamentals of MXene synthesis. *Nat. Synth., 1*(8), 601-614. doi:10.1038/s44160-022-00104-6

Lim, K. S., Klotz, B. J., Lindberg, G. C. J., Melchels, F. P. W., Hooper, G. J., Malda, J., . . . Woodfield, T. B. F. (2019). Visible Light Cross-Linking of Gelatin Hydrogels Offers an Enhanced Cell Microenvironment with Improved Light Penetration Depth. *Macromol. Biosci., 19*(6), 1900098. doi:https://doi.org/10.1002/mabi.201900098

Lim, K. S., Schon, B. S., Mekhileri, N. V., Brown, G. C. J., Chia, C. M., Prabakar, S., . . . Woodfield, T. B. F. (2016). New Visible-Light Photoinitiating System for Improved Print Fidelity in Gelatin-Based Bioinks. *ACS Biomater Sci Eng, 2*(10), 1752-1762. doi:10.1021/acsbiomaterials.6b00149

Lin, J. T., Liu, H. W., Chen, K. T., & Cheng, D. C. (2019). Modeling the Kinetics, Curing Depth, and Efficacy of Radical-Mediated Photopolymerization: The Role of Oxygen Inhibition, Viscosity, and Dynamic Light Intensity. *Front Chem, 7*, 760. doi:10.3389/fchem.2019.00760

Ling, Z., Ren, C. E., Zhao, M. Q., Yang, J., Giammarco, J. M., Qiu, J., . . . Gogotsi, Y. (2014). Flexible and conductive MXene films and nanocomposites with high capacitance. *Proc Natl Acad Sci U S A, 111*(47), 16676-16681. doi:10.1073/pnas.1414215111

Lipatov, A., Alhabeb, M., Lukatskaya, M. R., Boson, A., Gogotsi, Y., & Sinitskii, A. (2016). Effect of Synthesis on Quality, Electronic Properties and Environmental Stability of Individual Monolayer Ti$_3$C$_2$MXene Flakes. *Adv. Electron. Mater., 2*(12). doi:10.1002/aelm.201600255

Liska, R., Schuster, M., Inführ, R., Turecek, C., Fritscher, C., Seidl, B., . . . Stampfl, J. (2007). Photopolymers for rapid prototyping. *JCTR, 4*(4), 505-510. doi:10.1007/s11998-007-9059-3

Liu, H.-J., & Dong, B. (2021). Recent advances and prospects of MXene-based materials for electrocatalysis and energy storage. *Mater. Today Phys., 20*. doi:10.1016/j.mtphys.2021.100469

Liu, J., Zhang, H.-B., Sun, R., Liu, Y., Liu, Z., Zhou, A., & Yu, Z.-Z. (2017). Hydrophobic, Flexible, and Lightweight MXene Foams for High-Performance Electromagnetic-Interference Shielding. *Adv. Mater., 29*(38), 1702367. doi:https://doi.org/10.1002/adma.201702367

Liu, L., Ying, G., Zhao, Y., Li, Y., Wu, Y., Wen, D., . . . Wang, C. (2021). Attapulgite-MXene Hybrids with Ti(3)C(2)T(x) Lamellae Surface Modified by Attapulgite as a Mechanical Reinforcement for Epoxy Composites. *Polymers (Basel), 13*(11). doi:10.3390/polym13111820

Liu, R., & Li, W. (2018). High-Thermal-Stability and High-Thermal-Conductivity $Ti_3C_2T_x$ MXene/Poly(vinyl alcohol) (PVA) Composites. *ACS Omega, 3*(3), 2609-2617. doi:10.1021/acsomega.7b02001

Liu, Y., Hu, Q., Zhang, F., Tuck, C., Irvine, D., Hague, R., . . . Wildman, R. D. (2016). Additive Manufacture of Three Dimensional Nanocomposite Based Objects through Multiphoton Fabrication. *Polymers (Basel), 8*(9). doi:10.3390/polym8090325

Lukatskaya, M. R., Kota, S., Lin, Z., Zhao, M.-Q., Shpigel, N., Levi, M. D., . . . Gogotsi, Y. (2017). Ultra-high-rate pseudocapacitive energy storage in two-dimensional transition metal carbides. *Nat. Energy, 2*(8), 17105. doi:10.1038/nenergy.2017.105

Luo, W., Ma, Y., Li, T., Thabet, H. K., Hou, C., Ibrahim, M. M., . . . Guo, Z. (2022). Overview of MXene/conducting polymer composites for supercapacitors. *J. Energy Storage, 52*. doi:10.1016/j.est.2022.105008

Maleski, K., Ren, C. E., Zhao, M. Q., Anasori, B., & Gogotsi, Y. (2018). Size-Dependent Physical and Electrochemical Properties of Two-Dimensional MXene Flakes. *ACS Appl Mater Interfaces, 10*(29), 24491-24498. doi:10.1021/acsami.8b04662

Malucelli, G., Priola, A., Sangermano, M., Amerio, E., Zini, E., & Fabbri, E. (2005). Hybrid nanocomposites containing silica and PEO segments:

preparation through dual-curing process and characterization. *Polymer, 46*(9), 2872-2879. doi:10.1016/j.polymer.2005.02.045

Manapat, J. Z., Chen, Q., Ye, P., & Advincula, R. C. (2017). 3D Printing of Polymer Nanocomposites via Stereolithography. *Macromol. Mater. Eng., 302*(9), 1600553. doi:https://doi.org/10.1002/mame.201600553

Maruyama, T., Hirata, H., Furukawa, T., & Maruo, S. (2020). Multi-material microstereolithography using a palette with multicolor photocurable resins. *Optical Materials Express, 10*(10), 2522-2532. doi:10.1364/OME.401810

Mashtalir, O., Naguib, M., Mochalin, V. N., Dall'Agnese, Y., Heon, M., Barsoum, M. W., & Gogotsi, Y. (2013). Intercalation and delamination of layered carbides and carbonitrides. *Nat Commun, 4*, 1716. doi:10.1038/ncomms2664

Maturi, M., Pulignani, C., Locatelli, E., Vetri Buratti, V., Tortorella, S., Sambri, L., & Comes Franchini, M. (2020). Phosphorescent bio-based resin for digital light processing (DLP) 3D-printing. *Green Chem., 22*(18), 6212-6224. doi:10.1039/D0GC01983F

Mayerhöfer, T. G., Pahlow, S., & Popp, J. (2020). The Bouguer-Beer-Lambert Law: Shining Light on the Obscure. *Chemphyschem, 21*(18), 2029-2046. doi:10.1002/cphc.202000464

Mazzanti, V., Malagutti, L., & Mollica, F. (2019). FDM 3D Printing of Polymers Containing Natural Fillers: A Review of their Mechanical Properties. *Polymers (Basel), 11*(7). doi:10.3390/polym11071094

Medina, D. A. V., Figuerola, A., Rodriguez, F., Santos-Neto, Á. J., Cabello, C. P., Palomino, G. T., . . . Maya, F. (2019). Hyperporous carbon-coated 3D printed devices. *Appl. Mater. Today, 14*, 29-34. doi:https://doi.org/10.1016/j.apmt.2018.11.001

Mei, H., Huang, W., Liu, H., Pan, L., & Cheng, L. (2019). 3D printed carbon-ceramic structures for enhancing photocatalytic properties. *Ceram. Int., 45*(12), 15223-15229. doi:https://doi.org/10.1016/j.ceramint.2019.05.008

Melchels, F. P., Feijen, J., & Grijpma, D. W. (2010). A review on stereolithography and its applications in biomedical engineering. *Biomater, 31*(24), 6121-6130. doi:10.1016/j.biomaterials.2010.04.050

Meshkian, R., Näslund, L.-Å., Halim, J., Lu, J., Barsoum, M. W., & Rosen, J. (2015). Synthesis of two-dimensional molybdenum carbide, Mo 2 C, from the gallium based atomic laminate Mo 2 Ga 2 C. *Scr. Mater., 108*, 147-150. doi:10.1016/j.scriptamat.2015.07.003

Mohamed, A., Yousef, S., Nasser, W. S., Osman, T. A., Knebel, A., Sánchez, E. P. V., & Hashem, T. (2020). Rapid photocatalytic degradation of phenol from water using composite nanofibers under UV. *Environ. Sci. Eur., 32*(1), 160. doi:10.1186/s12302-020-00436-0

Mondschein, R. J., Kanitkar, A., Williams, C. B., Verbridge, S. S., & Long, T. E. (2017). Polymer structure-property requirements for stereolithographic 3D printing of soft tissue engineering scaffolds. *Biomater, 140*, 170-188. doi:10.1016/j.biomaterials.2017.06.005

Mun, S. J., Shim, Y. H., Kim, G. W., Koo, S. H., Ahn, H., Shin, T. J., . . . Kim, S. Y. (2021). Tailored growth of graphene oxide liquid crystals with controlled polymer crystallization in GO-polymer composites. *Nanoscale, 13*(4), 2720-2727. doi:10.1039/d0nr07858a

Naguib, M. (2014). *MXenes: A New Family of Two-Dimensional Materials and its Application as Electrodes for Li- ion Batteries.* (PhD Thesis). Drexel University,

Naguib, M., Halim, J., Lu, J., Cook, K. M., Hultman, L., Gogotsi, Y., & Barsoum, M. W. (2013). New Two-Dimensional Niobium and Vanadium Carbides as Promising Materials for Li-Ion Batteries. *J. Am. Chem. Soc., 135*(43), 15966-15969. doi:10.1021/ja405735d

Naguib, M., Kurtoglu, M., Presser, V., Lu, J., Niu, J., Heon, M., . . . Barsoum, M. W. (2011). Two-dimensional nanocrystals produced by exfoliation of Ti_3AlC_2. *Adv. Mater., 23*(37), 4248-4253. doi:10.1002/adma.201102306

Naguib, M., Mashtalir, O., Carle, J., Presser, V., Lu, J., Hultman, L., . . . Barsoum, M. W. (2012). Two-Dimensional Transition Metal Carbides. *ACS Nano, 6*(2), 1322-1331. doi:10.1021/nn204153h

Naguib, M., Mochalin, V. N., Barsoum, M. W., & Gogotsi, Y. (2014). *25th anniversary article: MXenes: a new family of two-dimensional materials* (1521-4095 (Electronic)

0935-9648 (Linking)). Retrieved from https://www.ncbi.nlm.nih.gov/pubmed/24357390

Naguib, M., Mochalin, V. N., Barsoum, M. W., & Gogotsi, Y. (2014). 25th Anniversary Article: MXenes: A New Family of Two-Dimensional Materials. *Adv. Mater., 26*(7), 992-1005. doi:https://doi.org/10.1002/adma.201304138

Naik, T. P., Singh, I., & Sharma, A. K. (2022). Processing of polymer matrix composites using microwave energy: A review. *Compos. Part A Appl. Sci. Manuf., 156*. doi:10.1016/j.compositesa.2022.106870

Nair, D. P., Cramer, N. B., Scott, T. F., Bowman, C. N., & Shandas, R. (2010). Photopolymerized thiol-ene systems as shape memory polymers. *Polymer, 51*(19), 4383-4389. doi:https://doi.org/10.1016/j.polymer.2010.07.027

Nakata, K., & Fujishima, A. (2012). TiO$_2$ photocatalysis: Design and applications. *J. Photochem. Photobiol. C: Photochem., 13*(3), 169-189. doi:10.1016/j.jphotochemrev.2012.06.001

Narupai, B., & Nelson, A. (2020). 100th Anniversary of Macromolecular Science Viewpoint: Macromolecular Materials for Additive Manufacturing. *ACS Macro Lett, 9*(5), 627-638. doi:10.1021/acsmacrolett.0c00200

Nasrazadani, S., & Hassani, S. (2016). Chapter 2 - Modern analytical techniques in failure analysis of aerospace, chemical, and oil and gas industries. In A. S. H. Makhlouf & M. Aliofkhazraei (Eds.), *Handbook of Materials Failure Analysis with Case Studies from the Oil and Gas Industry* (pp. 39-54): Butterworth-Heinemann.

Nazir, A., Abate, K. M., Kumar, A., & Jeng, J.-Y. (2019). A state-of-the-art review on types, design, optimization, and additive manufacturing of cellular structures. *J. Adv. Manuf. Technol, 104*(9-12), 3489-3510. doi:10.1007/s00170-019-04085-3

Ng, W. L., Lee, J. M., Zhou, M., Chen, Y. W., Lee, K. A., Yeong, W. Y., & Shen, Y. F. (2020). Vat polymerization-based bioprinting-process, materials, applications and regulatory challenges. *Biofabrication, 12*(2), 022001. doi:10.1088/1758-5090/ab6034

Nguyen, A. K., & Narayan, R. J. (2017). Two-photon polymerization for biological applications. *Mater. Today, 20*(6), 314-322. doi:10.1016/j.mattod.2017.06.004

Nguyen, C.-C., Vu, N.-N., Chabot, S., Kaliaguine, S., & Do, T.-O. (2017). Role of CxNy-Triazine in Photocatalysis for Efficient Hydrogen Generation and Organic Pollutant Degradation Under Solar Light Irradiation. *Solar RRL, 1*(5), 1700012. doi:https://doi.org/10.1002/solr.201700012

Nguyen, C. C., Vu, N. N., & Do, T.-O. (2015). Recent advances in the development of sunlight-driven hollow structure photocatalysts and their applications. *J. Mater. Chem. A., 3*(36), 18345-18359. doi:10.1039/C5TA04326C

Nguyen, D., Murialdo, M., Hornbostel, K., Pang, S., Ye, C., Smith, W., . . . Stolaroff, J. (2019). 3D Printed Polymer Composites for CO2 Capture. *Ind. Eng. Chem. Res., 58*(48), 22015-22020. doi:10.1021/acs.iecr.9b04375

Nguyen Thi, T. B., Ata, S., Morimoto, T., Kato, Y., Horibe, M., Yamada, T., . . . Hata, K. (2022). Annealing-induced enhancement of electrical conductivity and electromagnetic interference shielding in injection-molded CNT polymer composites. *Polymer, 245*, 124680. doi:https://doi.org/10.1016/j.polymer.2022.124680

Nicholson, J. W. (2012). *The chemistry of polymers / John W. Nicholson* (4th ed.). Cambridge: RSC Pub.

Noè, C., Tonda-Turo, C., Chiappone, A., Sangermano, M., & Hakkarainen, M. (2020). Light Processable Starch Hydrogels. *Polymers, 12*(6), 1359. Retrieved from https://www.mdpi.com/2073-4360/12/6/1359

Ohtsuki, A., Goto, A., & Kaji, H. (2012). Visible-Light-Induced Reversible Complexation Mediated Living Radical Polymerization of Methacrylates with Organic Catalysts. *Macromol., 46*(1), 96-102. doi:10.1021/ma302244j

Oleinik, E. F. (1987). Glassy Polymers as Matrices for Advanced Composites. *Polym J, 19*(1), 105-117. doi:10.1295/polymj.19.105

Ong, W.-J., Putri, L. K., Tan, Y.-C., Tan, L.-L., Li, N., Ng, Y. H., . . . Chai, S.-P. (2017). Unravelling charge carrier dynamics in protonated g-C3N4 interfaced with carbon nanodots as co-catalysts toward enhanced photocatalytic CO2 reduction: A combined experimental and first-principles DFT study. *Nano Research, 10*(5), 1673-1696. doi:10.1007/s12274-016-1391-4

P. M. Ajayan, L. Schadler, & Braun, P. V. (2003). *Nanocomposite Science and Technology*. New York: Wiley.

Pagac, M., Hajnys, J., Ma, Q. P., Jancar, L., Jansa, J., Stefek, P., & Mesicek, J. (2021). A Review of Vat Photopolymerization Technology: Materials, Applications, Challenges, and Future Trends of 3D Printing. *Polymers (Basel), 13*(4). doi:10.3390/polym13040598

Palmas, S., Castresana, P. A., Mais, L., Vacca, A., Mascia, M., & Ricci, P. C. (2016). TiO2–WO3 nanostructured systems for photoelectrochemical applications. *RSC Adv, 6*(103), 101671-101682. doi:10.1039/C6RA18649A

Pan, Y., Fu, L., Zhou, Q., Wen, Z., Lin, C. T., Yu, J., . . . Zhao, H. (2019). Flammability, thermal stability and mechanical properties of polyvinyl alcohol nanocomposites reinforced with delaminated $Ti_3C_2T_x$ (MXene). *Polym. Comp., 41*(1), 210-218. doi:10.1002/pc.25361

Parajuli, D., Murali, N., K, C. D., Karki, B., Samatha, K., Kim, A. A., . . . Pant, B. (2022). Advancements in MXene-Polymer Nanocomposites in Energy Storage and Biomedical Applications. *Polymers (Basel), 14*(16). doi:10.3390/polym14163433

Park, S., Shou, W., Makatura, L., Matusik, W., & Fu, K. (2022). 3D printing of polymer composites: Materials, processes, and applications. *Matter, 5*(1), 43-76. doi:https://doi.org/10.1016/j.matt.2021.10.018

Park, Y.-J., Lim, D.-H., Kim, H.-J., Joo, H.-S., & Do, H.-S. (2012). Curing Behavior and Adhesion Performance of UV-Curable Styrene–Isoprene–Styrene-Based Pressure-Sensitive Adhesives. *J. Adhes. Sci., 22*(13), 1401-1423. doi:10.1163/156856108x309549

Pastorek, M., & Kovalcik, A. (2018). Effects of thermal annealing as polymer processing step on poly(lactic acid). *Mater. Manuf. Process., 33*(15), 1674-1680. doi:10.1080/10426914.2018.1453153

Patel, D. K., Sakhaei, A. H., Layani, M., Zhang, B., Ge, Q., & Magdassi, S. (2017). Highly Stretchable and UV Curable Elastomers for Digital Light Processing Based 3D Printing. *Adv. Mater., 29*(15), 1606000. doi:https://doi.org/10.1002/adma.201606000

Peer, G., Dorfinger, P., Koch, T., Stampfl, J., Gorsche, C., & Liska, R. (2018). Photopolymerization of Cyclopolymerizable Monomers and Their Application in Hot Lithography. *Macromol., 51*(22), 9344-9353. doi:10.1021/acs.macromol.8b01991

Peng, C., Yang, X., Li, Y., Yu, H., Wang, H., & Peng, F. (2016). Hybrids of Two-Dimensional Ti_3C_2 and TiO_2 Exposing {001} Facets toward Enhanced Photocatalytic Activity. *ACS Appl Mater Interfaces, 8*(9), 6051-6060. doi:10.1021/acsami.5b11973

Peng, X., Kong, L., Fuh, J. Y. H., & Wang, H. (2021). A Review of Post-Processing Technologies in Additive Manufacturing. *J. manuf. mater., 5*(2). doi:10.3390/jmmp5020038

Persch, C., Müller, M. J., Yadav, A., Pries, J., Honné, N., Kerres, P., . . . Wuttig, M. (2021). The potential of chemical bonding to design crystallization and vitrification kinetics. *Nat Commun, 12*(1), 4978. doi:10.1038/s41467-021-25258-3

Pezzana, L., Melilli, G., Guigo, N., Sbirrazzuoli, N., & Sangermano, M. (2023). Cross-Linking of Biobased Monofunctional Furan Epoxy Monomer by Two Steps Process, UV Irradiation and Thermal Treatment. *Macromol. Chem. Phys., 224*(1), 2200012. doi:https://doi.org/10.1002/macp.202200012

Porcu, S., Castellino, M., Roppolo, I., Carbonaro, C. M., Palmas, S., Mais, L., . . . Ricci, P. C. (2020). Highly efficient visible light phenyl modified carbon nitride/TiO_2 photocatalyst for environmental applications. *Appl. Surf. Sci., 531*. doi:10.1016/j.apsusc.2020.147394

Porcu, S., Roppolo, I., Salaun, M., Sarais, G., Barbarossa, S., Casula, M. F., . . . Ricci, P. C. (2020). Come to light: Detailed analysis of thermally treated Phenyl modified Carbon Nitride Polymorphs for bright phosphors in lighting applications. *Appl. Surf. Sci., 504*. doi:10.1016/j.apsusc.2019.144330

Porcu, S., Secci, F., Abdullah, Q. A., & Ricci, P. C. (2021). 4-Nitrophenol Efficient Photoreduction from Exfoliated and Protonated Phenyl-Doped Graphitic Carbon Nitride Nanosheets. *Polymers (Basel), 13*(21). doi:10.3390/polym13213752

Porcu, S., Secci, F., & Ricci, P. C. (2022). Advances in Hybrid Composites for Photocatalytic Applications: A Review. *Molecules, 27*(20). doi:10.3390/molecules27206828

Posthumus, W., Magusin, P. C., Brokken-Zijp, J. C., Tinnemans, A. H., & van der Linde, R. (2004). Surface modification of oxidic nanoparticles using 3-methacryloxypropyltrimethoxysilane. *J. Colloid Interface Sci, 269*(1), 109-116. doi:10.1016/j.jcis.2003.07.008

Preethi, L. K., Antony, R. P., Mathews, T., Walczak, L., & Gopinath, C. S. (2017). A Study on Doped Heterojunctions in TiO(2) Nanotubes: An Efficient Photocatalyst for Solar Water Splitting. *Sci Rep, 7*(1), 14314. doi:10.1038/s41598-017-14463-0

Qin, L., Tao, Q., Liu, X., Fahlman, M., Halim, J., Persson, P. O. Å., . . . Zhang, F. (2019). Polymer-MXene composite films formed by MXene-facilitated electrochemical polymerization for flexible solid-state microsupercapacitors. *Nano Energy, 60*, 734-742. doi:10.1016/j.nanoen.2019.04.002

Rahman, M. A. (2014). A Review on Semiconductors Including Applications and Temperature Effects in Semiconductors. *ASRJETS, 7*, 50-70.

Rakhi, R. B., Ahmed, B., Hedhili, M. N., Anjum, D. H., & Alshareef, H. N. (2015). Effect of Postetch Annealing Gas Composition on the Structural and Electrochemical Properties of Ti_2CT_x MXene Electrodes for Supercapacitor Applications. *Chem. Mater., 27*(15), 5314-5323. doi:10.1021/acs.chemmater.5b01623

Rakhi, R. B., Nayak, P., Xia, C., & Alshareef, H. N. (2016). Novel amperometric glucose biosensor based on MXene nanocomposite. *Sci Rep, 6*, 36422. doi:10.1038/srep36422

Rasaki, S. A., Xiong, D., Xiong, S., Su, F., Idrees, M., & Chen, Z. (2021). Photopolymerization-based additive manufacturing of ceramics: A systematic review. *J. Adv. Ceram., 10*(3), 442-471. doi:10.1007/s40145-021-0468-z

Rathna, T., PonnanEttiyappan, J., & D, R. (2021). Fabrication of visible-light assisted TiO2-WO3-PANI membrane for effective reduction of chromium

(VI) in photocatalytic membrane reactor. *Environ. Technol. Innov., 24*, 102023. doi:https://doi.org/10.1016/j.eti.2021.102023

Ravi Kumar, Y., Deshmukh, K., Mohamed Naseer Ali, M., Rajabathar, J. R., Theerthagiri, J., Pandey, M., & Pasha, S. K. K. (2022). Structure defects and electronic properties of MXenes. In *MXenes and their Composites* (pp. 91-129).

Regehly, M., Garmshausen, Y., Reuter, M., König, N. F., Israel, E., Kelly, D. P., . . . Hecht, S. (2020). Xolography for linear volumetric 3D printing. *Nature, 588*(7839), 620-624. doi:10.1038/s41586-020-3029-7

Rehman, S., Ullah, R., Butt, A. M., & Gohar, N. D. (2009). Strategies of making TiO2 and ZnO visible light active. *J. Hazard. Mater., 170*(2), 560-569. doi:https://doi.org/10.1016/j.jhazmat.2009.05.064

Rekowska, N., Wulf, K., Koper, D., Senz, V., Seitz, H., Grabow, N., & Teske, M. (2023). Influence of PEGDA Molecular Weight and Concentration on the In Vitro Release of the Model Protein BSA–FITC from Photo Crosslinked Systems. *Pharmaceutics, 15*(4), 1039. Retrieved from https://www.mdpi.com/1999-4923/15/4/1039

Ren, Y., Yu, C., Tan, X., Wei, Q., Wang, Z., Ni, L., . . . Qiu, J. (2022). Strategies to activate inert nitrogen molecules for efficient ammonia electrosynthesis: current status, challenges, and perspectives. *Energy Environ. Sci., 15*(7), 2776-2805. doi:10.1039/D2EE00358A

Riccucci, G., Pezzana, L., Lantean, S., Tori, A., Spriano, S., & Sangermano, M. (2021). Investigation of the Thermal Conductivity of Silicon-Base Composites: The Effect of Filler Materials and Characteristic on Thermo-Mechanical Response of Silicon Composite. *Appl. Sci., 11*(12). doi:10.3390/app11125663

Rokesh, K., Sakar, M., & Do, T.-O. (2020). Calcium Bismuthate (CaBiO3): A Potential Sunlight-Driven Perovskite Photocatalyst for the Degradation of Emerging Pharmaceutical Contaminants. *ChemPhotoChem, 4*(5), 373-380. doi:https://doi.org/10.1002/cptc.201900265

Rokesh, K., Sakar, M., & Do, T. O. (2021). Emerging Hybrid Nanocomposite Photocatalysts for the Degradation of Antibiotics: Insights into Their Designs and Mechanisms. *Nanomaterials (Basel), 11*(3). doi:10.3390/nano11030572

Roppolo, I., Messori, M., Perruchas, S., Gacoin, T., Boilot, J.-P., & Sangermano, M. (2012). Multifunctional Luminescent Organic/Inorganic Hybrid Films. *Macromol. Mater. Eng. , 297*(7), 680-688. doi:10.1002/mame.201100267

Saeed, M., Usman, M., & Haq, A. (2018). Catalytic Degradation of Organic Dyes in Aqueous Medium. In.

Sajjad, R., Chauhdary, S. T., Anwar, M. T., Zahid, A., Khosa, A. A., Imran, M., & Sajjad, M. H. (2023). A review of 4D printing – Technologies, shape shifting, smart polymer based materials, and biomedical applications. *Adv Ind Eng Polym Res.* doi:10.1016/j.aiepr.2023.08.002

Salas, A., Pazniak, H., Gonzalez-Julian, J., Bianco, S., Amici, J., Ouisse, T., . . . Cocuzza, M. (2023). Development of polymeric/MXenes composites towards 3D printable electronics. *Compos. B Eng.* doi:10.1016/j.compositesb.2023.110854

Salas, A., Zanatta, M., Sans, V., & Roppolo, I. (2023). Chemistry in light-induced 3D printing. *ChemTexts, 9*(1). doi:10.1007/s40828-022-00176-z

Saleh Alghamdi, S., John, S., Roy Choudhury, N., & Dutta, N. K. (2021). Additive Manufacturing of Polymer Materials: Progress, Promise and Challenges. *Polymers (Basel), 13*(5). doi:10.3390/polym13050753

Samadian, H., Maleki, H., Allahyari, Z., & Jaymand, M. (2020). Natural polymers-based light-induced hydrogels: Promising biomaterials for biomedical applications. *Coord. Chem. Rev., 420*. doi:10.1016/j.ccr.2020.213432

Sander van Loon, B. F. (2018). Practical Determination and Application of HSP for the Paints & Coatings Industry. *Special Chem*. Retrieved from https://vlci.biz/wp-content/uploads/2018/07/Practical-Determination-and-Application-of-HSP-for-the-Paints-Coatings-Industry.pdf

Sangermano, M. (2012). Advances in cationic photopolymerization. *Pure Appl. Chem, 84*(10), 2089-2101. doi:10.1351/pac-con-12-04-11

Sangermano, M., Pegel, S., Pötschke, P., & Voit, B. (2008). Antistatic Epoxy Coatings With Carbon Nanotubes Obtained by Cationic Photopolymerization. *Macromol. Rapid Commun., 29*(5), 396-400. doi:10.1002/marc.200700720

Sangermano, M., Roppolo, I., & Chiappone, A. (2018). New Horizons in Cationic Photopolymerization. *Polymers (Basel), 10*(2). doi:10.3390/polym10020136

Saravanan, P., Rajeswari, S., Kumar, J. A., Rajasimman, M., & Rajamohan, N. (2022). Bibliometric analysis and recent trends on MXene research - A comprehensive review. *Chemosphere, 286*(Pt 3), 131873. doi:10.1016/j.chemosphere.2021.131873

Satheeshkumar, E., Makaryan, T., Melikyan, A., Minassian, H., Gogotsi, Y., & Yoshimura, M. (2016). One-step Solution Processing of Ag, Au and Pd@MXene Hybrids for SERS. *Sci Rep, 6*, 32049. doi:10.1038/srep32049

Schwarz, D., Pagac, M., Petrus, J., & Polzer, S. (2022). Effect of Water-Induced and Physical Aging on Mechanical Properties of 3D Printed Elastomeric Polyurethane. *Polymers (Basel), 14*(24). doi:10.3390/polym14245496

Scott, P. J., Meenakshisundaram, V., Hegde, M., Kasprzak, C. R., Winkler, C. R., Feller, K. D., . . . Long, T. E. (2020). 3D Printing Latex: A Route to Complex Geometries of High Molecular Weight Polymers. *ACS Appl Mater Interfaces, 12*(9), 10918-10928. doi:10.1021/acsami.9b19986

Sefene, E. M., Hailu, Y. M., & Tsegaw, A. A. (2022). Metal hybrid additive manufacturing: state-of-the-art. *Prog. Addit. Manuf., 7*(4), 737-749. doi:10.1007/s40964-022-00262-1

Seh, Z. W., Fredrickson, K. D., Anasori, B., Kibsgaard, J., Strickler, A. L., Lukatskaya, M. R., . . . Vojvodic, A. (2016). Two-Dimensional Molybdenum Carbide (MXene) as an Efficient Electrocatalyst for Hydrogen Evolution. *ACS Energy Letters, 1*(3), 589-594. doi:10.1021/acsenergylett.6b00247

Serpone, N., & Emeline, A. V. (2012). Semiconductor Photocatalysis - Past, Present, and Future Outlook. *J Phys Chem Lett, 3*(5), 673-677. doi:10.1021/jz300071j

Shahrubudin, N., Lee, T. C., & Ramlan, R. (2019). An Overview on 3D Printing Technology: Technological, Materials, and Applications. *Procedia Manuf., 35*, 1286-1296. doi:https://doi.org/10.1016/j.promfg.2019.06.089

Shahzad, F., Alhabeb, M., Hatter, C., Anasori, B., Hong, S., Min Koo, C., & Gogotsi, Y. (2016). Electromagnetic interference shielding with 2D transition metal carbides (MXenes). *Mat. Sci, 353*(6304), 1137-1140.

Shakeel Ahmad, M., Pandey, A. K., & Abd Rahim, N. (2017). Advancements in the development of TiO_2 photoanodes and its fabrication methods for dye sensitized solar cell (DSSC) applications. A review. *Renew. Sust. Energ. Rev., 77*, 89-108. doi:https://doi.org/10.1016/j.rser.2017.03.129

Shamsabadi, A. A., Isfahani, A. P., Salestan, S. K., Rahimpour, A., Ghalei, B., Sivaniah, E., & Soroush, M. (2020). Pushing Rubbery Polymer Membranes To Be Economic for CO_2 Separation: Embedment with $Ti_3C_2T_x$ MXene Nanosheets. *ACS Appl Mater Interfaces, 12*(3), 3984-3992. doi:10.1021/acsami.9b19960

Shanmugam, S., Xu, J., & Boyer, C. (2016). Light-Regulated Polymerization under Near-Infrared/Far-Red Irradiation Catalyzed by Bacteriochlorophyll a. *Angew. Chem., Int. Ed. , 55*(3), 1036-1040. doi:https://doi.org/10.1002/anie.201510037

Shanto, M. A. H., Chowdhury, M. I., Antu, A. B., Niloy, N. R., Alam, N., Ullah, M. A., & Anowar, M. S. (2022). MXene based Heterostructures for electrode materials of Batteries: A Review. *IOP Conf. Ser.: Mater. Sci. Eng., 1225*(1), 012018. doi:10.1088/1757-899x/1225/1/012018

Sharma, S., Gupta, V., & Mudgal, D. (2022). Current trends, applications, and challenges of coatings on additive manufacturing based biopolymers: A state of art review. *Polym. Comp., 43*(10), 6749-6781. doi:https://doi.org/10.1002/pc.26809

Shen, H., Shao, Z., Zhao, Q., Jin, M., Shen, C., Deng, M., . . . Luo, Z. (2020). Facile synthesis of novel three-dimensional Bi2S3 nanocrystals capped by polyvinyl pyrrolidone to enhance photocatalytic properties under visible light. *J. Colloid Interface Sci, 573*, 115-122. doi:https://doi.org/10.1016/j.jcis.2020.03.111

Shi, H., Zhang, P., Liu, Z., Park, S., Lohe, M. R., Wu, Y., . . . Feng, X. (2021). Ambient-Stable Two-Dimensional Titanium Carbide (MXene) Enabled by Iodine Etching. *Angew Chem Int Ed Engl, 60*(16), 8689-8693. doi:10.1002/anie.202015627

Shi, Y., Yan, C., Zhou, Y., Wu, J., Wang, Y., Yu, S., & Chen, Y. (2021). Chapter 1 - Overview of additive manufacturing technology and materials. In Y. Shi,

C. Yan, Y. Zhou, J. Wu, Y. Wang, S. Yu, & Y. Chen (Eds.), *Mater. Addit. Manuf.* (pp. 1-8): Academic Press.

Shirmardi, A., Teridi, M. A. M., Azimi, H. R., Basirun, W. J., Jamali-Sheini, F., & Yousefi, R. (2018). Enhanced photocatalytic performance of ZnSe/PANI nanocomposites for degradation of organic and inorganic pollutants. *Appl. Surf. Sci., 462*, 730-738. doi:https://doi.org/10.1016/j.apsusc.2018.06.252

Simon, U., & Dimartino, S. (2019). Direct 3D printing of monolithic ion exchange adsorbers. *J. Chromatogr. A, 1587*, 119-128. doi:https://doi.org/10.1016/j.chroma.2018.12.017

Sol-Gel Processing and Applications. (2012). Springer Book Springer New York, NY.

Soleymaniha, M., Shahbazi, M. A., Rafieerad, A. R., Maleki, A., & Amiri, A. (2019). Promoting Role of MXene Nanosheets in Biomedical Sciences: Therapeutic and Biosensing Innovations. *Adv Healthc Mater, 8*(1), e1801137. doi:10.1002/adhm.201801137

Soloukhin, V. A., Posthumus, W., Brokken-Zijp, J. C. M., Loos, J., & de With, G. (2002). Mechanical properties of silica–(meth)acrylate hybrid coatings on polycarbonate substrate. *Polymer, 43*(23), 6169-6181. doi:https://doi.org/10.1016/S0032-3861(02)00542-6

Sonawane, R. S., Kale, B. B., & Dongare, M. K. (2004). Preparation and photo-catalytic activity of Fe□TiO2 thin films prepared by sol–gel dip coating. *Mater. Chem. Phys., 85*(1), 52-57. doi:https://doi.org/10.1016/j.matchemphys.2003.12.007

Stagi, L., Carbonaro, C. M., Corpino, R., Chiriu, D., & Ricci, P. C. (2015). Light induced TiO2 phase transformation: Correlation with luminescent surface defects. *Phys. Status Solidi B Basic Res., 252*(1), 124-129. doi:https://doi.org/10.1002/pssb.201400080

Stassi, S., Fantino, E., Calmo, R., Chiappone, A., Gillono, M., Scaiola, D., . . . Roppolo, I. (2017). Polymeric 3D Printed Functional Microcantilevers for Biosensing Applications. *ACS Appl Mater Interfaces, 9*(22), 19193-19201. doi:10.1021/acsami.7b04030

Steinbach, F. (2006). Heterogeneous photocatalysis. In *Catal.* (pp. 117-154): Springer.

Strohmeier, L., Frommwald, H., & Schlogl, S. (2020). Digital light processing 3D printing of modified liquid isoprene rubber using thiol-click chemistry. *RSC Adv, 10*(40), 23607-23614. doi:10.1039/d0ra04186f

Sutar, R. S., Barkul, R. P., Delekar, S. D., & Patil, M. K. (2020). Sunlight assisted photocatalytic degradation of organic pollutants using g-C3N4-TiO2 nanocomposites. *Arab. J. Chem., 13*(4), 4966-4977. doi:https://doi.org/10.1016/j.arabjc.2020.01.019

Sycks, D. G., Wu, T., Park, H. S., & Gall, K. (2018). Tough, stable spiroacetal thiol-ene resin for 3D printing. *J. Appl. polym. Sci., 135*(22), 46259. doi:https://doi.org/10.1002/app.46259

Sztorch, B., Brząkalski, D., Pakuła, D., Frydrych, M., Špitalský, Z., & Przekop, R. E. (2022). Natural and Synthetic Polymer Fillers for Applications in 3D Printing—FDM Technology Area. *Solids, 3*(3), 508-548. doi:10.3390/solids3030034

Tang, Q., Zhou, Z., & Shen, P. (2012). Are MXenes promising anode materials for Li ion batteries? Computational studies on electronic properties and Li storage capability of Ti3C2 and Ti3C2X2 (X = F, OH) monolayer. *J Am Chem Soc, 134*(40), 16909-16916. doi:10.1021/ja308463r

Tang, R., Xiong, S., Gong, D., Deng, Y., Wang, Y., Su, L., . . . Liao, C. (2020). Ti3C2 2D MXene: Recent Progress and Perspectives in Photocatalysis. *ACS Appl Mater Interfaces, 12*(51), 56663-56680. doi:10.1021/acsami.0c12905

Tao, N., Zhang, D., Li, X., Lou, D., Sun, X., Wei, C., . . . Liu, Y. N. (2019). Near-infrared light-responsive hydrogels via peroxide-decorated MXene-initiated polymerization. *Chem Sci, 10*(46), 10765-10771. doi:10.1039/c9sc03917a

Taormina, G., Sciancalepore, C., Messori, M., & Bondioli, F. (2018). 3D printing processes for photocurable polymeric materials: technologies, materials, and future trends. *JABFM, 16*(3), 151-160. doi:10.1177/2280800018764770

Taşdemir, M., Şenaslan, F., & Çelik, A. (2021). Investigation of corrosion and thermal behavior of PU–PDMS-coated AISI 316L. *e-Polymers, 21*(1), 355-365. doi:10.1515/epoly-2021-0035

Tetik, H., Orangi, J., Yang, G., Zhao, K., Mujib, S. B., Singh, G., . . . Lin, D. (2022). 3D Printed MXene Aerogels with Truly 3D Macrostructure and Highly Engineered Microstructure for Enhanced Electrical and Electrochemical Performance. *Adv. Mater., 34*(2), e2104980. doi:10.1002/adma.202104980

Tumbleston, J. R., Shirvanyants, D., Ermoshkin, N., Janusziewicz, R., Johnson, A. R., Kelly, D., . . . DeSimone, J. M. (2015). Continuous liquid interface production of 3D objects. *Sci, 347*(6228), 1349-1352. doi:doi:10.1126/science.aaa2397

Urbankowski, P., Anasori, B., Makaryan, T., Er, D., Kota, S., Walsh, P. L., . . . Gogotsi, Y. (2016). Synthesis of two-dimensional titanium nitride Ti_4N_3 (MXene). *Nanoscale, 8*(22), 11385-11391. doi:10.1039/c6nr02253g

Vasques, A. L. Q., Torchynska, T. V., Polupan, G., Matsumoto, Y., Khomenkova, L., & Shcherbyna, L. V. (2008). *Size dependent photoluminescence of Si nano-crystals embedded in amorphous silicon.* Paper presented at the Solid State Phenomena.

Villotte, S., Gigmes, D., Dumur, F., & Lalevee, J. (2019). Design of Iodonium Salts for UV or Near-UV LEDs for Photoacid Generator and Polymerization Purposes. *Molecules, 25*(1). doi:10.3390/molecules25010149

Vitale, A., & Cabral, J. T. (2016). Frontal Conversion and Uniformity in 3D Printing by Photopolymerisation. *Materials (Basel), 9*(9). doi:10.3390/ma9090760

Wan, H., Liu, N., Tang, J., Wen, Q., & Xiao, X. (2021). Substrate-Independent $Ti_3C_2T_x$ MXene Waterborne Paint for Terahertz Absorption and Shielding. *ACS Nano*. doi:10.1021/acsnano.1c04656

Wang, D., Xin, Y., Wang, Y., Li, X., Wu, H., Zhang, W., . . . Lei, X. (2021). A general way to transform Ti3C2Tx MXene into solvent-free fluids for filler phase applications. *J. Chem. Eng., 409*. doi:10.1016/j.cej.2020.128082

Wang, H., Li, H., Chen, Z., Li, J., Li, X., Huo, P., & Wang, Q. (2020). TiO2 modified g-C3N4 with enhanced photocatalytic CO2 reduction performance. *Solid State Sci., 100*, 106099. doi:https://doi.org/10.1016/j.solidstatesciences.2019.106099

Wang, H., Wu, Y., Zhang, J., Li, G., Huang, H., Zhang, X., & Jiang, Q. (2015). Enhancement of the electrical properties of MXene Ti3C2 nanosheets by post-treatments of alkalization and calcination. *Mater. Lett., 160*, 537-540. doi:10.1016/j.matlet.2015.08.046

Wang, H., Zhang, L., Chen, Z., Hu, J., Li, S., Wang, Z., . . . Wang, X. (2014). Semiconductor heterojunction photocatalysts: design, construction, and photocatalytic performances. *Chem Soc Rev, 43*(15), 5234-5244. doi:10.1039/C4CS00126E

Wang, H.-W., Naguib, M., Page, K., Wesolowski, D. J., & Gogotsi, Y. (2015). Resolving the Structure of $Ti_3C_2T_x$ MXenes through Multilevel Structural Modeling of the Atomic Pair Distribution Function. *Chem. Mater., 28*(1), 349-359. doi:10.1021/acs.chemmater.5b04250

Wang, J., Chiappone, A., Roppolo, I., Shao, F., Fantino, E., Lorusso, M., . . . Grutzmacher, H. (2018). All-in-One Cellulose Nanocrystals for 3D Printing of Nanocomposite Hydrogels. *Angew Chem Int Ed Engl, 57*(9), 2353-2356. doi:10.1002/anie.201710951

Wang, J., Wang, G., Cheng, B., Yu, J., & Fan, J. (2021). Sulfur-doped g-C_3N_4/TiO_2 S-scheme heterojunction photocatalyst for Congo Red photodegradation. *Chin J Catal., 42*(1), 56-68. doi:https://doi.org/10.1016/S1872-2067(20)63634-8

Wang, K., Shen, L., Zhu, Q., Bo, R., Lu, R., Lu, X., & Fu, Z. (2023). Construction of modified MXene with "organic–inorganic" structure to enhance the interfacial and mechanical properties of UHMWPE fiber-reinforced epoxy composite. *Chem. Eng. J., 452*. doi:10.1016/j.cej.2022.139156

Wang, L., Zhang, H., Wang, B., Shen, C., Zhang, C., Hu, Q., . . . Liu, B. (2016). Synthesis and electrochemical performance of $Ti_3C_2T_x$ with hydrothermal process. *Electron. Mater. Lett., 12*(5), 702-710. doi:10.1007/s13391-016-6088-z

Wang, Q.-W., Zhang, H.-B., Liu, J., Zhao, S., Xie, X., Liu, L., . . . Yu, Z.-Z. (2019). Multifunctional and Water-Resistant MXene-Decorated Polyester Textiles with Outstanding Electromagnetic Interference Shielding and Joule Heating Performances. *Adv. Funct. Mater., 29*(7), 1806819. doi:https://doi.org/10.1002/adfm.201806819

Wang, X., Guo, Q., Cai, X., Zhou, S., Kobe, B., & Yang, J. (2014). Initiator-Integrated 3D Printing Enables the Formation of Complex Metallic Architectures. *ACS Appl Mater Interfaces, 6*(4), 2583-2587. doi:10.1021/am4050822

Warr, C., Valdoz, J. C., Bickham, B. P., Knight, C. J., Franks, N. A., Chartrand, N., . . . Cook, A. D. (2020). Biocompatible PEGDA Resin for 3D Printing. *ACS Appl Bio Mater, 3*(4), 2239-2244. doi:10.1021/acsabm.0c00055

Wazalwar, R., Tripathi, M., & Raichur, A. M. (2022). Curing Behavior and Mechanical Properties of Tetra-Functional Epoxy Reinforced with Polyethyleneimine-Functionalized MXene. *ACS Appl. Polym. Mater., 4*(4), 2573-2584. doi:10.1021/acsapm.1c01876

Wee, A. T., Hersam, M. C., Chhowalla, M., & Gogotsi, Y. (2016). An Update from Flatland. *ACS Nano, 10*(9), 8121-8123. doi:10.1021/acsnano.6b06087

Wei, J., Liao, M., Ma, A., Chen, Y., Duan, Z., Hou, X., . . . Yu, J. (2020). Enhanced thermal conductivity of polydimethylsiloxane composites with carbon fiber. *Compos. Commun., 17*, 141-146. doi:10.1016/j.coco.2019.12.004

Wei, M., Sun, L., Qi, P., Chang, C., & Zhu, C. (2018). Continuous phenomenological modeling for the viscosity of shear thickening fluids. *NANOMATER NANOTECHNO, 8*, 1847980418786551. doi:10.1177/1847980418786551

Wu, H., Sun, Q., Chen, J., Wang, G.-Y., Wang, D., Zeng, X.-F., & Wang, J.-X. (2021). Citric acid-assisted ultrasmall CeO_2 nanoparticles for efficient photocatalytic degradation of glyphosate. *J. Chem. Eng., 425*, 130640. doi:https://doi.org/10.1016/j.cej.2021.130640

Wu, Y., Wu, X., Lu, R., Li, M., Toro, L., & Stefani, E. (2016). Super-Resolution Light Microscopy: Stimulated Emission Depletion and Ground-State Depletion. In R. A. Bradshaw, G. W. Hart, & P. D. Stahl (Eds.), *Encyclopedia of Cell Biology (Second Edition)* (pp. 93-104). Oxford: Academic Press.

Xia, P., Cao, S., Zhu, B., Liu, M., Shi, M., Yu, J., & Zhang, Y. (2020). Designing a 0D/2D S-Scheme Heterojunction over Polymeric Carbon Nitride for Visible-Light Photocatalytic Inactivation of Bacteria. *Angew. Chem. Int. Ed., 59*(13), 5218-5225. doi:https://doi.org/10.1002/anie.201916012

Xu, C., Ravi Anusuyadevi, P., Aymonier, C., Luque, R., & Marre, S. (2019). Nanostructured materials for photocatalysis. *Ceram. Internat., 48*(14), 3868-3902. doi:10.1039/C9CS00102F

Xu, C., Wang, L., Liu, Z., Chen, L., Guo, J., Kang, N., . . . Ren, W. (2015). Large-area high-quality 2D ultrathin Mo_2C superconducting crystals. *Nat Mater, 14*(11), 1135-1141. doi:10.1038/nmat4374

Xu, J., Shanmugam, S., Fu, C., Aguey-Zinsou, K. F., & Boyer, C. (2016). Selective Photoactivation: From a Single Unit Monomer Insertion Reaction to Controlled Polymer Architectures. *J Am Chem Soc, 138*(9), 3094-3106. doi:10.1021/jacs.5b12408

Xu, X., Zhang, H., Diao, Q., Yongsheng, Z., Yang, G., & Ma, B. (2020). Highly sensitive fluorescent sensing for intracellular glutathione based on Ti3C2 quantum dots. *J. Mater. Sci.: Mater. Electron., 31*, 1-7. doi:10.1007/s10854-019-02682-2

Yagci, Y. (2006). Photoinitiated Cationic Polymerization of Unconventional Monomers. *Macromol. Symp, 240*(1), 93-101. doi:https://doi.org/10.1002/masy.200650812

Yagci, Y., Jockusch, S., & Turro, N. J. (2010). Photoinitiated Polymerization: Advances, Challenges, and Opportunities. *Macromol., 43*(15), 6245-6260. doi:10.1021/ma1007545

Yağci, Y., & Reetz, I. (1998). Externally stimulated initiator systems for cationic polymerization. *Prog. Polym. Sci., 23*(8), 1485-1538. doi:https://doi.org/10.1016/S0079-6700(98)00010-0

Yan, S. C., Li, Z. S., & Zou, Z. G. (2009). Photodegradation Performance of g-C3N4 Fabricated by Directly Heating Melamine. *Langmuir, 25*(17), 10397-10401. doi:10.1021/la900923z

Yang, H., He, D., Liu, C., Zhang, T., Qu, J., Jin, D., . . . Zhang, Y.-n. (2022). Visible-light-driven photocatalytic disinfection by S-scheme α-Fe2O3/g-C3N4 heterojunction: Bactericidal performance and mechanism insight. *Chemosphere, 287*, 132072. doi:https://doi.org/10.1016/j.chemosphere.2021.132072

Yang, J., Naguib, M., Ghidiu, M., Pan, L.-M., Gu, J., Nanda, J., . . . Barsoum, M. W. (2016). Two-Dimensional Nb-Based M_4C_3 Solid Solutions (MXenes). *J. Am. Ceram. Soc., 99*(2), 660-666. doi:https://doi.org/10.1111/jace.13922

Yang, J.-H., Han, Y.-S., & Choy, J.-H. (2006). TiO2 thin-films on polymer substrates and their photocatalytic activity. *Thin Solid Films, 495*(1), 266-271. doi:https://doi.org/10.1016/j.tsf.2005.08.195

Yang, L., & Kruse, B. (2004). Revised Kubelka–Munk theory. I. Theory and application. *Journal of the Optical Society of America A, 21*(10), 1933-1941. doi:10.1364/JOSAA.21.001933

Yang, R., Song, G., Wang, L., Yang, Z., Zhang, J., Zhang, X., . . . Yu, X. (2021). Full Solar-Spectrum-Driven Antibacterial Therapy over Hierarchical Sn3O4/PDINH with Enhanced Photocatalytic Activity. *Small, 17*(39), 2102744. doi:https://doi.org/10.1002/smll.202102744

Yang, R., Zhong, S., Zhang, L., & Liu, B. (2020). PW12/CN@Bi2WO6 composite photocatalyst prepared based on organic-inorganic hybrid system for removing pollutants in water. *Sep. Purif. Technol., 235*, 116270. doi:https://doi.org/10.1016/j.seppur.2019.116270

Yang, S., Zhang, P., Wang, F., Ricciardulli, A. G., Lohe, M. R., Blom, P. W. M., & Feng, X. (2018). Fluoride-Free Synthesis of Two-Dimensional Titanium Carbide (MXene) Using A Binary Aqueous System. *Angew. Chem. Int. Ed., 57*(47), 15491-15495. doi:https://doi.org/10.1002/anie.201809662

Yang, W., Yang, J., Byun, J. J., Moissinac, F. P., Xu, J., Haigh, S. J., . . . Barg, S. (2019). 3D Printing of Freestanding MXene Architectures for Current-Collector-Free Supercapacitors. *Adv. Mater., 31*(37), e1902725. doi:10.1002/adma.201902725

Yang, Y., Zhou, Y., Lin, X., Yang, Q., & Yang, G. S. (2020). Printability of External and Internal Structures Based on Digital Light Processing 3D Printing Technique. *Pharmaceutics, 12*, 207. doi:10.3390/pharmaceutics12030207

Yin, Z., Lu, Z., Xu, Y., Zhang, Y., He, L., Li, P., . . . Wang, H. (2021). Supported MXene/GO Composite Membranes with Suppressed Swelling for Metal Ion Sieving. *Membranes (Basel), 11*(8). doi:10.3390/membranes11080621

Ying, Y., Liu, Y., Wang, X., Mao, Y., Cao, W., Hu, P., & Peng, X. (2015). Two-dimensional titanium carbide for efficiently reductive removal of highly

toxic chromium(VI) from water. *ACS Appl Mater Interfaces, 7*(3), 1795-1803. doi:10.1021/am5074722

Yousif, E., & Haddad, R. (2013). Photodegradation and photostabilization of polymers, especially polystyrene: review. *Springerplus, 2*, 398. doi:10.1186/2193-1801-2-398

Yu, C., Schimelman, J., Wang, P., Miller, K. L., Ma, X., You, S., . . . Chen, S. (2020). Photopolymerizable Biomaterials and Light-Based 3D Printing Strategies for Biomedical Applications. *Chem Rev, 120*(19), 10695-10743. doi:10.1021/acs.chemrev.9b00810

Zang, S., Zhang, G., Lan, Z.-A., Zheng, D., & Wang, X. (2019). Enhancement of photocatalytic H2 evolution on pyrene-based polymer promoted by MoS2 and visible light. *Applied Catalysis B: Environmental, 251*, 102-111. doi:https://doi.org/10.1016/j.apcatb.2019.03.061

Zeng, W., Cai, T., Liu, Y., Wang, L., Dong, W., Chen, H., & Xia, X. (2020). An artificial organic-inorganic Z-scheme photocatalyst WO3@Cu@PDI supramolecular with excellent visible light absorption and photocatalytic activity. *J. Chem. Eng., 381*, 122691. doi:https://doi.org/10.1016/j.cej.2019.122691

Zeranska-Chudek, K., Lapinska, A., Siemion, A., Jastrzębska, A. M., & Zdrojek, M. (2020). Terahertz time domain spectroscopy of graphene and MXene polymer composites. *J. Appl. polym. Sci., 138*(10). doi:10.1002/app.49962

Zhakeyev, A., Jones, M. C., Thomson, C. G., Tobin, J. M., Wang, H., Vilela, F., & Xuan, J. (2021). Additive manufacturing of intricate and inherently photocatalytic flow reactor components. *Addit. Manuf., 38*. doi:10.1016/j.addma.2020.101828

Zhan, X., Yan, C., Zhang, Y., Rinke, G., Rabsch, G., Klumpp, M., . . . Dittmeyer, R. (2020). Investigation of the reaction kinetics of photocatalytic pollutant degradation under defined conditions with inkjet-printed TiO2 films – from batch to a novel continuous-flow microreactor. *React. Chem. Eng., 5*. doi:10.1039/d0re00238k

Zhang, C. J., McKeon, L., Kremer, M. P., Park, S. H., Ronan, O., Seral-Ascaso, A., . . . Nicolosi, V. (2019). Additive-free MXene inks and direct printing

of micro-supercapacitors. *Nat Commun, 10*(1), 1795. doi:10.1038/s41467-019-09398-1

Zhang, H. (2015). Ultrathin Two-Dimensional Nanomaterials. *ACS Nano, 9*(10), 9451-9469. doi:10.1021/acsnano.5b05040

Zhang, H., Li, M., Cao, J., Tang, Q., Kang, P., Zhu, C., & Ma, M. (2018). 2D a-Fe2O3 doped Ti3C2 MXene composite with enhanced visible light photocatalytic activity for degradation of Rhodamine B. *Ceram. Internat., 44*(16), 19958-19962. doi:10.1016/j.ceramint.2018.07.262

Zhang, J., Kong, N., Uzun, S., Levitt, A., Seyedin, S., Lynch, P. A., . . . Razal, J. M. (2020). Scalable Manufacturing of Free-Standing, Strong Ti3C2Tx MXene Films with Outstanding Conductivity. *Adv. Mater., 32*(23), 2001093. doi:https://doi.org/10.1002/adma.202001093

Zhang, J., Lalevée, J., Zhao, J., Graff, B., Stenzel, M. H., & Xiao, P. (2016). Dihydroxyanthraquinone derivatives: natural dyes as blue-light-sensitive versatile photoinitiators of photopolymerization. *Polym. Chem., 7*(47), 7316-7324. doi:10.1039/c6py01550f

Zhang, J., Wan, L., Gao, Y., Fang, X., Lu, T., Pan, L., & Xuan, F. (2019). Highly Stretchable and Self-Healable MXene/Polyvinyl Alcohol Hydrogel Electrode for Wearable Capacitive Electronic Skin. *Adv. Electron. Mater., 5*(7). doi:10.1002/aelm.201900285

Zhang, J., & Xiao, P. (2018). 3D printing of photopolymers. *Polym. Chem., 9*(13), 1530-1540. doi:10.1039/c8py00157j

Zhang, K., Zhou, W., Zhang, X., Sun, B., Wang, L., Pan, K., . . . Fu, H. (2017). Self-floating amphiphilic black TiO2 foams with 3D macro-mesoporous architectures as efficient solar-driven photocatalysts. *Appl. Catal., 206*, 336-343. doi:10.1016/j.apcatb.2017.01.059

Zhang, L., Shi, X., Zhang, Z., Kuchel, R. P., Namivandi-Zangeneh, R., Corrigan, N., . . . Boyer, C. (2021). Porphyrinic Zirconium Metal–Organic Frameworks (MOFs) as Heterogeneous Photocatalysts for PET-RAFT Polymerization and Stereolithography. *Angew. Chem., Int. Ed. , 60*(10), 5489-5496. doi:https://doi.org/10.1002/anie.202014208

Zhang, X., Tian, F., Lan, X., Liu, Y., Yang, W., Zhang, J., & Yu, Y. (2022). Building P-doped MoS2/g-C3N4 layered heterojunction with a dual-

internal electric field for efficient photocatalytic sterilization. *J. Chem. Eng., 429*, 132588. doi:https://doi.org/10.1016/j.cej.2021.132588

Zhang, Y., Pan, Q., Chai, G., Liang, M., Dong, G., Zhang, Q., & Qiu, J. (2013). Synthesis and luminescence mechanism of multicolor-emitting g-C3N4 nanopowders by low temperature thermal condensation of melamine. *Sci. Rep., 3*(1), 1943. doi:10.1038/srep01943

Zhang, Y.-F., Ng, C. J.-X., Chen, Z., Zhang, W., Panjwani, S., Kowsari, K., . . . Ge, Q. (2019). Miniature Pneumatic Actuators for Soft Robots by High-Resolution Multimaterial 3D Printing. *Adv. Mater. Technol., 4*(10), 1900427. doi:https://doi.org/10.1002/admt.201900427

Zhao, T., Li, X., Yu, R., Zhang, Y., Yang, X., Zhao, X., . . . Huang, W. (2018). Silicone–Epoxy-Based Hybrid Photopolymers for 3D Printing. *Macromol. Chem. Phys., 219*(10), 1700530. doi:https://doi.org/10.1002/macp.201700530

Zheng, Y., Lin, L., Wang, B., & Wang, X. (2015). Graphitic Carbon Nitride Polymers toward Sustainable Photoredox Catalysis. *Angew. Chem. Int. Ed., 54*(44), 12868-12884. doi:https://doi.org/10.1002/anie.201501788

Zhou, J., Allonas, X., Ibrahim, A., & Liu, X. (2019). Progress in the development of polymeric and multifunctional photoinitiators. *Prog. Polym. Sci., 99*. doi:10.1016/j.progpolymsci.2019.101165

Zhou, J., Zha, X., Chen, F. Y., Ye, Q., Eklund, P., Du, S., & Huang, Q. (2016). A Two-Dimensional Zirconium Carbide by Selective Etching of Al_3C_3 from Nanolaminated $Zr_3Al_3C_5$. *Angew. Chem. Int. Ed., 55*(16), 5008-5013. doi:https://doi.org/10.1002/anie.201510432

Zhou, T., Wu, C., Wang, Y., Tomsia, A. P., Li, M., Saiz, E., . . . Cheng, Q. (2020). Super-tough MXene-functionalized graphene sheets. *Nat Commun, 11*(1), 2077. doi:10.1038/s41467-020-15991-6

Zhu, Y.-P., Yin, J., Abou-Hamad, E., Liu, X., Chen, W., Yao, T., . . . Alshareef, H. N. (2020). Highly Stable Phosphonate-Based MOFs with Engineered Bandgaps for Efficient Photocatalytic Hydrogen Production. *Adv. Mater., 32*(16), 1906368. doi:https://doi.org/10.1002/adma.201906368

Appendix A

At the beginning, the main purpose of including TMPSM in the formulation was not only the possibility of experimentation with sol-gel reactions, but also to form later glassy polymers. This part of the project is found here, as there were no satisfactory results apart from their great resolution after the thermal post-treatment considering the degradation of the hybrid system past these temperatures.

The first figure shows complementary structures, printed with increased TMSPM concentrations.

Figure SI-0.1. 3D Printed Mole Antonelliana. 80%TMSPM

TMSPM rheology

The next image also included rheology from the chosen formulations in Chapter 5, confirming their Newtonian behavior under this shear rate range and very similar viscosity and shear stress though neat PEGDA results are slightly lower.
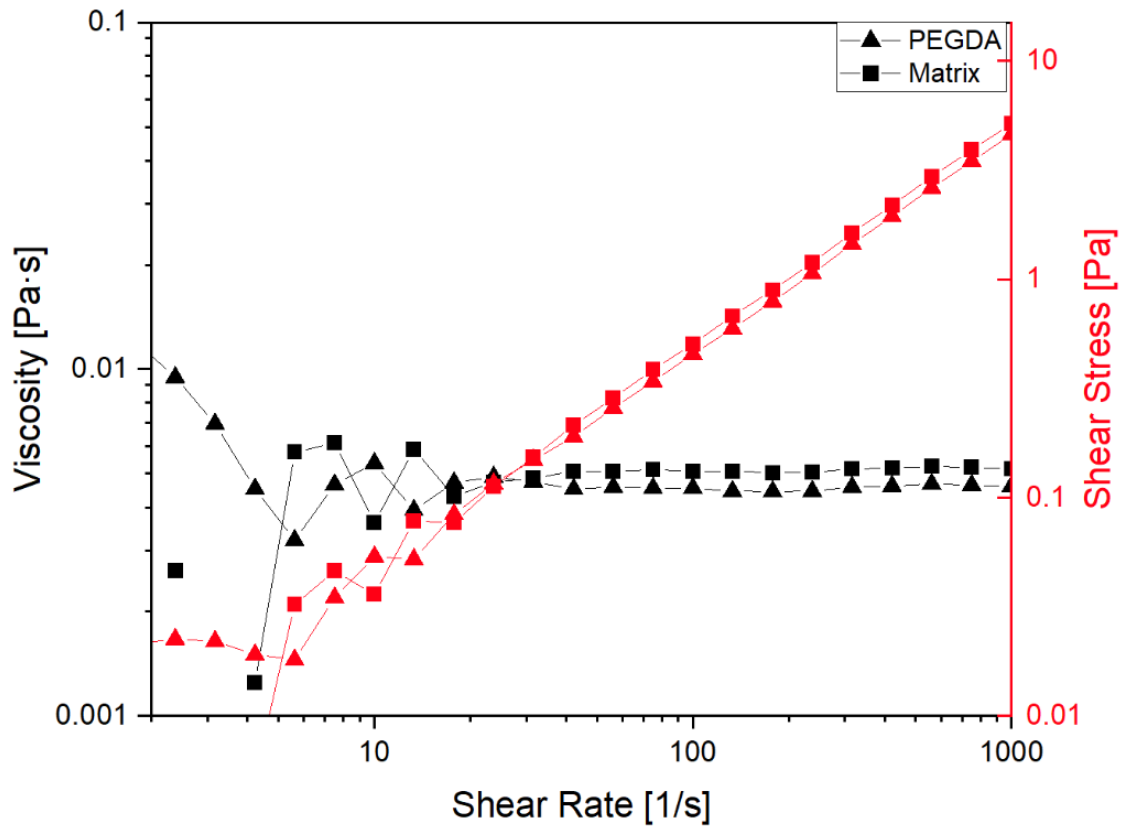

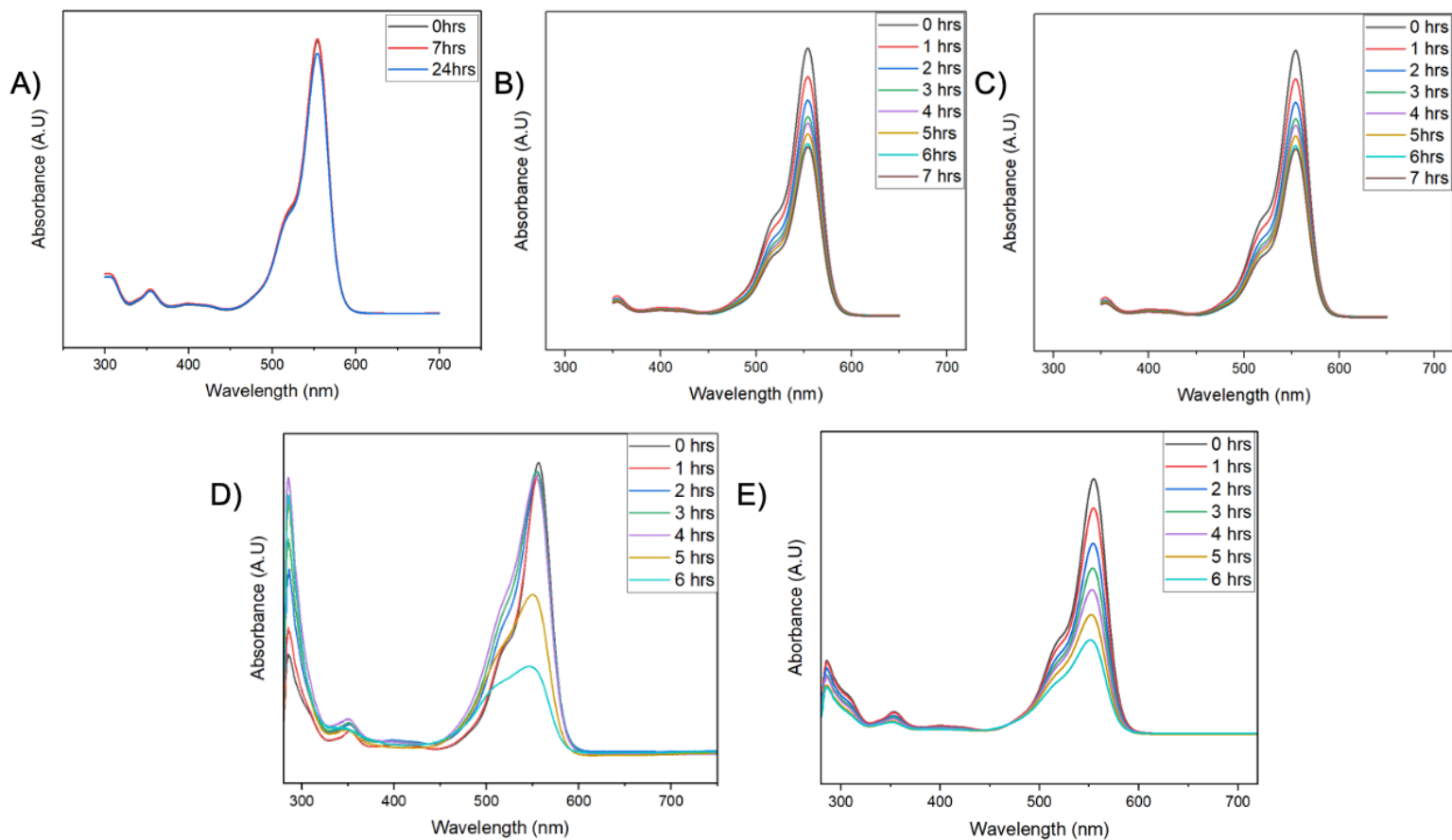Figure SI-0.2. Rheology profile PEGDA & TMPSM 58%

UV-Vis Liquid Spectra

Figure SI- 0.3.UV-Vis Spectra of RhB in solution with the different treatments and after the respective time exposed to LED light. A) RhB by itself. B) Composite (Matrix+10% HS). C) Neat Matrix. D) HS as Coating (Dip Coating). E) HS with Enhanced Attachment (Dip coating+Autoclave).

XRD of the Si-composites (Glassy polymers)

The XRD shows that the matrix follows a thermoset behavior, by showing a broad peak corresponding to amorphous polymers. However, this peak near 23º increases its intensity after the thermal treatment concerning the increased concentration of Silane or silicon species (Yanhui Li, Wang, Yin, & Yang, 2013; Vasques et al., 2008) after the given carbon degradation at high temperatures. The same effect has been seen in the EDS results after the FESEM characterizations and confirmed in the next figure by the XPS.
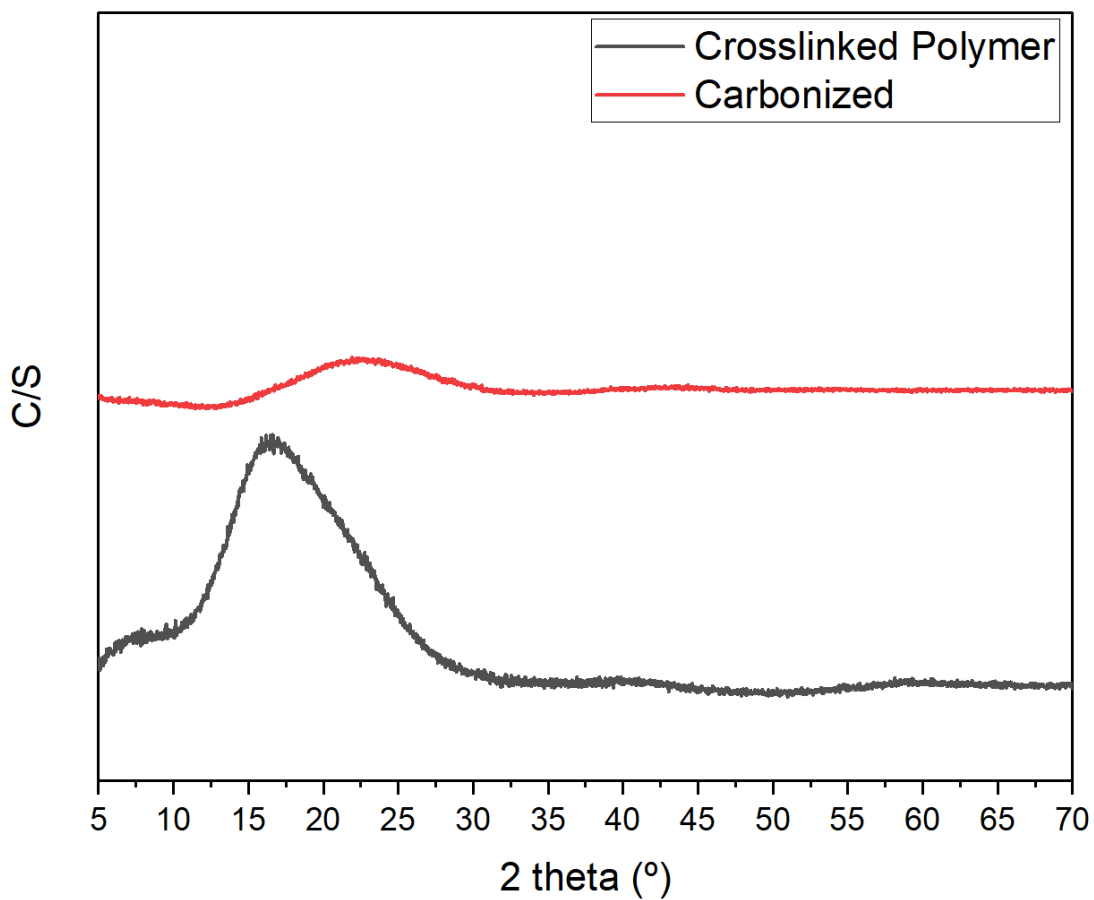

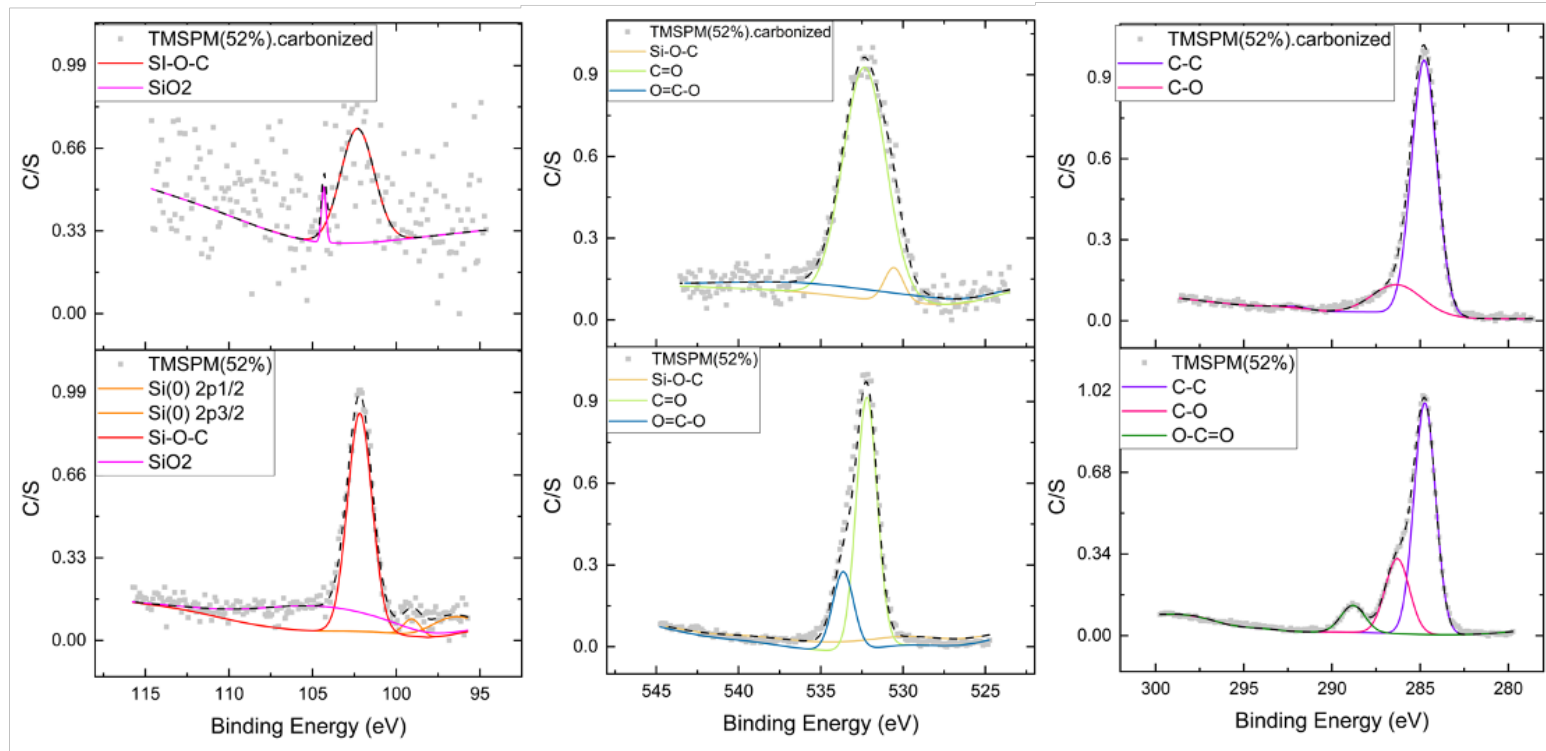Figure SI-0.4. XRD Polymeric matrix (58%TMPSM) & Glassy version

XPS (Glassy polymers)

Figure SI-0.5. XPS Polymeric Matrix (52%TMPSM) & Glassy version